



**EXPERIMENTAL UNCERTAINTY ASSOCIATED WITH TRAVELING WAVE
EXCITATION**

DISSERTATION

Geofrey S. Cox, Major, USAF

AFIT-ENY-DS-14-S-26

**DEPARTMENT OF THE AIR FORCE
AIR UNIVERSITY**

AIR FORCE INSTITUTE OF TECHNOLOGY

Wright-Patterson Air Force Base, Ohio

DISTRIBUTION STATEMENT A:
APPROVED FOR PUBLIC RELEASE; DISTRIBUTION UNLIMITED

The views expressed in this dissertation are those of the author and do not reflect the official policy or position of the United States Air Force, the Department of Defense, or the United States Government.

This material is declared a work of the U.S. Government and is not subject to copyright protection in the United States.

AFIT-ENY-DS-14-S-26

EXPERIMENTAL UNCERTAINTY ASSOCIATED WITH TRAVELING WAVE
EXCITATION

DISSERTATION

Presented to the Faculty
Graduate School of Engineering and Management
Air Force Institute of Technology
Air University
Air Education and Training Command
in Partial Fulfillment of the Requirements for the
Degree of Doctor of Philosophy in Aeronautical Engineering

Geofrey S. Cox, B.S.M.E., M.S.A.E.
Major, USAF

September 2014

DISTRIBUTION STATEMENT A:
APPROVED FOR PUBLIC RELEASE; DISTRIBUTION UNLIMITED

EXPERIMENTAL UNCERTAINTY ASSOCIATED WITH TRAVELING WAVE
EXCITATION

DISSERTATION

Geofrey S. Cox, B.S.M.E., M.S.A.E.
Major, USAF

Approved:

<u>/signed/</u> Anthony N. Palazotto, Ph.D. (Chairman)	<u>28 Aug 2014</u> Date
<u>/signed/</u> William P. Baker, Ph.D. (Member)	<u>27 Aug 2014</u> Date
<u>/signed/</u> Dursun A. Bulutoglu, Ph.D. (Member)	<u>27 Aug 2014</u> Date
<u>/signed/</u> Joseph A. Beck, Ph.D. (Member)	<u>25 Aug 2014</u> Date

Accepted:

<u>/signed/</u> A.B. Badiru Ph.D. PE Dean, Graduate School of Engineering and Management	<u>4 Sept 2014</u> Date
--	----------------------------

Abstract

This dissertation research produces the experimental techniques required to evaluate mistuning in any rotor. Within operation, a rotor is subjected to a unique pattern of frequencies acting to excite the rotor. Utilizing traveling wave excitation, a rotor's critical frequencies and the respective excitation pattern are reproduced. Individual rotor blade frequency response functions are evaluated and statistically analyzed. The experimental results serve to not only verify the degree to which a rotor is mistuned, but also to provide an indication of the forced response amplification the mistuning induces. Within the experiment, definitive specifications were developed to ensure peak rotor responses.

Numerical simulations of the experiment were performed in ANSYS using a model developed by way of structured light scanning. With experimental and numerical eigenvalue differences of less than 1%, the unique modeling technique, capturing a rotor's geometric mistuning, is a valid method to predict a rotor's natural frequencies. Furthermore these same numerical results serve to validate the experimental free boundary assumption.

To my wife

Acknowledgments

Above all else, I have to thank The Lord above to affording me this opportunity. I must also extend a sincere and gracious thanks to the men and women of the AFRL Turbine Engine Fatigue Facility: Dr. Tommy George, Dr. Onome Scott-Emuakpor, Mr. John Justice, Mrs. Angie Still, Mr. Phil Johnson, Mr. Bryan Langley, and Mr. Casey Holycross. Not only did you teach me the ways of the traveling wave, but you taught me to enjoy some of the finer things in life, such as the double-decker-pliance jump and its associated debris. You guys helped me maintain my sanity over the past three years. I would also like to thank Lt Col (ret) James M. Greer, Jr., Ph.D. As my academic advisor during my time at the Air Force Academy, you reinforced my love for the hard sciences. You continued to teach and mentor me even after I left the Academy. And for that, I will be forever grateful to you. I find it rather interesting how, when I first met you Jim, you began telling me about Dr. Anthony Palazotto - as you received your doctorate under his guidance. Little did I know that some ten years later, I too would be doing the same. With that being said, Dr. P, you have taught me so very much over the past three years. You believed in me sir, and like I said, over these past few years, you've been the closest thing I have had to a dad. Thank you sir; I will never forget what you've done for me.

Geofrey S. Cox

Table of Contents

	Page
Abstract	iv
Dedication	v
Acknowledgments	vi
Table of Contents	vii
List of Figures	xi
List of Tables	xviii
List of Acronyms	xxi
 I. Introduction	 1
1.1 Research Goal and Contribution	1
1.2 Motivation	2
1.3 Research Challenges	3
1.4 Dissertation Structure and Research Plan	4
 II. Literature Review	 6
2.1 Mistuning Defined	6
2.1.1 Physical Impact of Mistuning	7
2.1.2 Impact of Mistuning in the Frequency Domain	14
2.2 Previous Modeling and Experimental Endeavors	17
2.2.1 Modeling Efforts	17
2.2.1.1 Early Modeling Methods	17
2.2.1.2 Other Modeling Techniques in the Literature	23
2.2.2 Experimental Efforts	27
2.2.3 Stochastic Studies	35
2.3 Capturing Uncertainty	38
 III. Theory	 48
3.1 Cantilever Beam Forced Vibration Response Under the Effects of an Electromagnetic Actuator	48

	Page
3.1.1 Beam Theory for a General Case of Transverse Motion	48
3.1.2 Euler-Bernoulli Beam	49
3.1.2.1 Solution Procedure for the Non-Homogeneous Equation	
3.41	56
3.2 The Free-Free Beam	58
3.2.1 Supported Mode 1 Beam	62
3.2.2 Supported Mode 1 Plate	68
3.3 Structured Light Optical Measurement Technique	71
3.4 Traveling Wave Theory	77
3.5 Traveling Wave Calibration Process	83
3.6 Laser Vibrometer Theory	90
3.7 Developing the Solid Model	94
3.7.1 Merging	95
3.7.2 Decimation	95
3.7.3 Tessellation	96
3.7.4 Final Editing	96
3.7.5 CAD Model Creation	97
3.8 Modal Assurance Criterion	99
3.9 Coordinate Modal Assurance Criterion	100
3.10 Relationship Between Samples in the Time and Frequency Domains	100
3.11 Leakage	101
3.12 Validation Method	104
3.12.1 Degrees of Freedom Discussion	104
3.12.2 Validation Method	105
3.13 Analysis of Variance and Design of Experiments	107
3.13.1 Fixed Effects Model	107
3.13.2 Analysis of Variance	108
3.13.3 Three Factor Fixed Effects Model	111
3.14 Sufficient Sample Size	114
3.15 Cumulative Distribution Function	116
3.16 Cantilever Beam Forced Response Uncertainty Example	117
3.16.0.1 Example Cantilever Beam Properties	117
3.16.0.2 Example Cantilever Beam Forcing Function and Modal	
Information	118
3.16.1 Propagate Input Location Uncertainty	120
3.17 Cantilever Plate Forced Response Uncertainty Example	121
3.17.1 Cantilever Plate Example Properties and Equation	122
3.17.2 Forcing Function Information and Locations	126
3.17.3 Cantilever Plate Forced Response	127

	Page
IV. Experimental Equipment	132
4.1 Purdue Transonic Research Compressor	132
4.2 ATOS 3-D Scanner	133
4.3 Scanning Laser Vibrometer	136
4.4 Traveling Wave Excitation Equipment	137
4.4.0.1 Traveling Wave Excitation Signal Path - From Input Voltage to FRF Generation	142
V. Experimental Work and Related Discussion	154
5.1 Experimental Methodology	154
5.1.1 Initial Experimental Data Acquisition Details	154
5.1.2 Single Scan Point Justification	155
5.2 Effect of Calibration Process	157
5.3 Initial Experimental Results	158
5.3.1 Effect of Experimental Uncertainty	159
5.4 A Method to Produce Consistent Experimental Results	166
5.4.0.1 Centering the Rotor and Input Locations	167
5.4.0.2 Rotor 2D Alignment and Beam Focus	168
5.4.0.3 Scan Point Identification	169
5.4.0.4 Appropriate Scan Time Identification	178
5.4.0.5 New Experimental Data Acquisition Parameters	181
5.4.1 Experimental Results and Discussion	181
5.4.2 Initial Experimental Results	182
5.4.3 Refined Experimental Results	186
5.4.4 Section Conclusion	187
5.5 Summary of Experimental Technique	188
5.6 Mistuning Amplification Factor	191
5.7 The Experimental Free Boundary Condition	200
5.8 Using the Finite Element Model	204
5.8.1 The ANSYS Input File	204
5.8.2 Finite Element Model Exploration and Validation	205
5.9 ANOVA Study and Results	209
5.9.1 Theoretical Cantilever Plate Model: ANOVA Study	225
5.10 Deriving the Experimental Tolerances	227
5.11 Tolerance Generalities	238
5.11.1 Concern 1	238
5.11.2 Concern 2	239
VI. Conclusion, Contributions, and Future Work	242

	Page
Bibliography	248
Appendix A: Frequency Response Functions	257
Appendix B: Previous Authors' Equation Derivations	260
Appendix C: Physical Interpretation of the Statistical Concept of "P-Value"	276
Appendix D: Circular Plate Equation Derivation	277
Appendix E: ANSYS Input File Example	282
Appendix F: Additional Experimental Equipment and Revised Technique	290
Appendix G: Additional Details for the ANOVA Process in Chapter 5.9	292
Vita	299

List of Figures

Figure	Page
2.1 Tuned Rotor Modal Energy Distribution [1]	9
2.2 Mistuned Rotor Modal Energy Distribution [1]	10
2.3 Three Nodal Diameter Mode Shape of a Tuned Bladed Disk [1]	10
2.4 Sample Campbell Diagram [2]	14
2.5 Tuned versus Mistuned FRFs [3]	16
2.6 Transonic Campbell Diagram for 0 Nodal Diameter [2]	17
2.7 Finite Element Mesh for an Industrial Bladed Disk [4]	19
2.8 A Simple Model of a Bladed Disk [5]	20
2.9 Schematic of the Lumped Model [6]	21
2.10 Multiple Coupled Pendulum [7]	27
2.11 Bladed Disk Experimental Model [8]	29
2.12 Experimental Bladed Disk [9]	30
2.13 Closeup of Experimental Blade with Eddy Current Probe [9]	30
2.14 Broach Block and Blade Assembly [10]	32
2.15 Blade Sample points [10]	33
2.16 Second-Order Probability [11]	45
3.1 Supported Beam Example	64
3.2 Beam Schematic	64
3.3 Beam Schematic (L/D)	64
3.4 Isolation Mat with Support Pedestal	67
3.5 Supported Beam Mode 1 (Natural Freq. Within 4.5% of Free Beam)	67
3.6 Supported Plate Example	69
3.7 Supported Plate Schematic	69

Figure	Page
3.8 Supported Plate Schematic (D/d)	69
3.9 1-D Triangulation Schematic [12]	72
3.10 3-D Triangulation Schematic [13]	73
3.11 Structured Light Geometry Types [14]	74
3.12 Early 3D Image Capture Schematic [15]	75
3.13 Direct Projection of Line Patterns - At Right Angle with Observation [16] . . .	76
3.14 0 EO Excitation Forcing Function Pattern	79
3.15 1 EO Excitation Forcing Function Pattern	80
3.16 9 EO Excitation Forcing Function Pattern	80
3.17 EO Excitation Forcing Function Pattern	83
3.18 Actuator Magnitude and Phase [17]	84
3.19 Magnet Standoff Distance Illustration [18]	85
3.20 Effect of Magnet Standoff Distance on Field Strength at the Blade Tip	86
3.21 Traveling Wave Calibration Process	88
3.22 0 EO Forcing Function Pattern with Amplitude and Phase Adjustments	89
3.23 1 EO Forcing Function Pattern with Amplitude and Phase Adjustments	90
3.24 9 EO Forcing Function Pattern with Amplitude and Phase Adjustments	90
3.25 Optical Configuration in the PSV-400 Scanning Head [19]	92
3.26 Example of a Linearly Polarized Signal [20]	92
3.27 Quarter Wave Plate Effect on Beam [20]	93
3.28 Transonic Rotor Point Cloud [21]	96
3.29 Overall Process for Disk Construction	98
3.30 Extracted Airfoil Cross Sections [21]	98
3.31 Overall Process for Blade Construction	98
3.32 Modeled Rotor [21]	99

Figure	Page
3.33 Leakage Discussion: 3 Hz Signal	103
3.34 FFT of 3 Hz Signal, Observed for 30 Seconds	103
3.35 FFT of 3 Hz Signal, Observed for 17.16 Seconds	104
3.36 Example Probability Function	116
3.37 Example Cumulative Distribution Function	117
3.38 Ideal Response for the Cantilever Beam Example	120
3.39 Response Using Perturbed Input Locations for the Cantilever Beam Example .	121
3.40 Cantilever Plate Example [22]	122
3.41 Plate Amplitude Coefficients [22]	124
3.42 Eigenfunction Parameters [22]	124
3.43 Cantilever Plate Example Frequency Response Functions	128
3.44 Cantilever Plate Example Maximum Responses	129
3.45 Cantilever Plate Example Tolerances	131
4.1 Purdue Transonic Research Compressor	133
4.2 Jet Engine Schematic [23]	133
4.3 Projected Light Patterns from ATOS Scanner	134
4.4 ATOS Blue LED Structured Light Scanner [24]	135
4.5 Portion of the Scanning Process [21]	136
4.6 Scanning Laser Vibrometer Position	137
4.7 Magnetic Actuator Ring Beneath Rotor	139
4.8 Rotor Mounted on Pedestal Above Actuator Ring	140
4.9 Actuator Angle Within the Excitation Ring	141
4.10 Traveling Wave Overview Schematic [25]	142
4.11 One Sinusoidal Cycle With 10 Points [25]	144
4.12 Linear Chirp: 1Hz - 11Hz Sweep (First 3 Cycles) [25]	145

Figure	Page
4.13 Example of Multiplied Waveform: 1Hz - 11Hz Sweep [25]	146
4.14 Superimposed Square Wave onto Multiplied Waveform [25]	147
4.15 Stepped Output Waveform [25]	148
4.16 Ideal Frequency Sweep with Stepped Output [25]	149
4.17 All Waveforms for 1-11 Hz Frequency Sweep: 10 points [25]	150
4.18 NI TB-2705 Modules' Output Connection to Amplifiers	151
4.19 Typical Signal Window Arrangement for PolyTec Software	152
5.1 Example Blade Output Locations	156
5.2 Blade Overlap Dimensions	156
5.3 Calibration Convergence Response Curves	158
5.4 Calibration: Blade <i>N</i> Response to Blade <i>N</i> Excitation	158
5.5 Position 1 Magnitude FRFs: 1kHz - 2kHz (0EO)	160
5.6 Position 1 Normalized Responses: 1kHz - 2kHz (0EO)	161
5.7 Position 2 Magnitude FRFs: 1kHz - 2kHz (0EO)	162
5.8 Position 2 Normalized Responses: 1kHz - 2kHz (0EO)	163
5.9 Positions 1 and 2 Magnitude FRFs: 1kHz - 2kHz (0EO)	164
5.10 Alternate View, Positions 1 and 2 Magnitude FRFs: 1kHz - 2kHz (0EO)	165
5.11 Positions 1 and 2 Response Magnitudes at the 18 Resonant Frequencies: 1kHz - 2kHz (0EO)	166
5.12 Actuator Ring Center	168
5.13 Close Up View of Rotor Hub Diameter Reference Marks	171
5.14 Centered Rotor	171
5.15 View of Actuator Below Blade	172
5.16 Sample 2D Alignment Points	172
5.17 Rotor Global Coordinates Schematic	173

Figure	Page
5.18 Rotor Coordinate System Used for Placing Scan Points	176
5.19 Rotor Scan Point Variables	177
5.20 Example Rotor Frequency Response Function	180
5.21 FRFs for the Initial and Re-Positioned Rotor	183
5.22 Natural Frequency Response Magnitude Stem Plots for the Initial and Re- Positioned Rotor	184
5.23 CDF vs Response Magnitude for the Initial and Second Rotor Positions	185
5.24 First Rotor Position Magnitude FRF Using the New Techniques	194
5.25 Second Rotor Position Magnitude FRF Using the New Techniques	194
5.26 First Rotor Position Natural Frequency Responses Using the New Techniques .	195
5.27 Second Rotor Position Natural Frequency Responses Using the New Techniques	195
5.28 CDF vs Response Magnitude for the Initial and Second Rotor Positions Using the New Techniques	196
5.29 Indicating the Frequency Range of Interest	196
5.30 Indicating the Frequency Range of Interest	197
5.31 Tuned FRF for the Purdue Transonic Research Compressor	205
5.32 Comparison Between the Tuned and Mistuned ANSYS FRFs	206
5.33 Single Actuator Stand	211
5.34 Blade Input and Output Regions for the ANOVA	212
5.35 Blade 16 ANOVA Results: 1204.9 Hz and 1EO	218
5.36 Blade 17 ANOVA Results: 1204.9 Hz and 1EO	219
5.37 Average Responses for Multi-Blade ANOVA (Blade 16, 1EO)	220
5.38 Highlighted Frequencies: Average Responses for Multi-Blade ANOVA (Blade 16, 1EO)	220
5.39 Average Responses for Multi-Blade ANOVA (Blade 17, 1EO)	221

Figure	Page
5.40 Highlighted Frequencies: Average Responses for Multi-Blade ANOVA (Blade 17, 1EO)	222
5.41 Average Responses for Multi-Blade ANOVA (Blade 16, 2EO)	223
5.42 Highlighted Frequencies: Average Responses for Multi-Blade ANOVA (Blade 16, 2EO)	223
5.43 Average Responses for Multi-Blade ANOVA (Blade 17, 2EO)	224
5.44 Highlighted Frequencies: Average Responses for Multi-Blade ANOVA (Blade 17, 2EO)	224
5.45 Single Blade Response vs. Solenoid Position	228
5.46 Normalized Single Blade Response vs. Normalized Solenoid Position	229
5.47 Sketch of Validation Blade for Input Tolerances	230
5.48 Input Tolerance Validation Blade: Input Locations	231
5.49 Single Actuator Stand for the Validation Rotors	232
5.50 Input Tolerance Validation Blade: Normalized Single Blade Response vs. Normalized Solenoid Position	233
5.51 Polar Coordinate Input Location	234
5.52 Purdue Rotor Tolerance Schematic	235
5.53 Purdue Rotor Tolerance Schematic With Radial and Angular Measurements	235
A.1 Ideal System FRF	259
B.1 Simple Two Degree of Freedom System	260
B.2 Simple Two Degree of Freedom System Free Body Diagram	261
B.3 Substructuring of a Mistuned Rotor [26]	264
B.4 Characteristic Function Values for the Clamped-Free Beam [27]	271
B.5 Characteristic Function Values for the Free-Free Beam [27]	272
B.6 Plate Coordinate System [22]	273

Figure	Page
B.7 Cantilever Plate Symmetric Mode Coefficients [27]	275
G.1 Blade Input Regions for the ANOVA	292
G.2 Sample Data Table	294
G.3 Highlighted Sample Data Table	294
G.4 Extended Sample Data Table	295
G.5 Highlighted Extended Sample Data Table	296

List of Tables

Table	Page
3.1 Frequency Equation Arguments for a Beam on a Continuous Elastic Foundation	62
3.2 Supported Plate Material and Geometric Properties	63
3.3 Supported Beam Without Isolation Mat	66
3.4 Supported Beam With Isolation Mat	68
3.5 Supported Plate Material and Geometric Properties	70
3.6 Supported Plate Without Isolation Mat	70
3.7 Supported Plate With Isolation Mat	71
3.8 Inter-blade Phase Angle (θ) as Function of EO Excitation for an 18 Bladed Rotor	82
3.9 Confidence and Significance Levels	107
3.10 Definitions of Terms in 3 Factor Fixed Effects Model	112
3.11 ANOVA Table: 3 Factor Fixed Effects Model	113
3.12 Variables for 3 Factor Fixed Effects Model	114
3.13 Mechanical and Geometric Properties for the Example Cantilever Beam	118
3.14 First Ten $\beta_n L$ Terms for a Cantilever Beam	119
3.15 First Ten Natural Frequencies for the Example Cantilever Beam	119
3.16 Mechanical and Geometric Properties: Cantilever Plate Example	125
3.17 Cantilever Plate Natural Frequency Constants	125
3.18 Cantilever Plate Natural Frequencies	126
3.19 Cantilever Plate Input Output Locations	126
3.20 Cantilever Plate Example Normalized Input/Output Location Tolerances	130
4.1 Mechanical Properties for 17-PH Stainless Steel [28]	132
5.1 Data Acquisition Details	155
5.2 Example Global Scan Point Coordinates	175

Table	Page
5.3 Damping Ratio Estimates for Two Different Sweep Rates	192
5.4 Sweep Rate Settling Time Comparison	193
5.5 Modified Acquisition Parameters	194
5.6 Mistuning Amplification Factor After Initial Experimental Techniques	198
5.7 Mistuning Amplification Factor After Refined Experimental Techniques	199
5.8 1kHz-2kHz, 0EO ANSYS and TWE Eigenvalue Comparison	201
5.9 1kHz-2kHz, Additional EO Level ANSYS and TWE Eigenvalue Comparison	202
5.10 7.5kHz-8.5kHz, Additional 0EO Level ANSYS and TWE Eigenvalue Comparison	203
5.11 ANSYS and Experimental Eigenvalue Statistics	207
5.12 ANSYS Finite Element Model Rotor Model Mechanical Properties	208
5.13 Tuned and Mistuned Rotor: Blade First Bending Mode Comparison	209
5.14 Global Scan Points Used for Input-Output ANOVA Test: Increased EO Level	212
5.15 Example Data Collection Table	213
5.16 ANOVA 3: Increased EO Excitation - Main Effects - Rotor A	215
5.17 ANOVA 3: Increased EO Excitation - Main Effects - Rotor B	216
5.18 ANOVA 3: Increased EO Excitation - Main Effects - Rotor C	217
5.19 Theoretical Cantilever Plate Model ANOVA - Mechanical Properties	226
5.20 Theoretical Cantilever Plate Model ANOVA - I/O Locations	226
5.21 Theoretical Cantilever Plate Model ANOVA - Maximum Responses	227
5.22 Theoretical Cantilever Plate Model Resulting ANOVA Table	227
5.23 Input Tolerance Validation Blade: Normalized Dimensions	231
5.24 Input Tolerance Validation Blade: Normalized Input Locations	231
5.25 Global Input Location Positioning Tolerances: Purdue Transonic Research Compressor (Polar)	236

Table	Page
5.26 Global Input Location Positioning Tolerances: Purdue Transonic Research Compressor (Cartesian)	237
D.1 Natural Frequencies of Vibration for a Circular Plate with a Free Edge	281
E.1 Summary of MatLab File Function	283
G.1 DOE Pro Data Organization for ANOVA	297
G.2 Sample ANOVA Table from DOE Pro	298

List of Acronyms

Acronym	Definition
ANOVA	Analysis of Variance
CAD	Computer Aided Design
CCD	Charge Coupled Device
CDA	Controlled Diffusion Airfoil
CDF	Cumulative Distribution Function
CMM	Coordinate Measurement Machine
CNC	Computer Numerical Controlled
COMAC	Coordinate Modal Assurance Criterion
COTS	Commercial off the Shelf
DOE	Design of Experiments
EO	Engine Order
FFT	Fast Fourier Transform
FMM	Fundamental Mistuning Model
FRF	Frequency Response Function
HCF	High Cycle Fatigue
IBR	Integrally Bladed Rotor
MAC	Modal Assurance Criterion
MAF	Mistuning Amplification Factor
MMDA	Modified Modal Domain Approach
PDF	Probability Density Function
PSD	Power Spectral Density
SNM	Subset of Nominal Modes
TWE	Traveling Wave Excitation

EXPERIMENTAL UNCERTAINTY ASSOCIATED WITH TRAVELING WAVE EXCITATION

I. Introduction

In the late 1960s, a new term entered the turbomachinery industry's lexicon. This term was adopted to designate the blade-to-blade variations in both the geometric and material properties within in a bladed disk. These variations became known as *mistuning*.

Mistuning can be attributed to manufacturing and assembly tolerances, non-uniform wear realized during service, or even combinations of these factors. Thus, mistuning is unavoidable in all real bladed disks. As a stochastic phenomenon, mistuning is a random ailment. These small, random variances lead to amplifications in forced response magnitudes over and above what would otherwise be seen in an ideal, or *tuned*, rotor. With these increased forced response magnitudes, strain energy and stress are also increased. In turn, the amplified response can lead to drastically lower service lives.

1.1 Research Goal and Contribution

Using a purpose built research compressor, this research focuses on developing a process to experimentally evaluate mistuning for any rotor. Inside of an engine, other upstream and downstream rotors, and additional engine components, disrupt the incoming airstream. Together with the rotor's angular velocity, the airflow obstructions excite the rotor in a specific manner. This excitation pattern is unique to a rotor. This research utilizes a novel traveling wave setup which mimics the various excitation patterns a specific rotor is subjected to during operation. The experiment offers tremendous flexibility, in that any rotor and excitation pattern can be simulated.

Accounting for the rotor's critical excitation pattern, a specific process will be developed to ensure consistent experimental results when performing the traveling wave excitation experiment. Within the framework of consistent results, experimental input location tolerances and a technique to standardize these tolerances will be developed. During this process, the research compressor's finite element model will be validated using the experimental results. As part of this validation process, the experimental boundary condition assumption will be validated and a method to simulate a free boundary, by way of physical supports, will be developed and validated.

1.2 Motivation

While there are multitudes of academic works discussing various methods to model and predict mistuning, very few focus exclusively on the uncertainty associated with experimentally obtaining such information. As such, the experimental uncertainty is often an afterthought.

Early modeling techniques relied upon crude spring-mass-damper models in order to understand the basic mechanics of mistuning. The models primarily involved varying the blade stiffness values to destroy any inherent cyclic symmetry. As computing power increased, finite element models were developed to determine a mistuned rotor's forced response. It was quickly seen that these models became too cumbersome and large as a pragmatic means of solution. This led to many reduced order modeling methodologies. Even as the physical model size shrank, these models still primarily relied upon perturbing blade stiffness values in order to induce a mistuned condition. A brief overview of some of the various modeling methods is discussed in Section 2.2.1.

A 3-D scanner, utilizing a structured light field, was used to capture a rotor's global geometry and associated primitives. Using a multi-tiered approach, a solid model was developed from the scan data. Motivated by the new capabilities this automated scanner affords, this research focuses on the geometric aspect of mistuning and corresponding

experimental uncertainty. Brown [29] explains how, “traditionally, rotating turbomachinery design has used safety factors as an approach to compensate for any uncertainty.” Uncertainty present in problems is often categorized as randomness. This uncertainty is well understood and has been extensively studied in the literature. Chen [30] discusses how the stochastic aspect of “uncertainty arises from measurement or instrumentation errors involved in experiments as well as random distributions associated with manufacturing errors.” This is the specific type of uncertainty addressed in this research. Understanding the impacts of the experimental uncertainty will aid in more effectively assessing a mistuned rotor’s forced response.

1.3 Research Challenges

Vibration analysis of a mistuned rotor is categorized as either deterministic or probabilistic. In a deterministic analysis, a rotor’s mechanical and/or geometric properties are changed and the rotor’s response is calculated. This process is repeated for individual, specific instances. Keerti [31] explains, in contrast, a probabilistic analysis predicts the probability distribution of blade vibratory amplitudes due to mistuning. This is particularly useful for uncertainty quantification because of experimental errors and property variability.

The physical aspect of the research rotor introduces its own set of challenges. The primary hurdle is in the rotor material itself. The research compressor is constructed of steel. As such, the entire unit is magnetic. Since the rotor excitation system uses magnetic actuators to generate the forcing function, the precise input location on each blade is difficult to control. Hence, the rotor will respond to an input at any location. On the other hand, the rotor’s inherent ferro-magnetic properties, initially thought of as a detriment, will lend itself well to establishing input and output location tolerances for the experiment. True production rotors are often constructed of materials which do not typically respond to an

external magnetic disturbance. As such, special steel target disks (approximately 0.125 inch diameter) are adhered to the desired input location on each blade.

Another challenge in this research lies with the non-linear forcing function associated with the traveling wave excitation equipment. In contrast to conventional methods of excitation, such as air pressure or direct contact, the magnitude of the magnetic excitation is highly sensitive to the distance between the excitation source and blade input location. Within the existing finite element representation, the loading applied to each blade remains constant - independent of the blade's datum location within the analysis.

Addressing the rotors themselves, there are currently two types used inside of modern jet engines. The first type is a more traditional design where the blades are inserted into slots around a central hub. This design facilitates ease of maintenance and also affords a small degree of mechanical damping. This is in contrast to what is known as the Integrally Bladed Rotor (IBR). In the IBR, the blades and central hub are all manufactured from the same material - as a single unit or welded onto the central hub as a monolithic entity. This simpler design reduces the number of components within the engine as there are no mechanical fasteners attaching the blades to the central hub. A consequence of this design is that structural damping is very low. Avoiding a resonance condition with this rotor is especially important.

1.4 Dissertation Structure and Research Plan

The structure of this dissertation is as follows: Chapter 2 provides top level definitions and proceeds to illustrate some of the earlier techniques used to study mistuning. Furthermore, this discussion includes earlier work in modeling and experimentation. Lastly, this chapter covers stochastic approaches to examine mistuning, along with techniques to capture uncertainty within modeling and experimental frameworks. Chapter 3 covers the applicable theories which will be utilized in this research. This includes component mode synthesis, traveling wave theory, the laser vibrometer's operation, and

uncertainty areas within the experiment. Chapter 4 discusses the experimental equipment which will be used in this dissertation research. It discusses the research rotor's geometry, 3-D scanner, laser vibrometer, and the traveling wave excitation equipment. The signal generation methodology used within the traveling wave equipment is also covered. Chapter 5 provides the experimental results and the associated discussion. Here, research success is achieved if a method is produced to consistently evaluate the mistuning present in any rotor, when exciting the rotor at a specific excitation excitation pattern.

II. Literature Review

2.1 Mistuning Defined

Beck [1] defines mistuning as the “forced response amplification due to perturbations of airfoil characteristics which break down the rotational periodicity of an IBR”. In other words, small, random and inherent variations in all real materials and geometric deviations tends to render each blade in a rotor slightly different than its neighbor. Ideally, these rotor and blade systems are tuned, which means all blades are identical. However in practice, there always exists small, random differences between the blades due to operational wear. Manufacturing tolerances, which are specified in a rotor’s design, also contribute to the mistuned condition. Small material variations, manufacturing tolerances, and operational wear all effectively destroy the rotor’s cyclic symmetry.

Pierre [32] describes a tuned bladed-disk assembly as “featuring perfect cyclic symmetry in the sense that all blades are identical and the first blade is adjacent to the N th blade. There is always some difference in the natural vibration frequencies of all blades installed on the same disk”; Yan [33] reinforces that blade mistuning is “unavoidable”. Because of this random nature, a tuned system will only exist within the theoretical framework of a computer model. Computer simulations of tuned systems can be easily implemented because only a single rotor sector (blade and its corresponding section of the rotor disk) is modeled. Once the sector is created, it is simply replicated in a circular pattern to produce the tuned system.

Mistuning is a stochastic process, resulting from the randomness seen with the geometric and material property deviations. A stochastic process is one which involves randomly determined observation sequences. Each of these observations is assumed to be a single sample from a probability distribution. The stochastic process contrasts the deterministic process, wherein an equation can be used to produce an output from a

series of inputs. The inclusion of randomness in mistuning studies further adds to the complexity, and as Mignolet [34] says, “transforms the problem into one of parametric, random vibration”. Here, the system parameters are not known precisely, but rather, are derived from probability distributions. There exists nominal values for system parameters, but the actual values deviate from the nominal by some random quantity. The system parameter variation cascades into vibrations exhibiting the same random nature as the system parameters.

Beck [1] explains if “a pure deterministic approach is taken to examine mistuning, one is restricted from developing forced response amplitude confidence intervals affecting overall rotor life”. Deterministic solutions only provide information about a single, specific instance in the entire forced response distribution. The stochastic solution can give confidence bounds to the overall solution. These confidence intervals and probabilities of response levels can be used in conjunction with Goodman and S-N diagrams to estimate failure probabilities. Furthermore, the statistics of forced response for an entire population of mistuned rotor can be computed.

2.1.1 Physical Impact of Mistuning.

Because of the breakdown in rotational periodicity due to mistuning, modal energy is often concentrated in one localized area. Ideally, this energy would be evenly distributed throughout the rotor. This phenomenon is known as localization. Localization is what causes the mistuned system’s forced to be much greater than that of tuned system. In the presence of small irregularities, even in nearly perfect periodic structures, the propagation of vibration may be inhibited, and thus the vibration modes will be localized. Due to the increase in localized energy, the forced response amplitudes are higher in these regions. Pierre [35] discusses “for weakly coupled systems, mode shapes undergo dramatic changes to become strongly localized when even a small disorder is introduced”. This confines the energy associated with a given mode to a small geometric region.

In free response, mistuning results in the localization of the vibratory energy. In forced response, resonant amplitudes of some blades are significantly increased due to this localization phenomenon. Laxalde [36] discusses how this may lead to “fatigue failures, wear, or even rupture”. The peak response is the greatest concern with a mistuned rotor. The blade or blades exhibiting the greatest response will serve as the system’s weakest link. This greatest response can be a stress or displacement magnitude which is higher than what is seen in other parts of the rotor. Since only a small rotor area exhibits this increased response amplitude, it follows that this region could fail before other rotor components.

This energy localization directly contributes to the High Cycle Fatigue (HCF) failure mechanism. The concept of HCF is characterized by repeated elastic stress cycling until failure. A failure due to HCF is frequently characterized as occurring beyond 10,000 cycles. Bartsch [37] states that “between 1982 and 1996, HCF accounted for 56% of all Air Force *Class A* engine-related failure events”. “A *Class A* mishap is one which results in loss of human life or at least two million dollars in damage” [38]. “In 1994 alone, HCF required expenditure of 850,000 maintenance man-hours for repair, replacement, and inspections” [3]. Unlike other failure modes, HCF failure can occur seemingly at random with no prior warning.

For a mistuned cyclic structure under external forcing, a subcomponent’s response is often much larger than that of a perfectly tuned cyclic structure. Thus, Yoo [7] discusses the mechanical energy stored in a subcomponent of a cyclic mistuned structure is much different than that which is stored in other subcomponents. An illustration of this localized energy concentration is shown in Figure 2.1 and Figure 2.2.

These figures were produced using the finite element analysis program, ANSYS. The energy displayed in the figures is the strain energy developed due to bending and twisting in the blades. The resulting confinement in energy causes amplitudes higher than predicted from an analysis on a tuned rotor. This energy is developed within the component resulting

from the excessive displacement induced from the mistuned state. In Figure 2.1 and Figure 2.2, the red color indicates a high displacement and thus increased strain energy. The blue color represents an area of lower displacement indicating a reduced amount of strain energy. Note how the mode shape is symmetric around the rotor for the tuned response, while “the energy is localized to a single blade in the mistuned response” [1]. Another example of a tuned rotor’s mode shape is given in Figure 2.3. In this figure, the mode shape is described as having three nodal diameters. In rotor dynamics, a nodal diameter is analogous to a node point on a 1-D beam or a node line on a 2-D plate. As with the node points and lines, displacement along a nodal diameter is zero. The dashed lines show the nodal diameters.

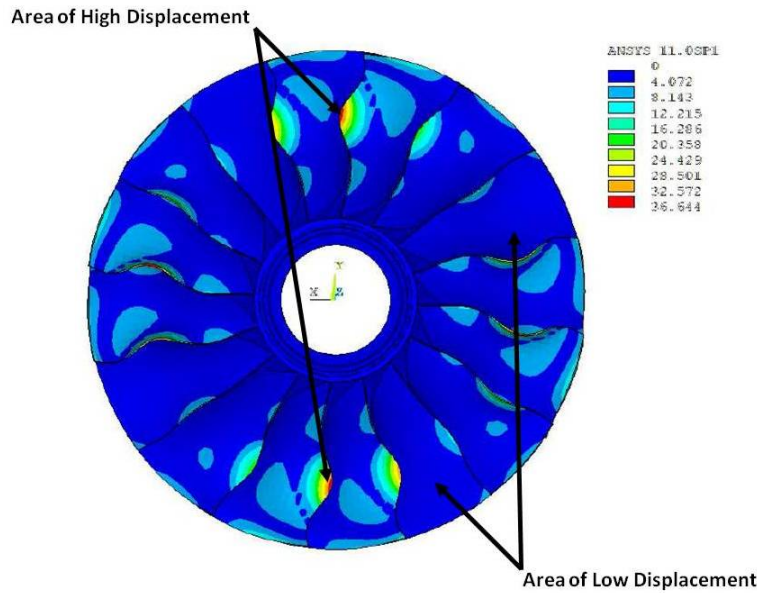


Figure 2.1: Tuned Rotor Modal Energy Distribution [1]

system's own natural frequency. At resonance, the physical system response is much greater than what is seen at other frequencies. Within a jet engine, a rotor's excitation comes in the form of a harmonic input driven by the interaction between rotating airfoils, stators, or any other obstruction in the flow field. Because the airfoils and stators are spaced in a symmetric pattern around the engine's inner annulus, the rotor's own rotation sets up a harmonic excitation which is a function of the number of these disturbances. Pressure variations exist behind these airfoils as a consequence of their cambered shape. The pressure variations induce the harmonic input which excites the rotor.

Designers may ultimately know the environment into which a specific rotor will be placed. As such, its operating conditions are also known. This includes both the operating speed and Engine Order (EO) excitation levels. The EO excitation is a periodic force induced by the number of equally spaced disturbances through which the rotor spins. The number and the intensity of the disturbance pulses depend on the architecture of the engine upstream and downstream of the rotor. This includes the number of combustion chambers, stages, or stator vanes. These disturbances can induce a wide range of frequencies which, in turn, excite the rotor. For example, if a rotor is spinning immediately behind a system of 12 inlet guide vanes, the EO excitation would be 12. The excitation frequencies on each blade are a multiple of the rotor angular speed. Firrone [39] defines the EO excitation as "the integer number multiplied by the rotor's angular speed to produce the excitation frequency." This concept will be discussed in greater detail in Chapter, 3, Section 3.4. In the case of a tuned rotor, where all the blades have identical natural frequencies, a given EO excitation will cause all blades to vibrate with equal amplitudes. For a mistuned rotor, where each blade's natural frequency varies slightly with respect to one another, "a given EO excitation will typically cause response localization and amplification above what would be seen in the tuned response" [17].

Nikolic [40] references Srinivasan [41] who says a rotor's excitation is "inherently unsteady, anything but uniform, either upstream or downstream, since the flow entering an engine inlet meets with static obstructions (struts, vanes, etc.), and rotating obstructions (blades) in its path from the inlet to the exhaust." This excitation is, in other words, induced by the number of equally spaced aerodynamic disturbances through which the rotor spins. Within the flow field, "blades experience time-varying forces at speed-dependent frequencies, so that the bladed disc modes can be excited into resonance at certain speeds of rotation" [40]. Ewins [42] states, "It is assumed that n equally spaced obstructions will cause the steady flow to contain a $\cos(n\theta)$ fluctuation superimposed upon its mean level and, in addition, smaller components of $\cos(2n\theta)$, $\cos(3n\theta)$, etc." The $n\theta$ component will excite any mode of the bladed disc which has an n nodal diameter component in its mode shape, and "will do so at a frequency equal to $n\Omega$, where Ω is the rotation speed" [40]. For a tuned rotor, the n^{th} engine order excitation level only excites n nodal diameters modes. For a mistuned system, multiple modes may be excited by a single engine order excitation level, not simply one mode as is seen with a tuned rotor.

One tool engineers often utilize to identify and avoid resonance conditions is called the Campbell diagram. An example Campbell diagram is shown in Figure 2.4. This diagram is a visual tool which plots resonant frequencies vs. rotating speed. While the diagrams can tell the designer when a resonance condition might occur, they do not consider either the detailed aerodynamic forcing function or the resulting airfoil unsteady aerodynamics. Fulayter [2] explains how these diagrams "provide no amplitude measure of the resulting vibration or stress at the resonant speeds." The Campbell diagram only tells the designer a resonant condition may exist if a prescribed set of conditions are met. These conditions are a specific EO excitation occurring at a specific rotational speed. With this tool, engineers can design the operational regime to be outside and away from these potentially dangerous conditions.

The EO excitation lines are shown with a positive slope beginning from the graph's origin. The EO values are typically given along the right vertical axis. Rotor frequency is given along the left vertical axis. The lines emanating from this axis represent airfoil resonant frequencies and “may either slope upward due to stress-stiffening with increased RPM or downward due to temperature effects” [1]. The stiffening effect which comes about from increased RPM is caused by centrifugal forces acting on the blades. Yan [33] also discusses this phenomenon. These forces serve to stiffen the blades and hence increase their natural frequencies. The opposite occurs with increased temperature; the blade material softens and thus has a reduced natural frequency. These behaviors are a direct consequence of the proportional relationship between material stiffness and natural frequency, $\omega_n \propto k$. Here, k , is the material's stiffness and ω_n is the natural frequency.

The industry-wide practice, according to Srinivasan [41], is to “place the frequencies of integral order vibration in the low engine orders (2EO, 3EO, and sometimes 4EO and 5EO) either outside the operating range of rotor speeds or at lower speeds within the operating range.” This is because lower EO excitation often induces fundamental blade modes, such as the first bending or the first torsion modes. These modes are characterized both by their low excitation frequency and the possibility of high vibration amplitudes. Unavoidable crossing of resonant blade frequencies, with known engine excitation, may occur for some blade designs. These interactions are usually for presumed weaker, higher order modes [1]. Figure 2.4 [2] shows a generic Campbell diagram.

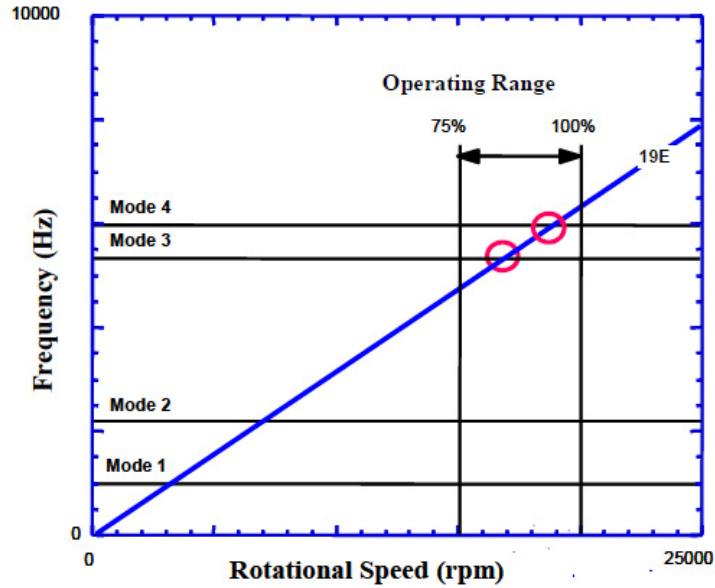


Figure 2.4: Sample Campbell Diagram [2]

Here, the rotor's operational regime is shown. This operating region lies between 15,000 and 20,000 RPM. As the chart indicates, this is 75% to 100% of the allowable operating speeds. Rotor frequencies are plotted along the ordinate. The rotor's first natural frequency occurs at 1,000 Hz. This frequency excites the rotor's mode 1 behavior. The second natural frequency, and its corresponding mode 2 excitation, occurs at approximately 2,250 Hz. Finally the third and fourth natural frequencies, exciting modes 3 and 4, occur at 5,300 Hz and 6,000 Hz, respectively. EO 19 is shown in the diagram. Physically, this means there is a radial pattern of 19 disturbances in the otherwise smooth air stream. From the diagram, EO 19 excites mode 1 if the rotor is spinning at 3,000 RPM, mode 2 at 7,000 RPM, and finally modes 3 and 4 at 17,000 RPM and 19,000 RPM respectively. Since the first 2 modes are outside of the operating regime, the rotor is unlikely to experience a resonance condition exciting modes 1 or 2 during its normal operation. This cannot be said of modes 3 and 4.

2.1.2 Impact of Mistuning in the Frequency Domain.

Aside from the physical responses seen with a mistuned rotor, the frequency response is where mistuning's immediate effects are seen. Because the mistuned rotor has many

natural frequencies instead of a single frequency, examining a rotor's Frequency Response Function (FRF) can immediately indicate a mistuned condition. An FRF is a graphical depiction of the system's steady-state response to a sinusoidal input. The FRF information is just one of the many useful pieces of information gleaned from analyzing data in the frequency domain. This domain allows for the clear decomposition of both spectral (frequency) content with its corresponding phase information. The spectral information indicates what frequencies tend to induce a resonance condition. The phase information, on the other hand, provides system motion information at that frequency. This information is not readily available when examining information in the time domain. Time domain data is only real valued. Examples of both tuned and mistuned magnitude FRFs are shown in Figure 2.5.

When comparing the mistuned system FRF to that of a tuned system FRF, the single tuned frequency has become several distinct frequencies. The additional resonant peaks represent the new system natural frequencies associated with each blade. In the presence of the random airfoil geometric variations, the rotor's ideal cyclic symmetry breaks down. This results in changes to the rotor response and the splitting of the tuned natural frequency. Instead of a single natural frequency, Brown [3] says there "will be N blade, closely spaced natural frequencies for an isolated family of modes." This is clearly seen in Figure 2.5 where the mistuned frequencies all closely surround the tuned case. The tuned natural frequency is seen with the single resonant peak, while the mistuned system is displayed with ten individual peaks.

Because of this behavior, when the system is excited at a natural frequency, multiple modes may be excited simultaneously. Modal energy associated with one mode adds with energy from other modes. This modal energy superposition leads to the energy localization and ultimately forced response amplitudes greater than what would otherwise be expected in a tuned system. Aside from the closely spaced peaks seen in the FRFs in

Figure 2.5, mistuning is also indicated by examining a rotor's Campbell diagram. If the natural frequency lines are far apart, this indicates clear, distinct regions where resonant conditions lie. Beck [1] illustrates that “two closely spaced airfoil resonant frequency lines can indicate the presence of mistuning.” The two lines are spaced closely together because of the asymmetry present within the system. Figure 2.6 is the Campbell Diagram for the rotor used in this research effort. This diagram was constructed for the 0 nodal diameter mode. The area indicated with the box is an area where three natural frequencies lie very close to one another, around 8,000 Hz. Exciting the rotor in or around this frequency range may excite these three modes simultaneously. This is sharply contrasted with the natural frequencies seen at approximately 2,900 Hz and 5,800 Hz. These two frequencies are very distinct and are relatively far apart on the Campbell diagram's ordinate.

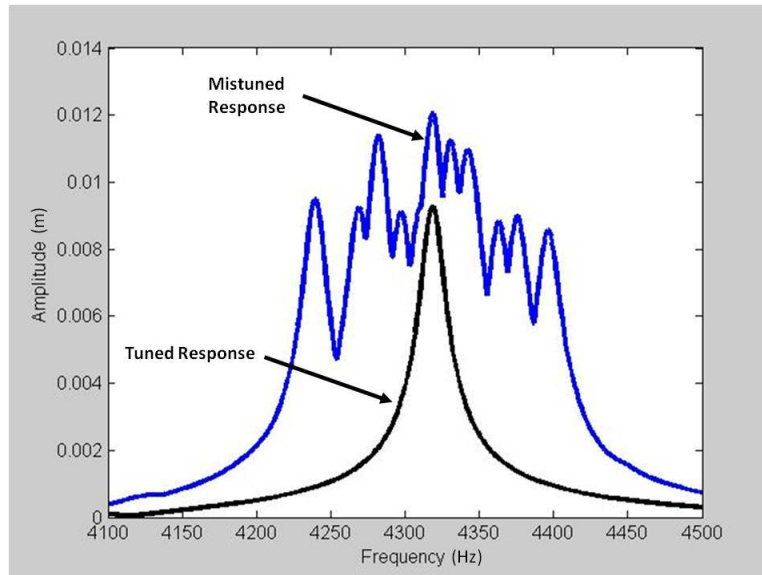


Figure 2.5: Tuned versus Mistuned FRFs [3]

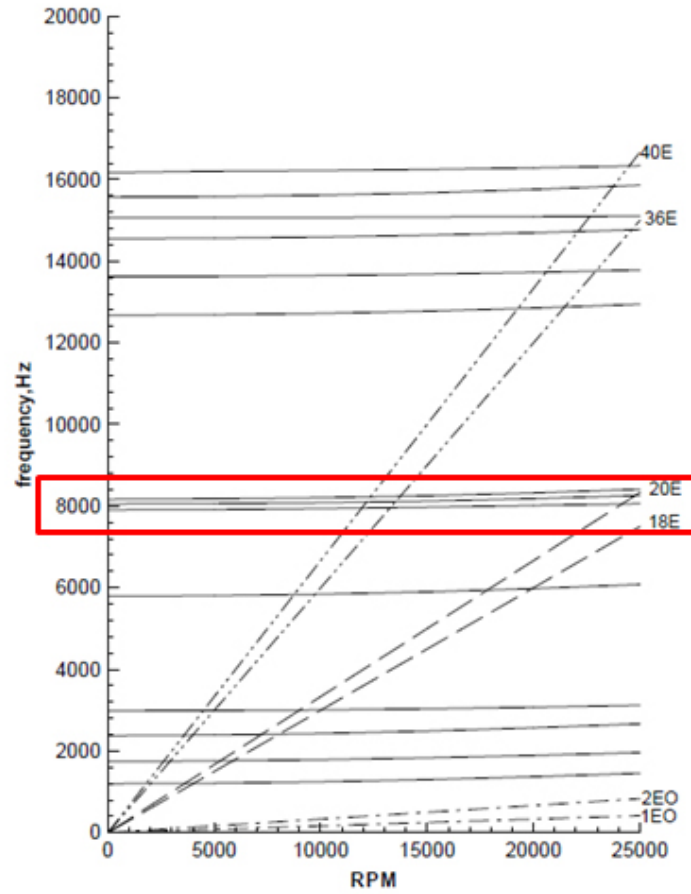


Figure 2.6: Transonic Campbell Diagram for 0 Nodal Diameter [2]

2.2 Previous Modeling and Experimental Endeavors

The following section summarizes several examples dealing with the modeling and experimental studies of mistuned systems.

2.2.1 Modeling Efforts.

2.2.1.1 Early Modeling Methods.

Some of the earlier modeling methodologies employed lumped parameter models wherein the component parameters and their associated properties are discretized within the system. These are “convenient models to study because the coupling, mistuning, and damping values are all distinct parameters” [6], and they provide researchers valuable

insight into the mechanisms behind mistuning. The system components, common to most models, involve both individual blades and their associated sectors along the disk. These components were modeled as point masses, springs, and dash pots. Some of the modeling techniques outlined in this section employ this methodology. To mistune these models, the component parameters, blade mass, blade stiffness, or disk sector stiffness values, are perturbed from some nominal value. Verified by experimental data, this process effectively simulates irregularities within the a rotor. Forced response studies would then follow. Though these lumped parameter models were reasonable at approximating a small number of system modes, they were very crude approximations of an actual industrial rotor design.

As finite element modeling and analysis became more widely used and accepted, this became the analytical weapon of choice. An example rotor model using the finite element technique is shown in Figure 2.7. “A major disadvantage of simulation techniques is that the computational cost may become prohibitive” [43], particularly for systems which are required to be analyzed using high-fidelity finite element models. This computation cost comes in the form of extremely long analysis times. The extended analysis time is due to the number of system degrees of freedom associated with complex geometries. Further, as mistuning is a stochastic phenomenon, analyzing the millions of possible combinations of material and geometric variations add to the analysis time.

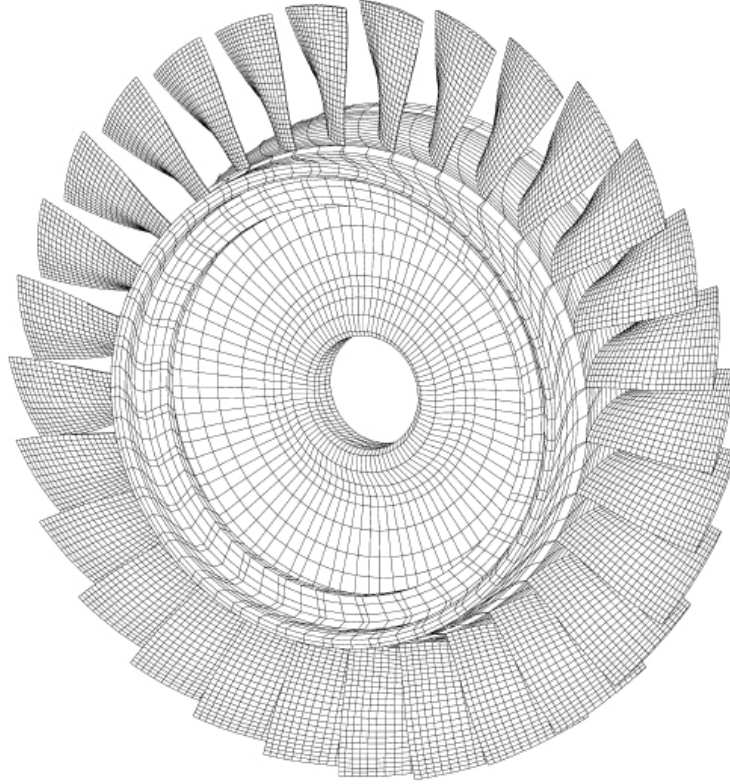


Figure 2.7: Finite Element Mesh for an Industrial Bladed Disk [4]

To simplify an analysis in exploring damping and energy dissipation, Lin [5] chose to model the rotor in a rather simple way. There are N blades comprising the disk. Each blade is a damped single degree of freedom system which is connected to its neighbor by identical springs and dashpots. The single degree of freedom in the blade is the simplest manner to simulate blade movement. This methodology is employed in order to simulate aeroelastic effects and disk flexibility. Because real rotors are not infinitely stiff, the inclusion of disk stiffness, k_j , and damping, c_j , terms allows for the disk portion of the model to interact with the blades. Further, the blades on real rotors are coupled to one another via aeroelastic effects. At a given speed, the alternating pockets of high and low pressure between blades act as small springs and dampers. Thus, the behavior of one blade has an influence on its neighbor. Figure 2.8 shows this interaction through the use of the k_c and c_c

coupling parameters. Had these terms not been included, each blade's behavior would be independent of one another.

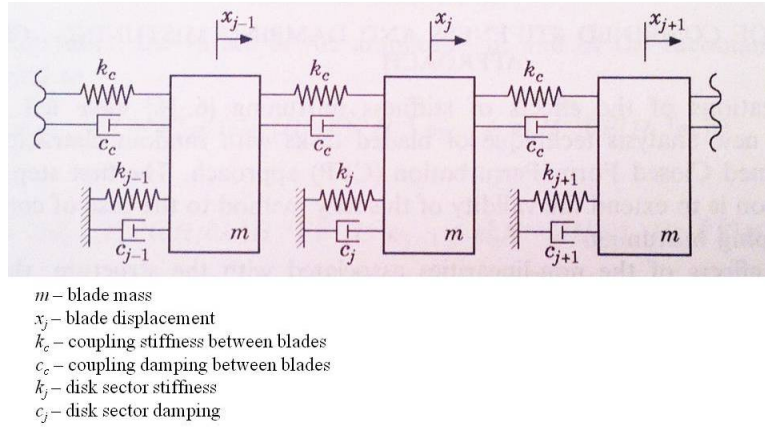


Figure 2.8: A Simple Model of a Bladed Disk [5]

Here, the authors assumed each blade contained an identical mass. The technique to mistune the model concentrated on varying blade stiffness, k_j , and damping coefficients, c_j . The uncertainties associated with the manufacturing process and energy dissipation mechanisms motivated Lin, as he modeled these parameters as independent random variables with prescribed probability density functions. The method the authors are employing recognizes the random nature of mistuning. System parameters are drawn, at random, from their respective probability distributions. Having these random parameters within the model simulates a mistuned rotor because, in effect, each blade's stiffness and damping properties vary slightly from one to the other.

Mignolet [44, 45] uses a modified version of this model by incorporating a second degree of freedom for each blade. He also adds an additional stiffness and damping element to each mass. This was an improvement in model fidelity from Lin's work where each blade was a single mass and thus moved as a single entity. Adding the additional degree of freedom to each blade allows the model to more accurately capture real blade motion. For example, the blade root and tip are now permitted to move out of phase with one another, allowing higher order modes to be captured.

Another example of lumped parameter modeling is shown in Hollkamp's work [6]. Here, the authors are again examining damping effects on the overall rotor assembly. While the damping terms are not shown explicitly, the model accounts for this energy dissipation mechanism by including a structural damping treatment on individual blades. Their model is shown in Figure 2.9. Its design is similar to the construction shown in Lin's model. Here, Hollkamp does not account for any disk flexibility. There are N blades with individual stiffness values, k_{b_i} , and masses, m_i , attached to a rigid disk. The blades are coupled by springs with the stiffness, k_c , between adjacent blades. This linear elastic coupling mechanism attempts to simulate the aeroelastic effects coupling blades in a real rotor. The stiffness of each blade is permitted to vary from the nominal stiffness to introduce mistuning.

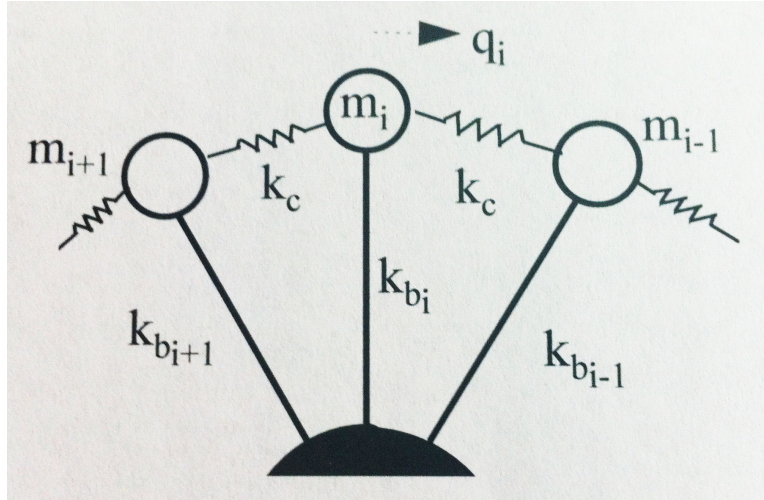


Figure 2.9: Schematic of the Lumped Model [6]

This model introduces a coupling coefficient which is defined relative to the nominal blade stiffness, k_b .

$$R = \frac{k_c}{k_b} \quad (2.1)$$

Assuming a constant blade stiffness, increasing the coupling stiffness will cause the coupling coefficient to increase. The same behavior occurs for reduced blade stiffness values, assuming a constant coupling stiffness. In the first case, increasing the strength of

the coupling serves to force all blades to behave in concert with one another. The effect of the individual blade stiffness becomes less significant. In the second case, where the coupling stiffness remains constant and the blade stiffness is decreased, the blade stiffness becomes less significant. Here, the coupling has more influence. This term is introduced simply to assign a numerical value to the degree of coupling between the blades. Assuming that all blade masses are equal, a nominal natural frequency is defined as:

$$\omega_b = \sqrt{\frac{k_b}{m}} \quad (2.2)$$

Since the authors introduce mistuning by way of stiffness perturbations, the frequency of each blade (in the absence of coupling) is defined as:

$$\omega_{bi}^2 = \omega_b^2(1 + \Delta f_i) \quad (2.3)$$

where Δf_i is the mistuning of the i^{th} blade. The mistuning is introduced by way of stiffness variations. The overall model is expressed as:

$$\{\ddot{q}\} + \omega_b^2[A]\{q\} = \frac{1}{m}\{F\} \quad (2.4)$$

where,

$$[A] = \begin{bmatrix} 1 + 2R^2 + \Delta f_1 & -R^2 & 0 & \dots & -R^2 \\ -R^2 & 1 + 2R^2 + \Delta f_2 & -R^2 & 0 & \dots \\ \dots & \dots & \dots & \dots & \dots \\ \dots & \dots & \dots & \dots & \dots \\ -R^2 & 0 & \dots & -R^2 & 1 + 2R^2 + \Delta f_N \end{bmatrix} \quad (2.5)$$

An explanation behind Hollkamp's equation of motion is shown in Appendix B. For N blades, the matrix of forcing functions, F is defined as:

$$\{F^T\} = F e^{j\omega t} [1, e^{j\theta_2}, \dots, e^{j\theta_N}] \quad (2.6)$$

$$\theta_i = \frac{2\pi C(i-1)}{N} \quad i = 1, 2, \dots, N \quad (2.7)$$

In this equation, F is the force magnitude and the expression $e^{j\omega t}$ represents the sinusoidal input into the rotor. The term C is the EO excitation on the input force. Letting $C = 0$ shows that the forcing will be the same phase for all blades. This model is next modified to include blade damping treatments through the additional stiffness term δA .

$$\{\ddot{q}\} + \omega_b^2[A + \delta A]\{q\} = \frac{1}{m}\{F\} \quad (2.8)$$

These additional stiffness terms δA are complex valued. This matrix is diagonal, with non-zero diagonal terms for the damped blades. The real part of the additional term is the added stiffness of the damping treatment. The imaginary part represents the added structural damping. The authors use this simplistic model to examine damped behavior. The authors continue next investigate the system response when only certain blades are damped. Holkamp details the process by which damping can be applied to individual blades. Solving the eigenproblem from Equation 2.8 produces the mistuned system's modal parameters.

Yang [46] discusses a methodology wherein closely spaced eigenvalues are examined. Recall from the discussion in Section 2.1.2 that a mistuned system will exhibit closely spaced natural frequencies. A problem of modal interaction is formulated in terms of a normalized modal eigenvalue problem. A first-order perturbation solution is presented for the case of two closely spaced modes. The author's process is discussed in Appendix B. The random perturbations simulate the effects of mistuning. Statistical behaviors of the normalized frequencies and modes are then determined from the results of the perturbation analysis. The author goes on to examine the perturbation solution's range of validity through the use of a Monte Carlo simulation.

2.2.1.2 Other Modeling Techniques in the Literature.

Yang [47] introduces a popular modeling technique known as the Subset of Nominal Modes (SNM). This technique became popular because of its innate ability to reduce the computational cost associated with analyzing a mistuned rotor's forced response. He used

this methodology to determine the effects of mechanical property variations on the system's vibratory response. This approach represents the mistuned system modes in terms of a limited sum, or subset, of the "nominal" system modes. Nominal system modes are defined as the modes of the system for a nominal blade and disk geometry. The authors' assertion is if the nominal system has modes with closely spaced natural frequencies, the mistuned system will also have modes with closely spaced natural frequencies in the same frequency range. The underlying assumption here is that a mistuned system mode can be represented as a linear combination of tuned system modes.

Yang explains that "a nominal geometry could ideally be one in which every blade and disk sector is identical." In this derivation, the rotor system is treated as a single entity - as opposed to breaking the system up into blade and disk components. This work is based on the efforts the author put forth in 1997, found in [46, 47], wherein nominal system modes can effectively describe the modes of a system if the system's properties are slightly altered. The accuracy of the subset of nominal modes technique depends on the number of degrees of freedom used to represent the structure. This should be intuitive, as increasing the number of system degrees of freedom more effectively captures realistic system behavior. In developing the SNM technique, the authors ensure the number of system degrees of freedom equal the number of modes used in the representation.

Capitalizing on the success of the SNM technique, Sinha [48] applies this method in deriving his own model. The author realized to accurately model geometric mistuning using this method, a sufficient number of tuned modes is required. If the number of tuned modes is lacking, the model fails to effectively model the geometric mistuning. The resulting method, Modified Modal Domain Approach (MMDA), yields another high fidelity model accounting for geometric mistuning. Here, the author allows the variation of a system's physical geometry, not just variations in material properties. The author accounts for this

by perturbing both the system mass and stiffness matrices simultaneously. These perturbed matrices were then used to perform forced response studies.

As engineers attempted to understand the most simplistic underlying mechanisms surrounding mistuning, Feiner and Griffin [49] devised a method which is mathematically simpler than a spring-mass model. Once derived, their model identifies the primary parameters controlling the mistuned response. This technique is aptly named the Fundamental Mistuning Model (FMM). The FMM is actually a derivative of the SNM technique Yang introduced just one year prior. “The SNM formulation may be simplified when the nominal modes used in the representation are limited to a single family” [49]. The FMM was derived from the SNM theory using three main assumptions: “only a single, isolated family modes is excited, the strain energy of that mode family is primarily in the blades, and finally the mode family’s frequencies are closely spaced.” These ideal “conditions are usually only found in the fundamental modes of a rotor”, such as the first bending mode. Feiner justifies these assumptions in stating how the “higher frequency families are often clustered close together, have a significant amount of strain energy in the disk, and span a large frequency range.” The FMM requires only a minimum amount of information in order to predict a mistuned response. One piece of information is the set of tuned system nominal frequencies. The second piece of information is the set of deviations of blade frequencies from their tuned value. The authors continue their work several years later in [50] and [51]. Here they present both the theoretical development for system parameter identification and applications for using these parameters for identifying mistuned modes within the rotor system. Ayers [52] provides a work based on the FMM technique. The author develops a new transient model of bladed disk vibration. An extension of the FMM, this new method relies on evaluating the system equations of motion to capture the transient effects. As the FMM will give mistuned modes, the methodology employed here provides the modal information as they decay over time. The equations of

motion are solved via numerical integration and the results are verified via experimentation. Ayers shows in this verification, “the transient response was more sensitive to small errors in the system’s natural frequencies than were the steady-state modal results.”

Deviating from the mistuning predictions of Feiner and Griffin, Yoo [7] returned to the investigation of mistuning’s impact on vibration localization under and external harmonic excitation. In contrast to a spring-mass model to describe the physical system, the authors chose to employ a coupled pendulum model to represent a rotor. This system is shown in Figure 2.10. System mistuning is introduced by altering pendulum lengths. All other system parameters are equal. A linear viscous proportional damping force is assumed to act on each pendulum mass - despite not being explicitly included in the model diagram. The development of Yoo’s equation of motion is shown in Appendix B, Section B.4. The author presents numerical results for weakly coupled, lightly damped systems with a range of pendulum length ratios. The authors also present results for difference dynamic magnifications factors of a weakly coupled system using different damping parameters. While not explicitly tailored to a rotor, this pendulum model easily illustrates how small deviations in both geometry and material effect the free and forced response system characteristics. Here, the pendulums only permit transverse motion. This corresponds to the blades’ bending modes.

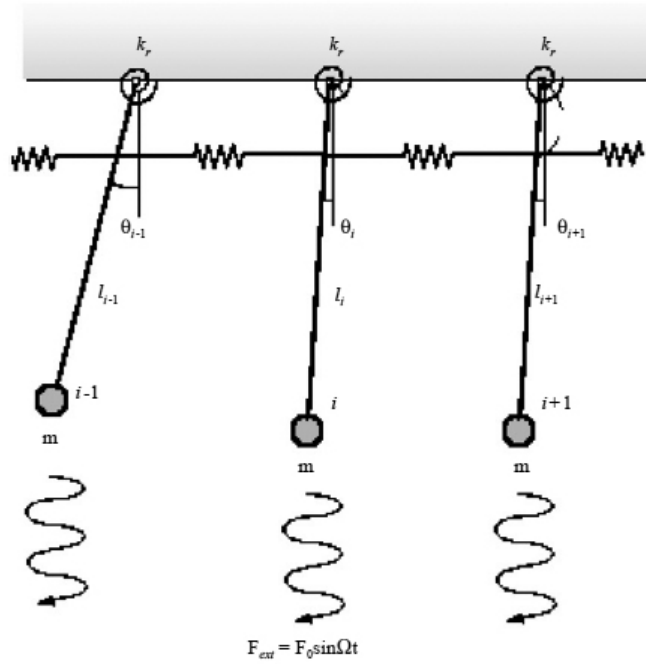


Figure 2.10: Multiple Coupled Pendulum [7]

2.2.2 Experimental Efforts.

Experimental work supporting mistuning research has almost always been carried out in parallel with the modeling efforts. Aside from the validation and verification processes, experimental work also serves to show the true to life effects mistuning plays on cyclic structures. In this section, some of the previous experimental techniques researchers employed are discussed. This outlines their path in chasing down not only the root cause of but also the fundamental understanding behind the mistuning phenomenon.

Hollkamp [8] provides an example of rotor modal testing. The authors were tasked to investigate new damping concepts for jet engine blades. In this study, modal tests were conducted on an 8-bladed model of a engine fan. Here only one blade possessed any additional damping over and above the natural damping properties of real materials. Since it is more economical to test a few damped blades while leaving the remaining blades unaltered, the researchers attempted to determine if the damping values measured with a

mix of blades equal the values measured if all the blades are damped. The authors employ a generic model of a first stage fan in a jet engine. Comprised of only 8 blades, the model had a diameter of 18 inches. Each blade was 6 inches long, 4.5 inches wide, and 0.063 inch thick. The center hub was cylindrical shaped and had a diameter of 6 inches and a wall thickness of 0.5 inch. Each blade was attached at a 45° angle with respect to the fan's axis of rotation. Figure 2.11 illustrates the experimental fan. Both the blades and hub were fabricated from low-alloy steel. The authors chose 8 blades because this was a "high enough number to sufficiently capture the complexities associated with a cyclic structure. Additional blades would have increased the model complexity without adding to the system's dynamic characteristics." For this study, each modal family in the model fan consisted of 8 modes. A finite element model of a cantilevered blade was used to predict modal frequencies of 412 Hz and 716 Hz, respectively, for the second bending and two-stripe modes. Hollkamp states how "the two modal families were expected to occur near these frequencies since the hub was relatively stiff." The authors utilize bonded actuators to serve as the means to energize the system. Additionally, their experiment used a scanning laser vibrometer as the measurement device. Acknowledging the small perturbations the bonded actuators induce was one reason behind using a non-contact means for vibration measurement.

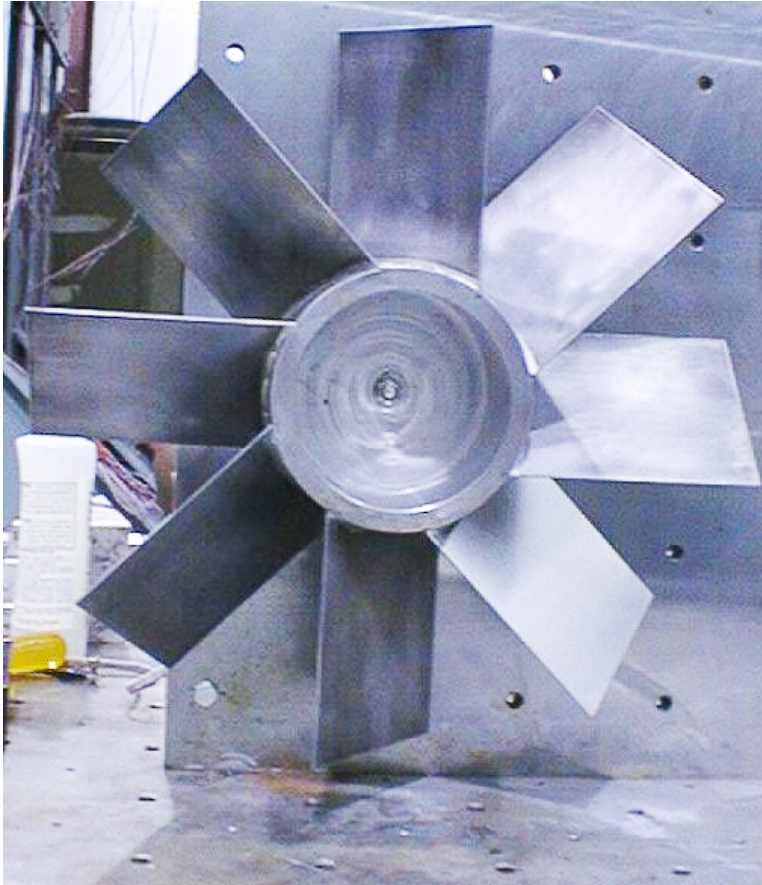


Figure 2.11: Bladed Disk Experimental Model [8]

Judge and Pierre [9] also constructed their own blade model while investigating mode localization and forced response amplitude magnification. Here, the authors recognized the effects of mass variation and its impact on forced response. They were attempting to experimentally perform the work, while simultaneously predict the response via finite element techniques. They also desired to verify their model effectively captured any localization effects. The authors used a flat, 12-bladed disk with a simple geometry. The experimental rotor is shown in Figure 2.12. During this experimental effort, the rotor was held stationary via a clamp in its center. The rotor was machined from a 3.24 mm thick, precision ground 4140 steel plate. The disk has a diameter of 300 mm and the blades are 92 mm long and 10.14 mm wide. The center was clamped using two spindles which interlock through a 25.4 mm hole in the rotor center. The spindles themselves are held in place by

a 20-ton capacity bearing press. Piezoelectric actuators, adhered to the root of each blade, provided the excitation. All vibration measurements were made using an eddy-current proximity probe. The probe was free to move from blade to blade. Figure 2.13 shows the measurement probe. A tip mass is also shown in this figure. Different masses were added to the blades once the tuned system investigation was complete. The tip masses were used to effectively mistune each blade by changing each blade's natural frequency. The authors go on to show good agreement between their experimental and finite element results.

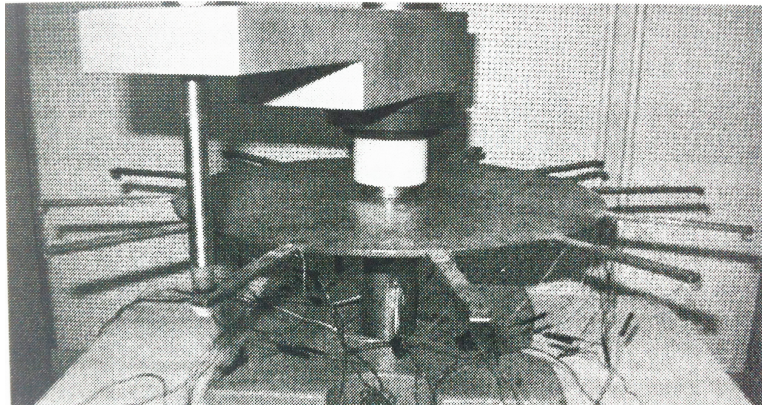


Figure 2.12: Experimental Bladed Disk [9]

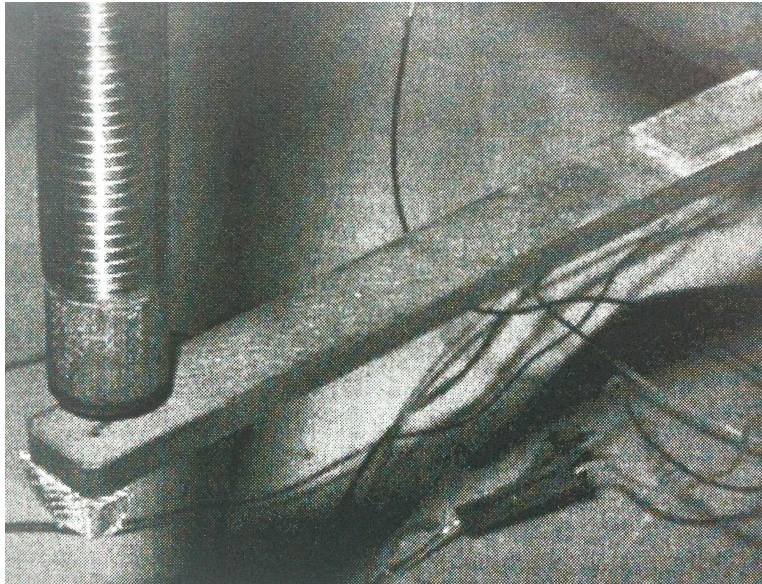


Figure 2.13: Closeup of Experimental Blade with Eddy Current Probe [9]

Feiner, Griffin, and Rossi [53] performed an experimental probabilistic study using their own FMM and FMM ID techniques. The authors were investigating whether or not the FMM technique can accurately predict the behavior of a rotor fleet. The authors' experimental approach first involved generating data to which Monte Carlo simulation results can be compared. This portion of the experiment involved measuring the forced response of several blades, each possessing the same design. Next, the authors applied a probabilistic procedure to simulate the response of a fleet of similarly constructed rotors. Measuring the frequencies of several rotors, each of which have an identical design, provides the required statistical framework. The FMM ID provides the necessary data used in this probabilistic analysis. Once the data is collected, statistical models of both tuned and mistuned systems were constructed. The statistical models were used with the FMM to perform the Monte Carlo simulations of the rotor fleet. To ensure the structure was tuned, the authors employed the FMM ID technique to measure each blade's natural frequency.

Each blade was essentially a simple beam. As such, beam theory was used to determine the effects of a length change on its natural frequency. Blade lengths were altered accordingly so as to result in a tuned system. For the mistuned statistical investigation, different masses were added to each blade tip to alter the natural frequencies. The masses were selected so as to produce a blade natural frequency variation approximately normally distributed with a standard deviation of 2% of the nominal blade natural frequency. The method the authors chose to excite the rotor closely resembles the traveling wave setup used in this research effort (discussed more in detail in Section 4.4).¹ The authors employed an array of electromagnets positioned directly beneath the rotor. Each magnetic actuator was energized in such a way so as to produce engine order excitation. In the end, the researchers

¹Pierre also utilized traveling wave excitation in [54] and [55]. Pierre once used an acoustic traveling wave system; it is discussed in [56].

show their FMM and FMM ID techniques, together with the probabilistic information gleaned from their experiments, can be used to assess fleet wide mistuning effects.

In a paper by O'hara et al. [10], the authors are directly concerned with experimentally investigating geometric uncertainty. This work also employs the scanning laser vibrometer as a means of non-contact based vibrations measurements. In examining the geometric uncertainty, the researchers examined single blades mounted inside a broach block specifically designed to hold the blade's dovetail securely. Figure 2.14 shows the broach block and blade setup. The broach block was secured to a linear motion table, as such, the system was only permitted to move in a single direction. System excitation was produced by a single 100 pound shaker unit. O'hara's "...measurement setup was optimized for four criteria: signal level, scanning head position, resolution, and scanning time. Each blade was measured at 140 different locations using a bandwidth of 10 Hz to 5 kHz." Figure 2.15 shows the measurement pattern.

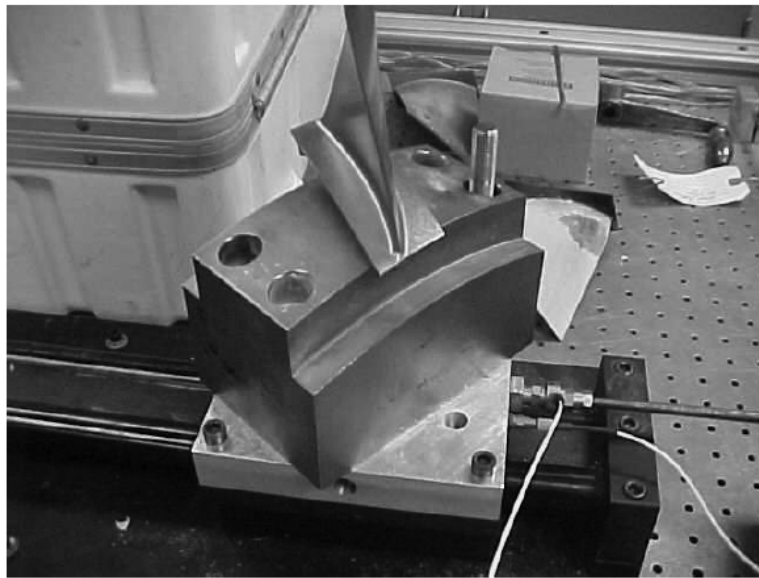


Figure 2.14: Broach Block and Blade Assembly [10]

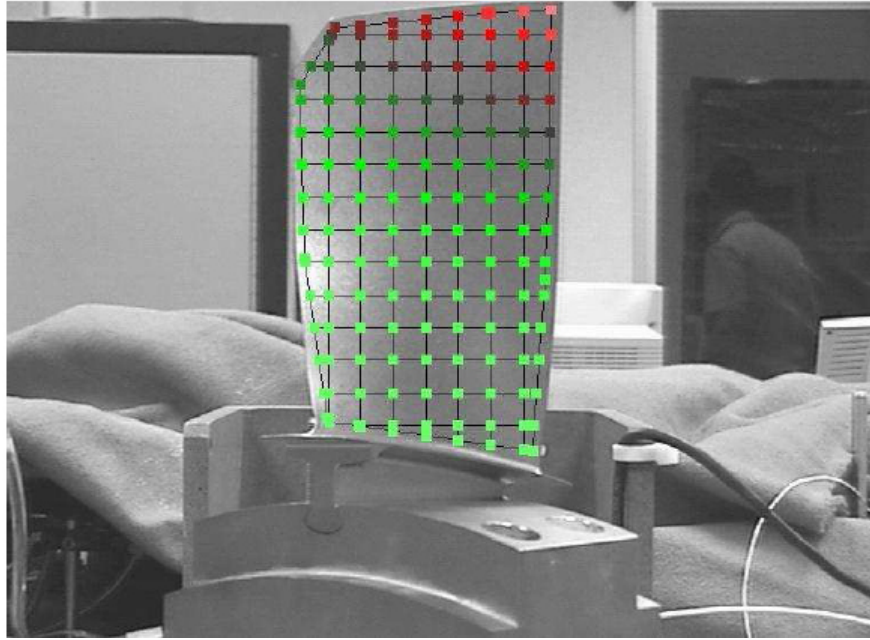


Figure 2.15: Blade Sample points [10]

During the experiment, the blade natural frequencies and mode shapes were obtained via the laser vibrometer and processed using the associated PolyTec software. The authors invoke both the modal assurance criterion and coordinate modal assurance criterion (Chapter 3, Section 3.8) as a means to indicate places along the blade which might be contributing negatively to the results. In addition, O'hara performed a one way analysis of variance on all coordinate modal assurance criterion values which helped aid in identifying locations consistently having poor correlation values.

Throughout the experimental methods previously outlined, there was very little mention of the optimal sensor placement locations. Several authors have devoted research to this very topic. Peng [57] emphasizes how in any experimental modal testing, the selected measurement locations have a major influence on the result quality.

An early publication by Yao [58] discusses sensor placement by means of a genetic algorithm. This work is focused on ideal sensor placement for large space structures. Because of weight and space limitations, ideal sensor placement for state of health and

modal information is of the utmost importance. Here, the genetic algorithm is applied and used to select the best sensor locations for modal identifications of a space station and its photovoltaic arrays. Numerical analysis shows the genetic algorithm produces a superior set of sensor locations, as compared with other sensor placement optimization methods. This advantage in sensor location comes at an expense of increased computational complexity.

Lastly, and possibly the most applicable to this current research, is a work published by Sensmeier in 1998 [59]. The authors specifically discuss the optimal sensor placement for turbine blade vibrations measurements. Similar to Yao [58], the authors here also employ a genetic algorithm to establish the proper sensor location. They also discuss more practical methods from which an ideal location can be chosen. The researchers acknowledge how sensor locations must be chosen such that the measured response values are as close as possible to the critical values of interest. However, these locations are often in regions of high response gradients. In these regions, the measurement sensitivity due to small inaccuracies of sensor placement is increased.

As vibratory mode shapes are mutually orthogonal [60],[61], if a full mode shape is known, determining other modes is a trivial task. However, response data is only known at discrete sensor locations. This collection of sensor data, in effect, produces a reduced mode shape. Sensmeier emphasizes since “the number of sensors is not infinite, the mode shapes do not retain their orthogonality.” If these mode shapes are considered as response vectors in an N -dimensional space, the angle between any two modes shapes can be expressed as follows:

$$\theta_{i-j} = \cos^{-1} \frac{\vec{\phi}_i \cdot \vec{\phi}_j}{\|\vec{\phi}_i\| \|\vec{\phi}_j\|} \quad (2.9)$$

An ideal instrumentation setup would exist if the angle between the two modes is as close to 90° as possible. “Optimally, it would be advantageous to place a sensor at the critical stress location for each mode” [59], but these areas are often in regions of high response gradients.

A sensor in these areas can lead to inaccurate results. As such, it is typically necessary to extrapolate the response at locations other than where a physical sensor is located; the maximum response must typically be estimated. Placing the sensors in optimal locations can aid in reducing experimental uncertainty. This drives the sensor to locations of reduced measurement gradients. Furthermore, the authors introduce a response ratio quantity. “The main objective of a good instrumentation design will be to maximize the response ratio for all modes of interest” [59].

$$\delta_{max_i} = \frac{\max[\delta_1, \delta_2, \dots, \delta_N]}{\delta_{max\ on\ blade}} \quad (2.10)$$

Also focusing on the experimental uncertainties associated with vibrations testing, Laborde [62] shows by means of Monte Carlo simulation, a “stochastic cloud of the output of interest can be generated. This provides an estimate of the test results’ global error. This cloud is generated by assuming errors are generated from specific test uncertainties.” In the case of the traveling wave test setup, these uncertainties would lie, for example, in the actuator position, input strength, or laser vibrometer measurement locations. The authors discuss how the “uncertain parameters are input as random variables into a Monte Carlo simulation. The uncertainties are assigned to their own probability distributions and the simulations use the parameters from these distributions.”

2.2.3 *Stochastic Studies.*

In 1989, Sinha and Chen [63] formulated a method to compute the statistics of a mistuned rotor’s forced response. A similar type of analysis is shown in Bah’s work [43]. The analytical technique presented in Sinha’s work produces complete information regarding the rotor’s blades’ amplitude Probability Density Function (PDF). By using the authors’ technique, the probability that a blade’s amplitude is less than a certain value can be readily determined. The authors develop the methodology first, and then go on to verify the technique using a spring-mass system, similar to the one seen in Figure 2.8.

First, the authors assume the tuned system's stiffness matrix has been contaminated due to mistuning. To that end, any cyclic symmetry is now destroyed. Each element of D_k is assumed to be non-zero and is a linear combination of independent, random Gaussian variables with a zero mean. There are as many independent random variables as there are blades in the system. This assumption is to state that each blade's mistuning is "equal" to the next. In other words, one blade does not have more random parameters than its neighbor. The following equation shows how the system stiffness matrix is generated.

$$K = K_t + D_k \quad (2.11)$$

And the external force on each blade will be assumed to represent a particular engine order excitation, and as a result, is sinusoidal in time, and differs in phase by a constant amount from blade to blade. The authors let the steady state response of the mistuned system differ from that of the tuned system by ΔX . Thus

$$X = X_t + \Delta X \quad (2.12)$$

This says the total system response is the sum of the tuned and mistuned responses. The authors ultimately provide a relationship which gives the probability that the response amplitude, A_j , will be less than a critical value, A_c :

$$Pr(A_j < A_c) = \frac{\int_0^{A_c} g_2(A_j) dA_j}{\int_0^{\infty} g_2(A_j) dA_j} \quad (2.13)$$

The specific parameter definitions are found in Sinha's work [63]. The authors indicate that predictive accuracy is a function of the system damping factor, ζ and the ratio of the standard deviation and the mean value of individual blade's natural frequency, R . Further, the authors show, given typical values of ζ and R , the technique developed in the paper yields reasonably accurate results.

In another work some five years later, the Air Force Research Laboratory [64] published an article describing its own internal methods to apply probabilistic techniques

for component life estimation. While this paper involves the use of probabilistics, the authors were not explicitly exploring forced response of mistuned rotors. This document, while not technically rigorous, provides a top level view of the various types of programs instated throughout the Air Force. Lee [65] provides a more technical assessment of specific probabilistic methods to assess the mistuned rotor response.

Soize [66] addresses specific modeling uncertainties through use of a non-parametric probabilistic approach. The author emphasizes how the mathematical-mechanical modeling process of systems introduces two fundamental types of uncertainties: (1) data uncertainties and (2) model uncertainties. These uncertainties must be taken into account for improving the model's predictive capabilities. In this work, the Soize introduces several terms used in a model uncertainty analysis, namely the differences between real and designed systems, and simple and complex real systems. He also introduces use of the mean model as a predictive model, and the errors and uncertainties associated with such an assumption. For general uncertainties, the author illustrates how the input and parameters related to the mean model will be designated as the data of the mean model. The mathematical modeling process of the designed system introduces two fundamental types of uncertainties - the data uncertainties and the model uncertainties. These are described next.

In addressing data uncertainties, the mean model's input does not exactly represent the real system's input. In addition, there are uncertainties on parameters used in the mean model. For instance, Soize states how "a static load represented by a point force is an approximation of reality and a material's Young modulus is not an exact value (which is unknown), but corresponds to an uncertain value. Data uncertainties must be taken into account in order to improve the mean model's capability." Soize recommends the best approach to take into account data uncertainties is "the parametric probabilistic approach consisting of modeling the data of the mean model by random quantities." The parametric

approach accounts for system and model parameters. For model uncertainties, the modeling process itself used to create the mean model induces model uncertainties with respect to the designed system. This uncertainty is mainly due to the simplifications used to reduce system complexities. Soize says, for instance, “a slender cylindrical elastic medium will be modeled using beam theory (such as an Euler or a Timoshenko beam), a thick rectangular plate elastic medium will be modeled by using the thick plate theory (such as the Mindlin plate theory).”

2.3 Capturing Uncertainty

In 1889, the famous physicist Lord Kelvin stated: “When you can measure what you are speaking about, and express it in numbers, you know something about it; otherwise your knowledge is of a meager and unsatisfactory kind” [67].

There has been a tremendous amount of effort in the area of capturing and quantifying uncertainty. The following discussion will cover a few of the methods which are applicable to the current research effort. The term *error* is often incorrectly confused with the term *uncertainty*. “As uncertainty is attributed to a *lack of knowledge*, error is defined as a recognizable deficiency in any phase or activity of the modeling, simulation, or experiment that is *not* due to a lack of knowledge” [68]. For example, an experiment might involve the use of temperature. Assuming a temperature, without using precise measurements will introduce a degree of uncertainty into the results. Ignoring the effects of temperature altogether would be an error. “Unacknowledged error is known as a mistake” [68]. Uncertainty within engineering analysis and design is also defined as knowledge incompleteness. Assumptions may be made regarding a specific material thickness. Thus, the exact thickness is uncertain.

Ayyub [69] states “uncertainty can also be used to characterize the state of a system as being in doubt - as in the uncertainty of an outcome.” If specific assumptions are made regarding a process or a random parameter is introduced into the system, the exact nature

of the outcome cannot be precisely defined. In general, uncertainty is categorized into two broad categories: aleatory and epistemic uncertainties. Aleatory uncertainty can be thought of as inherent randomness within the system. Mistuning fits within this framework as small geometric and material deviations are perceived as random occurrences. Any additional testing and evaluation does not fill in the gaps in knowledge associated with this type of uncertainty. The second kind, epistemic uncertainty, is due to a lack of complete knowledge. In contrast to those aleatoric events, additional testing and evaluation can make up the gap in epistemic uncertainty. If a material thickness is assumed during a test, this type of uncertainty is classified as epistemic. To alleviate this uncertainty, the experimentalist would be required to simply measure the thickness in question. Therefore, this parameter is no longer unknown or uncertain in its value. Swiler [11] discusses the use of probability theory to represent epistemic uncertainty.

Taking a probabilistic approach when examining uncertainty involves assigning probability distributions, such as a normal or uniform distribution, to the uncertain parameters at hand. When performing an experiment, these parameters are drawn from their respective distributions for use as inputs to the experimental process. Ayyub [69] states, “when uncertainty is understood, recognized, and quantified, the framework of probability can be used to represent it.” Many researchers have used such techniques in their quest for handling uncertainty.

Model validation is another area where uncertainty quantification is paramount. Thacker [70] points out that “validation is the process of determining the degree to which a model is an accurate representation of the real world.” Alvin [68] then adds that “uncertainty and error quantification is a two-step process. The first step requires identifying all sources of uncertainty and error during each phase of modeling and simulation. The second step is the assessment and propagation of the most significant uncertainties and errors through the phases of the modeling and simulation process - all

the way to the predicted response quantities.” Thacker [70] and Adhikari [71] echo the same steps. However, Adhikari goes on to address both parametric and non-parametric uncertainty propagation and computation as well. In this discussion, a parametric uncertainty involves any uncertainty associated with a system parameter. These may be parameters such as Poisson’s ratio or elastic modulus. A non-parametric uncertainty may involve an unquantified term within the system’s equation of motion or even the inclusion of noise on the output. The author addresses both parametric and non-parametric uncertainty propagation and computation methods to validate the predictions. Several of the techniques described in these works will be adopted in the current research, as they are applicable to both analytical and experimental work. In the current research, some specific non-parametric uncertainties are input and output measurement locations and measurement noise. The parametric uncertainties will come in the form of mass and stiffness variations as a function of the uncertain rotor geometries.

Several techniques involve perturbations in an effort to capture the unknown quantities. These perturbation techniques address the aleatoric nature of the uncertainty through perturbing nominal quantities by way a random variation. An early paper by Doyle [72], though not specifically tailored to the forced response of integrally bladed rotor, does cover such a technique. Here, the author employs a control system, together with feedback. The author accounts for uncertainties by perturbing system values and assessing the change in singular values compared to that of the nominal system. The singular values are, in effect, the system’s natural frequencies. The perturbations affecting the system’s physical makeup cascade downward and ultimately alter the system’s natural frequencies. The author was assessing the robustness of theoretical systems in handling property variations. Steinbuch [73] also employs singular values. Similar to the Doyle’s work, Steinbuch creates a theoretical system with a feedback loop. His uncertainty lies within the feedback loop itself, as opposed to being perturbations of system parameters

within the system plant matrix. The uncertainties inside this loop are variations of system parameters. Once the system is computed, singular values are examined and compared to those realized with the nominal system.

Hasselmann [74, 75] demonstrates another perturbation technique. In contrast to the previously mentioned papers, this author chooses to linearly perturb the system stiffness matrices and carry these perturbations through to a point where a statistical analysis can be performed. Here, mass and stiffness uncertainty is represented by the difference between the predicted and measured natural frequencies and mode shapes of generically similar structures. Assuming that mass and stiffness uncertainty are independent of damping and external forcing functions, the author begins with a homogeneous equation of motion.

$$M\ddot{x} + Kx = 0 \quad (2.14)$$

The author defines M and K as the true mass and stiffness matrices, respectively. Thus, the undamped eigenproblem is given as:

$$(K - \lambda_j M)\phi_j = 0 \quad (2.15)$$

where λ_j and ϕ_j are the j^{th} eigenvalue and eigenvector, respectively, for the true system. The matrix perturbation comes in the form of small variations of the true system, added to the analytical system matrices.

$$\begin{aligned} K &= K^o + \Delta K \\ M &= M^o + \Delta M \\ \lambda_j &= \lambda_j^o + \Delta\lambda_j \\ \phi_j &= \phi_j^o + \Delta\phi_j \end{aligned} \quad (2.16)$$

Here, the terms with the superscript “o” represent those associated with the analytical system. Substituting these definitions into Equation 2.15 produces:

$$(K^o - \lambda_j^o M^o)\Delta\phi_j + (\Delta K - \lambda_j^o \Delta M - \Delta\lambda_j M^o)\phi_j^o = 0 \quad (2.17)$$

From here, standard modal analysis techniques are employed to obtain the system eigenvalues and eigenvectors. The significance of this work lies with the results developed which ultimately quantify the modeling uncertainty. “When replicate test data are available, the results obtained from multiple perturbation trials can be used to quantify experimental uncertainty, apart from any model, by substituting mean test measurements for analytical model predictions” [74]. This would give a direct indication of the level of experimental uncertainty.

Rahimi [76] also provides a similar type of perturbation technique by varying nominal quantities by a random amount. The author presents a methodology which calculates the forced vibration response of a mistuned system based on an exact relationship between tuned and mistuned system representations. Uncertainty is accounted for using existing manufacturing tolerances as upper and lower bounds, for example. The author then goes on to find the worst case response for a given system, and finally introduces intentional mistuning to demonstrate how the maximum response is reduced. This intentional mistuning essentially counteracts the existing mistuning and reduces its effect.

Aside from perturbations, researchers have also employed methods to relate the transient response histories from a predictive model and experiment. Geers [77] and Russell [78] provide such a technique. These paper describes an objective error measure for assessing the discrepancy between a calculated and measured response history. The authors’ development produces what is called a “comprehensive error factor” which substantially reduces the amount of data involved with transient response calculations and quantifiably shows existing error between two time domain signals. The author attempts to correct for any error bias which occurs if one set of data is assumed to be true, while the other is not. This concept of biasing is important when examining entire responses, instead of a single point - where the error bias is not as significant. Here at this single point, it may simply be a coincidence that the two data sets are correlated.

In contrast to the previously mentioned papers discussing transient responses, Oberkampf [79] introduces a method for point comparisons. While this technique is not developed for a transient response, it does provide a measure of agreement between a model's prediction and the experimental results. The validation metric is based on the statistical concept of confidence intervals. "Using this fundamental concept, two specific metrics are constructed. One requires the interpolation of experimental data, and the other requires regression (curve fitting) of experimental data" [79]. "The emphasis in this work is not on optimizing the agreement between a given model and experimental measurements." Such techniques are used in model updating methods where a model is changed based on the results of an experiment. The authors focus on validation metric which is a blind assessment of the model's predictive capability.

Adhikari [80] provides an example in using both parametric and non-parametric uncertainty associated with their model and experimental evaluation of a fixed-fixed beam and vibrating plate. The authors propagate this uncertainty through the model. The goal is to quantify uncertainty with the aim of gaining more insight into the nature of uncertainties in medium and high frequency vibrations problems. In this paper, the authors adopt a probabilistic approach, using normal distributions to assign random mass and un-modeled dynamic values and locations. They authors utilize two experimental tests to investigate two different phenomena. The first experiment involved a beam with fixed-fixed boundary conditions. This experiment focused on capturing the uncertainty induced by randomly varying mass distribution. The second experiment is a vibrating cantilevered plate. The purpose of this experiment was to capture the effects of uncertain, un-modeled dynamics. The authors attached oscillators at random locations and obtained FRFs.

The work in this paper aligns with the motivation behind this current research effort because there will be uncertain force input and response output locations. In addition, the rotor geometry can be handled in a similar manner. Techniques used in this paper can be

modified to account for this geometric uncertainty, rather than only uncertain mass and dynamic properties, as the geometry change will affect both mass and stiffness. Murthy [81] performs a similar type of experiment and analysis.

Swiler, et al. [11], from Sandia National Laboratories, put together a paper highlighting three methods to propagate epistemic uncertainty.

- Interval Analysis
- Dempster-Shafer Evidence Theory
- Second-Order Probability

The authors employ interval analysis by way of ascertaining the output intervals given a set of inputs, also defined by intervals. The authors are attempting to answer the following question: If the system inputs are bound by specific intervals, what is the corresponding interval on the output? One technique they employed was a direct approach which used optimization to find the maximum and minimum values of the output measure of interest. This corresponds to the upper and lower interval bounds on the output, respectively. Another technique involved sampling from the uncertain interval inputs. After such sampling has taken place, the maximum and minimum values are used as an estimate for lower and upper bounds. The values in between are assumed to be normally distributed.

Dempster-Shafer evidence theory relaxes the usual assumptions of probability theory in situation where there is little information on which to evaluate a probability. For example, there may be a specific set of parameters, when considered together, lend more less credence to the likelihood of an event. In this theory, the epistemic uncertainties are modeled as sets of intervals. The intervals are propagated to calculate *belief* (“a lower bound on a probability which is consistent with the evidence”) and *plausibility* (“an upper bound on a probability which is consistent with the evidence”) [11]. The minimum and maximum values are collected to produce belief and plausibility curves.

The second-order probability attempts to propagate both aleatory and epistemic uncertainty. The process is illustrated by using an inner and outer loop. The epistemic variables are specified in the outer loop, while the inner loop takes a variable from the outer loop and performs sampling on the aleatory variables. Figure 2.16 below better illustrates this concept. Techniques employed in this paper would serve well in the current research as the unknowns with both the model and experimental setup could be modeled using probability distributions or intervals.

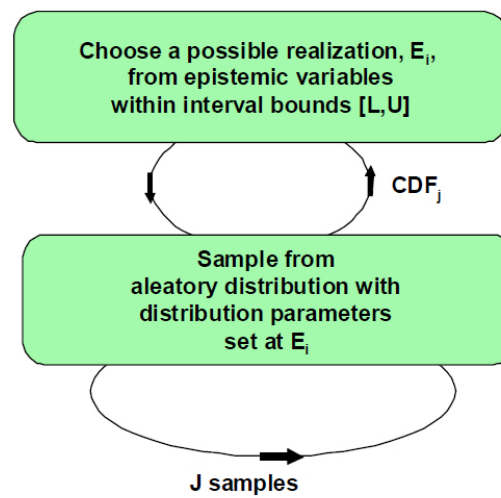


Figure 2.16: Second-Order Probability [11]

The well established finite element technique has also evolved to capture uncertainty quantities within the confines of the numerical simulations. DeLima [82] discusses such a technique. Here, a classical probabilistic approach is taken to account for random uncertainty. The random variables may terms identifying geometric characteristics, elastic moduli, displacements, or loads.

Huang [83] describes a method for perturbation finite element analysis. The author initially states that “traditional finite element approaches are based on well defined system input parameters.” This work is motivated by the fact that realistic structural models often have parameters which are not precisely known. These parameters might be material

properties, or in the case of this dissertation research, geometry. In Huang's work, the author derives the classical finite element technique using an imprecise variable approach. Here, he perturbs the "crisp" values with an unknown, imprecise parameter. Specifically in the paper, the author begins by perturbing the system constitutive matrix. For a crisp system, this matrix is defined as:

$$D = \frac{E}{(1 - \nu^2)} \begin{bmatrix} 1 & \nu & 0 \\ \nu & 1 & 0 \\ 0 & 0 & \frac{1 - \nu}{2} \end{bmatrix}, \quad (2.18)$$

where E is the system elastic modulus and ν is Poisson's ratio. These values will now be perturbed by an imprecise parameter.

$$\tilde{E} = E^o + \tilde{e} \quad (2.19)$$

$$\tilde{\nu} = \nu^o + \tilde{\nu} \quad (2.20)$$

With the perturbed parameters, the system constitutive matrix is now given as:

$$\tilde{D} = \frac{E^o + \tilde{e}}{1 - (\nu^o + \tilde{\nu})^2} \begin{bmatrix} 1 & \nu^o + \tilde{\nu} & 0 \\ \nu^o + \tilde{\nu} & 1 & 0 \\ 0 & 0 & \frac{1 - (\nu^o + \tilde{\nu})}{2} \end{bmatrix} \quad (2.21)$$

The body forces and applied forces can also be handled in a similar manner through perturbing their known values by a small, imprecise amount. The complete details of this method are found in [83].

Fraccone [84], [85] discusses the uncertainty associated with a rotor's forced response. The authors acknowledge both the material property and geometric deviations' role in rotor mistuning. The author models the rotor using beams which are then interconnected with springs. Perturbation techniques are used to address uncertainty due to input, sensor-based, and modeling anomalies.

This literature review covered several distinct topics. These topics covered mistuning and its impact in both the time and frequency domains. Second, this review discussed previous modeling and experimental mistuning work and emphasized methods to capture and characterize a mistuned structure's behavior. Lastly, the concept of uncertainty was explored. Here, several techniques were illustrated which capitalized on perturbations to account for both modeling and experimental uncertainty.

III. Theory

The following chapter will outline some of the overarching theories used in this current research.

3.1 Cantilever Beam Forced Vibration Response Under the Effects of an Electromagnetic Actuator

This section will provide a top level examination of the forced vibration response of a cantilever beam under excitation from an electromagnetic actuator. Rather than focusing on an accurate blade model, this section focuses attention on the forcing function and the response from a simple cantilever beam. Under magnetic excitation, as is the case when using the traveling wave excitation equipment, the forcing function driving the blades varies in magnitude both as a function of time and distance. The distance is measured between the actuator and the blade. The development here will provide insight into the nature of a rotor's forced response under electromagnetic excitation. The simple beam model is used because many earlier researchers used the beam model as an approximation of a blade.

3.1.1 Beam Theory for a General Case of Transverse Motion.

This development is taken from Rao [60]. The author gives the general differential equations for a beam's transverse vibration as:

$$-\frac{\partial}{\partial x} \left[kAG \left(\frac{\partial w}{\partial x} - \phi \right) \right] + \rho A \frac{\partial^2 w}{\partial t^2} = f(x, t) \quad (3.1)$$

$$-\frac{\partial}{\partial x} \left(EI \frac{\partial \phi}{\partial x} \right) - kAG \left(\frac{\partial w}{\partial x} - \phi \right) + \rho I \frac{\partial^2 \phi}{\partial t^2} = 0 \quad (3.2)$$

There are two separate equations here. The first equation depicts the beam's vertical displacement, w , due to an external forcing function. While the second equation describes the beam's rotation, ϕ , during its vertical displacement. Throughout the derivation, it is assumed that shear stress is uniform at every point in the cross section. Because this is not necessarily true in reality, Timoshenko introduced a constant term to correct for the effects

of a varying shear stress. This constant, k is defined as the shear correction factor. The variables ρ , G , A , and I are the beam's density, shear modulus, cross sectional area, and moment of inertia, respectively. Because the beam in this example is uniform, Equations 3.1 and 3.2 can be combined into a single equation of motion.

$$-kAG \frac{\partial^2 w}{\partial x^2} + kAG \frac{\partial \phi}{\partial x} + \rho A \frac{\partial^2 w}{\partial t^2} = f \quad (3.3)$$

or,

$$\frac{\partial \phi}{\partial x} = \frac{\partial^2 w}{\partial x^2} - \frac{\rho}{kG} \frac{\partial^2 w}{\partial t^2} + \frac{f}{kAG} \quad (3.4)$$

and

$$-EI \frac{\partial^2 \phi}{\partial x^2} - kAG \frac{\partial w}{\partial x} + kAG \phi + \rho I \frac{\partial^2 \phi}{\partial t^2} = 0 \quad (3.5)$$

Differentiating Equation 3.5 with respect to x produces:

$$-EI \frac{\partial^2}{\partial x^2} \left(\frac{\partial \phi}{\partial x} \right) - kAG \frac{\partial^2 w}{\partial x^2} + kAG \frac{\partial \phi}{\partial x} + \rho I \frac{\partial^2}{\partial t^2} \left(\frac{\partial \phi}{\partial x} \right) = 0 \quad (3.6)$$

Substituting Equation 3.4 into Equation 3.6 yields:

$$EI \frac{\partial^4 w}{\partial x^4} + \rho A \frac{\partial^2 w}{\partial t^2} - \rho I \left(1 + \frac{E}{kG} \right) \frac{\partial^4 w}{\partial x^2 \partial t^2} + \frac{\rho^2 I}{kG} \frac{\partial^4 w}{\partial t^4} + \frac{EI}{kAG} \frac{\partial^2 f}{\partial x^2} - \frac{\rho I}{kAG} \frac{\partial^2 f}{\partial t^2} - f = 0 \quad (3.7)$$

Expanding this equation produces:

$$EI \frac{\partial^4 w}{\partial x^4} + \rho A \frac{\partial^2 w}{\partial t^2} - \rho I \frac{\partial^4 w}{\partial x^2 \partial t^2} - \frac{\rho IE}{kG} \frac{\partial^4 w}{\partial x^2 \partial t^2} + \frac{EI}{kAG} \frac{\partial^2 f}{\partial x^2} - \frac{\rho I}{kAG} \frac{\partial^2 f}{\partial t^2} - f = 0 \quad (3.8)$$

The third term in the expanded expression accounts for the beam's rotary inertia. The fourth term accounts for any shear deformation occurring within the beam. Further, the fifth and sixth terms reflect any shear deformation induced by the applied force. The final term is the externally applied forcing function.

3.1.2 Euler-Bernoulli Beam.

If a beam's length is at least 100 times its thickness, the beam's rotary inertia, shear deformation, and damping is negligible. Further, it is assumed any deflection due to

bending does not exceed the beam's thickness. Lastly, lines perpendicular to the neutral axis prior to bending will remain perpendicular after the bending has occurred. Thus, the Timoshenko beam can be reduced to the Euler-Bernoulli beam model. By neglecting the terms accounting for rotary inertia and through the thickness shear, Equation 3.8 is reduced to

$$\frac{\partial^2}{\partial x^2}(EI \frac{\partial^2 w}{\partial x^2}) + \rho A \frac{\partial^2 w}{\partial t^2} = f(x, t) \quad (3.9)$$

This equation is the Euler-Bernoulli beam model. Here, the variable w is used for displacement, x represents the beam's linear dimension, and t is a temporal variable. For a cantilevered beam, the boundary conditions are clamped at $x = 0$ and free at $x = l$. To that end, there does not exist displacement or slope at $x = 0$, nor does there exist moment or shear at $x = l$. For the fixed end, the following are the mathematical relations expressing the boundary conditions:

$$\begin{aligned} w(0, t) &= 0 \\ \frac{\partial w}{\partial x}(0, t) &= 0 \end{aligned} \quad (3.10)$$

Following suit, the mathematical relations expressing the boundary conditions for the free end are given as:

$$\begin{aligned} EI \frac{\partial^2 w}{\partial x^2}(l, t) &= 0 \\ \frac{\partial}{\partial x}(EI \frac{\partial^2 w}{\partial x^2})(l, t) &= 0 \end{aligned} \quad (3.11)$$

In the traveling wave excitation equipment, each blade is actuated by way of an electromagnetic solenoid. The forcing function from an electromagnetic solenoid is unique in that its strength varies as functions of both distance away from the actuator and in time. The inverse square law dictates the field strength from a magnetic source. From Coey [86], the field strength, F , of an electromagnetic solenoid can be expressed as

$$F = \frac{(NI)^2 kA}{2g^2} \quad (3.12)$$

In this equation, N is the number of wire turns within the solenoid coil, I is the applied current (amps), A is the solenoid's cross sectional area (m^2), and g is the distance between the solenoid and the blade. The parameter k is called the magnetic constant, which has a value of $4\pi \times 10^{-7} \frac{V \cdot sec}{amp \cdot m}$. One drawback to this equation is that it assumes a constant distance between the solenoid and blade. To compensate for this, the distance, g , needs to be defined as a function of time. Assume the beam's motion is proportional to the driving frequency. The traveling wave system excites the blades by sweeping through a range of frequencies. Mark [25] derives an equation which defines the frequency sweep.

$$Y(t) = \sin\left(2\pi\left[\frac{1}{2}\left\{\frac{f_2 - f_1}{T_s}\right\}t + f_1\right]t + \phi\right) \quad (3.13)$$

In this equation f_1 and f_2 are the initial and final frequencies, respectively, T_s is the frequency sweep time, and ϕ is any phase difference between the two frequencies. Therefore, with an assumed initial blade to actuator standoff distance, s (m), the equation will now provide the beam tip distance as a function of time.

$$g(t) = s + Y(t) \quad (3.14)$$

Since the distance between the beam and actuator has been established, the forcing function, $F(t)$, expression is given as:

$$F(t) = \frac{(NI)^2 k A}{2g(t)^2} \quad (3.15)$$

with the distance between the blade and actuator tip as a function of time as given in Equation 3.14.

Solving this forced vibration equation involves solving both the homogeneous and non-homogeneous equations associated with the cantilever beam. The homogeneous equation represents the free vibration solution. Under the assumption the beam is both homogeneous and prismatic, the equation of motion for free vibration is given as:

$$c^2 \frac{\partial^4 w}{\partial x^4}(x, t) + \frac{\partial^2 w}{\partial t^2}(x, t) = 0 \quad (3.16)$$

The term c represents $\sqrt{\frac{EI}{\rho A}}$. E is the beam's elastic modulus, I is the moment of inertia, ρ is the material density, and A is the beam's cross sectional area.

The free vibration solution is found using the separation of variables technique. Let:

$$w(x, t) = W(x)T(t) \quad (3.17)$$

Using this definition in Equation 3.16 produces:

$$\frac{c^2}{W(x)} \frac{d^4 W(x)}{dx^4} = -\frac{1}{T(t)} \frac{d^2 T(t)}{dt^2} = a = \omega^2 \quad (3.18)$$

Since each side of the equation is a function of its own variable and forced equal to one another, each side of the equation is therefore equal to a constant term. Let this constant term be defined as: $a = \omega^2$. This single equation can thus be rewritten as two separate equations, each a function of its own variables.

$$\frac{d^4 W(x)}{dx^4} - \beta^4 W(x) = 0 \quad (3.19)$$

$$\frac{d^2 T(t)}{dt^2} + \omega^2 T(t) = 0 \quad (3.20)$$

where,

$$\beta^4 = \frac{\omega^2}{c^2} = \frac{\rho A \omega^2}{EI} \quad (3.21)$$

The solution to Equation 3.20 is given as:

$$T(t) = A \cos(\omega t) + B \sin(\omega t) \quad (3.22)$$

The constants A and B are found by using the initial conditions. The solution for Equation 3.19 is assumed to be of the form:

$$W(x) = C e^{sx} \quad (3.23)$$

The change to a capital W was made because the displacement equation is now a function of a single variable.

Substituting this solution into Equation 3.19 produces the following relation:

$$s^4 - \beta^4 = 0 \quad (3.24)$$

which has roots given as:

$$s_{1,2} = \pm\beta \quad s_{3,4} = \pm i\beta \quad (3.25)$$

Therefore the solution to Equation 3.19 can be written as:

$$W(x) = C_1 e^{\beta x} + C_2 e^{-\beta x} + C_3 e^{i\beta x} + C_4 e^{-i\beta x} \quad (3.26)$$

Another form of this equation is the following:

$$W(x) = C_1 \cos(\beta x) + C_2 \sin(\beta x) + C_3 \cosh(\beta x) + C_4 \sinh(\beta x) \quad (3.27)$$

where C_1, C_2, C_3 , and C_4 are constants which are determined using the system boundary conditions.

The beam's natural frequencies can be determined using Equation 3.21.

$$\omega = \beta^2 \sqrt{\frac{EI}{\rho A}} = (\beta l)^2 \sqrt{\frac{EI}{\rho A l^4}} \quad (3.28)$$

The boundary conditions for a cantilevered beam are given in Equations 3.10 and 3.11.

$$EI \frac{d^2 W}{dx^2}(l) = 0 \quad \text{or} \quad \frac{d^2 W}{dx^2}(l) = 0 \quad (3.29)$$

$$EI \frac{d^3 W}{dx^3}(l) = 0 \quad \text{or} \quad \frac{d^3 W}{dx^3}(l) = 0 \quad (3.30)$$

The displacement and slope boundary conditions in Equation 3.27 shows that:

$$C_1 = C_3 = 0 \quad (3.31)$$

Using the moment and shear boundary conditions in Equation 3.27 produces:

$$\begin{aligned} & C_2(\cos(\beta l) + \cosh(\beta l)) + C_4(\sin(\beta l) + \sinh(\beta l)) \\ & C_2(-\sin(\beta l) + \sinh(\beta l)) + C_4(\cos(\beta l) + \cosh(\beta l)) \end{aligned} \quad (3.32)$$

These two equations thus lead to the frequency equation. The roots of this equation aid in determining the beam's natural frequencies.

$$\cos(\beta l) \cosh(\beta l) + 1 = 0 \quad (3.33)$$

Therefore:

$$C_4 = -\frac{\cos(\beta l) + \cosh(\beta l)}{\sin(\beta l) + \sinh(\beta l)} C_2 \quad (3.34)$$

Therefore, the n^{th} mode shape is given as:

$$W_n(x) = (\cos(\beta_n x) - \cosh(\beta_n x) - \frac{\cos(\beta_n l) + \cosh(\beta_n l)}{\sin(\beta_n l) + \sinh(\beta_n l)} (\sin(\beta_n x) - \sinh(\beta_n x))) \quad (3.35)$$

where, for the first four bending modes and corresponding natural frequencies

- $\beta_1 l = 1.8751 \quad \omega_1 = (1.8751)^2 \sqrt{\frac{EI}{\rho A l^4}}$
- $\beta_2 l = 4.6941 \quad \omega_2 = (4.6941)^2 \sqrt{\frac{EI}{\rho A l^4}}$
- $\beta_3 l = 7.8547 \quad \omega_3 = (7.8547)^2 \sqrt{\frac{EI}{\rho A l^4}}$
- $\beta_4 l = 10.9956 \quad \omega_4 = (10.9956)^2 \sqrt{\frac{EI}{\rho A l^4}}$

The homogeneous solution produces the portion known as the system normal modes. The solution to the forced response is assumed to be a linear combination of all normal modes. This approach is analogous to the modal analysis techniques applied to discrete systems.

$$w(x, t) = \sum_{i=1}^{\infty} W_i(x) \eta_i(t) \quad (3.36)$$

where, $W_i(x)$ is the i^{th} normal mode found by solving Equation 3.35 and $\eta_i(t)$ is the i^{th} generalized, or modal, coordinate. Analogous to the discrete system modal analysis, $W_i(x)$, is a system eigenvector and $\eta_i(t)$ is a modal coordinate of that eigenvector. These modal coordinates, in contrast to their physical coordinate counterparts, do not measure a physical

distance. Rather, these terms give an indication as to the level of participation each mode, or eigenvector, has on the resulting solution.

The equation of motion can be expressed as:

$$\sum_{i=1}^{\infty} \frac{d^2}{dx^2} \left[EI \frac{d^2 W_i(x)}{dx^2} \right] \eta_i(t) + \rho A \sum_{i=1}^{\infty} W_i(x) \frac{d^2 \eta_i(t)}{dt^2} = f(x, t) \quad (3.37)$$

Using the relationship:

$$\frac{d^2}{dx^2} \left[EI \frac{d^2 W_i(x)}{dx^2} \right] - \rho A \omega_i^2 W_i(x) = 0 \quad (3.38)$$

Equation 3.37 can be rewritten as:

$$\rho A \sum_{i=1}^{\infty} \omega_i^2 W_i(x) \eta_i(t) + \rho A \sum_{i=1}^{\infty} W_i(x) \frac{d^2 \eta_i(t)}{dt^2} = f(x, t) \quad (3.39)$$

Here in this equation, the i^{th} mode shape is depicted through the term $W_i(x)$. Multiplying through by the j^{th} mode shape, $W_j(x)$, and integrating from 0 to l (integrating over the beam's length) produces:

$$\sum_{i=1}^{\infty} \eta_i(t) \int_0^l \rho A \omega_i^2 W_j(x) W_i(x) dx + \sum_{i=1}^{\infty} \frac{d^2 \eta_i(t)}{dt^2} \int_0^l \rho A W_j(x) W_i(x) dx = \int_0^l W_j(x) f(x, t) dx \quad (3.40)$$

This integration is performed in order to ultimately determine the entire beam's response. The beam's forced response is the sum of the responses for each infinitely small section within the beam.

Because of the orthogonality property realized with normal modes, all terms within the summations go to zero except where $i = j$, thus:

$$\frac{d^2 \eta_i(t)}{dt^2} + \omega_i^2 \eta_i(t) = Q_i(t) \quad (3.41)$$

The term $Q_i(t)$ is the generalized force corresponding to the i^{th} mode. The generalized, or modal, force is the realization of the applied force together with a mode shape of free vibration. When integrated over the entire beam's length, it gives the depiction of the

forcing function's influence on that particular mode shape. This generalized force is given in the next equation.

$$Q_i(x) = \int_0^l W_i(x)F(x, t)dx \quad (3.42)$$

The complete solution of Equation 3.41 is the sum of the homogeneous and non-homogeneous portions. Shown for completeness, the general procedure to solve the non-homogeneous problem is given in the next section.

3.1.2.1 Solution Procedure for the Non-Homogeneous Equation 3.41.

In general, the equation of motion for a viscously damped system is given by:

$$m\ddot{x}(t) + c\dot{x}(t) + kx(t) = f(t) \quad (3.43)$$

Dividing through by the mass:

$$\ddot{x} + 2\zeta\omega_n\dot{x} + \omega_n^2x = F(t) \quad (3.44)$$

Here, ζ is the system's damping ratio is given as:

$$\zeta = \frac{c}{2m\omega_n} = \frac{c}{c_c} \quad (3.45)$$

and the critical damping constant is defined as:

$$c_c = 2m\omega_n = 2\sqrt{km} \quad (3.46)$$

and finally

$$F(t) = \frac{f(t)}{m} \quad (3.47)$$

For a general forcing function, $f(t)$, the solution of Equation 3.44 is found by taking Laplace transforms of each term in the equation.

$$L[x(t)] = \bar{x}(s) \quad (3.48)$$

$$L[\dot{x}(t)] = s\bar{x}(s) - x(0) \quad (3.49)$$

$$L[\ddot{x}(t)] = s^2\bar{x}(s) - sx(0) - \dot{x}(0) \quad (3.50)$$

$$L[F(t)] = \bar{F}(s) \quad (3.51)$$

Therefore, using these definitions, Equation 3.44 can be expressed as:

$$[s^2\bar{x}(s) - sx(0) - \dot{x}(0)] + 2\zeta\omega_n[s\bar{x}(s) - x(0)] + \omega_n^2\bar{x}(s) = \bar{F}(s) \quad (3.52)$$

Stated alternately:

$$\bar{x} = \frac{1}{\Delta}[\bar{F}(s) + (s + 2\zeta\omega_n)x_0 + \dot{x}_0] \quad (3.53)$$

Where the initial displacement and initial velocity terms, x_0 and \dot{x}_0 , are equal to the $x(0)$ and $\dot{x}(0)$ terms respectively. And the Δ term is defined as:

$$\Delta = s^2 + 2\zeta\omega_n s + \omega_n^2 = (s + \zeta\omega_n)^2 + \omega_d^2 \quad (3.54)$$

Here, the term ω_d is defined as the damped natural frequency. Since ζ equals zero in this example, the damped natural frequency will equal the undamped natural frequency, ω_n . The relationship between the damped and undamped natural frequencies is given in Equation 3.55.

$$\omega_d = \omega_n \sqrt{1 - \zeta^2} \quad (3.55)$$

Now, by employing the inverse Laplace transform on each term produces the following expressions:

$$L^{-1}\left[\frac{1}{\Delta}\right] = \frac{e^{-\zeta\omega_n t}}{\omega_d} \sin(\omega_d t) \quad (3.56)$$

$$L^{-1}\left[\frac{s + \zeta\omega_n}{\Delta}\right] = e^{-\zeta\omega_n t} \cos(\omega_d t) \quad (3.57)$$

$$L^{-1}\left[\frac{\bar{F}s}{\Delta}\right] = \frac{1}{\omega_d} \int_0^t F(\tau) e^{-\zeta\omega_n(t-\tau)} \sin(\omega_d(t-\tau)) d\tau \quad (3.58)$$

The total solution to this problem is the combination of these inverse Laplace transform results.

$$x(t) = \int_0^t F(\tau) h(t-\tau) d\tau + g(t)x_0 + h(t)\dot{x}_0 \quad (3.59)$$

where:

$$h(t) = \frac{1}{\omega_d} e^{-\zeta\omega_n t} \sin(\omega_d t) \quad (3.60)$$

$$g(t) = e^{-\zeta\omega_n t} \left(\cos(\omega_d t) + \frac{\zeta\omega_n}{\omega_d} \sin(\omega_d t) \right) \quad (3.61)$$

Furthermore, there is no initial displacement (x_o) or initial velocity (\dot{x}_o). Therefore:

$$x(t) = \int_0^t F(\tau)h(t-\tau)d\tau \quad (3.62)$$

$$h(t) = \frac{1}{\omega_n} \sin(\omega_n t) \quad (3.63)$$

Therefore, the solution to Equation 3.41 is the sum of its homogeneous and non-homogeneous solutions.

$$\eta_i(t) = A_i \cos(\omega_i t) + B_i \sin(\omega_i t) + \frac{1}{\omega_i} \int_0^t Q_i(\tau) \sin(\omega_i(t-\tau))d\tau \quad (3.64)$$

Finally, the total solution to Equation 3.9 is given by Equation 3.36 and 3.64.

$$w(x, t) = \sum_{i=1}^{\infty} \left[A_i \cos(\omega_i t) + B_i \sin(\omega_i t) + \frac{1}{\omega_i} \int_0^t Q_i(\tau) \sin(\omega_i(t-\tau))d\tau \right] W_i(x) \quad (3.65)$$

Because the beam begins at rest and at an equilibrium position, the coefficients A and B are zero. This reduces the equation to:

$$w(x, t) = \sum_{i=1}^{\infty} \left[\frac{1}{\omega_i} \left(\int_0^t Q_i(\tau) \sin(\omega_i(t-\tau))d\tau \right) \right] W_i(x) \quad (3.66)$$

Using the first four bending modes, the following is an equation which describes the beam's forced response.

$$\begin{aligned} w(x, t) = & \left(\frac{1}{\omega_1} \left(\int_0^t Q_1(\tau) \sin(\omega_1(t-\tau))d\tau \right) W_1(x) \right) + \\ & \left(\frac{1}{\omega_2} \left(\int_0^t Q_2(\tau) \sin(\omega_2(t-\tau))d\tau \right) W_2(x) \right) + \\ & \left(\frac{1}{\omega_3} \left(\int_0^t Q_3(\tau) \sin(\omega_3(t-\tau))d\tau \right) W_3(x) \right) + \\ & \left(\frac{1}{\omega_4} \left(\int_0^t Q_4(\tau) \sin(\omega_4(t-\tau))d\tau \right) W_4(x) \right) \end{aligned} \quad (3.67)$$

3.2 The Free-Free Beam

The subject of system boundary conditions arises in all aspects of structural dynamics. Generally, the number of boundary conditions required to solve a given differential equation

is the same as the differential equation's order. In experimentation, it is often desirable to isolate the test article from any outside influence. This is particularly true in the field of vibrations analysis. Here, any energy imparted into the test article, should remain in the test article. When the article is free from any physical boundaries, only then can the true test article's behavior be captured. In practice, it is often extremely difficult to produce a pure clamped or simply supported boundary. From Reference [87], "experience has shown that the free conditions are easier to simulate than either fixed or clamped-type conditions that are meant to be representative of connections during operation."

Mathematically, these conditions are induced through a simple exercise of assigning zero displacements, slopes, and/or taking the proper time derivatives and setting these equal to zero. Furthermore, the mathematical representation of clamps and simply supports are theoretically perfect; they are applied at infinitesimally small discrete points. To that end, the free boundary is often simulated. A beam with free boundary conditions can be simulated by supporting/hanging the beam at known node points. For this method to work, the node points for the mode under excitation must be known *a priori*. For this dissertation research, suspending a rotor from a point would not be feasible. Therefore, an isolation mat is used to simulate the free condition. Manufactured by Fabreeka, the "FabCel pad material is specifically designed to provide vibration isolation/reduction in industrial applications where structure-borne noise and vibration occur." [88]

In this section, an analysis of the isolation pad will be used in conjunction with a beam to explore its ability to deliver an effective free boundary. First, the analysis of a beam with a continuous elastic support is examined. This beam is continuously supported with an elastic foundation along its entire length. For this analysis, the traditional Euler-Bernoulli beam equation (Equation 3.9) is modified. This theory and the associated numerical results will be used in conjunction with the assumed free experimental boundary in Chapter

$$\frac{\partial^2}{\partial x^2} \left(EI \frac{\partial^2 w}{\partial x^2} \right) + \rho A \frac{\partial^2 w}{\partial t^2} + k_f w = f(x, t) \quad (3.68)$$

For the case of free vibration:

$$EI \left(\frac{\partial^4 w}{\partial x^4} \right) + \rho A \frac{\partial^2 w}{\partial t^2} + k_f w = 0 \quad (3.69)$$

In each equation, the term $k_f w$ is defined as the *foundation modulus*. It is the “load per unit length of the beam necessary to produce a compression in the foundation equal to unity [89].” The solution to this equation is assumed as the linear superposition of all homogeneous and non-homogeneous modal solutions. It is assumed to be of the form:

$$w(x, t) = \sum_{i=1}^{\infty} W_i(x) (C_i \cos(\omega_i t) + D_i \sin(\omega_i t)) \quad (3.70)$$

Here, $W_i(x)$ is the i^{th} mode shape and ω_i is i^{th} the natural frequency. This solution is then substituted back into the original equation to produce:

$$\frac{d^4 W_i(x)}{dx^4} + \left(-\frac{\rho A \omega_i^2}{EI} + \frac{k_f}{EI} \right) W_i(x) = 0 \quad (3.71)$$

This expression can be further simplified by allowing:

$$\alpha_i^4 = \left(-\frac{k_f}{EI} + \frac{\omega_i^2}{c^2} \right) \quad (3.72)$$

where:

$$c = \sqrt{\frac{EI}{\rho A}} \quad (3.73)$$

Thus, the natural frequency is found via:

$$\omega_i = c \alpha_i^2 \sqrt{1 + \frac{k_f}{EI \alpha_i^4}} \quad (3.74)$$

This gives:

$$\frac{d^4 W_i(x)}{dx^4} - \alpha_i^4 W_i(x) = 0 \quad (3.75)$$

The solution to this equation is analogous to the solution shown in Equation 3.27.

$$W_i(x) = C_{1i} \cos(\alpha_i x) + C_{2i} \sin(\alpha_i x) + C_{3i} \cosh(\alpha_i x) + C_{4i} \sinh(\alpha_i x) \quad (3.76)$$

Here, the beam's only support is only the elastic foundation. Since there are no additional end supports, it is assumed there is no shear or moment at either end ($x = 0$ and $x = L$). Therefore, at the end $x = 0$, and taking the required derivatives of Equation 3.76 gives, for shear:

$$W'''(0) = 0 \quad (3.77)$$

$$-C_2\alpha^3 + C_4\alpha^3 = 0 \quad (3.78)$$

$$C_2 = C_4 \quad (3.79)$$

and for the moment:

$$W''(0) = 0 \quad (3.80)$$

$$-C_1\alpha^2 + C_3\alpha^2 = 0 \quad (3.81)$$

$$C_1 = C_3 \quad (3.82)$$

Similarly, at $x = L$, for shear:

$$W'''(L) = 0 \quad (3.83)$$

$$C_3(\alpha^3 \sin(\alpha L) + \alpha^3 \sinh(\alpha L)) + C_4(-\alpha^3 \cos(\alpha L) + \alpha^3 \cosh(\alpha L)) = 0 \quad (3.84)$$

$$(3.85)$$

and for the moment:

$$W''(L) = 0 \quad (3.86)$$

$$C_3(-\alpha^2 \cos(\alpha L) + \alpha^2 \cosh(\alpha L)) + C_4(-\alpha^2 \sin(\alpha L) + \alpha^2 \sinh(\alpha L)) = 0 \quad (3.87)$$

$$(3.88)$$

For these two equations at $x = L$, there exists two equations and two unknowns. For the non-trivial solution, the determinate of these equations' coefficient matrix must equal zero. The resulting equation is:

$$\cos(\alpha L)\cosh(\alpha L) - 1 = 0 \quad (3.89)$$

And using Equation 3.86, C_4 can be defined as:

$$C_4 = C_3 \frac{-\cos(\alpha L) + \cosh(\alpha L)}{\sin(\alpha L) - \sinh(\alpha L)} \quad (3.90)$$

Therefore, using Equation 3.76, the mode shape equation can be expressed as:

$$W(x) = C_3 (\cos(\alpha x) + \cosh(\alpha x)) - \frac{(\cos(\alpha L) - \cosh(\alpha L))(\sin(\alpha x) + \sinh(\alpha x))}{\sin(\alpha L) - \sinh(\alpha L)} \quad (3.91)$$

Solving Equation 3.89 and verifying this result by plotting Equation 3.91, Table 3.1 gives the individual arguments for the frequency equation (Equation 3.89)

Table 3.1: Frequency Equation Arguments for a Beam on a Continuous Elastic Foundation

Mode	Argument ($\alpha_i L$)
1	4.73
2	7.8532
3	10.9956
4	14.1372

Not surprisingly, these are the same values found when examining a free-free beam. Examining the natural frequency expression for this continuously supported beam in Equation 3.74 corroborates this. As the foundation modulus term in Equation 3.74 approaches zero, the natural frequency for the continuously supported beam and the free-free beam equal one another. The issue here lies with the relatively high stiffness in the isolation mat used in the laboratory. Perhaps the solution here lies in only supporting the beam at discrete points.

3.2.1 Supported Mode 1 Beam.

Rather than continuously supporting the beam along its length, the beam will be supported at its node points for a given mode. A beam's first bending mode examined here. For mode 1, the beam's first and second node points are located at 24.4159 and 77.5849 percent of the beam's length, respectively. A beam's node points are determined by solving

for the zeros in its unique mode shape equation. Any text on continuous vibrations, such as Rao [60], provides the necessary relationships to determine the node points' locations.

For the numerical exercise, a free-free beam's 1st natural frequency will be directly compared to that of a beam supported at its nodes. Furthermore, the beam length to support diameter (L/D) relationship will be established based on these numerical results. This can then be used to size a beam vibrations experiment where a free-free condition is desired. Figure 3.1 shows the typical setup for this series of analyses. Figures 3.2 and 3.3 show the pertinent dimensions used during this analysis.

Table ?? gives the beam's material and geometric properties. The beam will be supported on 7075-T6 aluminum supports, 0.1016 m (4 in.) tall. The support diameter will be altered with each iteration to change the (L/D) ratio.

Table 3.2: Supported Plate Material and Geometric Properties

Beam Material	Al 7075-T6
Beam Length (m)	1
Beam Thickness (m)	0.01
Beam width (m)	0.1
Beam Stiffness (GPa)	71.7
Beam Density ($\frac{kg}{m^3}$)	2810
Poisson's Ratio	0.33
Beam Mass (kg)	2.81

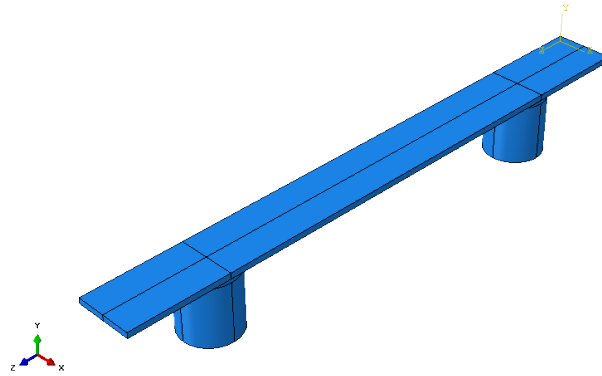


Figure 3.1: Supported Beam Example

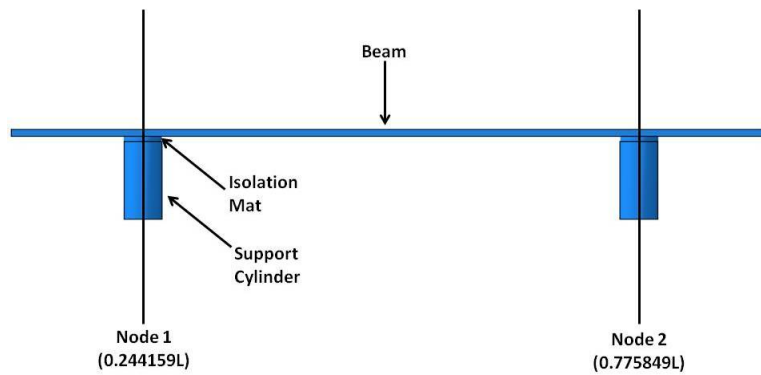


Figure 3.2: Beam Schematic

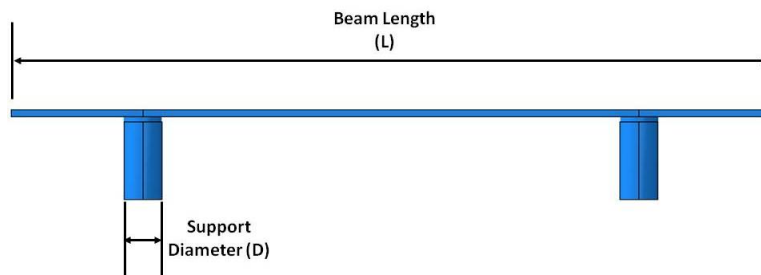


Figure 3.3: Beam Schematic (L/D)

First, a series of analyses were conducted by supporting the beam on the aluminum pedestals without the isolation mat. For each case, the beam was modeled using 5120 C3D20R elements. The support was modeled using 4352 C3D20R elements. Tie

constraints were used to connect the support to the beam. The support was fully constrained at its bottom face. Table 3.3 shows how the first bending mode natural frequency decreases drastically as the (L/D) ratio increases. The natural frequency drops below that of the free-free beam because the slender supports begin to buckle and are thus interfering with the overall beam's modal behavior.

Table 3.3: Supported Beam Without Isolation Mat

Case Number	Support Diameter (m)	(L/D)	1st Natural Freq. (Hz)
1	0.1	10	162.03
2	0.05	20	134.51
3	0.025	40	115.75
4	0.0125	80	72.856
5	0.00625	160	50.321
6	0.003125	320	47.858
7	0.0015625	640	47.404
8	0.00078125	1,280	45.857

The mat was next placed between the beam and support column. The mat's material properties were estimated from manufacturer supplied technical specifications in Reference [88]. Because the material is a foam/rubber type material, Possion's ratio is assumed to be 0.49. The mat thickness is a constant 0.00635 m (0.25 inch). The mat density was estimated using a precisely cut specimen and determining its mass ($657.3 \text{ (kg/m}^3\text{)}$). The mat was modeled using 2162 C3D20R elements. During the analysis, the mat and support are the same diameter. Tie constraints were used between all material interfaces, except for the support's base. The support was fully constrained at its bottom face. The finite element representation for both the pedestal and isolation mat are shown in Figure 3.4.

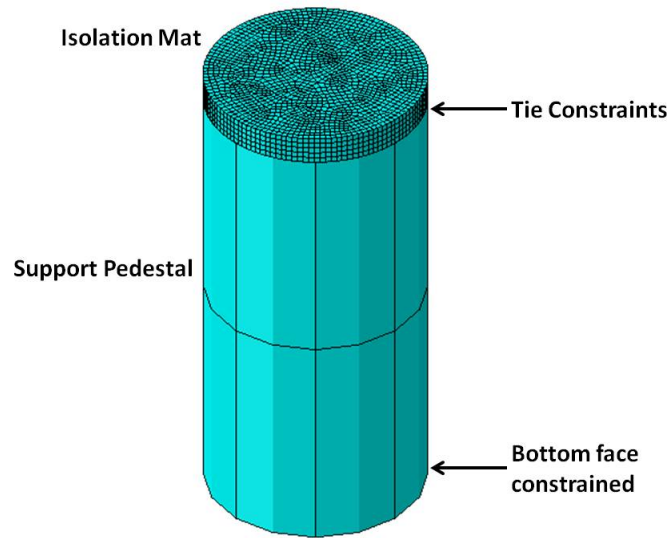


Figure 3.4: Isolation Mat with Support Pedestal

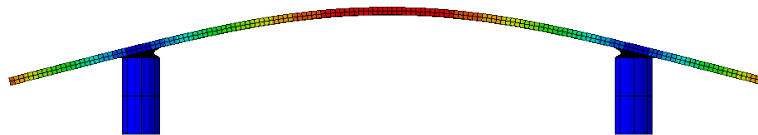


Figure 3.5: Supported Beam Mode 1 (Natural Freq. Within 4.5% of Free Beam)

Table 3.4 summarizes the supported beam's results. Using the isolation mat, a beam at least 20x longer than the support diameter, gives a first bending natural frequency within 4.5% as a free-free beam. If the beam is 40x longer than the support diameter, the first bending natural frequency is 0.08% different than that seen in the free-free beam. Increasing the (L/D) to 80 sees a significant decrease in natural frequency. This is caused from the slender support buckling and interfering with the beam's modal energy distribution.

Table 3.4: Supported Beam With Isolation Mat

Case Number	Support and Mat Diameter (m)	(L/D)	1st Natural Freq. (Hz)
1	0.1	10	86.237
2	0.05	20	49.555
3	0.025	40	51.983
4	0.0125	80	44.083

3.2.2 Supported Mode 1 Plate.

Analogous to the support technique in Section 3.2.1, the circular plate will be supported along a nodal diameter, at the plate's center. The same support configuration (Figure 3.4) is used in this numerical analysis. For modes exhibiting nodal diameters, the plate's center will always lie on this node line. Based on the numerical results, a relationship will be established between the ratio of plate diameter to support diameter (D/d) to the natural frequency giving one nodal diameter. Figure 3.6 shows the typical setup for this series of analyses. Figures 3.7 and 3.8 show the pertinent dimensions. Appendix D provides the derivation for the theoretical circular plate with a free edge.

The plate is supported on a single 7075-T6 aluminum pedestal, 0.1016 m (4 in.) tall. As with the supported beam, the support diameter will be altered with each iteration to change the (D/d) ratio. The support is located at the plate's center during each iteration.

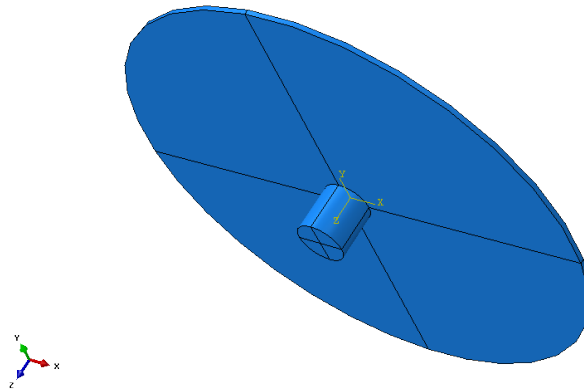


Figure 3.6: Supported Plate Example

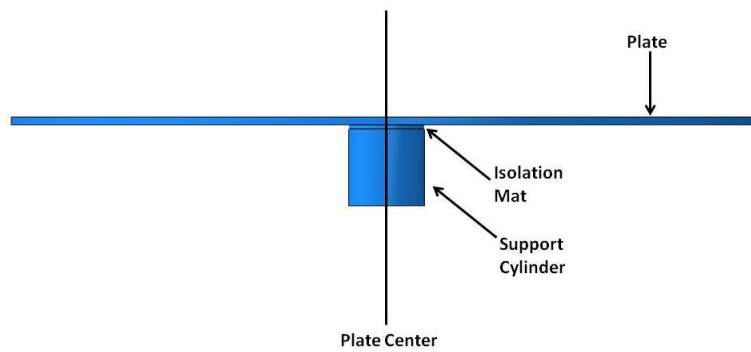


Figure 3.7: Supported Plate Schematic

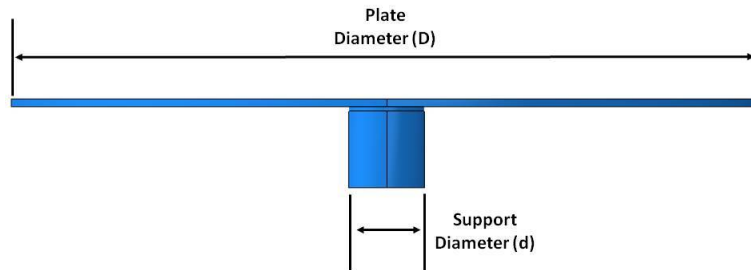


Figure 3.8: Supported Plate Schematic (D/d)

A series of analyses were performed by supporting the plate on the aluminum pedestal without any aid of the isolation mat. The pedestal was fully constrained at its bottom face. The support was modeled using 240 C3D20R elements. Tie constraints were used to

Table 3.5: Supported Plate Material and Geometric Properties

Plate Material	Al 7075-T6
Plate Diameter (m)	1
Plate Thickness (m)	0.01
Plate Stiffness (GPa)	71.7
Plate Density ($\frac{kg}{m^3}$)	2810
Poisson's Ratio	0.33
Plate Mass (kg)	0.007853982

connect the support to the beam. From Table 3.6, using a (D/d) ratio of 80 gives a natural frequency 0.015% different from the free circular plate's natural frequency.

Table 3.6: Supported Plate Without Isolation Mat

Case Number	Support Diameter (m)	(D/d)	1st Natural Freq. (Hz)
1	0.2	5	329.33
2	0.1	10	262.29
3	0.05	20	218.02
4	0.025	40	215.08
5	0.0125	80	201.33
6	0.00625	160	201.33
7	0.003125	320	201.33

The mat was then placed atop the plate's central pedestal. Poission's ratio is again assumed to be 0.49, and the mat thickness is a constant 0.00635 m (0.25 inch). The mat density remained 657.3 (kg/m³). The mat was modeled using 2162 C3D20R elements. During the analysis, the mat and support are the same diameter. Tie constraints were again used between all material interfaces, and the support's bottom face was completely

constrained. From Table 3.7, using a plate at least 20x larger in diameter than the support will effectively give the same behavior as a free plate. Using a plate with a diameter at least 10x larger than its support diameter exhibits less than 1% difference from the free plate first natural frequency. This method is applicable for supporting a plate whose modes shapes exhibit nodal diameters or exhibit node points at its center.

Table 3.7: Supported Plate With Isolation Mat

Case Number	Support and Mat Diameter (m)	(D/d)	1st Natural Freq. (Hz)
1	0.1	5	238.93
2	0.05	10	202.47
3	0.025	20	201.42
4	0.0125	40	201.33

3.3 Structured Light Optical Measurement Technique

The section provides a basic overview of structured light scanning, to include an overarching view of the theory. The motivation behind using the structured light optical measurement technique, as opposed to traditional contact based measurement methods, lies in its speed. Conventional coordinate measurement machines measure a single point at a time, by way of a mechanical touch probe. In contrast, the structured light scanner uses a field of light to measure numerous points simultaneously.

In the computer vision field, Xin [90] defines “structured light as light with a certain feature, such as a stripe pattern.” The basic principle behind the structured light approach is to project known light patterns onto an object, and with a digital camera, take images of the object with the known projection patterns imposed upon it. Because of surface curvature and any irregularities on the surface, this image appears distorted. Through a process of locating pattern positions and matching them to locations on the projected pattern, realistic textured surfaces can be reproduced through a triangulation process. Peng

[57] discusses how the “images are analyzed to construct a 3-D point cloud which is capable of introducing the observed distortions in the images.” Since the light pattern has a specific structure, or shape, to it, “there exists a direct correspondence between points on the resulting image and points on the projected light pattern.” It is this correspondence which aids in the triangulation process to reconstruct the textured surfaces. The principle of triangulation is a crucial component in the scanned object’s reconstruction. In standard projective imaging, “one dimension (usually depth or distance information) from a 3-D scene is lost” [12]. This is the rationale behind utilizing triangulation theory: to reconstruct this “lost” dimension.

In the most basic sense, a 1-D triangulation scheme, is shown in Figure 3.9.

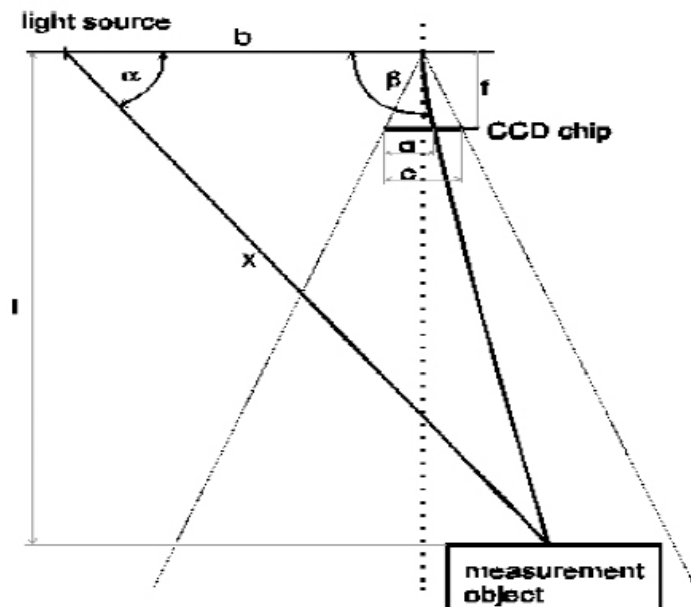


Figure 3.9: 1-D Triangulation Schematic [12]

In this figure, b , is called the triangulation optical basis. The light source ray angle, α , is fixed. “The angle on the detector side, β , changes and is defined by the illuminated point on the internal Charge Coupled Device (CCD). Based on the the knowledge of these two angles, one side of the triangle and the attributes of camera and objective (CCD chip size

and objective focal length), the distance can be determined” [12].

$$b = \frac{l}{\tan(\alpha)} + \frac{l}{\tan(\beta)} \quad (3.92)$$

Thus:

$$l = \frac{b}{\frac{1}{\tan(\alpha)} + \frac{1}{\tan(\beta)}} \quad (3.93)$$

And since $\tan(\alpha) = \frac{\sin(\alpha)}{\cos(\alpha)}$ and $\sin(\alpha + \beta) = \sin(\alpha)\cos(\beta) + \cos(\alpha)\sin(\beta)$, the distance l can be expressed as:

$$l = \frac{b \sin(\alpha) \sin(\beta)}{\sin(\alpha + \beta)} \quad (3.94)$$

Figure 3.10 depicts a 3-D triangulation scenario.

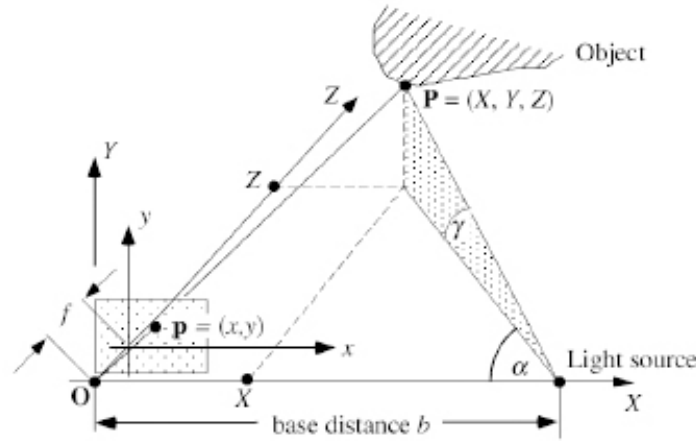


Figure 3.10: 3-D Triangulation Schematic [13]

There have always been requirements for the accurate sensing of three-dimensional data in real applications since, after all, the real world is three-dimensional. “To achieve this goal, many 3-D range finding techniques have been developed such as laser, ultrasonic, triangulation, time of flight, Moire fringing, or structured light” [91]. An overview of the Moire technique can be found in Boone and Chen’s work, References [16] and [92].

Although optical techniques provide measurement accuracy and reproductions which are photo realistic, they do have several significant drawbacks. Since the technique

involves a light source, it is more or less restricted to an indoor or other low ambient light environments. Additionally, not all points on the surface can be viewed in both the camera and projector. Keizer [91] discusses how “a scan’s spatial resolution is limited since the structured light system can only compute the 3-D data of the surface onto which the pattern is projected.” If the surface is extremely complex, and the light patterns cannot reach all portions of the object, there will not be any data for these areas. This was a challenge in scanning the rotors used in this current research. To alleviate this problem, the scanner was moved around the rotor to ensure all surfaces were captured.

Fofi [14] explains:

“In its simplest form, structured light is a laser beam projecting a single dot on the scene. Since only one point is projected, the correspondence is direct. However, scanning along both x and y axes is required Figure 3.11(i). A second solution consists of projecting a light plane, which appears as a single slit on the object surface. Scanning only along one axis is necessary Figure 3.11(ii). In order to avoid a time consuming mechanical scanning process, the last solution consists of projecting a multi-stripe pattern, a grid field, or multiple dots Figure 3.11(iii and iv). Figure 3.11 below illustrates each type.”

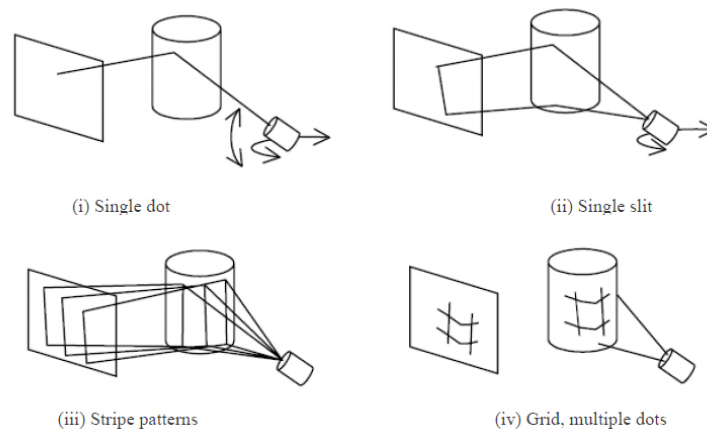


Figure 3.11: Structured Light Geometry Types [14]

As early as the 1970s, the recent advances in holographic imagery motivated researchers to search for alternate methods to record and reconstruct three dimensional scenes. As discussed in [15] ambient light was used, along with photosensitive film, to capture an object's three dimensional presence. Figure 3.12 below illustrates this technique.

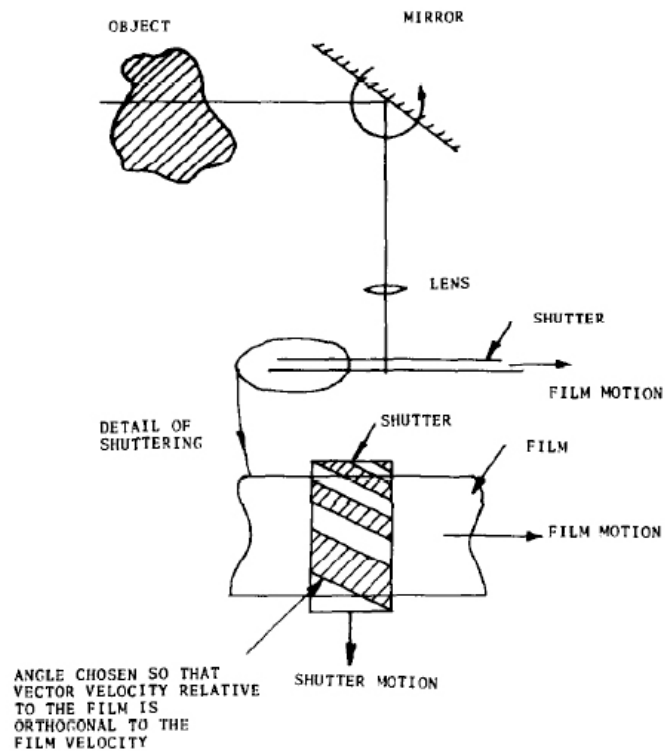


Figure 3.12: Early 3D Image Capture Schematic [15]

Through advancing optical technologies in the mid 1980s, the ability to project accurate patterns onto subjects evolved. The simplest of techniques utilize a “single strip of light or a stripe pattern projected by a slide projector” [16]. This can then be recorded sequentially for a number of projection directions. An advantage of projecting a line is that the projection direction does not need to be at a right angle to the viewing direction. The curved lines can be considered as intersections of planes with the object. An example of this is shown in

Figure 3.13 below. The distortions in the stripe pattern indicate surface texture which will be recorded as different point coordinates in the resulting model.

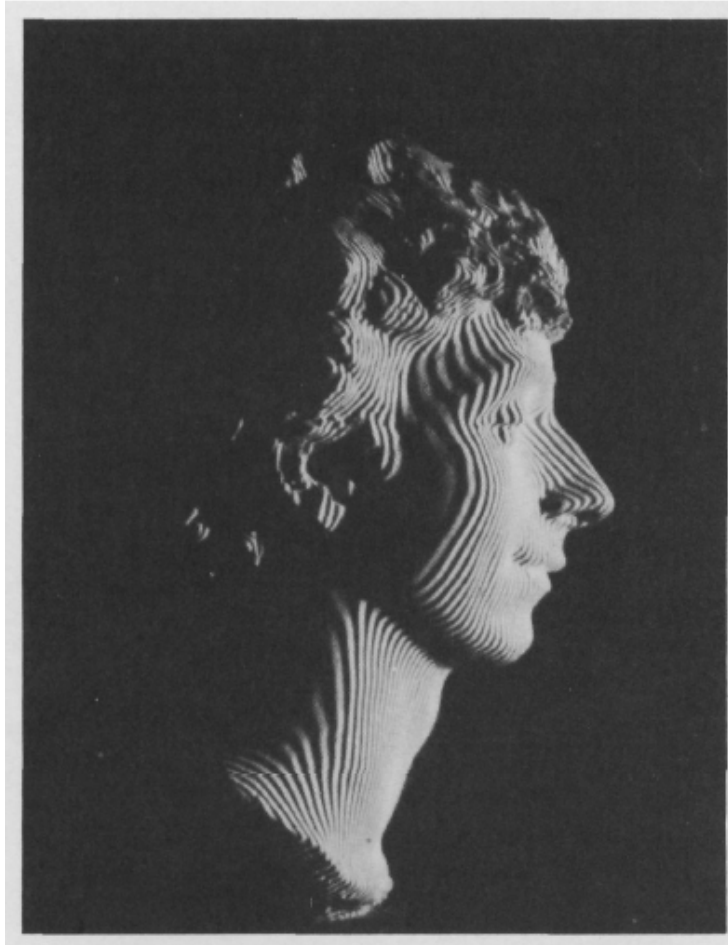


Figure 3.13: Direct Projection of Line Patterns - At Right Angle with Observation [16]

Since the light pattern is structured, it has a known pattern. Examining Figure 3.13 clearly show a distorted stripe pattern on the statue's cheek. The severity of these distortions is directly related to the surface curvature. Based on these distortions, a 3-D triangulation technique is employed to gauge the points' distance from the light projector. Therefore, the surface can be reconstructed in three dimensions by calculating the spatial coordinates of the object in question.

As optical technology continued to advance, systems involving light stripes of multiple colored evolved. “This technique was employed in an effort to mitigate effects of object surface colors, system noise, or limitations in camera/projector resolution for real-time imaging in a single video frame (“one shot”) and for near real time imagine in double video frames (“two shots”)” [93]. In addition, coloring the stripes stemmed from the need to “maximize the contrast between the light and the object, especially if the object itself is colored. This reduces ambiguities in reconstructing the object surface geometry.” Invisible structured light techniques are also used for these same reasons, as Fofi discusses in Reference [14]. Newer technologies evolved, incorporating special wavelengths of the structured light in an effort to decrease sensitivity to ambient lighting in virtually any environment.

The solid model created in this research was created from a system of such a design. The narrow-band blue light this scanner affords enables precise measurements to be carried out “independently of environmental lighting conditions” [94]. Schneider [95] has performed validation work of models developed using this equipment. In his validation scheme, a mechanical forming process was performed and then simulated. Because the simulation required a model identical to that used during the actual forming process, a narrow-band, blue structured light scanner was employed to recreate the model.

3.4 Traveling Wave Theory

The forced response of a bladed disk can be experimentally studied one of two ways. First, the disk can be rotated through a stationary excitation source. Alternately, the excitation can be rotated around the bladed disk. Spinning bladed disks at realistic engine speeds requires complex and expensive test equipment. Because of the inherent danger associated with a spinning rotor, increased testing cost, and equipment complexities, it is desired to produce engine order excitation in a stationary bladed disk wherein standard laboratory vibration measurement equipment can be used. Numerically, the rotor can be

studied using computational fluid dynamics routines and finite element analysis previously discussed in this chapter.

Jones [17] has said “engine order excitation can be simulated in stationary BLISKs² by applying harmonic excitation to all blades whereby the excitation differs from blade to blade by a constant inter-blade phase angle.” The inter-blade phase angle is a phase relationship representing the motion of one blade with respect to the other blades. For example, in a well-defined traveling wave mode, the motion of a blade can be shown to be identical to the motion of its neighbor, except for a phase angle between them. Srinivasan [41] summarizes that “each blade will experience exactly the same motion, except at a slightly different time.” This is illustrated in the following equations from Jones [17]; for the i^{th} blade:

$$F_i = A \sin(\omega t + i\theta) \quad (3.95)$$

$$i = 1, \dots, n - 1 \quad (3.96)$$

$$\theta = 2\pi \frac{c}{n} \quad (3.97)$$

Here, A is the forcing amplitude, ω is the angular input frequency to the blades, t is time, i is the blade number, c is the EO excitation, n is the total number of blades, and θ is a constant inter-blade phase angle.

While traveling wave excitation cannot replicate the effects of centrifugal stiffening seen in a real rotating rotor, it can, however, replicate the blades' behavior under different kinds of frequency excitation patterns. For a given rotor, there exists a critical EO excitation value. Together with the rotor's angular velocity, this EO value induces the excitation into the rotor. The experimental equipment simulates this phenomenon by way of the constant inter-blade phase angle. Each blade is hit with the peak signal amplitude at a slightly different time, driven by the EO value. Figures 3.14, 3.15, and 3.16 further illustrate this concept. These figures assume the rotor has 18 blades. For simplicity, forcing on 5 adjacent

²BLISK is an acronym - short for bladed disk

blades will be shown. This is done purely for figure clarity. A sinusoidal input with unit amplitude is assumed.

It is important to keep in mind, for any moment in time, all blades are excited simultaneously. For this first figure, the EO excitation 0. Physically, this implies all blades are receiving the same input amplitude at the same time. Because there is no EO excitation, there is no input phase difference between each blade. Each blade's input signal is superimposed onto the next.

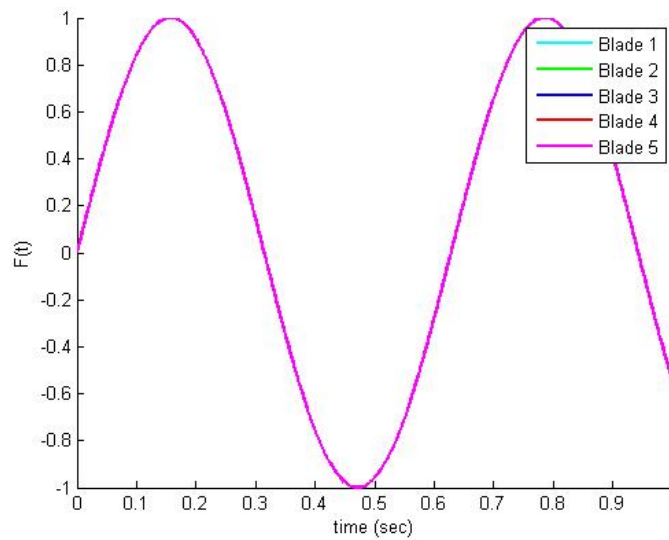


Figure 3.14: 0 EO Excitation Forcing Function Pattern

In Figure 3.15, the EO excitation has been increased to 1. Using Equations 3.95 through 3.97, Figure 3.15 is produced. Note how at a given moment in time now, the maximum input amplitude to each blade has been shifted slightly. Specifically the phase difference between each blade's maximum signal amplitude is $\frac{\pi}{9}$. This pattern of slight phase shifting continues for increased EO values.

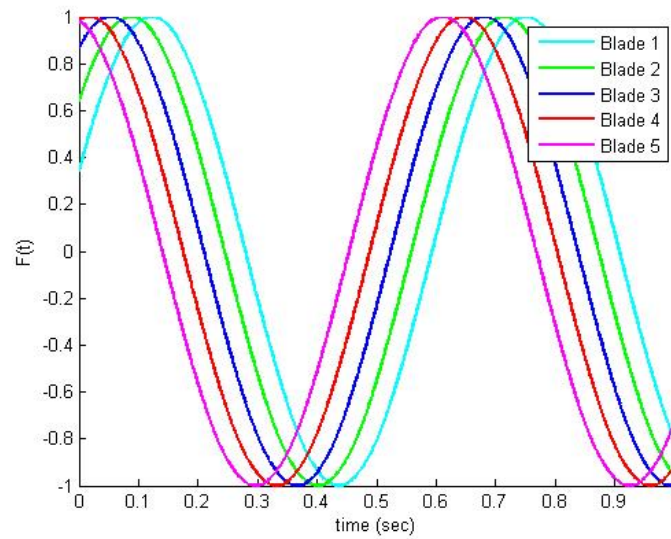


Figure 3.15: 1 EO Excitation Forcing Function Pattern

Since there are 18 blades on the Purdue Transonic Research Compressor, EO of 9 places every other blade in phase with one another. This is shown in Figure 3.16. With an EO of 9, the phase difference between each blade's maximum amplitude is π . The figure illustrates how blades 1, 3, and 5 are in phase with one another. Similarly, blades 2 and 4 are in phase with one another.

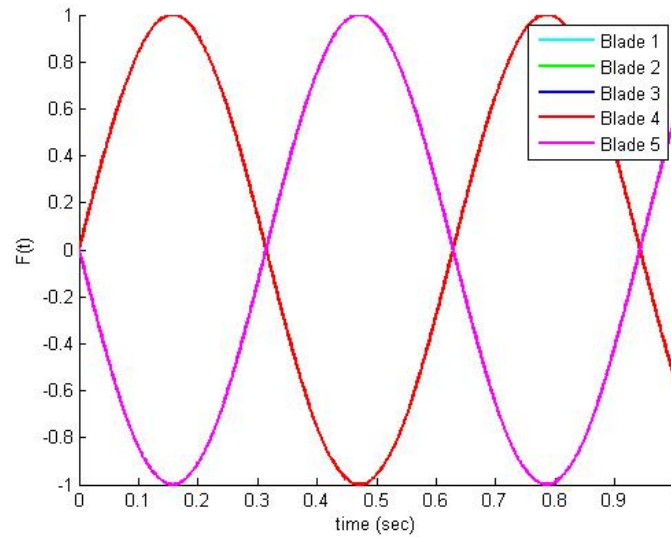


Figure 3.16: 9 EO Excitation Forcing Function Pattern

These previous graphs assume a perfect system in that all actuators are firing with an equal force magnitude and at an equal phase. The next section discusses calibration within the traveling wave system. These same figures will be revisited again, after taking into account small variations existing in the experimental setup, for which the calibration process attempts to account.

Spinning Rotor and EO Excitation. For a spinning rotor within a jet engine, the EO excitation is what provides the harmonic input to the blades. The rotor spins through the incoming air stream which has been disturbed due to the circumferential obstructions within the engine annulus. The rotor excitation frequency is directly related to the number of obstructions in the air stream and the rotor RPM. This is shown below:

$$\underbrace{\frac{\text{pulse}}{\text{rev}}}_{\text{EO}} \underbrace{\frac{\text{rev}}{\text{min}}}_{\text{RPM}} \frac{1 \text{ min}}{60 \text{ sec}} = \frac{\text{pulse}}{\text{sec}}$$

Here, the resulting (pulse/sec) is the excitation applied to each blade.

Stationary Rotor and EO Excitation. For a stationary rotor, as is utilized with the traveling wave experiment, the EO excitation serves solely to drive the phase shift between each blade's input. In contrast to the spinning rotor, the stationary EO excitation does not act as a multiplicative harmonic index. This phase shift between each actuator has values from 0 to 2π . Using modulo arithmetic, the phase shift can readily be calculated.

$$\theta = \text{mod} \left(\frac{2\pi c}{n}, 2\pi \right) \quad (3.98)$$

This equation provides the remainder after completing the division of $2\pi c$ by n . Again, c is the EO excitation number and n is the number of blades on the rotor. For example, 18 EO is also equivalent to 0 EO and 20 EO has the same phase shift as 2 EO. This is more clearly illustrated when plotting the inter-blade phase angle against the EO excitation level. Table 3.8 is generated using Equation 3.98. Figure 3.17 depicts this pattern graphically.

Table 3.8: Inter-blade Phase Angle (θ) as Function of EO Excitation for an 18 Bladed Rotor

EO Excitation	θ (rad)	EO Excitation	θ (rad)
0	0.00	18	0.00
1	0.35	19	0.35
2	0.70	20	0.70
3	1.05	21	1.05
4	1.40	22	1.40
5	1.75	23	1.75
6	2.09	24	2.09
7	2.44	25	2.44
8	2.79	26	2.79
9	3.14	27	3.14
10	3.49	28	3.49
11	3.84	29	3.84
12	4.19	30	4.19
13	4.54	31	4.54
14	4.89	32	4.89
15	5.24	33	5.24
16	5.59	34	5.59
17	5.93	35	5.93

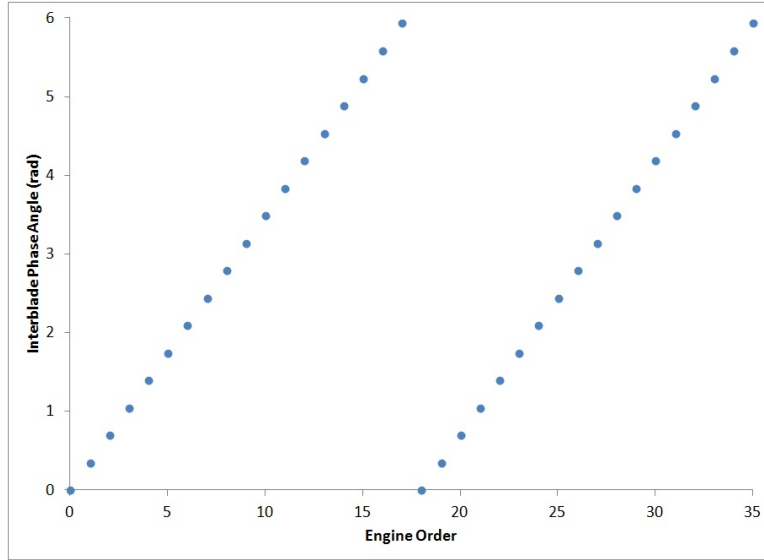


Figure 3.17: EO Excitation Forcing Function Pattern

3.5 Traveling Wave Calibration Process

The calibration process permits the traveling wave excitation to better approximate the harmonic forcing a rotor experiences during operation.

The calibration frequency is set such that a 0 nodal diameter mode shape is induced. In this mode shape, all blades move in phase with one another. This mode is chosen so as to ensure there are no node lines passing through blades, measurement points, or input locations. It is assumed that once the system can impart a force with a certain magnitude and phase to induce the 0 nodal diameter using 0 EO excitation, any other mode can be excited using other EO values of interest. Determining the frequency to induce this mode requires performing initial traveling wave scans at 0EO. Since the scanning software records both blade magnitude and phase, determining this specific mode shape is relatively simple. The software permits active exploration of the entire frequency range used in the test. The frequency inducing this mode is noted; it becomes the calibration frequency.

The calibration process attempts to attenuate two types of errors: non-uniformity and position errors. These errors need to be minimized so as to ensure that each blade is being actuated with an equal force. A *non-uniformity error* acknowledges that each

magnetic actuator is a real component, and as such, there exists variability within each unit originating from manufacturing tolerances or other physical variations affecting output signal quality. Jones [17] explains how “the *position error* is caused by amplitude and phase differences induced by the varying distances between the exciters and the blades.”

The position error is significant because the input force into the blades is sinusoidal. Despite careful actuator placement, there will always exist a degree of variability in the standoff distances between adjacent actuators. Shown in Figure 3.18, both the amplitude and phase are functions of the actuator standoff distance. Having small variations in actuator placement from blade to blade affects both the input magnitude and phase. The variable e in Figure 3.18 represents the standoff distance error between two actuators; ideally, each actuator is placed in the same location and using the same standoff distance on each blade.

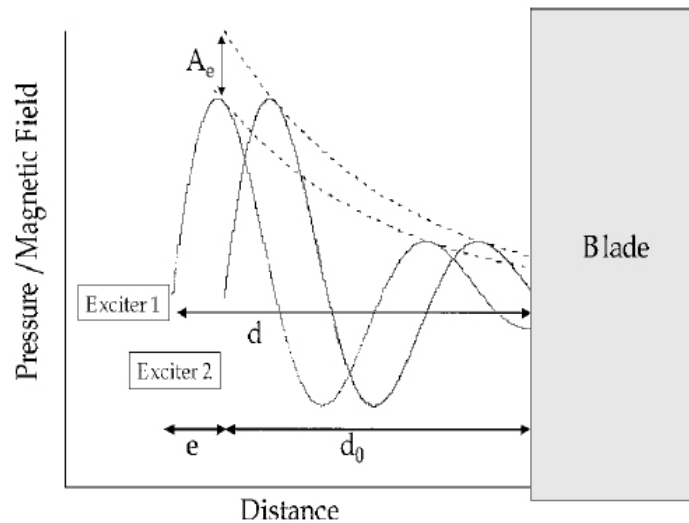


Figure 3.18: Actuator Magnitude and Phase [17]

Position errors are primarily controlled by precise placement of the exciters. Since the actuators are electromagnets, their force amplitudes can be very sensitive to position errors - namely the standoff distance, or gap between the actuator tip and blade. This sensitivity is

driven by the inverse square law relationship. Figure 3.19 below illustrates the gap between the magnet and blade tip.

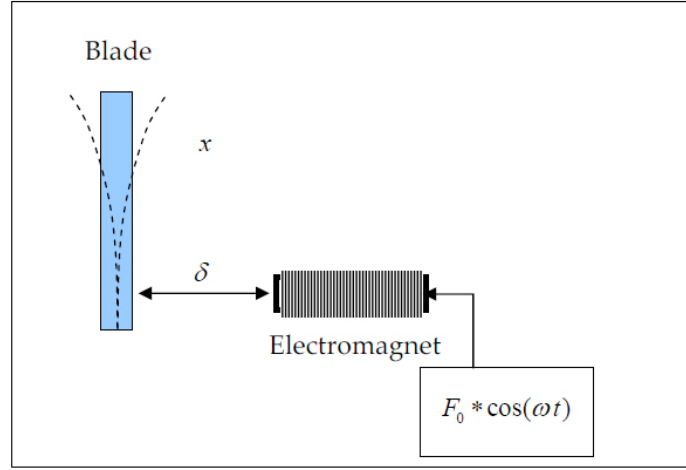


Figure 3.19: Magnet Standoff Distance Illustration [18]

To demonstrate the effect of the actuator-to-blade standoff distance, 3.20 is shown. If the magnetic excitation is driven at a frequency ω , in the form

$$f(t) = F_o \sin(\omega t) \quad (3.99)$$

and since the electromagnetic force is directly proportional to the supplied current, and is thus always positive, DiMaio [18] states the “force the blade experiences may be related to the standoff distance as”:

$$F(t) \longrightarrow \left| \frac{1}{\delta^2} F_o \sin(\omega t) \right| \quad (3.100)$$

The $\frac{1}{\delta^2}$ scales the magnetic field strength, via the inverse square law, as a function of the standoff distance. In Figure 3.20, a 1 Hz signal of 1×10^{-6} lbf amplitude is applied. The field strength, $f(t)$, using difference standoff distances, δ , is shown. The following standoff distances are typically seen during traveling wave testing: 0.02 inch, 0.03 inch, and 0.04 inch. Despite small variations in the standoff distance, there can be a significant difference in force amplitude.

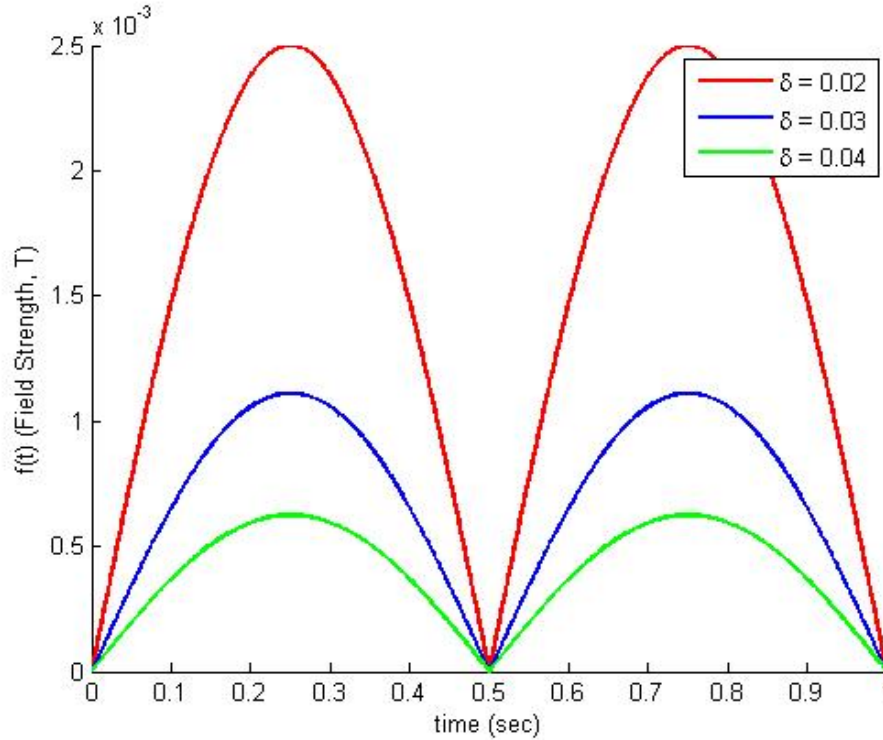


Figure 3.20: Effect of Magnet Standoff Distance on Field Strength at the Blade Tip

Through an iterative process, calibration attempts to drive each magnetic actuator with an input magnitude and phase such that the overall system response is the same, regardless of the input location. For example, the system response recorded at Blade 5 when Blade 18 is excited will be the same as the system response recorded at Blade 13 when Blade 4 is excited.

Holland [96] discusses a similar type of calibration procedure. When calibrating, only a single blade is excited at a time - in contrast to a performing an actual traveling wave test where all the blades are excited simultaneously. The resulting output from this single input is measured at each blade. For example, blade 1 is initially excited at the calibration frequency. The output is measured at blade 1. Blade 1 is excited again; the output at blade 2 is taken. This process continues until the output is measured at all 18 blades. Then blade 2 is excited. The output for all 18 blades is measured. This cycle of exciting a single blade and measuring the output at all blades continues until all blades have been

excited. Since the rotor used in this research has 18 blades, 18 separate calibration scans will be performed. At the conclusion of all calibration scans, the responses from each blade are sent to the actual calibration software. This program, based in MatLab, utilizes the principle of reciprocity to adjust each actuator's input magnitude and phase such that an identical response at each blade is achieved.

The principle of reciprocity says when a force is applied at blade A, the resulting response at blade B will be the same as when the force is applied at blade B and the response is measured at blade A. For this rotor, this is a reasonable approximation because the system is lightly damped and behaves in a linear fashion, for the frequency ranges used in this research. The calibration code produces an output file. This output file contains magnitude and phase adjustments for each actuator. The traveling wave system reads this file and makes the necessary adjustments to each actuator's signal. The calibration process is performed again. This process continues until no further adjustments are needed to achieve an identical rotor response, independent of the input location. The calibration process is summarized in the next figure.

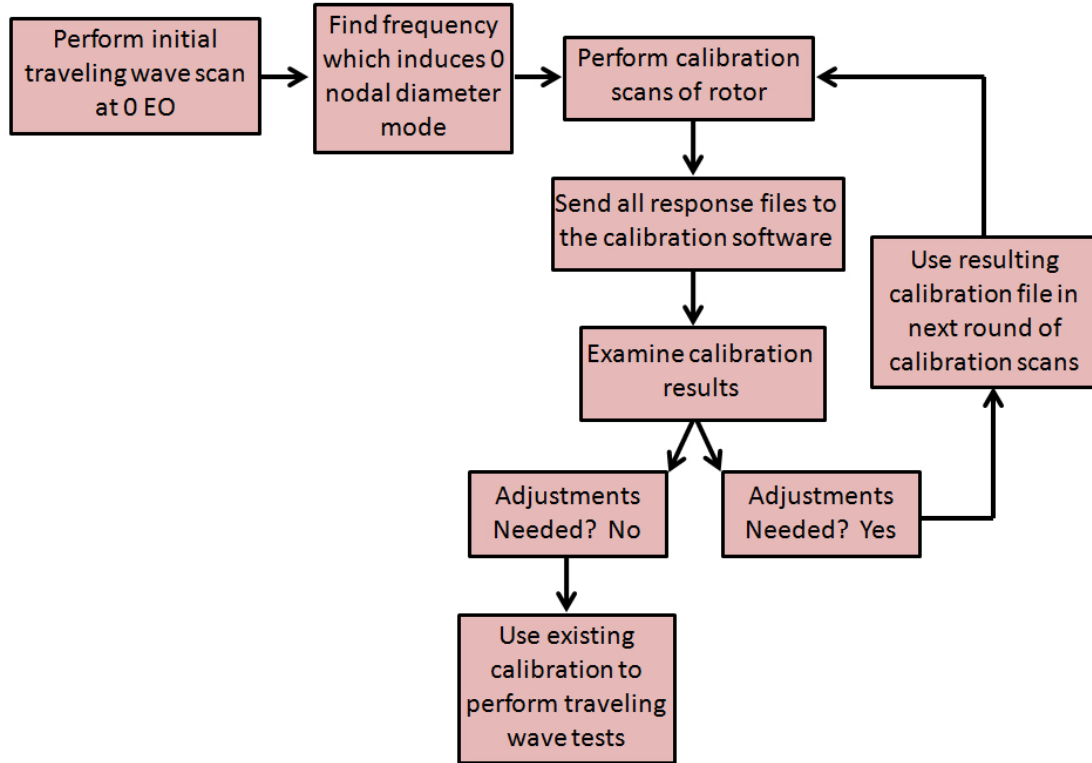


Figure 3.21: Traveling Wave Calibration Process

Figures 3.14, 3.15, and 3.16 are now revisited, taking into account small variations existing in the experimental setup. The calibration process attempts to account for these variations. A perturbation method can be employed to simulate the forcing function characteristics under the influence of both amplitude and phase changes to each actuator's signal. The perfect actuator and rotor assumption of Equation 3.95 is modified to incorporate the slight variations in input signal which would result from the calibration process. This produces Equation 3.101. In this example, pseudo-random values from a normally distributed population between 0 and 1 attempt to simulate the variation between each actuator and or blade. This variation is given as the Δ shown in Equation 3.101.

This gives a more realistic depiction of the forcing functions used in the Traveling Wave Excitation (TWE) experiment, in contrast to the perfect signals in Figure 3.14, Figure 3.15, and Figure 3.16. These changes in input signals stem from subtle differences in construction between the actuators themselves, position differences between the actuators

and blade, and variations to the blades' mass and stiffness. For example, a slightly stiffer blade would require more input force to achieve the same response amplitude than its more compliant neighbor. A 10 Hz sinusoid with unit amplitude is again used to generate each figure.

$$F_i = (A + \Delta A_i) \sin(\omega t + i(\theta + \Delta \theta_i)) \quad (3.101)$$

where ΔA_i and $\Delta \theta_i$ are the amplitude and phase deviations respectively.

During the calibration process, the reference is the “weakest” blade. In Figure 3.22, the reference is Blade 4. Thus, this example graph may be interpreted as indicating blade 2 requires almost twice the input power than blade 4 to achieve the same response. Note blades 1 and 2 are almost identical in their power requirements. Since the EO equals 0 in this example, any phase irregularities are not seen. However, this added complexity clearly shows up in Figure 3.23 where the EO excitation is now 1. Here, the effect of the phase shift is noted. Figure 3.18 illustrates this concept. The phase angle between each input signal continues to shift as the EO excitation level is increased. Figure 3.24 shows the effects of the more realistic input signals if the EO excitation is increased to 9. The system imperfections are evident and sharply contrast the input pattern seen in Figure 3.16.

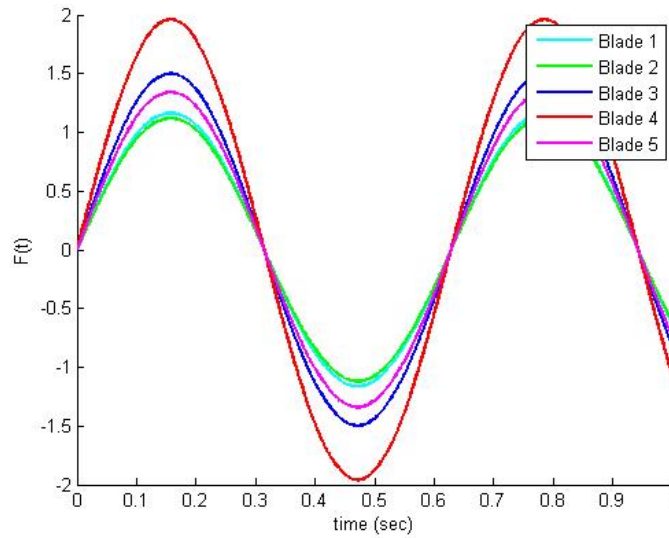


Figure 3.22: 0 EO Forcing Function Pattern with Amplitude and Phase Adjustments

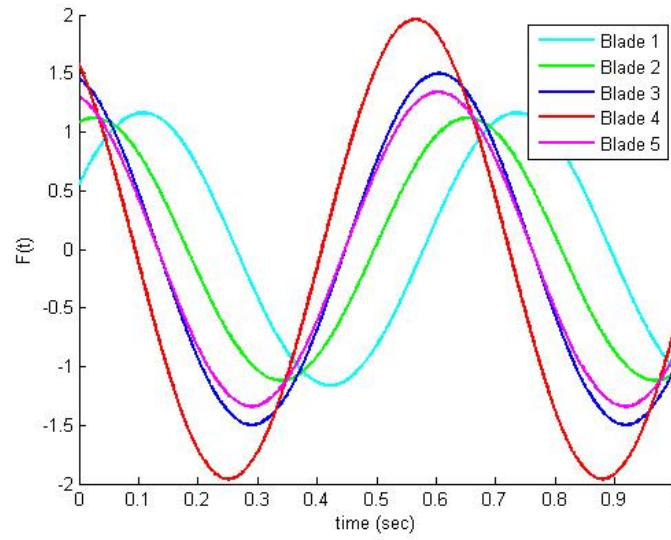


Figure 3.23: 1 EO Forcing Function Pattern with Amplitude and Phase Adjustments

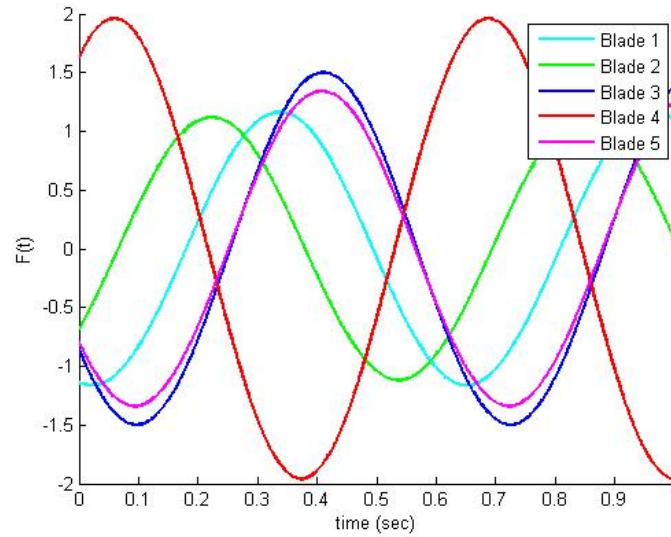


Figure 3.24: 9 EO Forcing Function Pattern with Amplitude and Phase Adjustments

3.6 Laser Vibrometer Theory

The laser vibrometer is a well established as an effective non-contact alternative to using a traditional contact based vibration transducer. This device is used to perform all rotor measurements during the TWE experiments. O'hara [10] used this technology in his work because it allowed the “identification of blade natural frequency and displacements

of the associated mode shapes.” Pai [97] lauds the laser vibrometer as it provides “non-contact (measuring velocities of a dynamic system by checking the frequency shift of a back-scattered laser beam), remote (up to 30 m away), large-area scanning (up to $40^\circ \times 40^\circ$), dense (up to 512×512 points), high-frequency bandwidth (0.2 Hz-20 MHz), and accurate (a velocity resolution of $0.1 \mu\text{m/s}$) measurements.” The non-contact measurement quality is especially attractive for mistuning research because there is no need to attach additional measurement devices, such as accelerometers, to the rotor. These items would add additional mass and would further exacerbate the mistuning problem. The scanning head both launches a probe beam to the rotors surface and collects the back-scattered light signal. Pai [97] provides an overview of the vibrometer controller functions. The “controller provides power for the scanning head, controls the rotation of the two mirrors within the head, scanning of the laser beam, and processing the interferometry created by the back-scattered laser beam and the reference laser beam in the sensor head.” The principle behind this unit relies on the detection of a Doppler shift in the frequency of coherent light scattered by a moving target. From this, a time resolved measurement of the target velocity is obtained.

Figure 3.25 shows the optical configuration in the scanning laser vibrometer. In this figure, *BS*, stands for “beam splitter”. The Bragg Cell is a unit that determines which direction the object is moving - either away from or towards the laser vibrometer. It accomplishes this by examining the beam’s frequency, or Doppler shift. A higher frequency would indicate the object is moving towards the detector, while a lower frequency would indicate the object is moving in the opposite direction. In the PolyTec laser vibrometer used with the traveling wave equipment, the Bragg Cell determines the direction the object is moving by comparing the reference and object beams.

The following discussion addresses the theory behind how this unit makes its vibrations measurements. This includes an overview of the pertinent equations and

mathematical relationships used within the laser vibrometer software to determine an object's velocity.

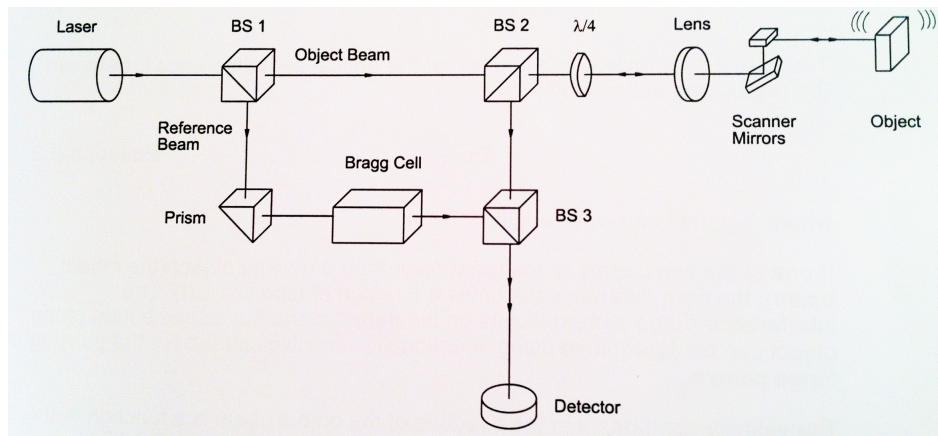


Figure 3.25: Optical Configuration in the PSV-400 Scanning Head [19]

The laser itself is a helium-neon (HeNe) beam which is split into two separate beams: the object beam and the reference beam. These beams are linearly polarized, which means the light waves are all moving in the same plane - like a sine wave moving in space.

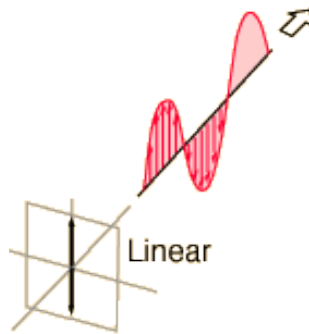


Figure 3.26: Example of a Linearly Polarized Signal [20]

The object beam passes through another splitter and a quarter-wave plate. This plate reduces the wavelength by one-quarter and thus transforms the beam into one possessing circular polarization.

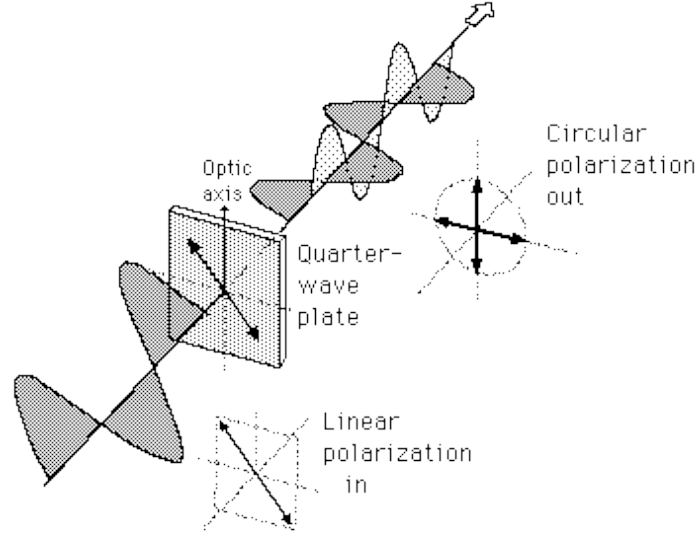


Figure 3.27: Quarter Wave Plate Effect on Beam [20]

The beam is then focused through the lens onto the directional mirrors which control where the beam will be pointed. The beam is then reflected back to the vibrometer where it is compared with the reference beam at the detector. The resulting difference, or interference, signal between the reference and object beams is converted into an electrical pulse within the detector. This electrical pulse is next passed to the vibrometer controller where it is decoded into a velocity measurement. This interference is observed when the reference and object beams coincide. The resulting intensity on the detector varies with the beams' phase difference. This is governed by the next equation (the following equations are also found in Reference [19]). The next equations provide a mathematical description of the vibrometer's operation.

$$I(\phi) = \frac{I_{max}}{2} \cdot (1 + \cos(\phi)) \quad (3.102)$$

In this equation, I_{max} is the maximum beam intensity. The phase angle difference, ϕ , is a function of the optical path difference L between the two beams. The optical path in this system is the product of the geometric length the light path through the system and air's refractive index. Since the reference beam is unaltered, it will have a different optical path

than the beam returning from the object. The refractive index is defined as the ratio of the speed of light in a vacuum to the speed of light in air. It describes how light beam propagates through the air. This phase angle between difference between the object and reference beams can be expressed as:

$$\phi = 2\pi \cdot \frac{L}{\lambda} \quad (3.103)$$

where, λ is the laser beam wavelength. As the two beams have different optical paths, the velocity component of the object beam is a function of the paths' difference, L . Thus the velocity is twice the time derivative of this path difference.

$$\frac{dL(t)}{dt} = v(t) \cdot 2 \quad (3.104)$$

For a constant velocity, v :

$$\left| \frac{dL(t)}{dt} \right| = \frac{\lambda}{2\pi} \cdot \left| \frac{d\phi}{dt} \right| = f_D \cdot \lambda = |v| \cdot 2 \quad (3.105)$$

where:

$$f_D = 2 \cdot \frac{|v|}{\lambda} \quad (3.106)$$

The movement of the object causes a frequency shift in the object beam, called the Doppler shift, f_D . When the reference beam and object beam are superimposed onto the detector, their phase difference sets up a beat frequency. This beat frequency is equal to the Doppler shift. This equation, when used to determine the velocity, is always positive because of the absolute value sign. This is corrected by introducing a fixed frequency shift, f_B , within the device. This is added to the Doppler shift and results in the following expression for the frequency at the detector:

$$f_{detector} = f_B + 2 \cdot \frac{v}{\lambda} \quad (3.107)$$

3.7 Developing the Solid Model

When an object is scanned using structured light, its faces and surface textures are represented using a finite number of closely spaced points. The points form a dense point

cloud which, to a degree, describe the object's shape. The section describes the processes used to develop the solid rotor model. This section is based upon work Kaszynski provided in [21]. The scanning process results in a dense point cloud depicting the overall geometry. The point cloud is processed in the following steps: merging, decimation, tessellation, and final editing. Several of these processes take place within the scanning software itself. The next sections describe each step.

3.7.1 *Merging.*

In order to effectively capture all aspects of the rotor's geometry, multiple scans must be performed. As discussed in Section 3.3, scanning the object from multiple angles to ensure all details of the object are captured. If the structured light is not able to reach all surfaces from one angle, the scanner is re-positioned, and the object is scanned again. For the rotor used in this dissertation research, the rotor's top surface was scanned, along with the bottom surface. Furthermore, multiple scans were performed around the rotor's perimeter so as to capture the geometric makeup of each blade.

The merging process collects all of the individual scans and *merges* them into a single point cloud. Adhesive markers are affixed to the rotor's surface for use as common reference points between the individual scans. The software uses these markers as a method to relate and orient each image to one another. Kaszynski [21] says "the processing software is able to recognize and identify these markers within the point cloud, merge the scans, and then remove the the marker geometries from the measured part."

3.7.2 *Decimation.*

The point cloud for the Purdue Transonic Research Compressor contained approximately 2,000,000 points. The decimation process reduces the number of data points in the cloud to a more reasonable number. The rotor's point cloud was reduced to about 500,000 points. This process is performed by removing "redundant" points. Enough points are kept so as to ensure the object is still faithfully represented. The same theory is realized if 100

points are used to represent a line. All of these points aren't absolutely necessary, as only the end points are needed to faithfully represent the line. Figure 3.28 below shows the resulting point cloud after the decimation process. This is a lower resolution point cloud than what was initially produced from scanning the rotor. Note how the rotor's physical shape is still readily identifiable, despite the 75% reduction in the number of points describing its shape.

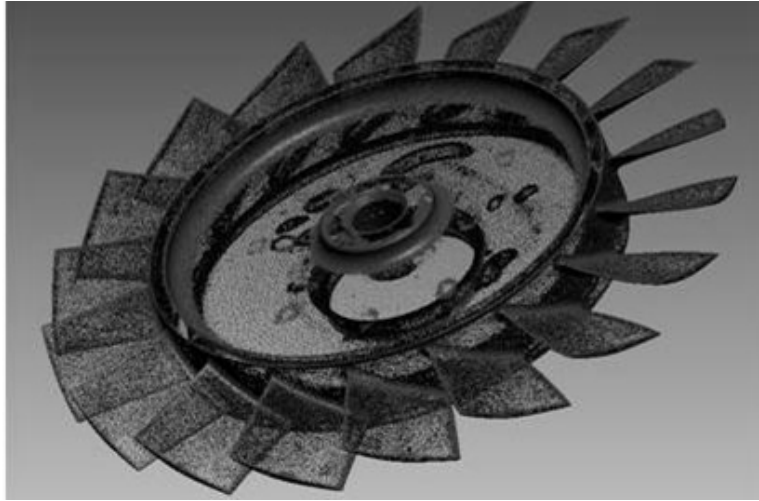


Figure 3.28: Transonic Rotor Point Cloud [21]

3.7.3 Tessellation.

In the field of computer generated graphics, the term *tessellation* “describes the organization of information which gives the appearance of surfaces to represent realistic three-dimensional objects” [98]. The tessellation process generates a mesh connecting each retained data point to its three closest measurements. This process is performed within the scanning software. Since each retained data point is connected to its three closest points, a surface of triangles is created.

3.7.4 Final Editing.

The final editing process is required when, on occasion, extraneous data is captured, such as a fixture holding the scan article or a piece of the table. Data can also be curiously absent because the light was not able to reach an area or the location was highly reflective.

Keizer [91] discussed this very issue. Final editing can be performed manually or by using a software tool. The process of repairing a point cloud can be extremely time consuming. To reduce the chances of capturing extra information or missing object pieces, care should be taken during the scanning process. The light pattern should be projected directly onto the object of interest, with minimal overlap onto the surrounding areas.

Prior to exporting the final data set, the rotor's point cloud is brought into a common reference frame. This process is known as registration. The registration process performs an optimization process which attempts to minimize any deviations seen between the scan data and a reference object. Mitra [99] says "the goal of registration is to find a transformation that optimally positions the data with respect to the model." The reference object can be a nominal Computer Aided Design (CAD) model, an existing point cloud, or the actual scanned object itself - by way of the the attached reference markers. This process can also be performed in the MatLab environment using an iterative closest point algorithm.

3.7.5 CAD Model Creation.

With a properly registered and tessellated point cloud mesh, the process continues by reverse engineering the data into a CAD model. This was the process by which the rotor model was created for use in this research. For the purposes of creating this solid model, Kaszynski [21] utilized software focusing on solid modeling and found it to be the most effective for model construction. To create the model, the disk for the rotor population was assumed to be both axisymmetric and identical for all rotors. As a consequence of this assumption, a single disk sector was modeled and then replicated around a central axis. Thus, for each rotor, only the blades required modeling and meshing.

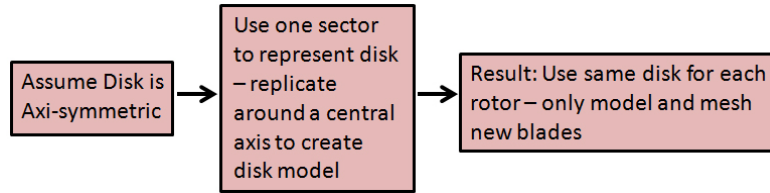


Figure 3.29: Overall Process for Disk Construction

To define surfaces, curves were first produced. The curves defining airfoil surfaces were created directly from point cloud data. The airfoil cross sections could be readily extracted and the blade surfaces could be created by interpolating between the sets. Figure 3.30 below shows the results of extracting the blade shape from the point cloud.

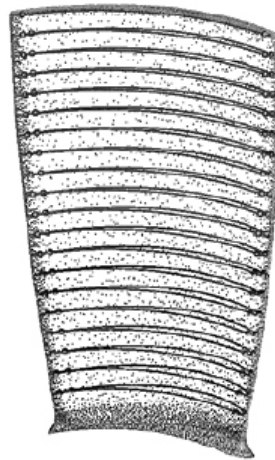


Figure 3.30: Extracted Airfoil Cross Sections [21]

Blade volumes were created by interpolating between the surfaces beginning at the disk-blade interface and extending through either the blade leading edge, trailing edge, suction side, or pressure side. This volume is then meshed inside the modeling software.

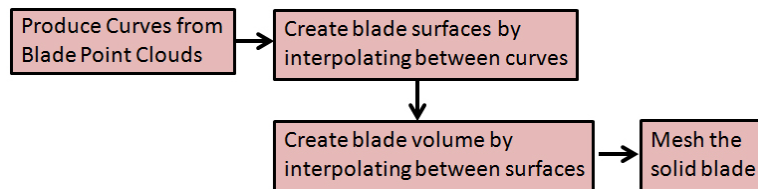


Figure 3.31: Overall Process for Blade Construction

Figure 3.32 shows the results of the aforementioned processes.

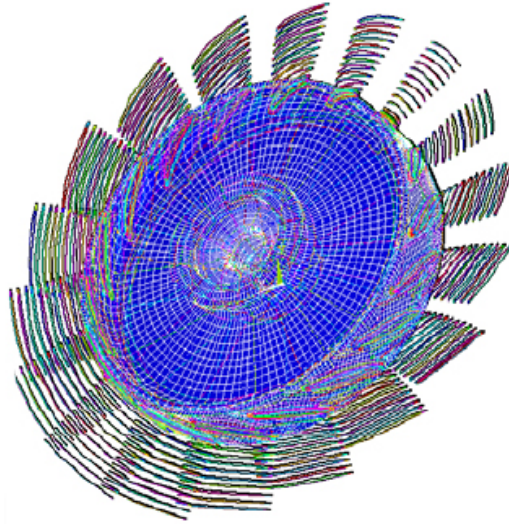


Figure 3.32: Modeled Rotor [21]

In summary, developing the solid model takes several steps. The first step involves scanning the rotor using a structured light scanner. Next, the resulting scan data are merged into a single point cloud. The point cloud is then reduced in size, through the process of decimation, into a smaller, more manageable size. The smaller point cloud is now tessellated with triangles to form a surface. Next, the model is edited, to ensure all information has been sufficiently captured in the scanning process. Finally, the solid model is created.

3.8 Modal Assurance Criterion

Developed by Allemang [100], “the Modal Assurance Criterion (MAC) serves as a means to measure the consistency, or degree of linearity, between two modal vectors. The MAC is a scalar value which ranges from zero, representing no correspondence between the two vectors, and one, which represents a consistent correspondence.” A MAC matrix formulation can be employed in which the matrix will be close to identity when good

correlation exists between the experimental and modeled of mode shapes.

$$MAC_{q,t} = \frac{|\phi_q^{T(experiment)} \phi_t^{(model)}|^2}{|\phi_q^{T(experiment)} \phi_q^{(experiment)}| |\phi_t^{T(model)} \phi_t^{(model)}|} \quad (3.108)$$

Blaschke [101] provides additional examples of using this well known method.

3.9 Coordinate Modal Assurance Criterion

Allemang [102] also discusses the Coordinate Modal Assurance Criterion (COMAC) and how this technique attempts to identify which measurement degree of freedom negatively contributes to a low MAC value. Recall a low MAC value indicates poor correspondence between the two vectors under investigation. There will be a COMAC value computed for each measurement point in the two modal vectors. The MAC illustrates whether or not the two vectors are depicting the same mode. Once the MAC has identified the modal pair, the following equation computes the COMAC.

$$COMAC_q = \frac{\sum_{r=1}^L |\psi_{qr} \phi_{qr}|^2}{\sum_{r=1}^L \psi_{qr} \psi_{qr}^* \sum_{r=1}^L \phi_{qr} \phi_{qr}^*} \quad (3.109)$$

In this equation, ψ_{qr} represents the modal coefficients for mode r obtained at point q . Similarly, ϕ_{qr} represents the other mode's coefficients for mode r measured at point q . For example, the experimental mode could be ψ_{qr} , where point q is located on the blade tip and the r^{th} mode is the blade's first bending mode. The mode found in the model would be represented as ϕ_{qr} . Here, point q would be same measurement output location as used in the experiment, and mode r would be the model's predicted first bending mode. Each of the products are summed over the number of modes of interest, from $r = 1$ to L in the desired frequency range.

3.10 Relationship Between Samples in the Time and Frequency Domains

Because the Fourier Transform is the map between the time and frequency domains (See Appendix A), there exists a direct correspondence between sampling in each of these domains.

The time step, or time between samples, is simply the inverse of the signal sampling rate. In this equation, Δt is the time step in $\frac{\text{second}}{\text{sample}}$, and f_s is the sampling rate in $\frac{\text{sample}}{\text{second}}$.

$$\Delta t = \frac{1}{f_s} \quad (3.110)$$

Analogous to the time between samples in the time domain, there is a similar type of frequency spacing in the frequency domain. This is known as the frequency resolution, Δf . It is inversely proportional to the total acquisition time T . This total acquisition time is given through the following equation.

$$T = N\Delta t \quad (3.111)$$

In this equation, N is the total number of samples taken and Δt is the time step between samples. Therefore, the frequency resolution is given by:

$$\Delta f = \frac{1}{N\Delta t} \quad (3.112)$$

The frequency resolution also exhibits a relationship with both the sampling rate and the total number of samples taken.

$$\Delta f = \frac{f_s}{N} = \frac{1}{N\Delta t} \quad (3.113)$$

The frequency resolution is also related to the number of spectral (FFT) lines, or total number of “frequency bins” in which the measured signal can be discretized, and to the maximum resolvable frequency. The finer the discretization of a given maximum measurable frequency equates to a finer frequency resolution.

$$\frac{1}{\Delta f} = \frac{\text{No. of FFT Lines}}{\text{Max Resolvable Frequency}} \quad (3.114)$$

3.11 Leakage

Because a continuous phenomenon is being discretely sampled, a phenomenon known as *leakage* occurs. The rotor’s continuous response is observed using finite pieces of time. Rather than the single, discrete frequency in a PSD (Reference Appendix A), there will be

multiple frequency components observed in and around the prominent peak. It results from an assumption, when performing an FFT, that the time domain signal is periodic and this period is precisely contained within the length of time the signal occupies.

Windowing aids in reducing any leakage effects because the window forces a signal to adopt a periodic nature by zeroing out the signal at its beginning and end. Fortunately, in following the procedures in Chapter 5, Section 5.4, Subsection 5.4.0.4, the user will define a scan time such that the response effectively decays to zero before each input is applied. Had the response signal not decayed to zero, there would exist a discontinuity at the moment the input signal is applied. Not only will the existing response superpose with the new response in the time domain, but also in the frequency domain. The signal analyzer attempts to place unique signal components onto their respective spectral line, but this cannot happen. As such, smaller and smaller frequency components are spread to adjacent spectral lines until all components have been distributed. This reinforces the need to ensure a proper data acquisition time.

This phenomenon is illustrated in the following discussion. Assume there exists a 3 Hz signal, sampled at 100 Hz, and observed for 30 seconds (Figure 3.33). Because the signal is periodic, there exists 90 distinct cycles during the observation period. Each cycle starts and ends at the same value: zero. The corresponding FFT produces Figure 3.34. Here, there is a clear, distinct peak at 3 Hz. The frequency components surrounding the peak are a necessary evil of discretely sampling a continuous phenomenon. Now let the observation time be changed to 17.16 seconds. Rather than an integer number of cycles, there are now 51.78 cycles during the observation time. Clearly, a non integer number of cycles is seen in this time interval. Figure 3.35 gives the resulting FFT of this signal. Note here, there are significant signal portions spread to the adjacent spectral lines. Because of the significant leakage effect, the signal amplitude at 3 Hz has been reduced from unity to approximately 0.8.

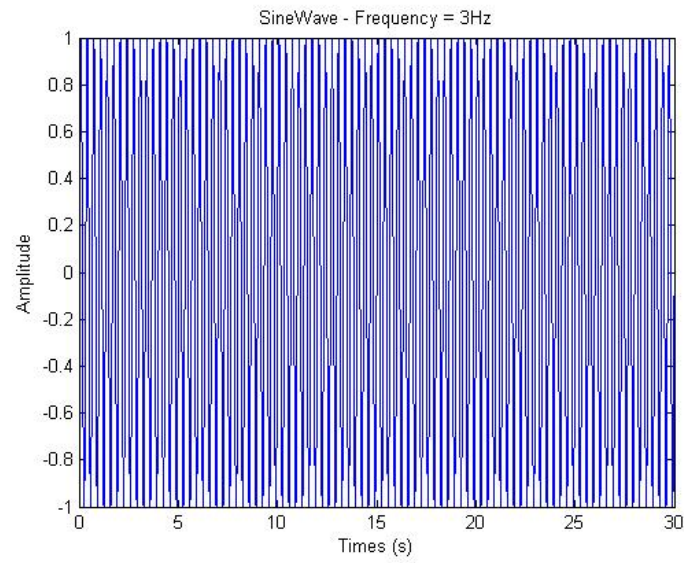


Figure 3.33: Leakage Discussion: 3 Hz Signal

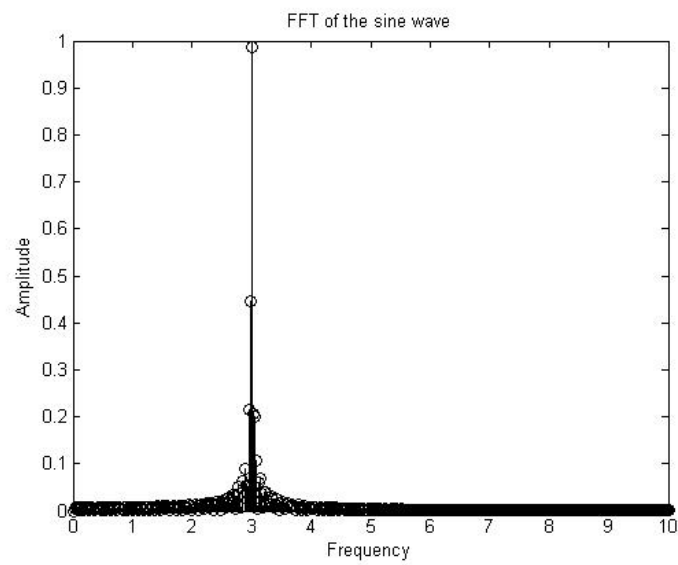


Figure 3.34: FFT of 3 Hz Signal, Observed for 30 Seconds

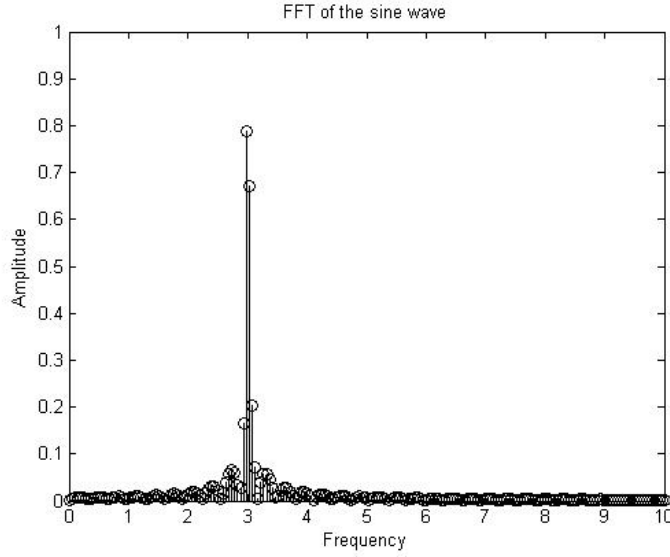


Figure 3.35: FFT of 3 Hz Signal, Observed for 17.16 Seconds

3.12 Validation Method

3.12.1 Degrees of Freedom Discussion.

This section will further illustrate the concept of degrees of freedom. Assume each of the 18 blades on the rotor each have a random displacement, x . Let these displacements be normally distributed. These displacements can be represented by a random vector. Since the vector is completely random, each value can exist anywhere in an n -dimensional space. Therefore, this vector has n degrees of freedom. Because the mean blade displacement is easily obtained, \bar{X} , this random vector of blade displacements can be decomposed into a sum of the sample mean and residual vector.

$$\begin{pmatrix} X_1 \\ X_2 \\ \vdots \\ X_n \end{pmatrix} = \bar{X} \begin{pmatrix} 1 \\ 1 \\ \vdots \\ 1 \end{pmatrix} + \begin{pmatrix} X_1 - \bar{X} \\ X_2 - \bar{X} \\ \vdots \\ X_n - \bar{X} \end{pmatrix} \quad (3.115)$$

The first vector on the right hand side of the equation can only be the quantity \bar{X} , as such, it has 1 degree of freedom. The second vector on the right hand side of the equation is constrained via:

$$\sum_{i=1}^n (X_i - \bar{X}) = 0 \quad (3.116)$$

The first $n - 1$ quantities of this vector can be any value. Once the first $n - 1$ quantities are known, the constraint states that the final value is now known. As such, this vector has $n - 1$ degrees of freedom.

3.12.2 Validation Method.

Here, in lieu of comparing complex vector quantities, for magnitude and phase analysis, direct quantities, such as eigenvalues, will be correlated. At a minimum, this process will give confidence into the finite element model's ability to accurately predict a rotor's natural frequencies. Additionally, it will validate the process by which the rotor model was created. Because a population of natural frequencies can easily be obtained using both the the experiment and finite element model, a hypothesis test on the difference between the two population means can be performed. Navidi [103] explains it is often desirable "to determine whether the difference between two means might be equal to some specified value." This is performed via hypothesis testing on the difference of the two population means, $\mu_x - \mu_y$.

The null hypothesis³, H_o is $\mu_x - \mu_y = \Delta_o$. Navidi gives the H_o distribution of $\bar{X} - \bar{Y}$ as:

$$\bar{X} - \bar{Y} \sim N\left(\Delta_o, \frac{\sigma_X^2}{n_X} + \frac{\sigma_Y^2}{n_Y}\right) \quad (3.117)$$

And the test statistic is given as:

$$z = \frac{\bar{X} - \bar{Y} - \Delta_o}{\sqrt{\frac{\sigma_X^2}{n_X} + \frac{\sigma_Y^2}{n_Y}}} \quad (3.118)$$

³The null hypothesis says any effects seen in the sample is due to random variation between the sample and overall population.

Here, \bar{X} and \bar{Y} , represent the two sample means. The terms n_X and n_Y are the number of samples in each respective group.

Commonly, researchers utilize tables which graphically display the relationship between the Z-Score and the P-Value. Given the Z-Score, the tables quickly provide an indication as to how likely the data were to have occurred by chance. From References [104] and [103], Equation 3.119 gives the relationship between the Z-Score and P-Value. This can be used if exact tables are not available.

$$P(z) = \int_{-\infty}^z \left(\frac{1}{\sqrt{2\pi}} e^{-\frac{u^2}{2}} \right) du \quad (3.119)$$

Once the P-value is known, a decision can be made on whether or not to reject the null hypothesis, for a specific level of confidence. Establishing a 95% confidence level, defines the significance level, α , as 0.05. This is determined by subtracting 0.95 from 1.00. Table 3.9 gives several other confidence levels and their respective significance levels. If the P-Value is greater than α , then the the null hypothesis is plausible (fail to reject the null hypothesis).

Table 3.9: Confidence and Significance Levels

Confidence Level (%)	α
99	0.01
95	0.05
90	0.10

3.13 Analysis of Variance and Design of Experiments

“A Design of Experiments (DOE) is the design of any information-gathering exercises where variation is present” [105]. This variation may or may not be under the experimenter’s control. With the DOE, an Analysis of Variance (ANOVA) examination is performed in order to test hypotheses and examine the differences between experimental groups. A DOE approach is taken because it will illustrate any dependence the results have on either the single, main experimental factors, or any interactions between the factors. Discussed in Montgomery [106], there are several ANOVA models from which to choose. For this research, the fixed effects models will be used.

3.13.1 Fixed Effects Model.

The development shown here is taken from Montgomery [106]. A single factor ANOVA using the fixed effects model is shown. It can be extended to account for the three factors used in this research. Let $y_{i.}$ be the sum of the observations under the i^{th} treatment and $\bar{y}_{i.}$ represent the average of the observations using the i^{th} treatment. Similarly, let $y_{..}$ represent the grand total of all observations and \bar{y} be the grand average of all observations.

$$y_{i.} = \sum_{j=1}^n y_{ij} \quad \bar{y}_{i.} = \frac{y_{i.}}{n} \quad i = 1, 2, \dots, a \quad (3.120)$$

$$y_{..} = \sum_{i=1}^a \sum_{j=1}^n y_{ij} \quad \bar{y} = \frac{y_{..}}{N} \quad (3.121)$$

In this model, N is the total number of observations. In the fixed effects model, the equality of a treatments is tested. In the following equation, the expected value, $E(\cdot)$, of the i^{th} treatment and j^{th} replication is the overall mean μ plus some additional treatment effect.

$$E(y_{ij}) = \mu + \tau_i = \mu_i, \quad i = 1, 2, \dots, a \quad (3.122)$$

In the fixed effects model, the i^{th} treatment mean, μ_i can be separated into two components, where $\mu_i = \mu + \tau_i$. The overall mean μ is given as:

$$\frac{\sum_{i=1}^a \mu_i}{a} = \mu \quad (3.123)$$

This implies:

$$\sum_{i=1}^a \tau_i = 0 \quad (3.124)$$

Each treatment effect is a deviation from the overall mean.

With this model, the null hypothesis is that each treatment produces the same results. The alternate hypothesis states that a given treatment level produces a different response.

$$H_o : \mu_1 = \mu_2 = \dots = \mu_a \quad (3.125)$$

$$H_a : \mu_i \neq \mu_j \quad \text{for at least one pair (i,j) (such that } i \neq j) \quad (3.126)$$

An alternate way to state the previously hypotheses is in terms of treatment effects.

$$H_0 : \tau_1 = \tau_2 = \dots = \tau_a = 0 \quad (3.127)$$

$$H_1 : \tau_i \neq 0 \quad \text{for at least one } i \quad (3.128)$$

The method of examining the equality of a treatments is the analysis of variance.

3.13.2 Analysis of Variance.

From Montgomery [106], “the name analysis of variance is derived from a partitioning of total variability into its component parts.” The total corrected sum of the squares is used as a measure of overall variability within the data.

$$SS_T = \sum_{i=1}^a \sum_{j=1}^n (y_{ij} - \bar{y}_{..})^2 \quad (3.129)$$

The total sum of squares can also be expressed as

$$SS_T = \sum_{i=1}^a \sum_{j=1}^n \left[(\bar{y}_{i.} - \bar{y}_{..}) + (y_{ij} - \bar{y}_{i.}) \right]^2 \quad (3.130)$$

Or equivalently as

$$SS_T = n \sum_{i=1}^a (\bar{y}_{i.} - \bar{y}_{..})^2 + \sum_{i=1}^a \sum_{j=1}^n (y_{ij} - \bar{y}_{i.})^2 + 2 \sum_{i=1}^a \sum_{j=1}^n (\bar{y}_{i.} - \bar{y}_{..})(y_{ij} - \bar{y}_{i.}) \quad (3.131)$$

The cross-product terms in the previous equation are zero because

$$\sum_{j=1}^n (y_{ij} - \bar{y}_{i.}) = y_{i.} - n\bar{y}_{i.} = y_{i.} - n\frac{y_{i.}}{n} = 0 \quad (3.132)$$

Therefore

$$SS_T = n \sum_{i=1}^a (\bar{y}_{i.} - \bar{y}_{..})^2 + \sum_{i=1}^a \sum_{j=1}^n (y_{ij} - \bar{y}_{i.})^2 \quad (3.133)$$

This equation says that the total variability within the data can be expressed as the sum of squares of the differences *between* the treatment averages and the grand average plus a sum of the squares of the differences of observations *within* treatments from the treatment average. Symbolically, Equation 3.133 can be expressed as:

$$SS_T = SS_{Treatments} + SS_E \quad (3.134)$$

Where $SS_{Treatments}$ is the sum of the squares between treatments and SS_E is the sum of the squares due to error (within treatments). Since there are $an = N$ total observations, SS_T has $N - 1$ degrees of freedom. Because there are a treatment levels, $SS_{Treatments}$ has $a - 1$ degrees of freedom. Lastly, there are n replicates within any treatment. Therefore, there are $n - 1$ degrees of freedom with which to estimate experimental error. Since there are a treatments, there are $a(n - 1) = an - a = N - a$ degrees of freedom for error.

Examining the error sum of squares expression:

$$SS_E = \sum_{i=1}^a \sum_{j=1}^n (y_{ij} - \bar{y}_{i.})^2 = \sum_{i=1}^a \left[\sum_{j=1}^n (y_{ij} - \bar{y}_{i.})^2 \right] \quad (3.135)$$

Dividing the term within the brackets by the number of degrees of freedom for error, $n - 1$, gives the sample variance for the i^{th} treatment.

$$S_i^2 = \frac{\sum_{j=1}^n (y_{ij} - \bar{y}_{i.})^2}{n - 1} \quad (3.136)$$

A single estimate for the population variance can be determined using a sample variances.

$$\frac{\sum_{i=1}^a \left[\sum_{j=1}^n (y_{ij} - \bar{y}_{i.})^2 \right]}{\sum_{i=1}^a (n - 1)} = \frac{SS_E}{(N - a)} \quad (3.137)$$

This is a pooled estimate of the common variance within each of the a treatments. If there were no difference between each of the treatment means, the variation of treatment averages from the grand average could be used to estimate the overall experimental variance, σ^2 .

$$\frac{SS_{Treatments}}{a - 1} = \frac{n \sum_{i=1}^a (\bar{y}_{i.} - \bar{y}_{..})^2}{a - 1} \quad (3.138)$$

Two estimates of experimental variance are provided. One is based on the inherent variability within treatments, while the other is based on the variability between treatments. If there is no difference between treatment means, the two estimates will be similar in value.

The following equations give the mean square of the treatments and error, respectively. These expressions are the sum of squares terms divided by their respective degrees of freedom.

$$MS_{Treatments} = \frac{SS_{Treatments}}{a - 1} \quad (3.139)$$

$$MS_{Error} = \frac{SS_{Error}}{N - a} \quad (3.140)$$

Montgomery [106] also says “since the sum of degrees of freedom for treatments and error is $N - 1$, a test statistic can be constructed.” This test statistic is defined as follows:

$$F_0 = \frac{MS_{Treatments}}{MS_{Error}} \quad (3.141)$$

A *P-Value* approach can be used to investigate the test statistic and make a recommendation on which hypothesis to accept. “The P-Value is the probability the test statistic will take

on a value which is at least as extreme as the test statistic's observed value, when the null-hypothesis is true" [106]. Appendix C gives a physical description of the P-Value. "The null hypothesis is rejected when the P-Value is less than predetermined significance level which is often, 0.05" [107]. This indicates the observed result would be highly unlikely under the null hypothesis. Stated alternately, the observation is not likely the result of random chance. An $F_{Percentage}$ table can be used to find the bounds on the P-Value. Such a table is found in Montgomery [106]. A small P-Value implies that the null hypothesis cannot be correct.

Once F_0 is calculated, it is compared to the $F_{Percentage}$ found using the appropriate table in [106]. An F_0 larger than $F_{Percentage}$ implies there is more variability between treatments rather than within the treatments. The null hypothesis is then rejected and the alternate hypothesis is not rejected. Therefore, the treatments have an effect on the outcome.

3.13.3 Three Factor Fixed Effects Model.

The model in Chapter 3, Section 3.13 is thus modified to handle the three factors; this model is given in Equation 3.142. This will be used in Chapter 5, Section 5.9 to handle the three factors under experimental control. Table 3.10 defines the individual terms in Equation 3.142. Here, factor A contains a levels, factor B contains b levels, and factor C contains c levels. If there are n replicates, there exists a total of $N = abc n$ observations. Table 3.12 gives the experimental definitions to the variables. The developed here is extended from the two factor fixed effects model discussed in Montgomery [106].

$$y_{ijkl} = \mu + \alpha_i + \beta_j + \gamma_k + (\alpha\beta)_{ij} + (\alpha\gamma)_{ik} + (\beta\gamma)_{jk} + (\alpha\beta\gamma)_{ijk} + \epsilon_{ijkl} \quad (3.142)$$

Table 3.10: Definitions of Terms in 3 Factor Fixed Effects Model

μ	Grand Mean
α_i	Factor A Main Effect
β_j	Factor B Main Effect
γ_k	Factor C Main Effect
$(\alpha\beta)_{ij}$	Interaction of A and B
$(\beta\gamma)_{jk}$	Interaction of B and C
$(\alpha\gamma)_{ik}$	Interaction of A and C
$(\alpha\beta\gamma)_{ijk}$	Interaction of A, B, and C

The total sum of squares is given by:

$$SS_T = \sum_i \sum_j \sum_k \sum_l (y_{ijkl} - \bar{y}_{....})^2 \quad (3.143)$$

The error sum of squares is given as:

$$SS_E = \sum_i \sum_j \sum_k \sum_l (y_{ijkl} - \bar{y}_{ijk.})^2 \quad (3.144)$$

Following suit, the sum of squares for each main effect are given as:

$$SS_A = bcn \sum_i (\bar{y}_{i...} - \bar{y}_{....})^2 \quad (3.145)$$

$$SS_B = acn \sum_j (\bar{y}_{.j..} - \bar{y}_{....})^2 \quad (3.146)$$

$$SS_C = abn \sum_k (\bar{y}_{..k.} - \bar{y}_{....})^2 \quad (3.147)$$

$$(3.148)$$

Similarly, the sum of squares for the two-factor interactions are:

$$SS_{AB} = cn \sum_i \sum_j (\bar{y}_{ij.} - \bar{y}_{i..} - \bar{y}_{.j.} + \bar{y}_{...})^2 \quad (3.149)$$

$$SS_{AC} = bn \sum_i \sum_k (\bar{y}_{i.k.} - \bar{y}_{i..} - \bar{y}_{..k.} + \bar{y}_{...})^2 \quad (3.150)$$

$$SS_{BC} = an \sum_j \sum_k (\bar{y}_{.jk.} - \bar{y}_{.j.} - \bar{y}_{..k.} + \bar{y}_{...})^2 \quad (3.151)$$

$$(3.152)$$

The three-factor interaction sum of squares is give as:

$$SS_{ABC} = n \sum_i \sum_j \sum_k (\bar{y}_{ijk.} - \bar{y}_{ij.} - \bar{y}_{i.k.} - \bar{y}_{.jk.} + \bar{y}_{i..} + \bar{y}_{.j.} + \bar{y}_{..k.} + \bar{y}_{...})^2 \quad (3.153)$$

And lastly, the ANOVA table is constructed:

Table 3.11: ANOVA Table: 3 Factor Fixed Effects Model

Source	Sum of Squares	Degrees of Freedom	Mean Square
A	SS_A	a - 1	$\frac{SS_A}{a-1}$
B	SS_B	b - 1	$\frac{SS_B}{b-1}$
C	SS_C	c - 1	$\frac{SS_C}{c-1}$
AB	SS_{AB}	(a - 1)(b - 1)	$\frac{SS_{AB}}{(a-1)(b-1)}$
AC	SS_{AC}	(a - 1)(c - 1)	$\frac{SS_{AC}}{(a-1)(c-1)}$
BC	SS_{BC}	(b - 1)(c - 1)	$\frac{SS_{BC}}{(b-1)(c-1)}$
ABC	SS_{ABC}	(a - 1)(b - 1)(c - 1)	$\frac{SS_{ABC}}{(a-1)(b-1)(c-1)}$
Error	SS_E	abc(n-1)	$\frac{SS_E}{abc(n-1)}$
Total	SS_{total}	abcn - 1	N/A

Table 3.12: Variables for 3 Factor Fixed Effects Model

Factor	Definition	Variable	No. of Levels
A	EO Excitation	a	2
B	Input Location	b	3 per blade
C	Output Location	c	5 per blade

3.14 Sufficient Sample Size

When performing an experiment, or series of experiments, determining the sample size from which statistical information can be drawn is of critical importance. Statistically inaccurate information may be inferred if the sample size is too small. In this experiment, there are 3 rotors, each with 18 blades. Examining the frequencies exciting the blades' first bending mode, there exists 18 separate natural frequencies for each rotor. For simplicity, only the first bending mode family will be examined here. This results in 54 responses which could potentially be measured in an experiment. From Montgomery [106] and Mandell [104], Equation 3.154 gives the required sample size, and Equation 3.155 corrects for a finite population.

$$\text{Sample Size}_{\text{infinite}} = \left(\frac{Z_{\text{score}}(1 - \sigma)}{E} \right)^2 \quad (3.154)$$

$$\text{Sample Size}_{\text{finite}} = \frac{\text{Sample Size}_{\text{infinite}}}{1 + \frac{\text{Sample Size}_{\text{infinite}} - 1}{\text{population}}} \quad (3.155)$$

Dodge [108] defines the *Z-Score* as the number of standard deviations an observation is above or below the mean. A positive Z-Score represents an observation above the mean, while a negative standard score indicates an observation below the mean. The Z-Score is a dimensionless quantity found using the following steps:

- Subtract Population Mean from Individual Observation
- Divide this Difference by the Population Standard Deviation

The Z-Score is typically associated with a prescribed confidence level. For a 95% level of confidence, the Z-Score is 1.96 and for a 99% level of confidence, the Z-Score is 2.326 (Reference [109]). The term σ is the response standard deviation. As discussed in References [108] and [109], because the response standard deviation is unknown at this point, this value can take on the value of 0.5. This will ensure the sample size will be large enough. Lastly, the term E is the margin of error associated with the sample and population means. Stated another way, this value describes how much higher or lower one permits the sample mean to fall.

Using a 95% confidence interval, a response standard deviation of 0.5, and a 5% margin of error, Equation 3.154 produces:

$$\text{Sample Size}_{\text{infinite}} = \frac{Z_{\text{score}}^2 - \sigma(1 - \sigma)}{E^2} \quad (3.156)$$

$$\text{Sample Size}_{\text{infinite}} = \frac{1.96^2 - 0.5(1 - 0.5)}{0.05^2} \quad (3.157)$$

$$\text{Sample Size}_{\text{infinite}} = 385 \quad (3.158)$$

This says, for an infinite population of responses, 385 samples are required to draw any significant conclusions. If a confidence level of 99% is used, 542 samples are required, assuming the same margin of error and response standard deviation. Using a confidence level of 95%, and assuming the population of responses is *finite*, Equation 3.155 gives:

$$\text{Sample Size}_{\text{finite}} = \frac{\text{Sample Size}}{1 + \frac{\text{Sample Size} - 1}{\text{population}}} \quad (3.159)$$

$$\text{Sample Size}_{\text{finite}} = \frac{385}{1 + \frac{385 - 1}{54}} \quad (3.160)$$

$$\text{Sample Size}_{\text{finite}} = 48 \quad (3.161)$$

Thus, since there are 54 possible response magnitudes, corresponding to each blade's first bending mode, 48 samples is sufficient. This says to maintain a 95% level of confidence in the experimental results, the responses from 48 blades should be obtained.

3.15 Cumulative Distribution Function

In the study of statistical analysis, a distribution function is one of the most fundamental concepts. Typically a probability distribution “function $f(x)$ gives the probability $p_i = f(x_i)$ that x is exactly x_i ” [110]. Oftentimes, a researcher may be interested in the probability that some random event is less than or equal to x . If a certain probability function is known, this implies the probability of an event is also known. Therefore the probability of an event less than or equal to a number x is just the sum of all of the probabilities of the event leading up to x . Taken from Boas in Reference [110], Figure 3.36 shows the probability of the sum of numbers for a toss of two dice. ”The probability that x is say, less than or equal to 4 is the sum of the probabilities that x is 2, 3, or 4, that is, $\frac{1}{36} + \frac{2}{36} + \frac{3}{36} = \frac{1}{6}$.” [110]. Following the same principle, the probability x is less than or equal to a given number can be readily determined. This resulting function of x is called the Cumulative Distribution Function (CDF). The CDF for the data here, in Figure 3.37, can be interpreted as such: the probability of the sum of two thrown dice being less than or equal to 12 is 100%. This makes intuitive sense as the maximum sum of two dice must be less than or equal to 12, as the largest number on each die is 6.

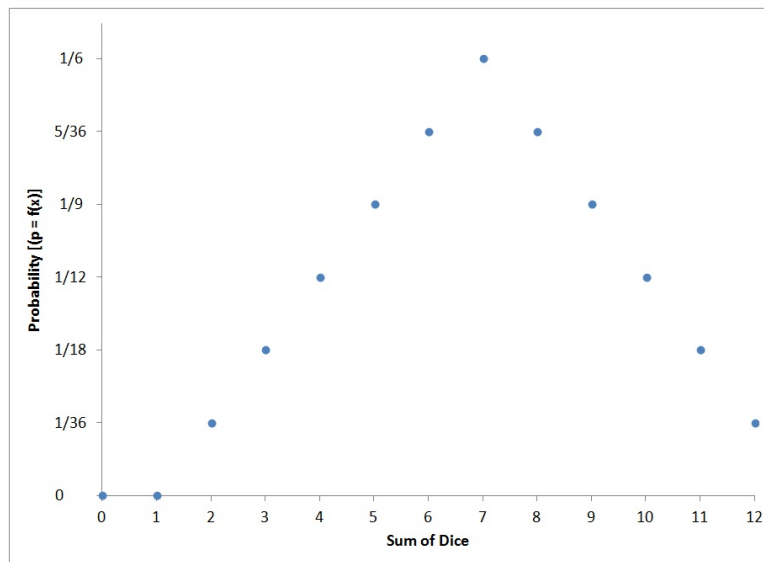


Figure 3.36: Example Probability Function

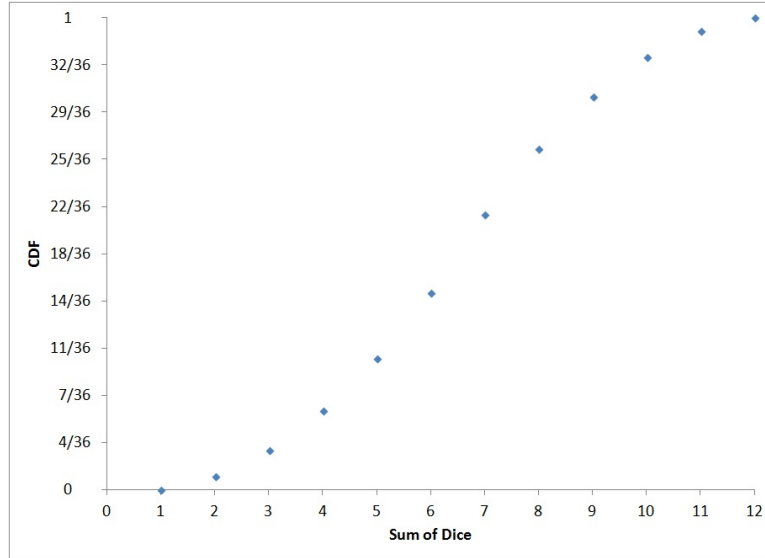


Figure 3.37: Example Cumulative Distribution Function

3.16 Cantilever Beam Forced Response Uncertainty Example

Because of the difficulty in both producing and quickly manipulating an analytic rotor model, a cantilever beam model is used. Here, much like in a real experiment, material properties remain constant. As with the traveling wave excitation experiment, the main factors under experimental control, and hence influencing the experimental outcome, are the input and output locations. Section 3.1.2 details the process by which the forced response for a cantilever beam is determined. In this present section, however, the force is a constant magnitude sinusoid applied at a point. The forcing function's frequency sweeps through a predetermined range.

3.16.0.1 Example Cantilever Beam Properties.

The mechanical and geometric properties of this example beam are given in Table 3.13.

Table 3.13: Mechanical and Geometric Properties for the Example Cantilever Beam

Length (in)	25
Width (in)	0.05
Thickness (in)	0.0063
Density ($\frac{slug}{in^3}$)	0.0032
Elastic Modulus (psi)	10,500,000

3.16.0.2 Example Cantilever Beam Forcing Function and Modal Information.

In this example, the force is unit magnitude applied downward at the beam's midpoint. The forcing frequency ranges from 0 to $200 \frac{rad}{sec}$ (0 - 31.831 Hz). Table 3.14 gives the first ten modes for the cantilever beam.

Table 3.14: First Ten $\beta_n L$ Terms for a Cantilever Beam

Mode	$\beta_n L$	Mode	$\beta_n L$
1	1.8751	6	17.2788
2	4.6941	7	20.4204
3	7.8547	8	23.5619
4	10.9956	9	26.7035
5	14.1372	10	29.8451

The values, together with the beam's mechanical and geometric properties produces the first ten natural frequencies using Equation 3.28.

Table 3.15: First Ten Natural Frequencies for the Example Cantilever Beam

Mode	ω (rad/sec)	ω (Hz)	Mode	ω (rad/sec)	ω (Hz)
1	0.5861	0.0933	6	49.764	7.9202
2	3.6728	0.5845	7	69.505	11.062
3	10.284	1.6367	8	92.536	14.728
4	20.152	3.2074	9	118.86	18.917
5	33.313	5.3020	10	148.47	23.630

The maximum response at each forcing frequency is retrieved and then plotted against its respective forcing frequency. This frequency response function⁴ is displayed in Figure 3.38.

⁴The detailed process by which a frequency response function is developed is shown Appendix A

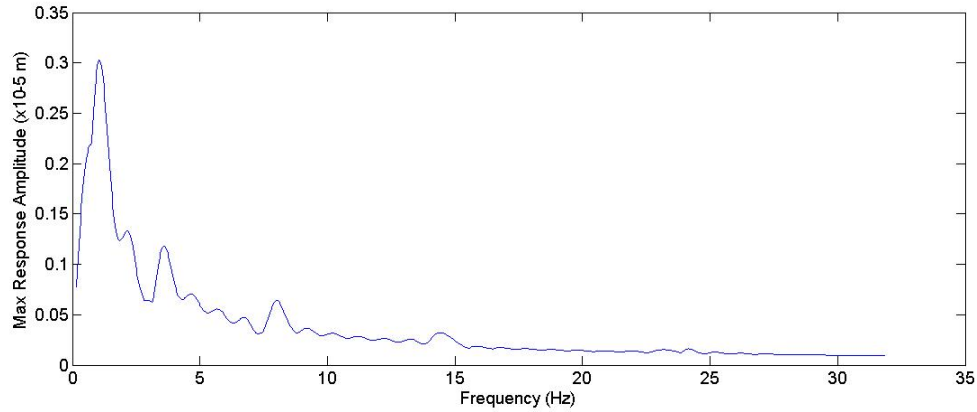


Figure 3.38: Ideal Response for the Cantilever Beam Example

3.16.1 Propagate Input Location Uncertainty.

Here, the forced response for the cantilever beam is once again calculated. Rather than using a single, crisp input location at $x = L/2$, the input location is slightly perturbed. This simulates the events taking place in an actual laboratory, as measurement locations cannot be exact for multiple experimental runs. To aid in this example, a Monte Carlo simulation of 300 separate forced responses is performed. For each run, the input location is perturbed away from the ideal location. This is accomplished by way of adding a scalar value drawn from a normal distribution on the interval -0.5 to 0.5 . Physically, this implies the input is applied anywhere from $L = 12$ to $L = 13$ inches - since the ideal input is applied at $L = 12.5$ inches. For each input location, a new frequency response function is developed. The results of these 300 simulations are shown in Figure 3.39.

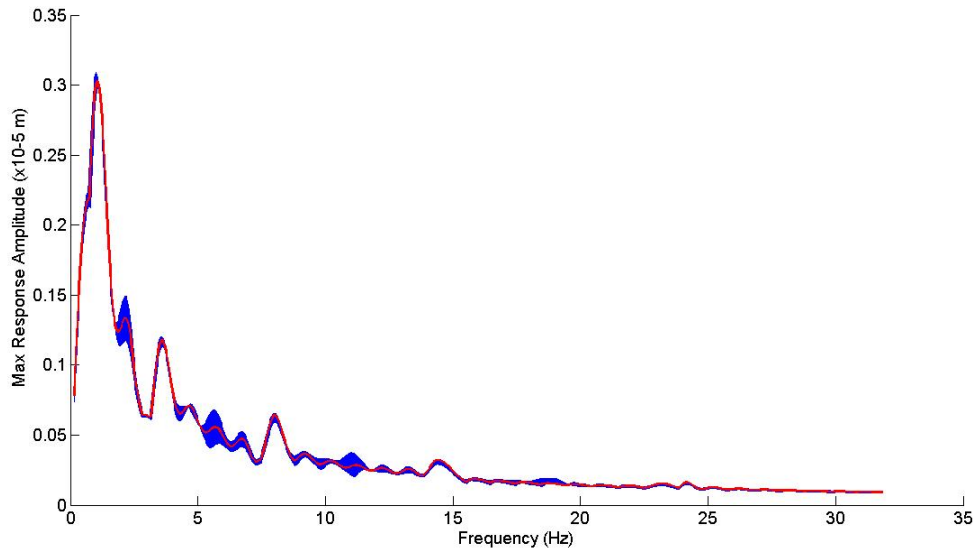


Figure 3.39: Response Using Perturbed Input Locations for the Cantilever Beam Example

The red curve is the ideal frequency response, and the cloud of blue curves are the 300 separate frequency response functions - each corresponding to a separate input location. For this example, since only the uncertain quantity is the precise input location, this quantity is the only system variable contributing the overall response uncertainty. The effect of this input location uncertainty serves to produce a $\pm 3\%$ from the ideal response at the prominent response peak. While this may not appear to be significant in terms of a simple cantilever beam, within the strict tolerance existing inside of a jet engine, this uncertainty could induce a premature failure. The effect of input location uncertainty is even more pronounced at the resonant peak around 2.2 Hz. The same level of uncertainty produces a response variance of approximately $\pm 13.5\%$ from the perfect response curve. Another significant region for response variance occurs around 5.5 Hz. Here, the uncertainty produces response magnitudes approximately $\pm 30\%$ away from the ideal situation.

3.17 Cantilever Plate Forced Response Uncertainty Example

While the previous example illustrated the tremendous impact experimental and material variability play on simple beams, this example shows the impact both input and

output location uncertainty plays on a cantilever plate. Here, the cantilever plate is sized to approximately match that of a single blade on the Purdue Transonic Research Compressor.

3.17.1 Cantilever Plate Example Properties and Equation.

Classical analysis methods do not permit a cantilever condition for a plate. Young [27] states that “an exact solution of the differential equation of a vibrating plate is known for the case of a rectangular plate which is simply supported at all four edges and also for a rectangular plate which is simply supported along one pair of opposite edges with any conditions at the other two edges.” Rayleigh and Timoshenko discuss the same phenomenon in References [111] and [89], respectively. As such, approximate methods have been used to explore plate behavior with other boundary conditions - such as one edge clamped with the remaining edges free. Leissa [22] presents such a solution for a cantilever plate. This solution is developed in [27] and is summarized in Appendix B Section B.5. Figure 3.40 shows the plate’s coordinate system and geometric configuration to which the solution makes reference.

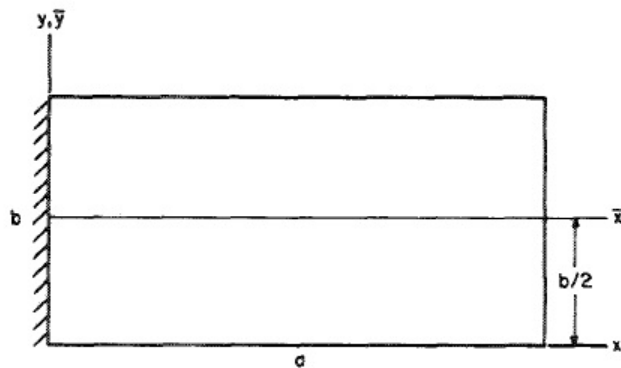


Figure 3.40: Cantilever Plate Example [22]

Leissa [22] gives the following equation depicting a cantilever plate’s mode shapes:

$$W(x, y) = \sum_{m=1}^p \left\{ A_{m1} + A_{m2} \sqrt{3} \left(1 - 2 \frac{y}{a} \right) + \sum_{n=3}^q A_{mn} \left[\cosh \frac{\epsilon_n y}{b} + \cos \frac{\epsilon_n y}{b} - \alpha_n \left(\sinh \frac{\epsilon_n y}{b} + \sin \frac{\epsilon_n y}{b} \right) \right] \right\} \\ \left[\cosh \frac{\epsilon_m x}{a} - \cos \frac{\epsilon_m x}{a} - \alpha_m \left(\sinh \frac{\epsilon_m x}{a} - \sin \frac{\epsilon_m x}{a} \right) \right] \quad (3.162)$$

In this expression, the terms A_{mn} are defined as amplitude coefficients and α and ϵ are defines as eigenfunction parameters. These amplitude coefficients for a cantilever plate's first five modes are given in Figure 3.41. The plate's eigenfunction parameters are shown in Figure 3.42.


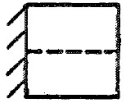


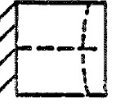
Mode.....	1	2	3	4	5
$\omega a^2 \sqrt{\rho/D}$	3.494	8.547	21.44	27.46	31.17
Nodal lines.....					
Amplitude coefficients.	$A_{11} = 1.0000$ $A_{13} = -0.0087$ $A_{15} = -0.0008$ $A_{21} = -0.0026$ $A_{23} = -0.0050$ $A_{25} = -0.0011$ $A_{31} = 0.0001$ $A_{33} = -0.0014$ $A_{35} = -0.0006$	$A_{12} = 1.0000$ $A_{14} = -0.0134$ $A_{16} = -0.0011$ $A_{22} = 0.1212$ $A_{24} = 0.0044$ $A_{26} = 0.0006$ $A_{32} = -0.0020$ $A_{34} = -0.0011$ $A_{36} = -0.0006$	$A_{11} = 0.0054$ $A_{13} = 0.2731$ $A_{15} = 0.0092$ $A_{21} = 1.0000$ $A_{23} = 0.0713$ $A_{25} = 0.0079$ $A_{31} = -0.0118$ $A_{33} = 0.0050$ $A_{35} = -0.0003$	$A_{11} = 0.0090$ $A_{13} = 1.0000$ $A_{15} = -0.0120$ $A_{21} = -0.2866$ $A_{23} = 0.1786$ $A_{25} = 0.0009$ $A_{31} = -0.0451$ $A_{33} = 0.0125$ $A_{35} = -0.0023$	$A_{12} = -0.1201$ $A_{14} = 0.0627$ $A_{16} = 0.0080$ $A_{22} = 1.0000$ $A_{24} = -0.0388$ $A_{26} = -0.0013$ $A_{32} = 0.0776$ $A_{34} = 0.0086$ $A_{36} = 0.0024$

Figure 3.41: Plate Amplitude Coefficients [22]

m, n	α_m	α_n	ϵ_m	ϵ_n
1.....	0.7340955		1.8751041	
2.....	1.01846644		4.6940911	
3.....	.99922450	0.98250222	7.8547574	4.7300408
4.....	1.00003355	1.00077731	10.9955407	7.8532046
5.....	.99999855	.99996645	14.1371684	10.9956078
6.....	1.0	1.00000145	$(2m-1)\pi/2$	14.1371655

Figure 3.42: Eigenfunction Parameters [22]

For this example, the plate's material and geometric properties (Figure 3.16) mirror those found on the Purdue Transonic Research Compressor.

Table 3.16: Mechanical and Geometric Properties: Cantilever Plate Example

Length (a)	0.0508 (m)
Width (b)	0.0508 (m)
Thickness (h)	0.00127 (m)
Elastic Modulus (E)	205 (GPa)
Poisson's Ratio (ν)	0.29
Mass per Area (ρ)	9.9695 (kg/m ²)
Flexural Rigidity (D)	38.2064 (N-m)

Here, the thickness measurement is the experimental rotor's average blade thickness. While the actual blade tapers towards its edges and exhibits a slight twist, this plate model is only applicable for a constant cross section, flat plate. The equation defining flexural rigidity is given in Equation 3.163.

$$D = \frac{Eh^3}{12(1 - \nu^2)} \quad (3.163)$$

The plate's first five natural frequencies are obtained using the constants shown in the top portion of Figure 3.41. Here, each constant is equated to the plate's frequency equation.

$$\omega a^2 \sqrt{\frac{\rho}{D}} = \text{constant} \quad (3.164)$$

For convenience, Table 3.17 gives these constant terms.

Table 3.17: Cantilever Plate Natural Frequency Constants

Mode	Constant
1	3.494
2	8.547
3	21.44
4	27.46
5	31.17

As such, Table 3.18 provides the natural frequencies used in this example.

Table 3.18: Cantilever Plate Natural Frequencies

Mode	Frequency ($\frac{rad}{sec}$)	Frequency (Hz)
1	2,650.5	421.76
2	6,483.6	1,031.9
3	16,264	2,588.5
4	20,830.7	3,315.31
5	23,645.1	3763.23

3.17.2 Forcing Function Information and Locations.

Since only modal information is known for the first five modes, the forcing function information must be appropriately defined so as to excite these modes. Therefore, the forcing function frequency vector is defined as ranging from 2,000 to 24,000 rad/sec. Different locations are defined because the purpose of this example is to analytically explore the effect of input-output variation. Table 3.19 provides the different locations in terms of Cartesian Coordinates. (Reference Figure 3.40 for the plate's axis system)

Table 3.19: Cantilever Plate Input Output Locations

Run No.	Input Location (x,y) [m]	Output Location (x,y) [m]
1	(0.0508, 0.0508)	(0.0508, 0)
2	(0.04826, 0.04826)	(0.04826, 0.00254)
3	(0.04572, 0.04572)	(0.04572, 0.00508)
4	(0.04826, 0.04572)	(0.04572, 0)
5	(0.04826, 0.04572)	(0.04826, 0.00508)
6	(0.04953, 0.04953)	(0.04953, 0.00127)
7	(0.0508, 0)	(0.0508, 0)

Notice the pattern of these locations. The first run applies input and output at corners along the plate's free edge. For runs 2 and 3, the locations are both moving towards the plate's center by the same length increment. Runs 4, 5, and 6 move the locations around arbitrarily. Lastly, run 7 co-locates the input and output.

3.17.3 *Cantilever Plate Forced Response.*

The solution for the forced response problem is assumed to be a summation of the product of the plate's normal modes and generalized coordinates (modal participation factors). The sum here only uses five terms because there are only five normal modes used in this analysis procedure. This process is shown for completeness.

$$W(x, y, t) = \sum_{i=1}^5 W_{nm}(x, y) \eta_i(t) \quad (3.165)$$

The first step in the cantilever plate forced response analysis is to calculate the generalized force for a given mode.

$$N_{nm}(t) = \int_0^a \int_0^b [W_{nm}(x, y) f(x, y, t)] dx dy \quad (3.166)$$

Since the sinusoidal input force is assumed to be applied at a point, the generalized force is zero everywhere except at the point of load application.

$$f(x, y, t) = F_o(x_o, y_o) \sin(\Omega t) \delta(x - x_o) \delta(y - y_o) \quad (3.167)$$

The generalized force for mode nm assumes the form:

$$N_{nm}(t) = F_o W_{nm} \sin(\Omega t) \quad (3.168)$$

The next step involves calculating the generalized coordinate, or modal participation factor, for each mode. Assuming the plate begins at rest - with no initial displacement or velocity, the generalized coordinate for the i^{th} mode is given as:

$$\eta_i(t) = \frac{1}{\omega_i} \int_0^t [N_i(\tau) \sin(\omega(t - \tau))] d\tau \quad (3.169)$$

The forced response is finally determined by the relationship in Equation 3.165. Using the seven different input-output locations the frequency response function shown in Figure 3.43.

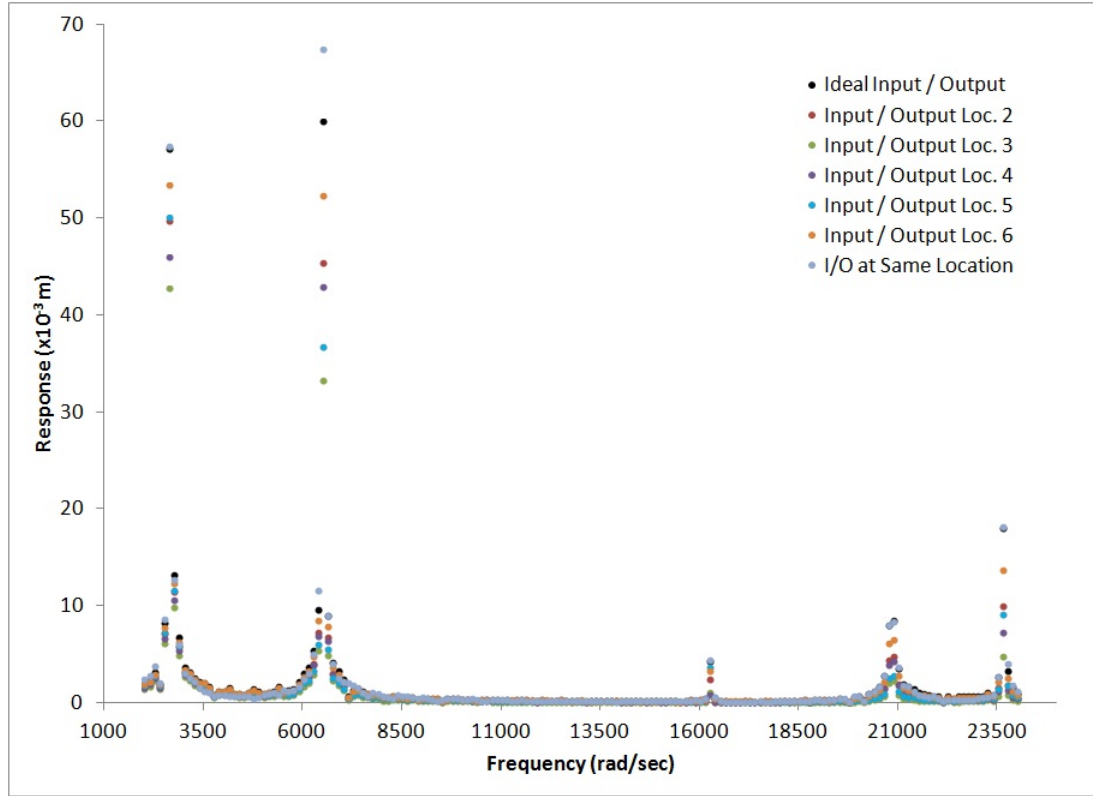


Figure 3.43: Cantilever Plate Example Frequency Response Functions

The legend indication of “Ideal I/O Location” corresponds to the location of Run 1 shown in Table 3.19. Examining the data points shown in this figure clearly indicate the effects of input-output location changes. Shown at the second mode, the response at the coincident input-output location is more than 4x larger than what is considered the “ideal” location. This is caused by the by the amplitude coefficients and eigenfunction parameters Young developed in [27].

At the remaining 4 modes, the coincident and “ideal” locations exhibit very similar responses. Exploring the forced responses associated with the 1st, 2nd, and 3rd positions show a relative constant ratio of maximum responses for each of the five modes. This is

because these three different locations were incrementally changed by a constant amount (0.00254 m). Figure 3.44 summarizes the peak responses for the cantilever plate's five modes.

		Responses				
<i>coordinates are in meters</i>		Mode 1	Mode 2	Mode 3	Mode 4	Mode 5
Ideal I / O						
Input	Output	57.1358	59.972	4.25676	8.54667	18.0091
(0.0508, 0.0508)	(0.0508, 0)					
Input / Output 2						
Input	Output	49.7088	45.4196	2.467	4.847	10.0659
(0.04826, 0.04826)	(0.04826, 0.00254)					
Input / Output 3						
Input	Output	42.7945	33.3486	1.1736	2.315	4.8981
(0.04572, 0.04572)	(0.04572, 0.00508)					
Input / Output 4						
Input	Output	45.9578	42.9463	0.86673	4.2554	7.24751
(0.04826, 0.04572)	(0.04572, 0)					
Input / Output 5						
Input	Output	50.0113	36.6758	3.59446	2.75491	9.05418
(0.04826, 0.04572)	(0.04826, 0.00508)					
Input / Output 6						
Input	Output	53.3591	8.42717	3.30135	6.54118	13.6441
(0.04953, 0.04953)	(0.04953, 0.00127)					
Input / Output 7						
Input	Output	57.4802	11.6991	4.40307	8.36916	18.231
(0.0508, 0)	(0.0508, 0)					

Figure 3.44: Cantilever Plate Example Maximum Responses

Input-Output locations 4, 5, and 6 used arbitrary locations on the blade planform. The responses for these locations fell within the envelope established using the locations for runs 1, 2, and 3. In general for this example, Input-Output Locations 1 and 3 can be thought of as maximum and minimum bounds, respectively, for the cantilever plate's forced response. To create a non-dimensional tolerance bound for the input-output locations, each value is normalized by the respective horizontal and vertical blade dimensions. Therefore, if the input and output locations are kept within the established percentages for plate's horizontal and vertical dimensions, the plate's forced response will be captured. Here, the

input location should be placed greater than or equal to 90% of both the blade's horizontal and vertical dimensions. The output location is restricted to lying within a region bounded by greater than or equal to 90% of the horizontal dimension and less than or equal to 10% of the vertical dimension. Figure 3.45 gives a graphical depiction of these tolerances.

Table 3.20: Cantilever Plate Example Normalized Input/Output Location Tolerances

Location 1				
	Input		Output	
	x	y	x	y
Dimension (m)	0.0508	0.0508	0.0508	0.0000
Normalized Dim.	1	1	1	0.0000
Location 2				
	Input		Output	
	x	y	x	y
Dimension (m)	0.04826	0.04826	0.04826	0.00254
Normalized Dim.	0.95	0.95	0.95	0.05
Location 3				
	Input		Output	
	x	y	x	y
Dimension (m)	0.04572	0.04572	0.04572	0.00508
Normalized Dim.	0.9	0.9	0.9	0.1

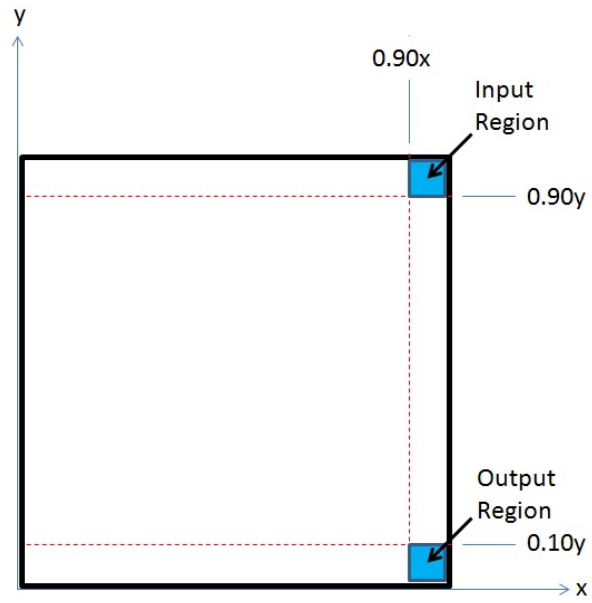


Figure 3.45: Cantilever Plate Example Tolerances

IV. Experimental Equipment

4.1 Purdue Transonic Research Compressor

The rotor used in this study is the Purdue Transonic Research Compressor. The rotor was “designed by Prof. S. Fleeter at Purdue University in cooperation from Pratt & Whitney Aircraft to reflect the aerodynamic and structural properties of a modern compressor” [51]. The research compressor is constructed of 17PH⁵ stainless steel.

Table 4.1: Mechanical Properties for 17-PH Stainless Steel [28]

Property	Value
Elastic Modulus (GPa)	196
Density (kg/m^3)	7750
0.2% Offset Yield Strength (MPa)	760
Ultimate Tensile Strength (MPa)	1030

This compressor is representative of the front stages of advanced aircraft engine high-pressure compressor designs. The rotor itself has 18 blades, and a tip diameter of 12 inches. The rotor blades consist of Controlled Diffusion Airfoil (CDA) profiles having a 1.8 in. to 2.0 in. chord from hub-to-tip and a thickness distribution varying from 11.6% at the root to 7.8% at the tip [2]. This rotor is shown in Figure 4.1. The white powder coating is used to facilitate the blue-light scanning process, which is the initial step used in developing the finite element model.

⁵Precipitation Hardening

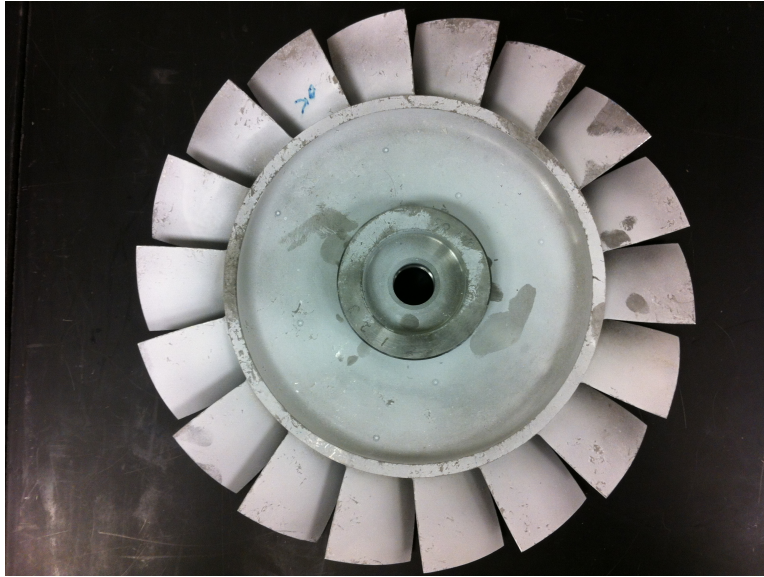


Figure 4.1: Purdue Transonic Research Compressor

Figure 4.2 shows a typical location for both the compressors and stators.

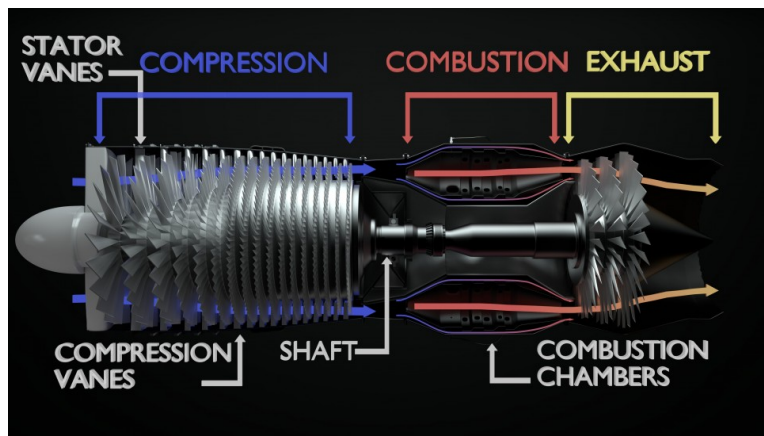


Figure 4.2: Jet Engine Schematic [23]

4.2 ATOS 3-D Scanner

In this research, the ATOS Scanner will be used to construct three dimensional models of the Purdue Transonic Research Compressors. The process by which the model is created was outlined in Chapter 3, Section 3.7. The optical scanning system employs a structured light approach with a stereoscopic camera configuration. On the scanning device, a central blue LED illuminates the part with a pattern of lines. These lines are photographed by two

8 megapixel cameras on either side of the central LED source. Their projected shapes on the part are used to triangulate surface coordinates. Figure 4.3 shows one particular light pattern. The object in the figure is a 1-2-3⁶ calibration block. The pattern is depicted as alternating blue and black stripes, known as a sinusoidal fringe pattern.

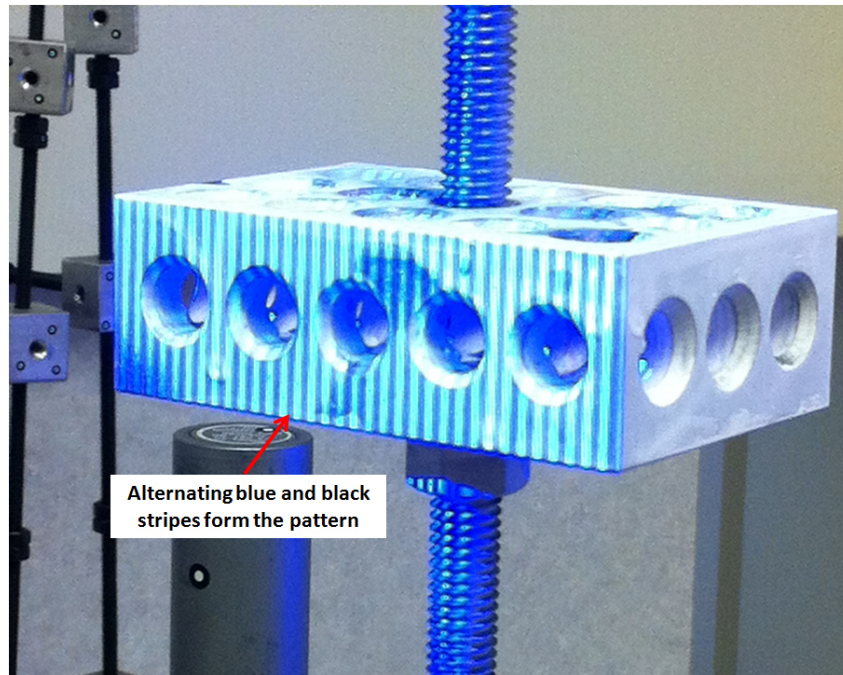


Figure 4.3: Projected Light Patterns from ATOS Scanner

“Accuracy of these systems has been shown to be accurate to within 0.0001 inch” [21]. The scanner is used in lieu of the more traditional contact based Coordinate Measurement Machine (CMM) because of the complexity associated with the rotor’s geometry. The CMM certainly provides a concise set of data points from which a solid model can be created, but the process is extremely time consuming and is more suited for quality control purposes than for developing a solid model from a complex object. Another advantage of the optical scanner lies in its ability to capture large measurements of surface data rather than singular point data at a time. Figure 4.4 shows the scanner used in this research. In this figure, this two cameras are seen. They are each housed within a red colored fairing.

⁶Named as such for its 1 inch thickness, 2 inches width, and 3 inches length

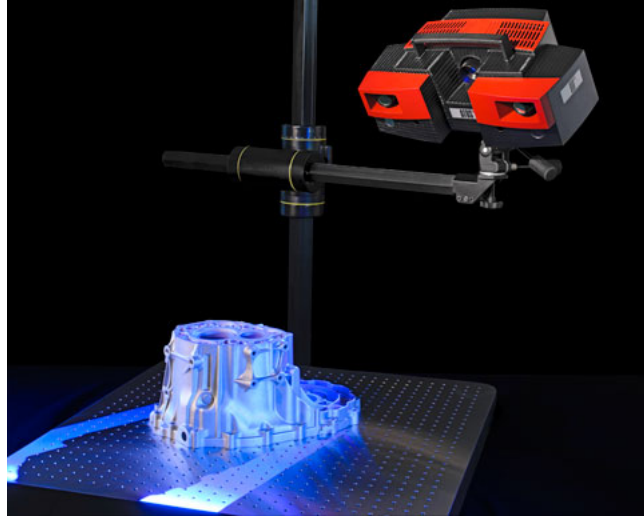


Figure 4.4: ATOS Blue LED Structured Light Scanner [24]

Different camera lenses can be used on the scanner to alter the size of each scan image. As such, smaller scan images will be used for smaller parts, and larger scan images will be used as the object size increases.

The rotor is placed atop a Computer Numerical Controlled (CNC) rotating table. The scanning software is linked to the table and controls its rotation. This allows multiple images to be automatically captured circumferentially at a given scanning head height and angle. “After circling the part with images, the scanner head can then be manually adjusted to a new height and angle in order to capture all interblade surface passages” [21]. Figure 4.5 below illustrates a portion of the scanning process. The rotor is resting on the CNC table. The scanner is elevated on the right, and the blue LED light is seen illuminating the fan. The monitor on the left shows several blades’ worth of data collected in a single scan.

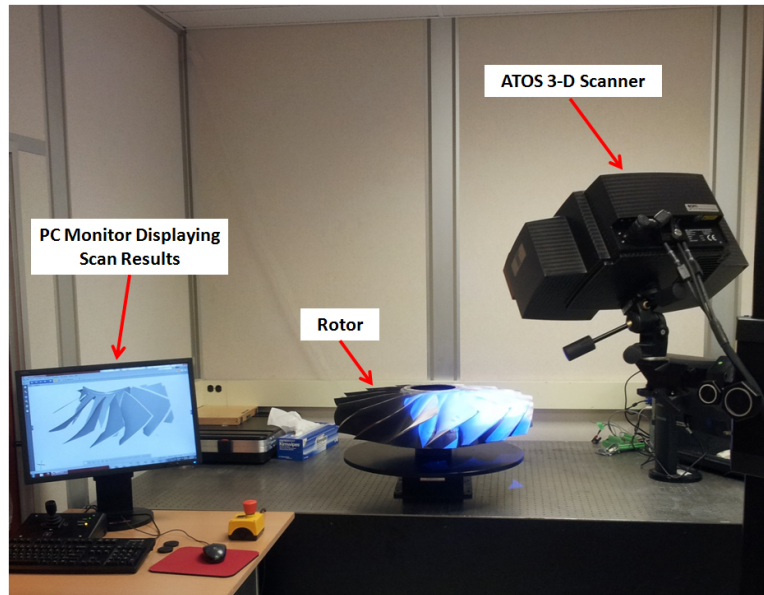


Figure 4.5: Portion of the Scanning Process [21]

4.3 Scanning Laser Vibrometer

A PolyTec PSV-400 scanning laser vibrometer will be used to measure the rotor's transverse velocities under traveling wave excitation. As discussed in Chapter 3, Section 3.6, the laser vibrometer is used because measurements can be made without contacting the rotor. Therefore, the measurement system will not induce further anomalies into the rotor. The unit is mounted in a vertical position above a vibrations isolation table so its laser is shining downward onto the tested rotor. Figure 4.6 shows this configuration.

PolyTec PSV-400 Scanning
Laser Vibrometer

Traveling Wave Excitation
Signal Generation and
Amplifier Cabinet

Purdue Transonic Research
Compressor



Figure 4.6: Scanning Laser Vibrometer Position

4.4 Traveling Wave Excitation Equipment

This section describes the traveling wave excitation equipment used in this research. As a rotor spins during operation, flow disturbances set up periodic forcing on each blade. Recall from Chapter 3, Section 3.4, this excitation is known as EO excitation. This concept was also discussed in Section 2.1.1.

In the case of a tuned rotor, the EO excitation causes all blades to vibrate with equal amplitude. In contrast, when the rotor is mistuned, “the EO excitation usually causes response localization and amplifications above the tuned response” [17]. Some blades will experience displacements and vibration amplitudes greater than others. As discussed

Chapter 3, Section 3.4, when testing a rotor's response to some external forcing, the rotor can either be rotated around a disturbance field or have the disturbance field rotated around the rotor. "Rotating a BLISK at realistic speeds requires complex and expensive test fixtures, therefore it is desired to produce engine order excitation in a stationary bladed disk where standard laboratory vibration measurement devices can be used" [17]. Producing the required EO excitation on a stationary disk is called traveling wave excitation.

The traveling wave system employed in this research effort is flexible enough to test bladed disks of varying sizes and blade numbers. The excitation source can be either magnetic and acoustic. For this research, magnetic excitation was chosen because of its ability to faithfully reproduce engine order excitation. There are several chief advantages realized when using the TWE equipment. "First, a traveling wave excitation system provides harmonically pure sinusoidal excitation. Next, the design is flexible; the equipment can be easily configured to test a variety of different bladed disks. And finally, the TWE used in this research is equipped with a phase shifting circuit which allows for smooth and accurate EO excitation" [17].

The system consists of a mounting fixture to hold the bladed disk and its associated array of magnetic actuators. For the current research, the actuators are held in place using a nylon ring produced from a 3-D printer by way of a CAD generated stereo-lithography file. The ring fixture is shown in Figure 4.7 and Figure 4.8.

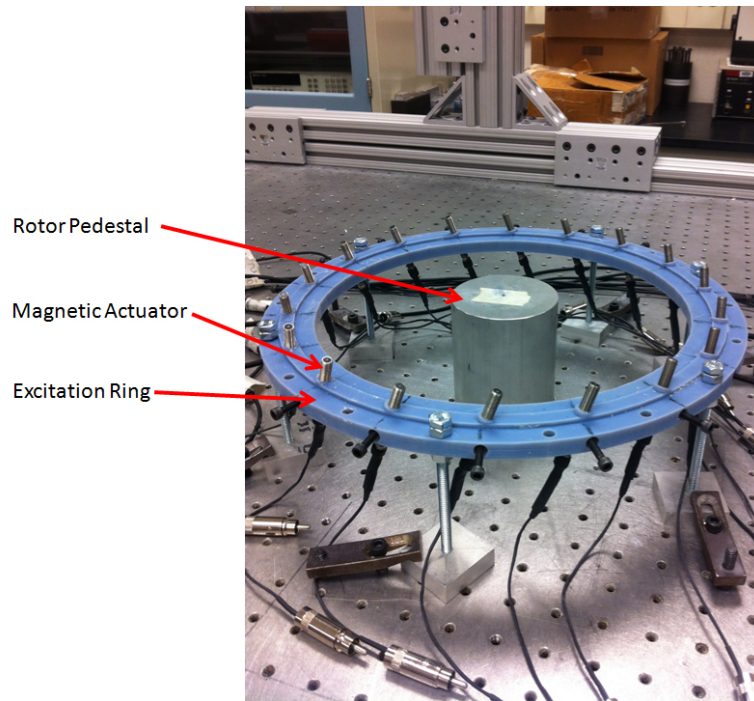


Figure 4.7: Magnetic Actuator Ring Beneath Rotor

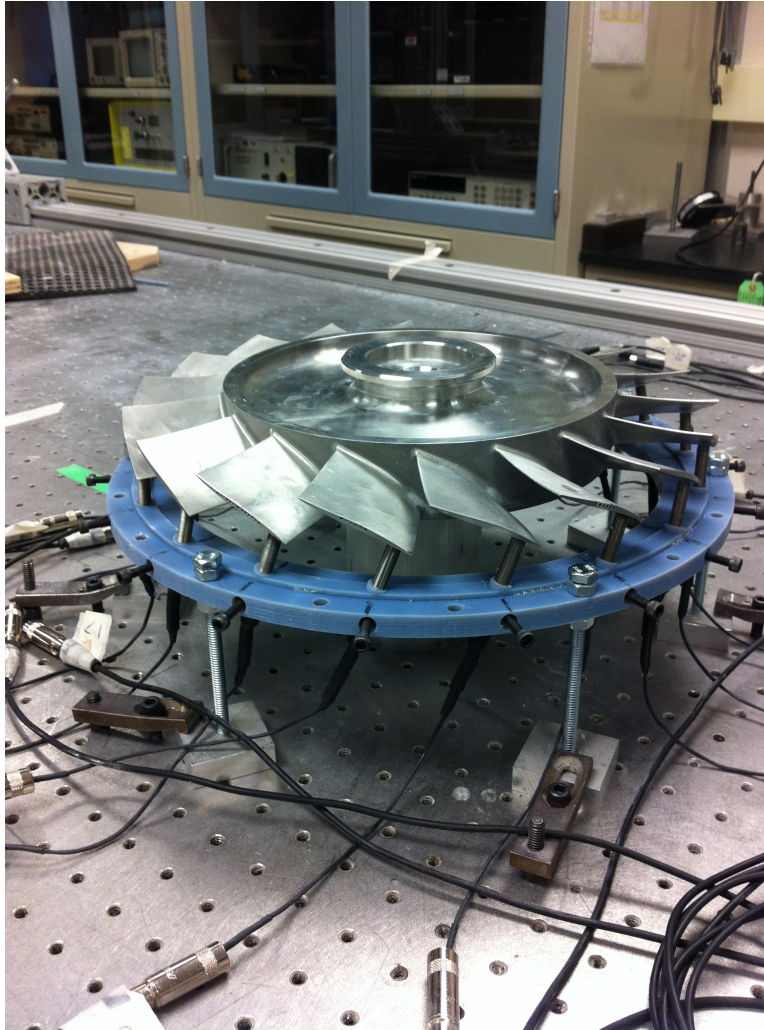


Figure 4.8: Rotor Mounted on Pedestal Above Actuator Ring

Each magnetic actuator is positioned below each blade, close, but not so close as to contact the blade. Traveling wave testing experience has shown that a 0.020 inch initial standoff distance is practical for most applications. Chapter 3, Section 3.4 illustrated the standoff distance and its effect on excitation force strength. This distance is driven by the frequencies and forcing function magnitudes most often used during traveling wave excitation. The calibration process, discussed in Chapter 3, Section 3.5, illustrates how the forcing magnitude can be adjusted to account for standoff distance errors between actuators or adjusted if the forcing is not of the correct magnitude to induce the desired

mode shape in the rotor. Figure 4.9 shows the actuator orientation within the excitation ring. This orientation is set so as to ensure the actuator is as close to perpendicular to the blade surface as possible. By orienting the actuator normal to the surface, each blade's forcing function input is maximized. Further, this design is attempting to control the exact location where the input is applied. If the actuator is not normal to the blade, the input area is less controlled and the input force is applied over a larger, less defined area. And because the input force is in the form of an electromagnetic field, the input would not be uniform over the target area. Another consequence of this would be the great difficulty arising in attempting to model the traveling wave process using the finite element technique. The input force would be spread out, and its magnitude would be non-uniform over the application area. Forcing the actuator normal to the blade surface effectively minimizes these effects. As indicated in the figure, this angle is fixed at 69° .

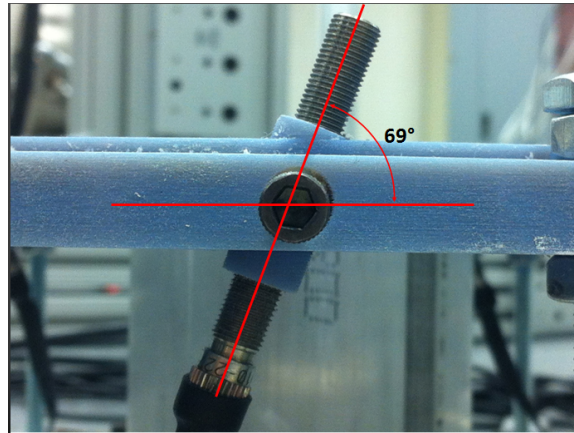


Figure 4.9: Actuator Angle Within the Excitation Ring

An overall schematic is shown next in Figure 4.10.

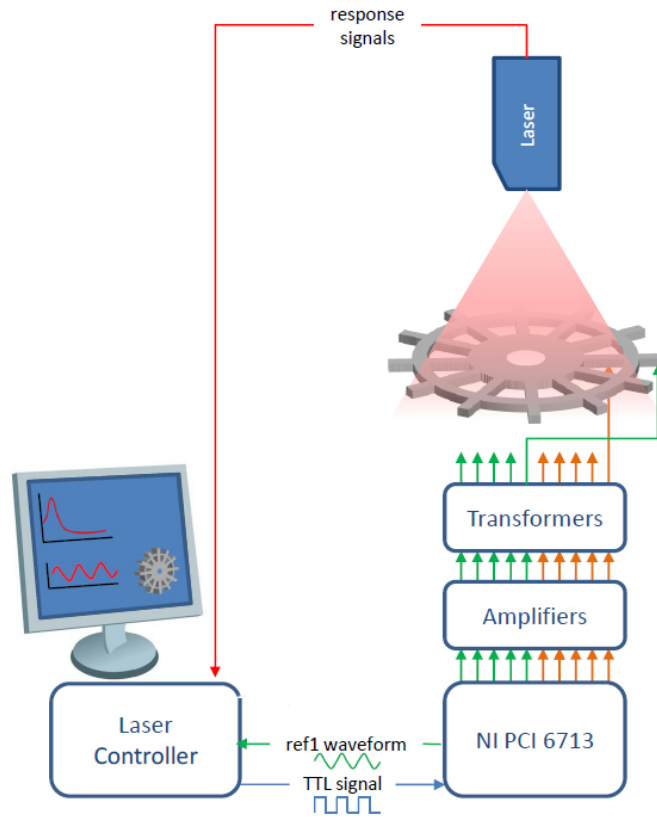


Figure 4.10: Traveling Wave Overview Schematic [25]

4.4.0.1 *Traveling Wave Excitation Signal Path - From Input Voltage to FRF Generation.*

This section provides a signal flow path for the TWE equipment. In doing so, it will clarify the system's overall operation. There are two main parts to the TWE setup: the signal generation component and the signal recording and processing component. The signal generation component is based in LabView. The signal recording and processing component is a PolyTec Commercial off the Shelf (COTS) item.

Signal Generation Component. Prior to signal generation, the operator inputs the number of blades, desired EO excitation, and frequency range. These inputs initialize the system by instructing the software on the number of amplifiers needed (8 blades can be excited by a single amplifier), and appropriate phase shifting between each actuator. A

National Instruments PXIe-1065 chassis houses 13 individual PXI-6713 12-bit high speed analog output cards. All phase shifting and amplitude modulation is performed within these cards using the waveform stored in their internal buffers.

The output cards have a maximum output rate of 740,000 points/second. Within the TWE software, this rate was decreased to 700,000 points/second so as not to intrude on the hardware's physical limits. In its current design iteration, the TWE software uses a minimum of 10 points and a maximum of 2000 points to define each output cycle. This output cycle is the sinusoidal waveform, at the prescribed frequency, sent to the magnetic actuator. Given the maximum card output rate and the minimum and maximum points per cycle, it follows that the maximum frequency output is 70kHz and the minimum is 370Hz. Based on the user defined frequency range, the software selects the appropriate integer value for the number of output points used to describe each cycle.

The TWE software employs this technique of using “points” to represent a continuous signal in a discrete manner. This method is known as the “single cycle algorithm”. The algorithm uses a single cycle of a sinusoid to depict the signal. This one cycle of data is stored in the memory, and the number of points used to represent the waveform is consistent throughout the waveform. The first step in signal generation involves discretizing one complete sinusoidal cycle into N segments. This produces $N + 1$ points. The amplitude of each point is stored in memory. Here, a sinusoid is discretized using 11 points, making 10 segments.

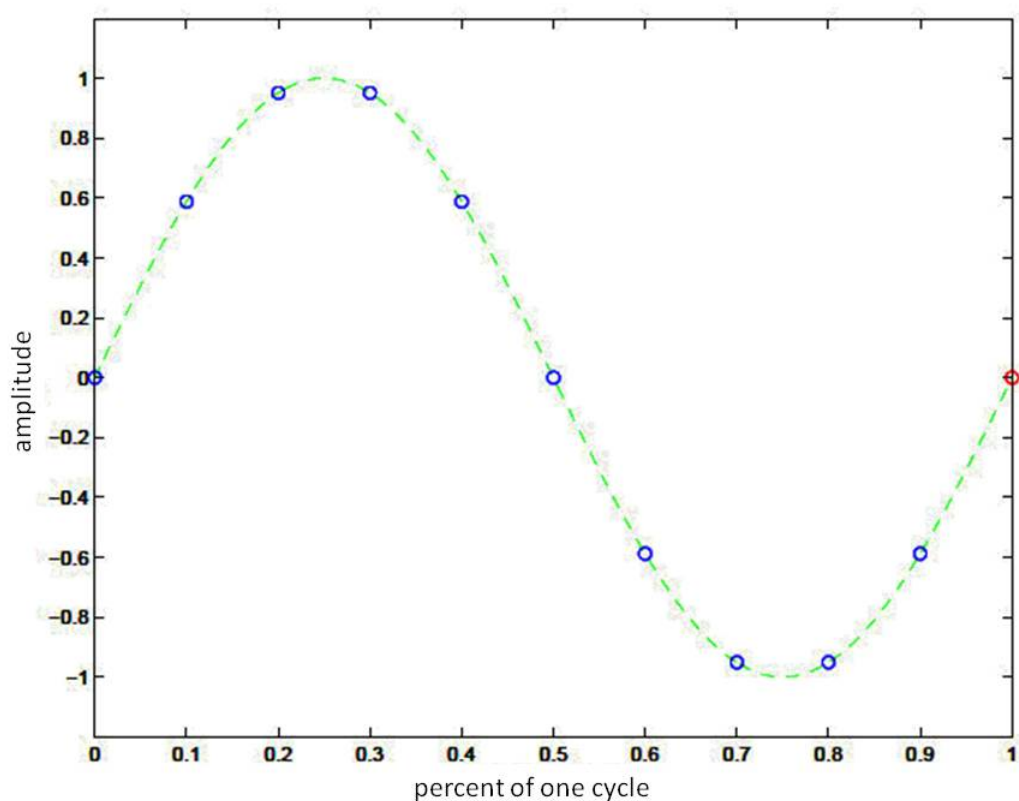


Figure 4.11: One Sinusoidal Cycle With 10 Points [25]

Since the first and last amplitude values are the same, only the first N points are used. In Figure 4.11, note how the points at 0% and 100% of the cycle are equal. Because this cycle is continually repeated to generate the waveform, “storing the last point of the sinusoid (shown in red) would cause leakage in the signal, which would drastically affect the results in the frequency domain and cause varying excitation to the component under test” [25]. These points are then output when triggered by an external timing signal. This permits a variable update rate which ultimately creates the user defined frequency sweep. As the timing signal increases in frequency, so does the point output. This is what generates the frequency sweep signal output.

A National Instruments PCI-5402 function generator card, located within the signal generation computer, generates this timing signal in the form of a square wave. The

square wave is a function of both the initial and final sweep frequencies and the number of points used to discretize the initial cycle. The following equations describe this frequency behavior. Here, f_1 and f_2 are the initial and final desired sweep frequencies, respectively.

$$\begin{aligned} f_{1_square} &= f_1 N \\ f_{2_square} &= f_2 N \end{aligned} \quad (4.1)$$

For example, the desired frequency sweep has an initial and final frequency of 1 and 11Hz, respectively, is shown in Figure 4.12. Here only the first three cycles are displayed.

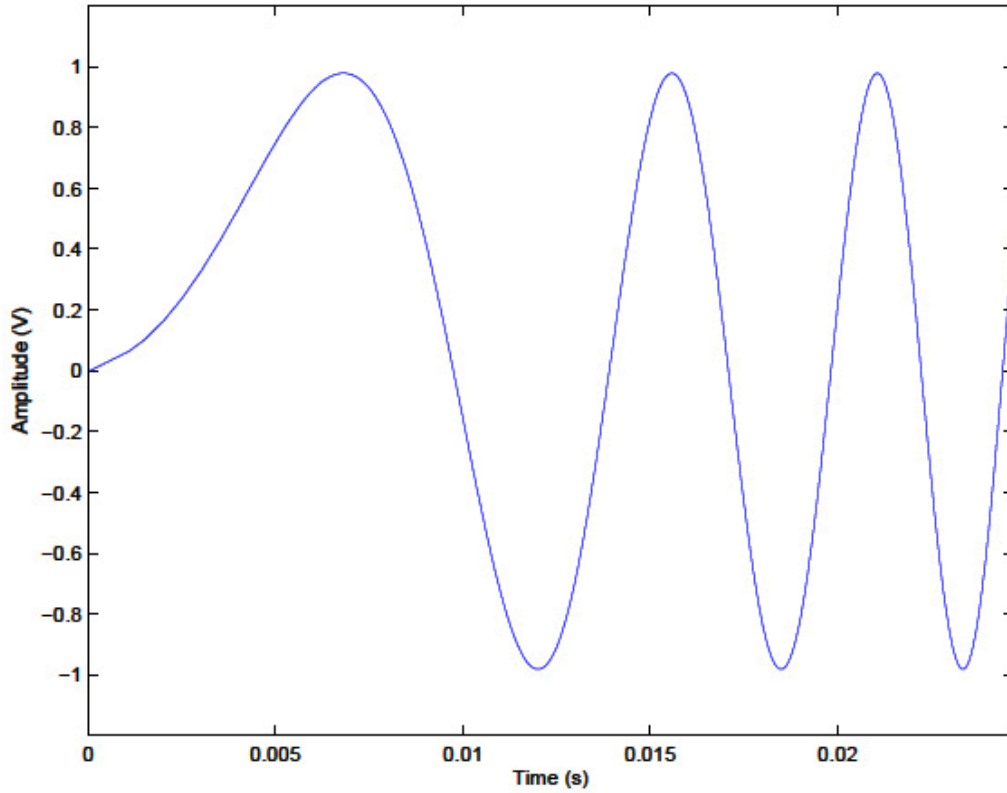


Figure 4.12: Linear Chirp: 1Hz - 11Hz Sweep (First 3 Cycles) [25]

From Chapter 3, Section 3.1, the equation defining a frequency sweep is given as: (T_s is signal sweep ending time)

$$Y(t) = \sin\left(2\pi\left[\frac{1}{2}\left\{\frac{f_2 - f_1}{T_s}\right\}t + f_1\right]t + \phi\right) \quad (4.2)$$

This produces the signal shown in Figure 4.13.

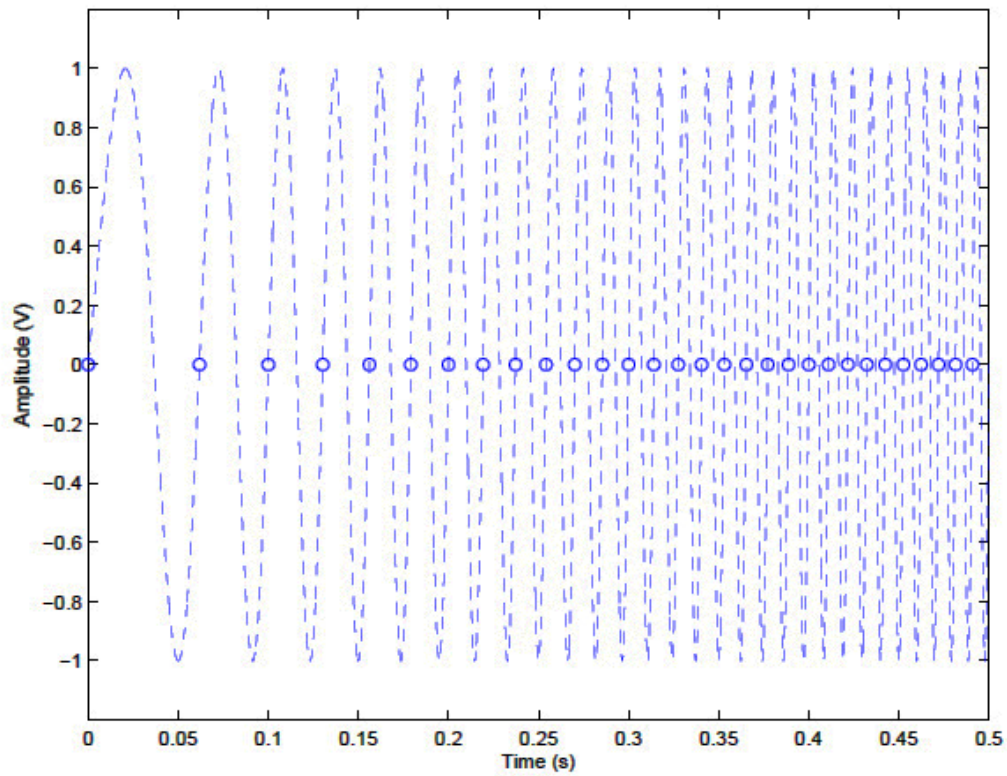


Figure 4.13: Example of Multiplied Waveform: 1Hz - 11Hz Sweep [25]

The square wave timing signal is generated from this waveform in Figure 4.13. When the waveform is positive, the square wave is also positive. This relationship also holds for a negative waveform value; the square wave is negative or zero. Figure 4.14 illustrates this concept.

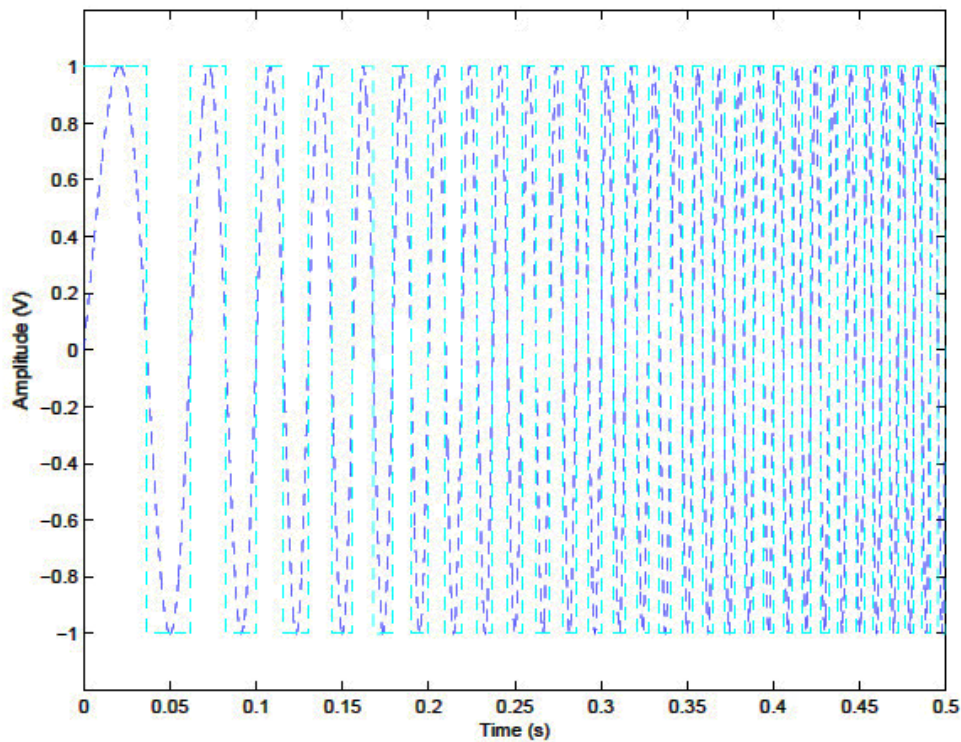


Figure 4.14: Superimposed Square Wave onto Multiplied Waveform [25]

This waveform is sent to the PXI-6713 analog output cards where it is used to trigger the cards. The square wave, of varying frequency, ultimately serves as an indication to begin the signal output. The PolyTec system sends its own timing signal to the function generator to begin the frequency sweep.

The user specifies the initial and final frequencies of interest for the traveling wave excitation. The square wave timing signal then sweeps from the initial frequency to the final frequency. Proceeding along the square wave, when a rising edge in the wave is detected, the output waveform voltage amplitude is updated from the single cycle stored in the memory. Recall the discretized single cycle shown in Figure 4.11. In other words, a single point from this stored sinusoid is used. The voltage remains the same until another rising edge is detected, where the next point is used. This signal is sent to its respective amplifier by way of an externally mounted National Instruments TB-2705 terminal block

module. Because the timing signal is a square wave, the output waveform is stepped. For the same 1-11Hz frequency, this stepped output is shown in Figure 4.15. With each rise in the square wave, the analog output cards change output voltage to that value defined corresponding to the next point stored in memory. Since the square wave timing signal's frequency increases through time, the output cards fire their internal signals faster and faster. This simulates the frequency sweep for the TWE experiment.

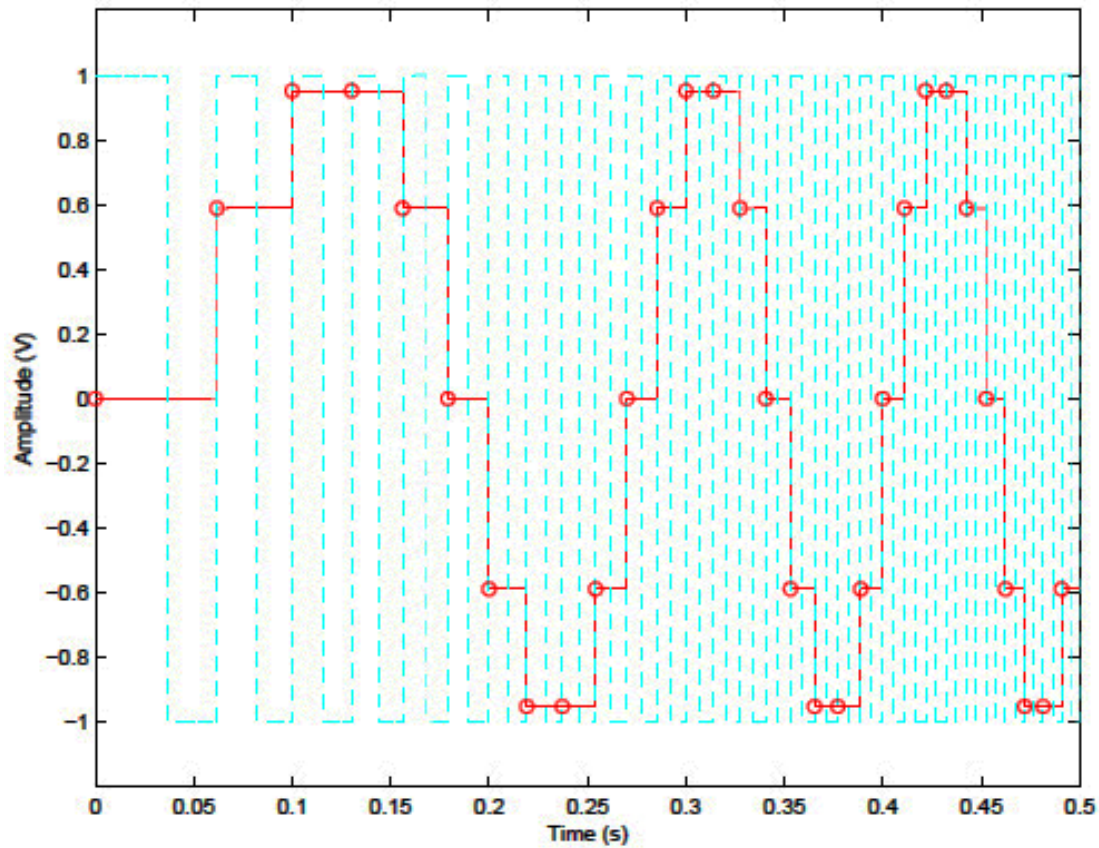


Figure 4.15: Stepped Output Waveform [25]

Each point corresponds to a point lying on the initially discretized sinusoidal wave shown in Figure 4.11. Note how there are 10 points defining each cycle. Figure 4.16 shows the step function type of output with the corresponding ideal frequency sweep.

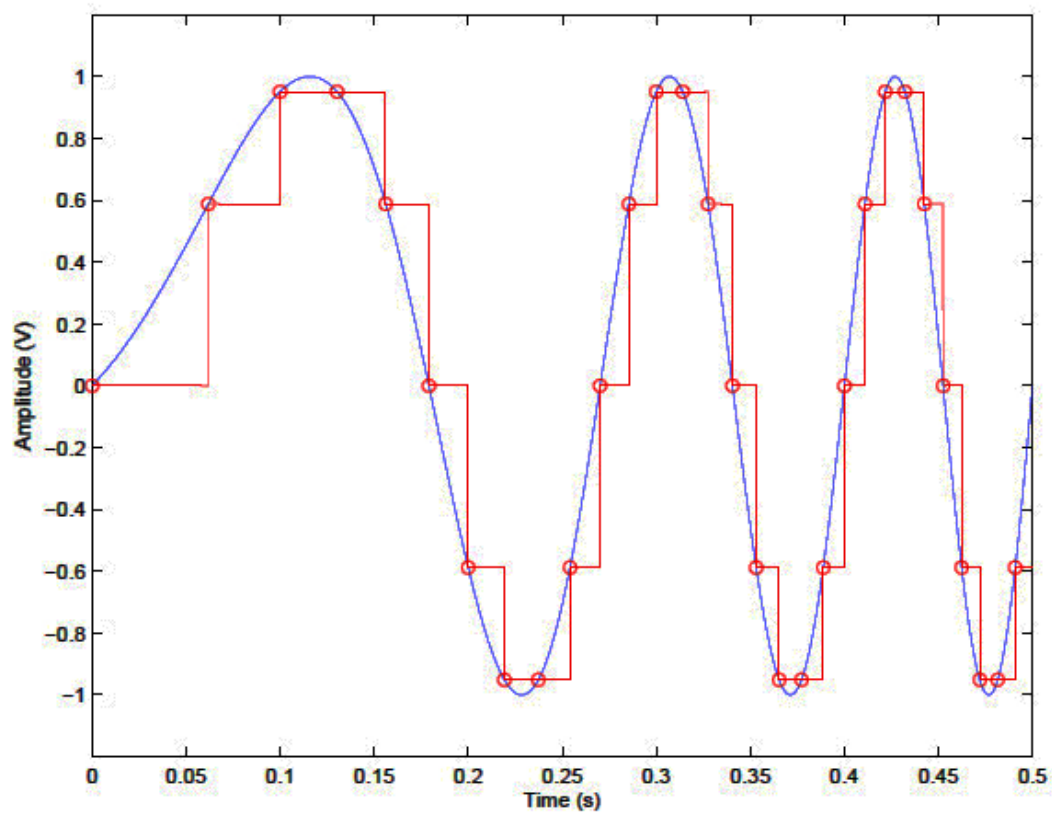


Figure 4.16: Ideal Frequency Sweep with Stepped Output [25]

It is intuitive how with more points discretizing the stored sinusoid, its discrete representation would more closely resemble the continuous waveform. All waveforms are shown together in Figure 4.17.

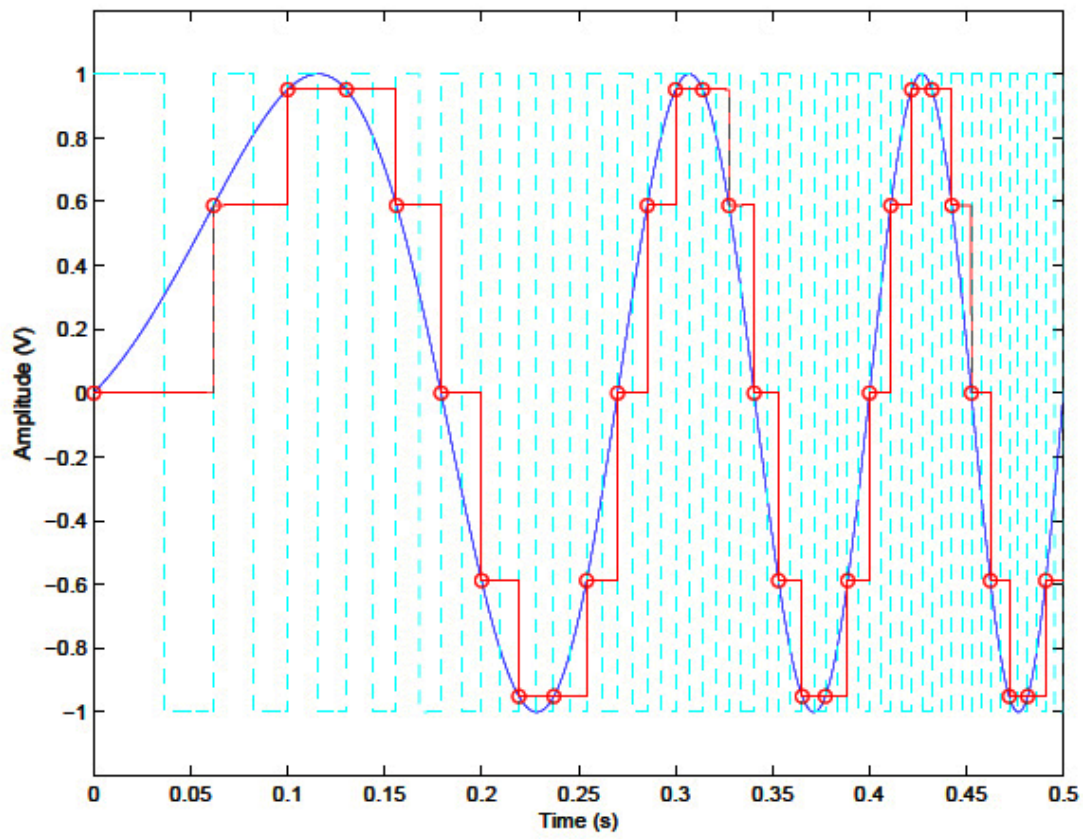


Figure 4.17: All Waveforms for 1-11 Hz Frequency Sweep: 10 points [25]

Figure 4.18 shows the TB-2705 terminal block module modules and amplifier cable connections. Each output module is connected to a single amplifier. Amplifiers are required to increase signal power to drive the magnetic actuators.

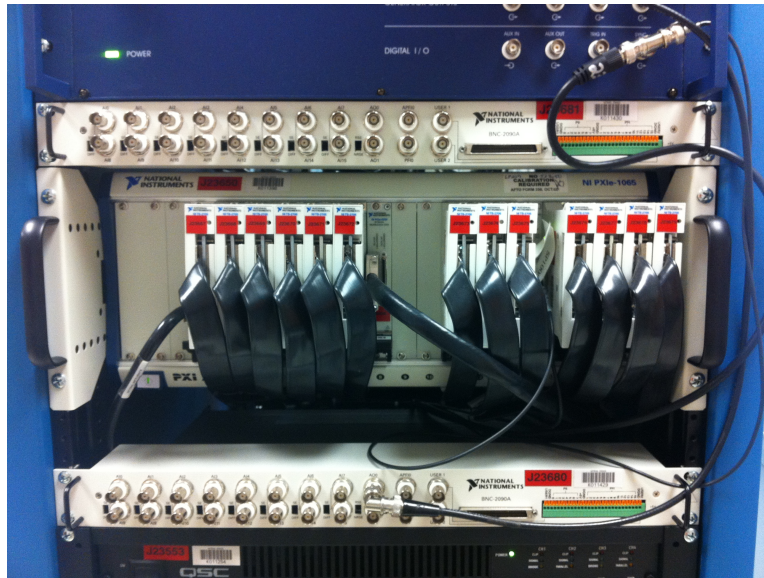


Figure 4.18: NI TB-2705 Modules' Output Connection to Amplifiers

Depending on the desired forcing function, the amplifiers can increase this amplitude approximately 6 times but not exceed 30V into the actuators. This limit is driven by the magnetic actuator's physical capacity. A voltage over this limit will overheat the magnetic actuators. The amplified signal, now at the proper amplitude and at the initially prescribed phase is sent to the magnetic actuators.

A reference signal is also captured. This signal is simply split away from the first analog output card. It is this signal, to which, calibrations and the signal from the laser vibrometer channel are compared. This reference channel is a 2V peak to peak. There is no additional amplification or phase shifting applied to this reference channel. The reference signal displays the same frequency sweep as the output sent to the magnetic actuators.

Signal Recording and Processing Component. The signal recording component is a COTS system. PolyTec manufactures both the scanning laser vibrometer and its associated software. The PolyTec system allows for flexible scan point assignments of virtually any location on the object's surface. The software also provides the pertinent data required for a vibrations test. As the laser vibrometer scans the object, various pieces of information can be viewed in real-time. The PolyTec software controls the entire measurement system,

which “includes the high-speed Fast Fourier Transform (FFT) processor, analog-to-digital converters, laser focus and position, vibrometer electronics, and a live video system” [97].

The reference signal sweeps from the initial to the final frequency in the user-defined time interval. The laser vibrometer velocity is the velocity of the point currently being measured. Finally the displayed FRF, gives a real time indication of the structure’s resonant frequency content. Figure 4.19 shows a typical layout for several information windows within the PolyTec software.

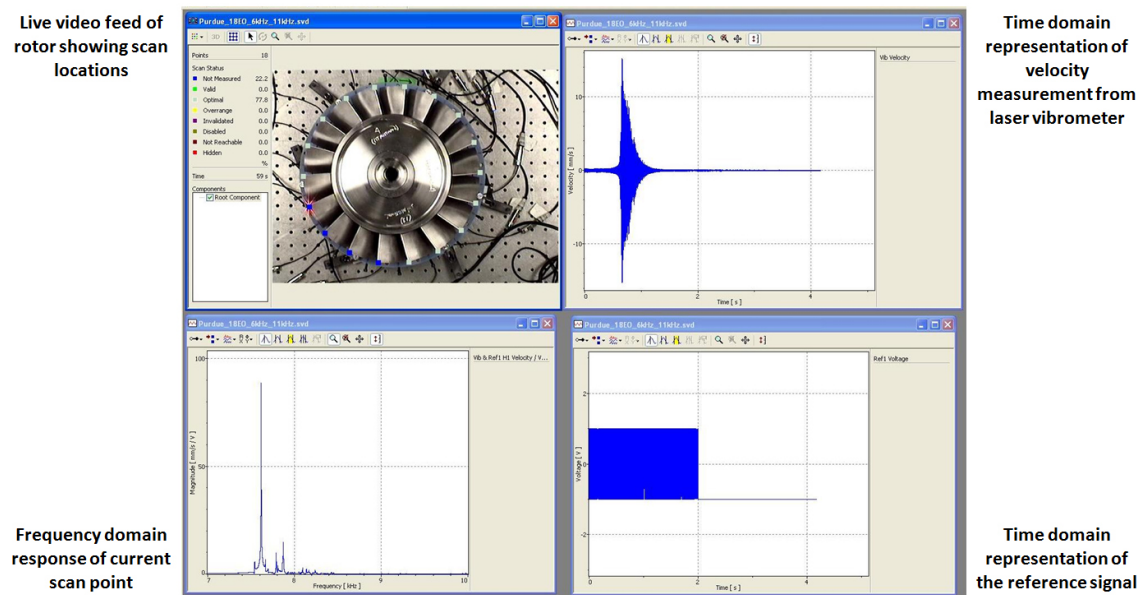


Figure 4.19: Typical Signal Window Arrangement for PolyTec Software

The upper left quadrant shows a real time view of the laser position with the scan points superimposed onto the rotor imaged. The upper right quadrant is the laser vibrometer measured point velocity in the time domain. This can also be changed to display the recorded displacement or to the actual voltage within the system. The lower left quadrant is the real time FRF for the current scan point. In this figure, the ordinate is displayed in velocity/volt (ratio of measured velocity to reference voltage). Flexibility is afforded within the software to display the desired information in virtually any format. Lastly, the lower right quadrant shows the reference signal voltage.

The PolyTec software also has its own internal function generator. This feature is used strictly for timing. The PolyTec software sends its timing signal to the external signal generation component discussed in the previous section. In doing so, the PolyTec system lets the signal generation component know when it is ready to begin scanning, and thus when to begin providing the input signal to the magnetic actuators. When the signal is sent to the magnets, the magnetic actuators excite the rotor at the blade tips. The laser vibrometer measures this movement as a change in voltage. This change in voltage is digitized and processed as the vibrometer signal. Since the input and output signals are known, the corresponding FRF can be calculated. When the actuators excite the rotor, the laser vibrometer begins to record the response. Chapter 3, Section 3.6 discusses the theory behind the laser vibrometer's operation. The vibrometer's signal is sent to the PolyTec software computer and processed into a real-time display for analysis (Reference Figure 4.19).

V. Experimental Work and Related Discussion

Prior to performing a traveling wave test on a particular rotor, some idea of its operational environment should be known. This information is typically garnered from the specific rotor's Campbell diagram. For example, the researcher should be aware of the pertinent frequency range and with that, which modes will be excited. Additionally, the rotor's EO excitation should be known. During operation, a rotor is subjected to specific harmonic inputs induced by EO excitation. The traveling wave test should effectively reproduce this loading. Granted, the loading magnitude won't be representative of the operational environment, but the frequency content will be present. Prescribing the frequency sweep information and excitation pattern (dictated by EO) tailors the traveling wave experiment to the specific rotor under investigation.

5.1 Experimental Methodology

5.1.1 Initial Experimental Data Acquisition Details.

In order to ensure all information collected is consistent from blade to blade and rotor to rotor, the PolyTec software was set up to maintain a constant frequency resolution, and thus sample rate, for all scans. A maximum resolvable frequency of 40kHz was used throughout all testing. Within the PolyTec software, this is known as the *bandwidth*. Physically, this sets a maximum frequency which could be recorded. This frequency was chosen because it was much larger than any frequency used in the experiments. Additionally, 409,600 FFT lines (Chapter 3, Section, 3.10) were used in each test. The combination of this maximum frequency and number of FFT lines dictated the response acquisition time, frequency resolution, and sampling frequency. Reference Chapter 3, Section 3.10.

Existing lab practices and prior experience indicate when performing a frequency sweep, the end frequency should not exceed twice the starting frequency. Since the rotor is stationary in the experiment, 0EO through 9EO ($N/2$) will produce all the necessary phase angles between blade inputs. The time to sweep through each of the input frequency bands is a constant 5 seconds. This input time is kept shorter than the response acquisition time to ensure the laser vibrometer captures both transient and steady state rotor responses. The following table details these initial acquisition parameters.

Table 5.1: Data Acquisition Details

Frequency Bandwidth (kHz)	40
Total FFT Lines	409,600
Sampling Frequency (kHz)	102.4
Frequency Resolution (mHz)	97.656
Response Acquisition Time (sec)	10.24
Input Signal Sweep Time (sec)	5

5.1.2 Single Scan Point Justification.

In the traveling wave experiment, a single measurement, or scan point, is employed per blade. The scan point location is chosen for several reasons. First, there will always be a portion of the blade in view of the scanning laser vibrometer oriented above the table. Figure 5.1 illustrates the typical blade portions in view of the laser vibrometer. For the Purdue Transonic Research Compressor, there is no overlap between adjacent blade. In other types of rotors, there is significant overlap between adjacent blades. Figure 5.2 shows the blade overlap dimension, indicated with the capital letter A. As the dimension A becomes smaller, and eventually negative, the blade positions are closer and eventually overlap. The overlapped region would therefore be invisible to the overhead scanning laser vibrometer. Additionally, the point opposite the input location was theoretically shown to exhibit the largest displacement magnitude. Reference Table 5.21 for an illustration of this

phenomenon. Lastly, the modes of interest to engineers researching rotor dynamics do not exhibit nodes or nodal diameters near the measurement locations. This could not be said if the measurement location was placed near the blade root or blade center.



Figure 5.1: Example Blade Output Locations

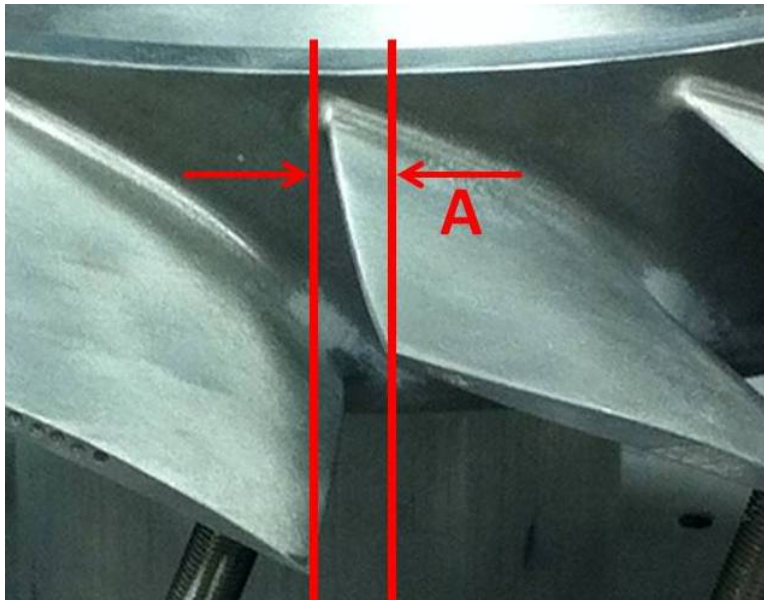


Figure 5.2: Blade Overlap Dimensions

5.2 Effect of Calibration Process

The theory behind the calibration process was discussed in Chapter 3, Section 3.5. Here, the practical effects of calibrating the electromagnetic actuators will be shown. Recall calibrating is an iterative process which adjusts the voltage, and hence strength, of each actuator such that the input at one blade will induce the same response at each blade - at the calibration frequency. As each actuator is activated, the response at each blade is recorded. Figure 5.3 illustrates the average response convergence seen with three consecutive calibration iterations. Blade numbers are given along the abscissa. The curves depict the average rotor response when a blade's actuator is energized. Here, the most significant change occurs between the first and second calibration iterations. The differences in response curves between the second and third calibrations illustrate how a blade's input signal has converged. Between the first and second iterations, there is, on average a 56% difference in the average response curves. Between the second and third iterations, the average percent difference has decreased to 10%. This is within the acceptable tolerance level to indicate satisfactory convergence. A fourth calibration, used to verify the convergence, was performed. Those results were almost identical to those seen in the third calibration iteration. There was less than a 0.01% change in response between the third and fourth calibrations trials.

An alternate way to envision the calibration data is to examine a given blade's response when its actuator is energized. Since the experimental research rotor has 18 blades, a given calibration iteration produces an 18 x 18 matrix of response. Each column represents the response at that blade. For example, column 1 represents the rotor response when blade 1 is excited, column 2 is the response when blade 2 is excited, and so on. Therefore, the diagonal terms provide the response at blade N when blade N is excited.

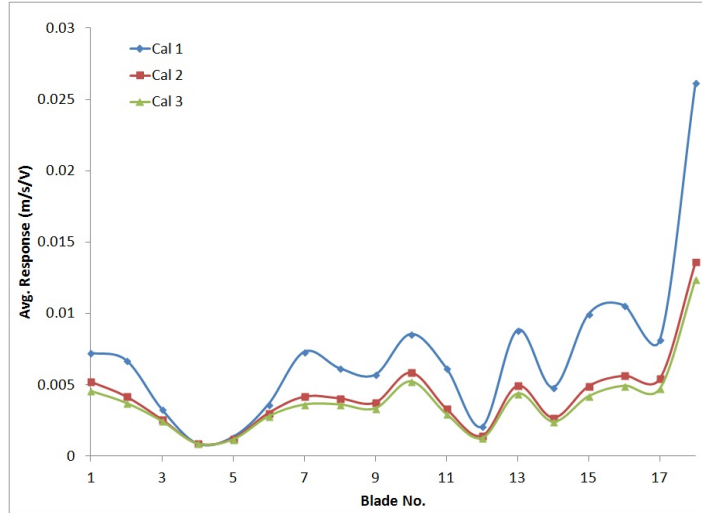


Figure 5.3: Calibration Convergence Response Curves

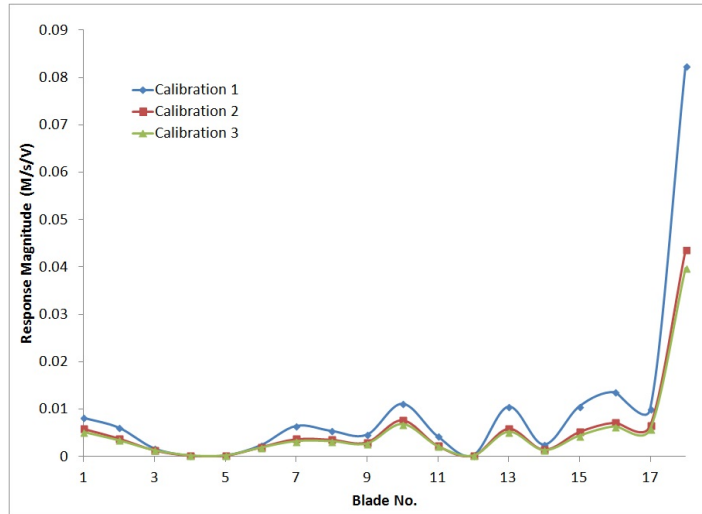


Figure 5.4: Calibration: Blade N Response to Blade N Excitation

5.3 Initial Experimental Results

The initial experimental results shown in this section will reveal the degree of mistuning present in the Purdue Transonic Research Compressor. Recall from Chapter 2, Section 2.1.2, a tuned rotor will exhibit blades with identical natural frequencies. In other words, for a given mode, a tuned system will exhibit a single natural frequency, as all blades behave in an identical manner. These experimental results will also be used to

validate a finite element model developed by way of structured light. The process by which the validation is performed is outlined in Chapter 3, Section 3.12.2.

5.3.1 Effect of Experimental Uncertainty.

Repositioning the rotor forces the need to re-center the rotor on its pedestal, re-measure each blade to actuator standoff distance, re-measure each blade tip to actuator radial distance, and each blade trailing edge to actuator distance. These actuator positions are absolutely critical if the need arises to maintain a consistent forced response measurement for multiple rotors. Even with careful positioning and measurements, these distances will likely differ each time the rotor is lifted off of its pedestal and placed down again. Because the rotor is a continuous system, there exists a unique FRF for each input-output combination.

Figures 5.5 and 5.7 illustrate the drastic difference in forced response one rotor can experience by merely lifting the rotor from its pedestal, re-positioning it, and placing it back down again. The first figure shows the magnitude FRF for five separate runs, at EO 0, sweeping from 1kHz - 2kHz. This was not entirely unexpected, as removing and replacing the rotor onto the test setup completely changed the experimental configuration. Here, there was no degree of precision embedded within the setup procedures.

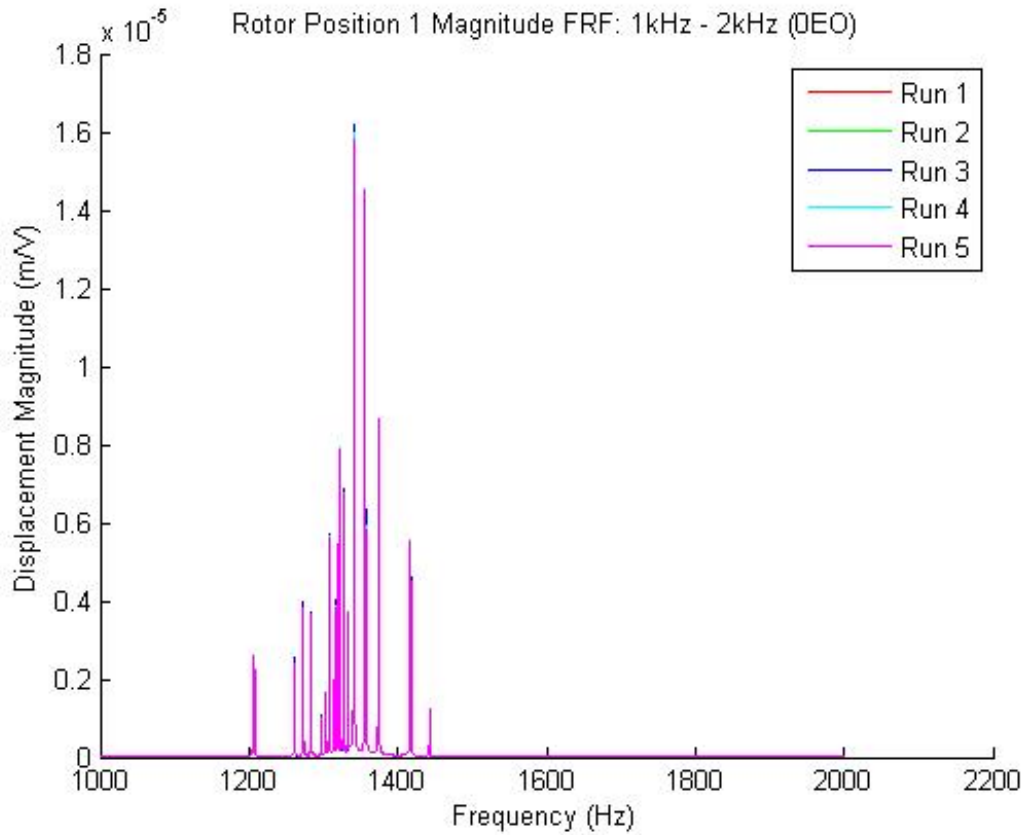


Figure 5.5: Position 1 Magnitude FRFs: 1kHz - 2kHz (0EO)

In this frequency band, there are 18 separate natural frequencies. Each of these frequencies correspond to each blade's first bending mode. Figure 5.6 depicts a normalized response plot at each natural frequency for all five runs. The response magnitude at each natural frequency was normalized by the overall average response for that respective run. This gives an indication as to the level of mistuning present in each blade, as compared to the overall average response.

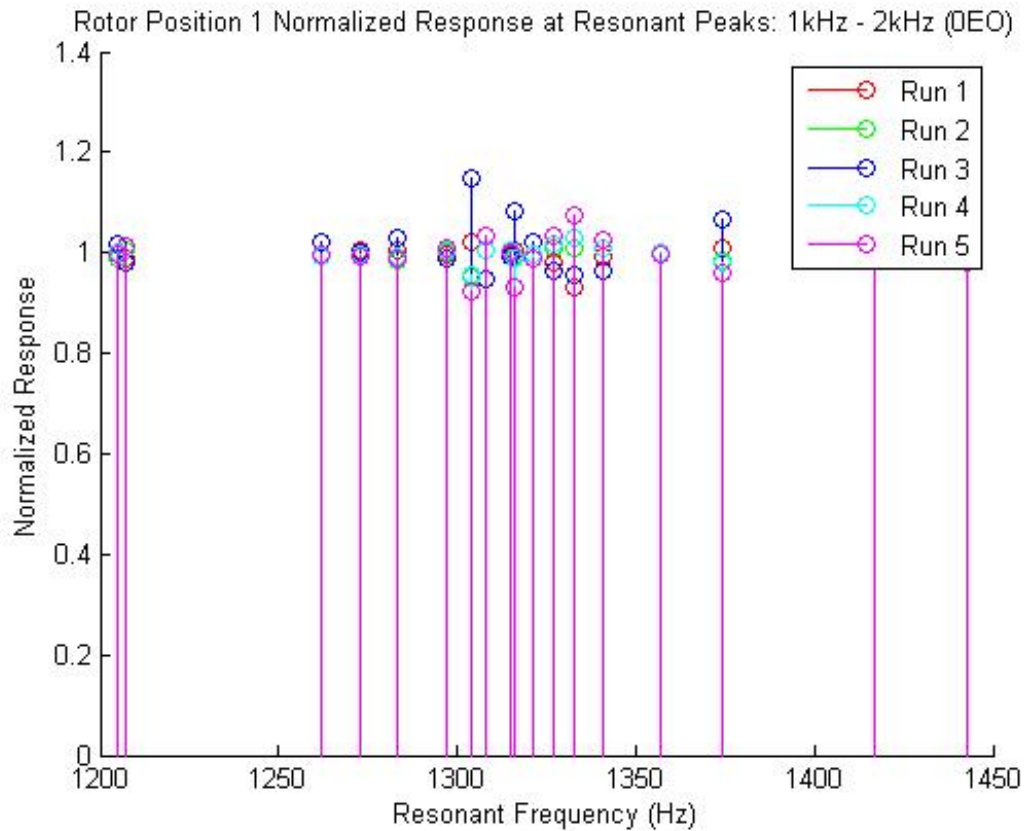


Figure 5.6: Position 1 Normalized Responses: 1kHz - 2kHz (0EO)

The rotor was then lifted off its pedestal, turned 90° clockwise. This introduces experimental variability in the form of varying the rotor's position. Because the rotor's position was altered, the measurement points and input locations were redefined. Five more runs, sweeping from 1kHz - 2kHz. Figure 5.7 shows each of the five FRFs superimposed onto one another.

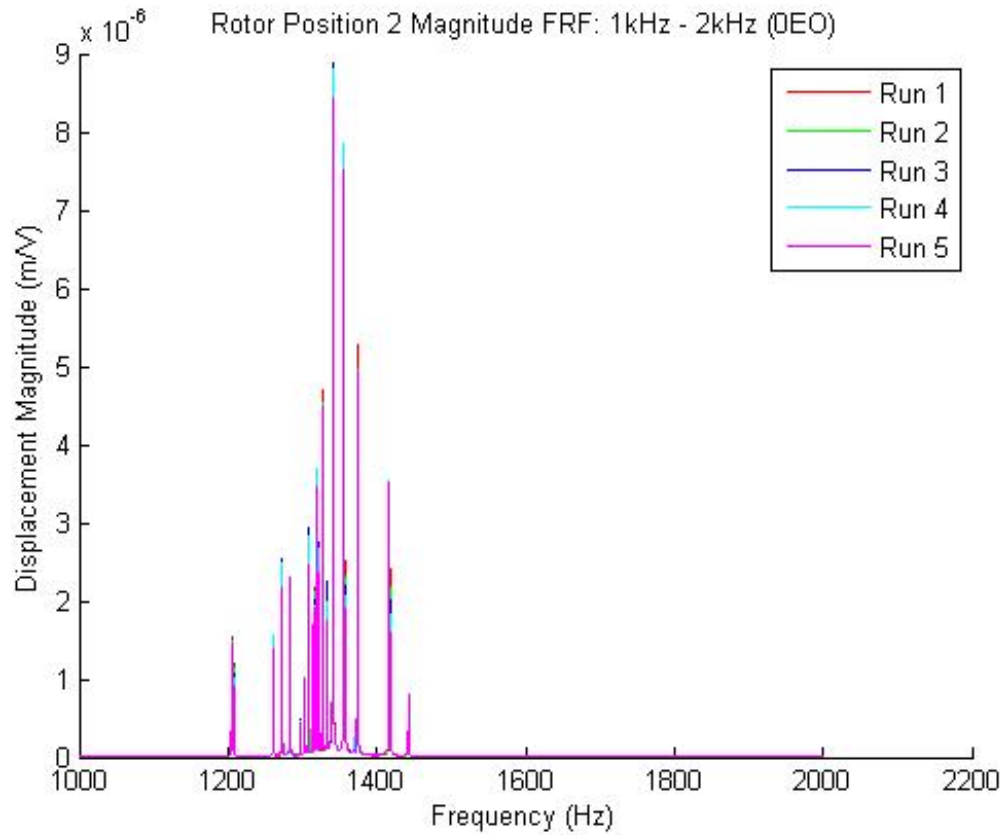


Figure 5.7: Position 2 Magnitude FRFs: 1kHz - 2kHz (0EO)

In this instance, while the natural frequencies line up consistently with those seen in Figure 5.5, variance realized between individual runs is evident. Rather than all five FRFs lying perfectly on top of one another, each individual FRF is clearly seen. The experimental variability is even more apparent when the responses at each natural frequency are normalized by the average response of that respective run, as shown in Figure 5.8.

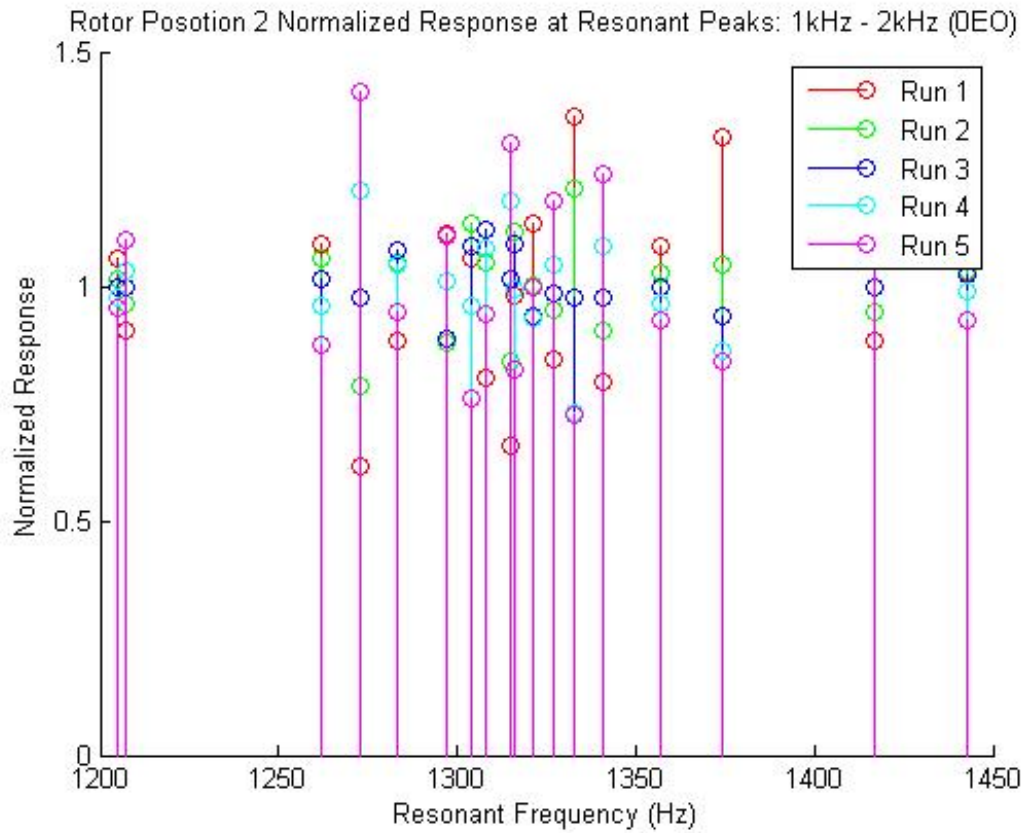


Figure 5.8: Position 2 Normalized Responses: 1kHz - 2kHz (0EO)

Finally, in superimposing each position's average magnitude FRF, the effect of this variability is immediately evident.

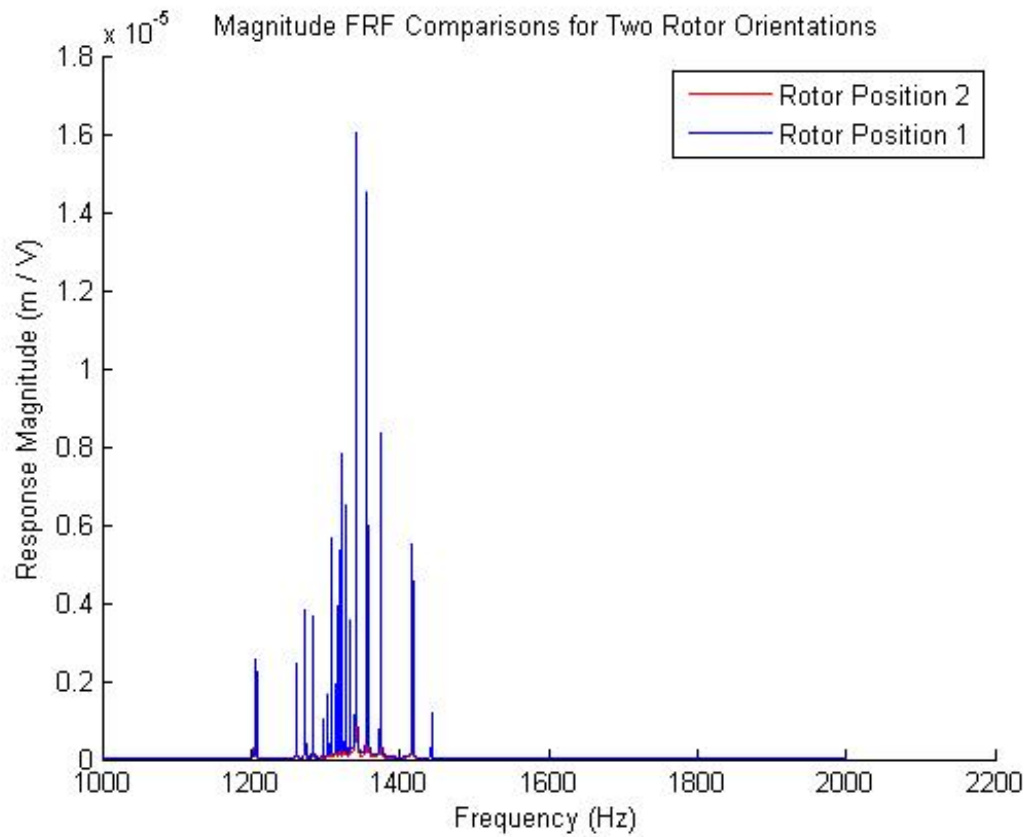


Figure 5.9: Positions 1 and 2 Magnitude FRFs: 1kHz - 2kHz (0EO)

Figures 5.10 5.11 depict a closer view of the resonant peaks for each position's magnitude FRF. Here, the abscissa scale has been reduced to closely fit the range of frequencies.

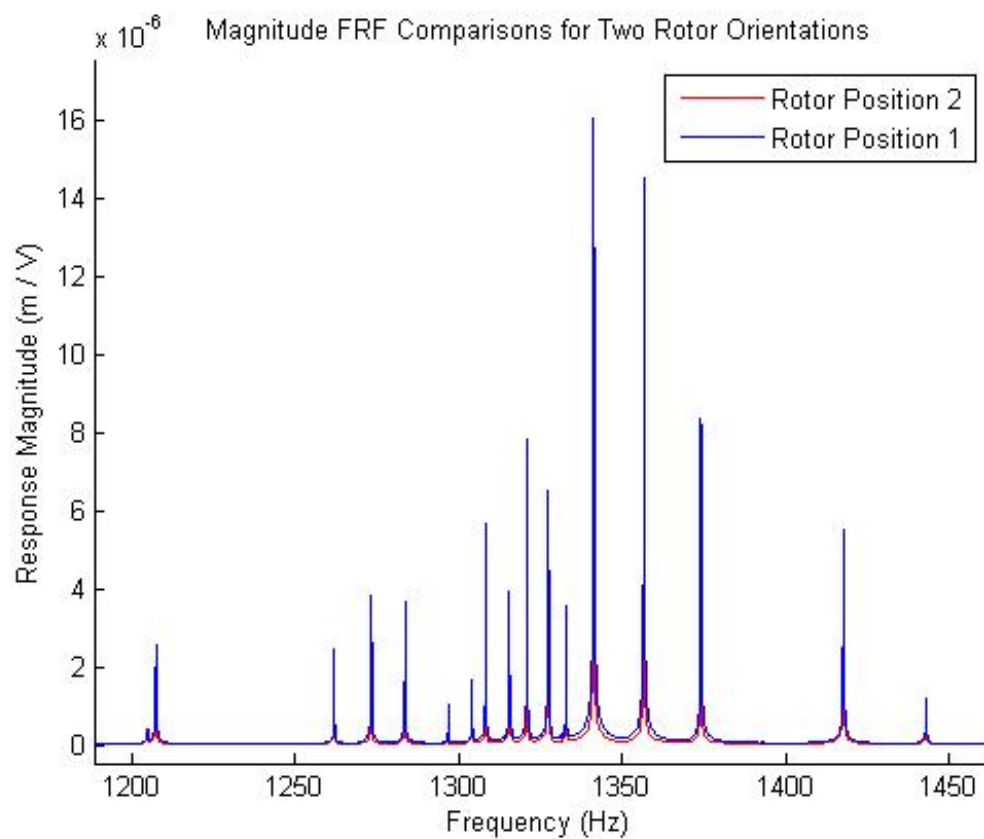


Figure 5.10: Alternate View, Positions 1 and 2 Magnitude FRFs: 1kHz - 2kHz (0EO)

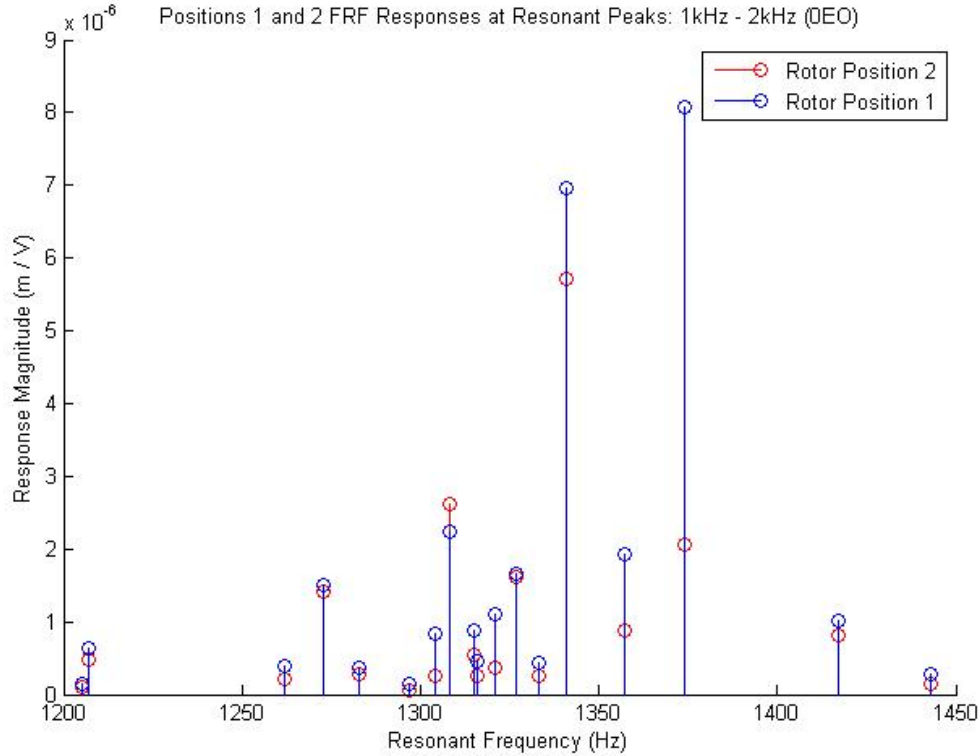


Figure 5.11: Positions 1 and 2 Response Magnitudes at the 18 Resonant Frequencies: 1kHz - 2kHz (0EO)

Here, the magnitude FRF obtained for the rotor's first position is significantly greater than that determined from the second position. The following section details a procedure to mitigate the effects of rotor re-positioning, defining input locations, and defining output locations.

5.4 A Method to Produce Consistent Experimental Results

The data acquisition parameters here supersede those shown in Section 5.1.1. The process detailed in this current section came about after examining the experimental results in Section 5.3.1. The procedure detailed here is used for all remaining traveling wave tests, and is taken from Cox' work in Reference [112]. The following list shows the items required for consideration in developing a method to ensure consistent experimental results.

1. Rotor Position
 - (a) Identify Center of Actuator Ring
 - (b) Align Ring Center with Laser Vibrometer Home Position
 - (c) Identify Center of Rotor
 - (d) Position Rotor at Actuator Ring Center
2. Rotor 2D Alignment
3. Focus Laser Vibrometer Beam
4. Define Rotor Measurement Locations
5. Define an Appropriate Scan Time

5.4.0.1 Centering the Rotor and Input Locations.

Rotor input and response output locations are examined as the experimenter has the most control of these two variables. To that end, the experimental setup is of prime importance. The initial setup steps involve precise rotor positioning and establishing the input locations. After powering up the laser vibrometer, the actuator/excitation ring (Figure 4.7) is positioned beneath the unit such that the laser's *home position* is approximately at the ring's center. The home position is the default beam location and reference point for all beam location coordinates. In a sense, it becomes the rotor's global coordinate system origin.

To identify the ring's center, Thales' Theorem is employed. The theorem states: "the diameter of a circle always subtends a right angle to any point on the circle" [113]. Invoking this theorem, the actuator ring's center is identified by marking its diameter in two places around the ring. This was performed using two alignment lasers and a T-square. The intersection of these diameters identifies the center (Figure 5.12). This location is established so as to coincide with the laser vibrometer's home position.

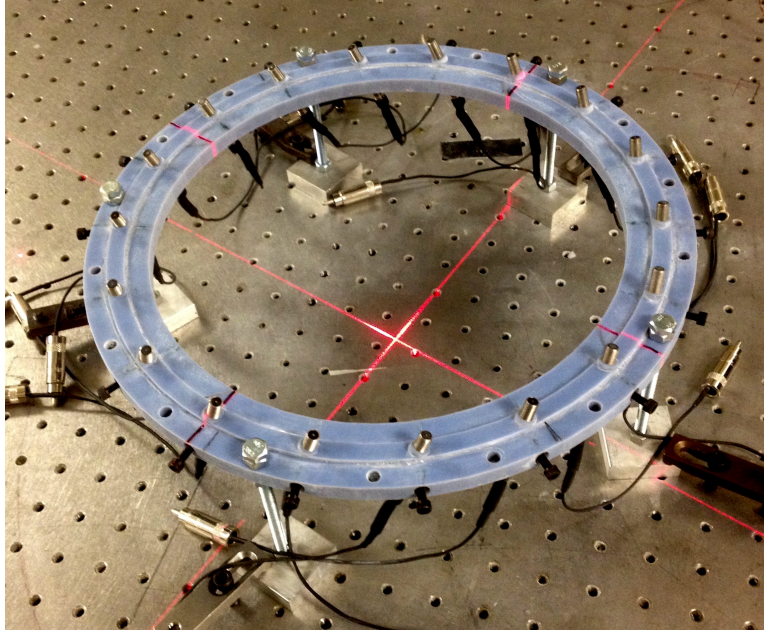


Figure 5.12: Actuator Ring Center

The rotor is next centered within the actuator ring. The same alignment lasers are used to ensure the rotor is centered on the vibrometer's home position and within the ring center. To aid in this process, Thales' Theorem is once again employed. The rotor's central hub is marked with several diameter indications (Figure 5.13 and Figure 5.14). Additionally, these reference marks lie coincident with the *lower corners* on each blade. This was performed in order to both center the rotor and align the blades with the input locations. This process consistently places each actuator 0.150 ± 0.02 inch from each blade's radial and trailing edges, as measured using laboratory feeler gauges. Each actuator is then threaded up through the ring, stopping at 0.02 inch from each blade (Figure 5.15).

5.4.0.2 Rotor 2D Alignment and Beam Focus.

When performing the TWE experiment, it is imperative to give the laser vibrometer software sufficiently accurate information regarding the plane in which to measure

information. This is performed by way of a 2D alignment. The user instructs, or “teaches”, the system the two dimensional plane where the velocity returns will be measured. For optimum consistency, locations returning maximum signal returns should be chosen. Shown in Figure 5.16, these 2D alignment points are chosen on the actual blade measurement locations. Intuitively, the more locations chosen for the alignment process results in a greater degree of accuracy when measuring the response. During this process, it is also crucial to re-focus the laser vibrometer’s beam. The beam is focused on a point which lies on the reflective tape. This ensures an optimal signal return. These pieces of reflective tape are placed in areas where the scan points will ultimately lie.

5.4.0.3 Scan Point Identification.

Peng [57] emphasizes how in any experimental modal testing, the measurement locations have a major influence on the result quality. The TWE experiment is no exception. Within the experimental setup, individual blade input locations are positioned with respect to their own blade. Each output location, on the other hand, is established by way of transforming local blade locations back to a global rotor location. This relationship between local and global coordinates is established because blade locations change with respect to their position around the rotor hub. Relating the unique blade measurement positions to a fixed global coordinate system establishes a consistent relationship between the scan points.

In general, the global coordinate system can be visualized as a three dimensional orthogonal set of Cartesian axes whose origin lies at the rotor center. This is depicted in Figure 5.17. Here, the measurement plane is depicted as the oval. This plane was established by way of the 2D alignment process described in Section 5.4.0.2. The angle ϕ is displayed in the PolyTec software desktop window as the beam position, measured in *degrees* from the horizontal and vertical axes which emanates from the laser’s home position / origin. The angle β is the angular position around the rotor. Ideally each measurement location is at the same local location on each blade. For a given rotor, there

exists n blades equally dividing a single 2π radian revolution. For a single measurement point per blade, the angle, β , between each measurement location is defined as:

$$\beta = \frac{2\pi}{n} \quad (5.1)$$

The three dimensional coordinate system is projected onto the two-dimensional x-y measurement plane. Both the three and two dimensional coordinate systems share the same origin at the rotor center. Further, the origin and the Z-axis lie coincident with the laser vibrometer's home position.

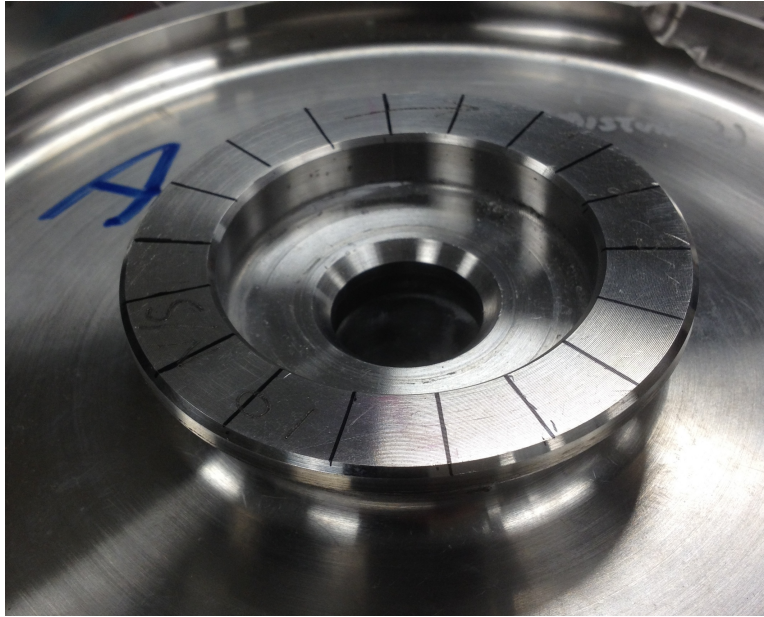


Figure 5.13: Close Up View of Rotor Hub Diameter Reference Marks

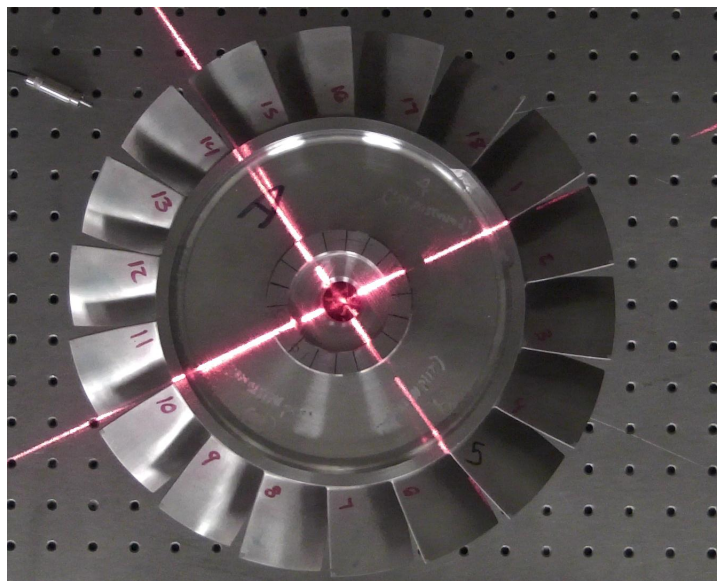


Figure 5.14: Centered Rotor

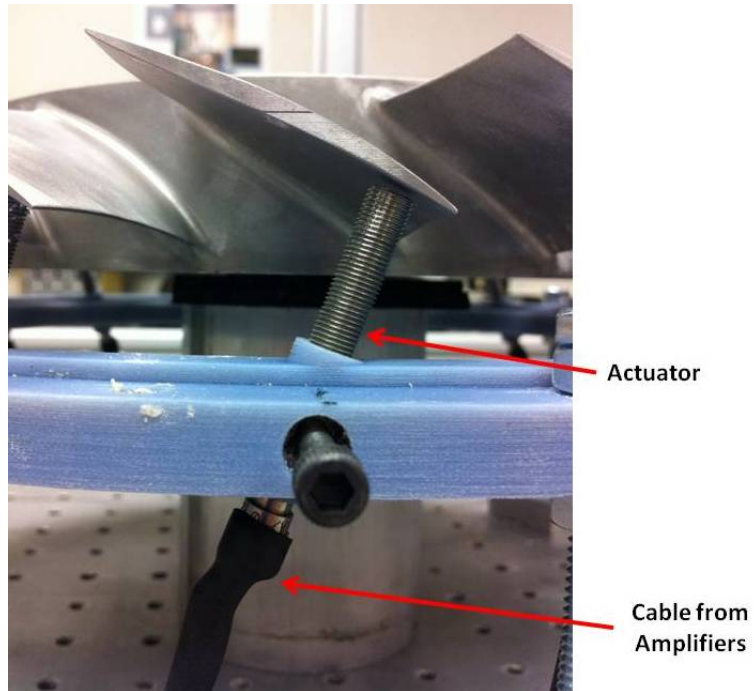


Figure 5.15: View of Actuator Below Blade

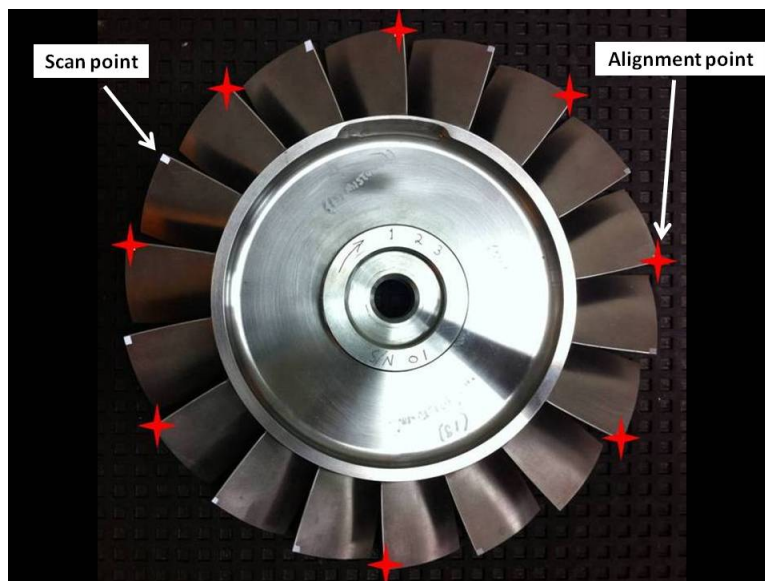


Figure 5.16: Sample 2D Alignment Points

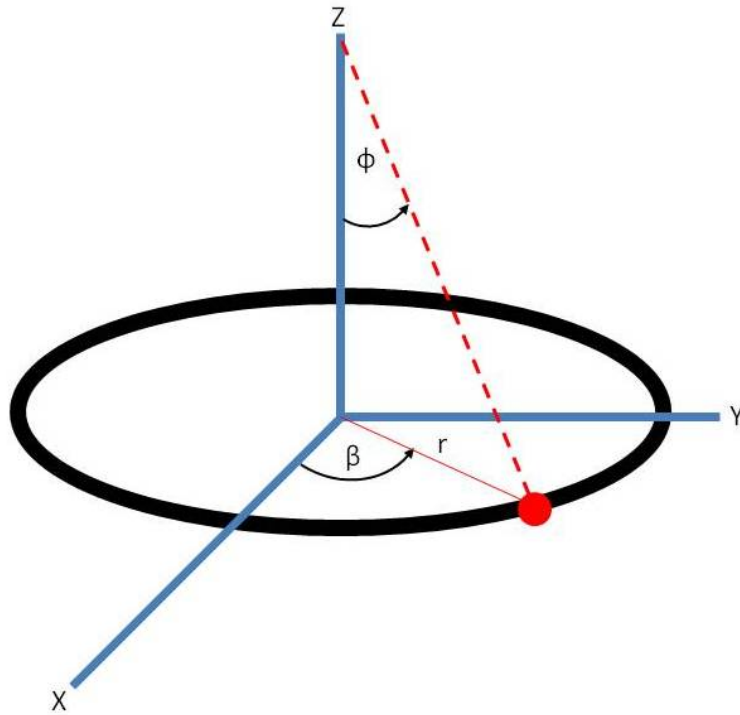


Figure 5.17: Rotor Global Coordinates Schematic

The global rotor and local blade coordinate systems are seen when viewing the rotor from above, as shown in Figure 5.18. From this view, the global rotor information is mapped to each blade. Since the laser position is given in terms of degrees from both the horizontal and vertical axes, the use of a Polar to Cartesian Coordinate map is appropriate. Locally, there exists an axis tangent to the rotor hub and an axis parallel to the blade's leading edge. The origin for each local coordinate system is at the intersection of the hub to blade interface and blade leading edge.

By allowing one axis of the coordinate system to lie on the blade's edge, any variation in blade width is not a concern. A local measurement location is thus given in terms of an ordered pair: (r, β) . Each system is shown in Figure 5.18. The global coordinates are shown with their origin at the rotor center, and the local coordinates are shown superimposed onto each blade. In general, the global scan point location, (x, y) , on the $(c - 1)^{th}$ blade is given

as:

$$x = r \cos [(c - 1)\beta], \quad y = r \sin [(c - 1)\beta] \quad (5.2)$$

Here, x and y are the global coordinates on the blade of interest. The blade counter is $(c - 1)$. For example, the first blade's counter would be 0 and the eighteenth blade's counter would be 17. The radial component of the local scan point location is given as r . Because there are 18 blades on this research rotor, the angle, β , between each scan point is $(2\pi/18)$.

For this research, each scan point was placed at the same location on each blade. The PolyTec software provides real-time laser vibrometer beam location information through an desktop display. This readout is given in terms of beam location, in horizontal and vertical degrees, from beam home position. For this experimental configuration, 1 inch of beam displacement translates to 1.099 degrees. This is a direct function of the scanning head height from the rotor. This measurement should be checked prior to testing a new rotor or if the laser vibrometer's position is altered.

Table 5.2 gives the global locations for each scan point. The columns x *degree* and y *degree* shown in Table 5.2 are the global angular scan point positions which appear in the software window. Figure 5.19 shows the rotor variables superimposed onto a rotor. For clarity, only a single scan point for a single blade is shown.

Table 5.2: Example Global Scan Point Coordinates

Blade No.	Blade Ctr.	Local r (in)	Local β (rad)	Global x (in)	Global y (in)	x deg.	y deg.
1	0	6	0.000	6.000	0.000	6.594	0.000
2	1	6	0.349	5.638	2.052	6.196	2.255
3	2	6	0.698	4.596	3.857	5.051	4.239
4	3	6	1.047	3.000	5.196	3.297	5.711
5	4	6	1.396	1.042	5.909	1.145	6.494
6	5	6	1.745	-1.042	5.909	-1.145	6.494
7	6	6	2.094	-3.000	5.196	-3.297	5.711
8	7	6	2.443	-4.596	3.857	-5.051	4.239
9	8	6	2.793	-5.638	2.052	-6.196	2.255
10	9	6	3.142	-6.000	0.000	-6.594	0.000
11	10	6	3.491	-5.638	-2.052	-6.196	-2.255
12	11	6	3.840	-4.596	-3.857	-5.051	-4.239
13	12	6	4.189	-3.000	-5.196	-3.297	-5.711
14	13	6	4.538	-1.042	-5.909	-1.145	-6.494
15	14	6	4.887	1.042	-5.909	1.145	-6.494
16	15	6	5.236	3.000	-5.196	3.297	-5.711
17	16	6	5.585	4.596	-3.857	5.051	-4.239
18	17	6	5.934	5.638	-2.052	6.196	-2.255

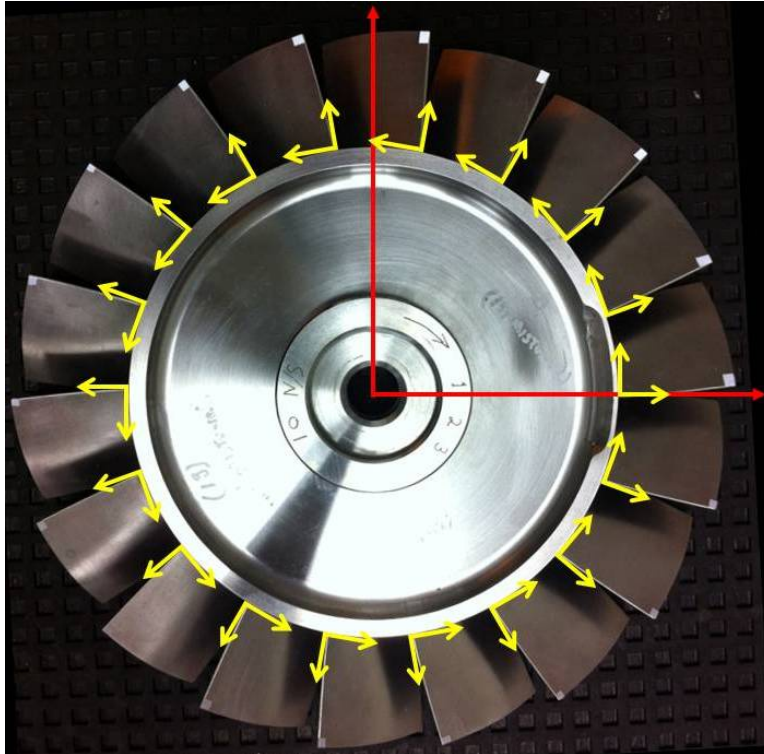


Figure 5.18: Rotor Coordinate System Used for Placing Scan Points

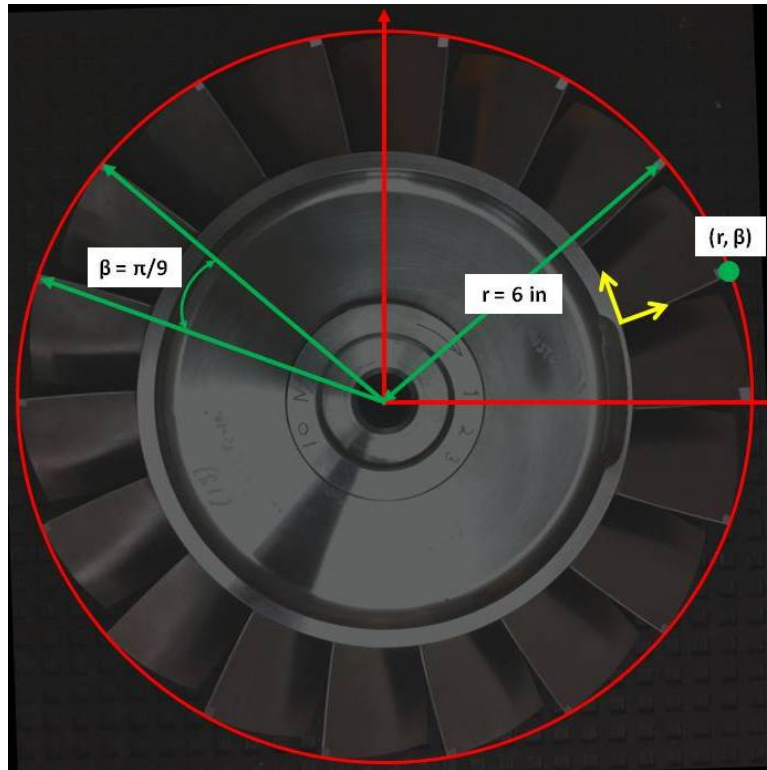


Figure 5.19: Rotor Scan Point Variables

5.4.0.4 *Appropriate Scan Time Identification.*

During excitation, all blades are excited simultaneously. However, only output from a single blade is measured at any one time. For example: the rotor is excited, and the response at blade 1 is measured; the rotor is excited, and the response at blade 2 is measured. Because of its own physical limitations, the laser vibrometer can only measure a single point at a time. This is because the unit only produces a single laser beam for its velocity measurements.

The PolyTec software generates the overall rotor FRF by taking the average of the individual blade FRFs. Since input signals are applied successively in the TWE experiment, it is important to make certain any response from the $(i - 1)^{th}$ input has sufficiently decayed before applying the i^{th} input. Rationale for this stems from the additive nature of the a response with an input. If the rotor response from the $(i - 1)^{th}$ input is present when the i^{th} input is applied, the response for this input will superpose onto what remains from the previous input. This will lead to erroneous and inconsistent forced response results. To alleviate this potential source of error, a system time constant and an associated settling time are defined. Torvik [114] defines a system time constant as:

$$\tau = \frac{2}{\eta\omega_n} \quad (5.3)$$

In this equation, η is the system's loss factor and ω_n is the natural frequency. Torvik gives the loss factor as:

$$\eta = \frac{1}{Q} \quad (5.4)$$

Meirovitch [61] defines quality as:

$$Q = \frac{1}{2\zeta} \quad (5.5)$$

Therefore, the time constant can be expressed in terms of the damping ratio, ζ , and natural frequency, ω_n .

$$\tau = \frac{1}{\zeta\omega_n} \quad (5.6)$$

The time constant is the time required for a system's transient response to decay from some initial value to a steady state value. Rao [60] says the time for a system to settle to 2% of its original value is given as 4 time constants. This will later be used to develop a total time in between successive inputs.

As the rotor is a continuous system, there exists an infinite number of natural frequencies. However, for the frequency band examined in this research (1kHz - 2kHz), and at 0EO⁷, each blade's first bending mode is excited. While not truly representative of EO excitation inside a real engine, this EO level is chosen as an initial, simple experimental parameter because all blade input signals are in phase with one another. Excitation at 0EO implies no up or downstream disturbances in the airflow exciting the rotor - which is not entirely realistic for a real engine.

Within the aforementioned band, there are 18 distinct natural frequencies to examine (Figure 5.20). Here, each frequency corresponds to a different blade's first bending mode. Since each blade contributes to the overall rotor's forced response, it follows that defining the appropriate scan time is ultimately a function of the natural frequency exhibiting the least damping. Since the TWE equipment utilizes a frequency sweep for rotor excitation, Torvik [114] recommends using several different sweep rates to investigate whether or not the sweep rates adversely affect the damping estimates. He explains how too high of a sweep rate can lead to erroneously high values of damping. Having an accurate damping estimate is important because the settling time is a function of damping. A high estimate can lead to low settling times which would exacerbate the problem of superposing the i^{th} input with the response from the $(i - 1)^{th}$ input. Before moving forward, the sweep rate's effect on the damping estimate was explored. Tests using two different sweep rates were performed. The first test swept from 1kHz - 2kHz in 5 seconds and the second test swept the same frequency range in 1 second. Using the half-power method, as detailed in Meirovitch

⁷The 0EO dictates there is no phase shift between input signals. That is to say, the input signal peak reaches each blade at the same time.

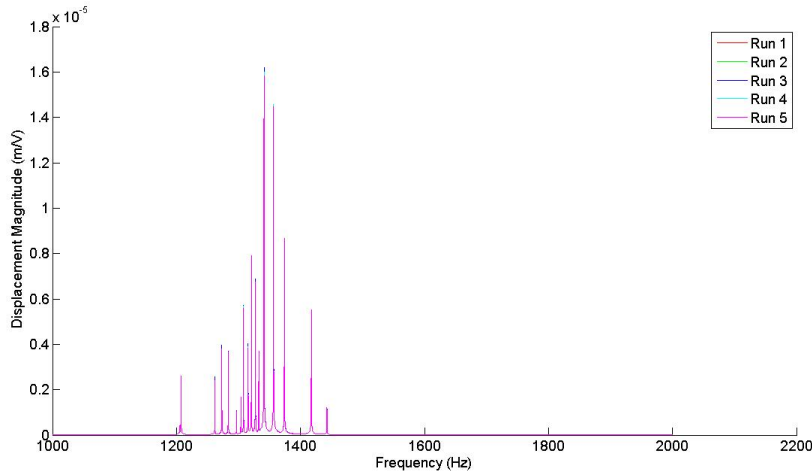


Figure 5.20: Example Rotor Frequency Response Function

[61], the damping for each natural frequency can be readily estimated. Damping ratio estimates for these two different sweep rates are shown in Table 5.3. Here, the effect of different sweep rates on damping estimates is apparent. Given the variance in damping estimates, it behooves the experimenter to compare the resulting settling times for each sweep rate. Table 5.4 compares the settling times for each sweep rate.

The appropriate total data acquisition time is defined in such a way so as to ensure the response from the frequency exhibiting the largest settling time is exceeded. Using the 5 second sweep time, Table 5.4 indicates that 1262.02 Hz exhibits the largest settling time. This time is 14.802 seconds. For a sweep rate of 1 second, the settling time is 11.368 seconds at the 1332.98 Hz natural frequency. This frequency will be used to determine the appropriate time constant, settling time, and ultimately the total acquisition time. As the sweep rate is 1 second, the settling time for the rotor, at the conclusion of the input signal, is maximized. This frequency and its associated damping ratio corresponds to a time constant

of 2.8421 seconds. This time constant is calculated using Equation 5.6.

$$\begin{aligned}\tau = \frac{1}{\zeta\omega_n} &= \frac{1}{(4.201 \times 10^{-5})(1332.98 \frac{\text{cycle}}{\text{sec}})(2\pi) \frac{\text{rad}}{\text{cycle}}} \\ &= 2.8421 \text{ sec}\end{aligned}\tag{5.7}$$

Using the 2% criterion from Rao [60], 4 time constants gives:

$$4T = 4(2.8421 \text{ sec}) = 11.368 \text{ sec}\tag{5.8}$$

Therefore, when using the 1 second input frequency sweep, the total acquisition time must be greater than or equal to 12.368 seconds. Since the input time is 1 second, the remaining 11.368 seconds will allow the rotor response to sufficiently decay.

5.4.0.5 New Experimental Data Acquisition Parameters.

Table 5.5 gives the data acquisition parameters used for the refined TWE process. In the experimental frequency range, the highest natural frequency is approximately 1,443 Hz. Therefore, the bandwidth was adjusted to the next higher increment, as permitted in the PolyTec software package. The number of Fast Fourier Transform (FFT) lines, frequency resolution, and total acquisition time are all directly related. Cox [112] provides an overview of their relationships. Each of these terms were adjusted to ensure a sufficient data acquisition time which allows the rotor's forced response to sufficiently decay as the 2% criteria dictates. Further, the parameters themselves have only limited values within the software's internal constraints. From Section 5.4.0.4, Table 5.4, the 2% criterion says the total acquisition time should be approximately 11.37 seconds. Given existing software constraints, the ideal total data acquisition time will be 16.38 seconds. During this time, the input is applied for 1 second, leaving 15.38 seconds for the response to decay before the next input.

5.4.1 Experimental Results and Discussion.

This section illustrates experimental results obtained using both the existing and newly developed TWE experimental methods. In each case, the rotor is tested in one orientation

on its pedestal. Next the rotor is removed from its pedestal, re-positioned, and tested again. For each rotor orientation, multiple test replicates are performed. Comparisons are made between results using both experimental techniques. It is shown how using a higher degree of experimental precision, repeatable, consistent forced response results are produced.

5.4.2 Initial Experimental Results.

Baseline results were obtained using existing laboratory practices. These practices did not include any rigorous methods to position the rotor nor were there any guidelines for data acquisition parameters. These baseline settings were shown in Table 5.1. Here, the bandwidth is 40kHz. Existing practices suggested setting the bandwidth to a maximum frequency much greater than what would be measured in the TWE experiment. Using these settings, a sufficient acquisition time is not permitted. This is driven primarily by software limitations. These settings indicate the input signal is applied for 5 seconds; the sweep from 1kHz-2kHz takes 5 seconds. Since the laser vibrometer is continuously measuring the rotor response, this total acquisition time only allows for a 5.24 second response decay time before the next input is applied. Based on the discussion in Section 5.4.0.4, this is insufficient.

In addition to performing a traveling wave experiment with the rotor in a single orientation, the rotor was removed from its support, rotated, and replaced back onto its pedestal. This was done to introduce experimental uncertainty. Not only was the rotor boundary condition completely altered, but the entire experimental setup must be reestablished. This includes rotor positioning, laser vibrometer alignment, and input and output location definitions. Since the same rotor is being tested again, it follows that the forced response should be the same. Figure 5.21 shows the average FRFs for both rotor orientations. From this graph, the impact of the experimental disturbances and uncertainty is clearly evident. The bottom graph shows the FRF for the altered rotor position, while top graph is the original position's FRF. Figure 5.22 provides a clearer indication of the

disturbances' impact on the rotor's forced response. Here, the result for each experimental run is also shown. Figure 5.21 illustrates the difference in forced response amplitude between the two rotor orientations. The first orientation is approximately twice that which is seen in the second orientation. This is readily observed by examining the ordinate range in each FRF.

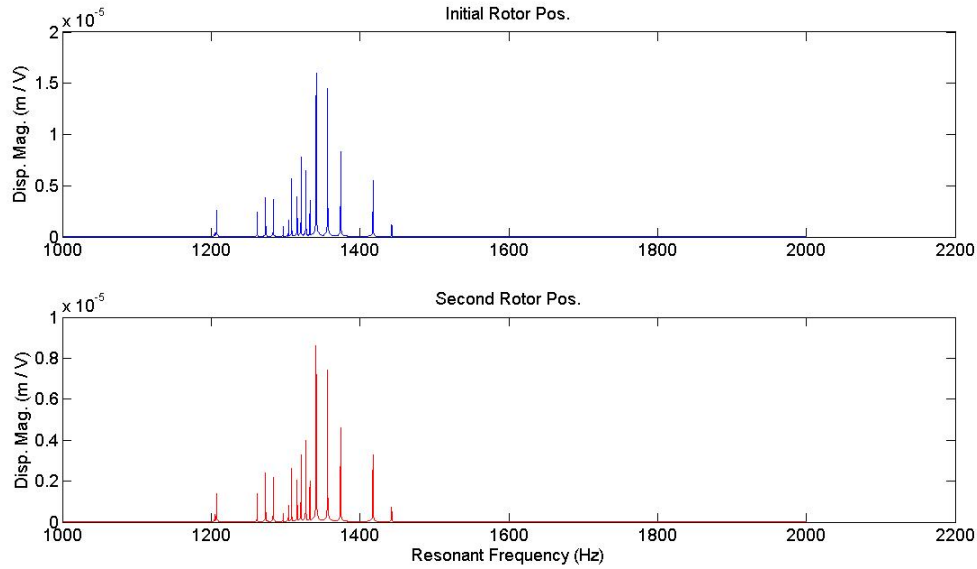


Figure 5.21: FRFs for the Initial and Re-Positioned Rotor

Using a technique shown in Reference [115], a cumulative distribution function (CDF) can be used to express a degree of comparison between two sets of results. This method is known as an area validation metric. Here, the system response quantity of interest is the rotor forced response magnitude. The CDF gives the probability of having a response magnitude less than x . This concept is covered in more detail in Chapter 3, Section 3.15. In this method, there is no relationship established between a natural frequency and its corresponding magnitude. Rather, the relationship is made between an assumed distribution of the individual response magnitudes. The area between the two curves can be thought of as the error between the two quantities. For the two CDFs shown in Figure 5.23,

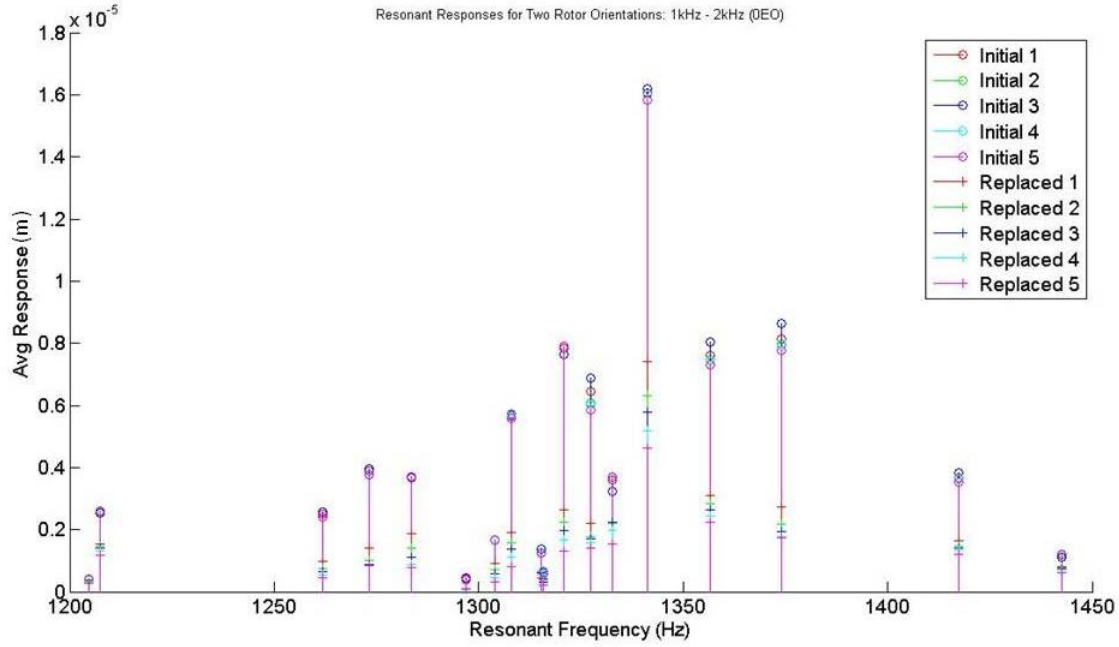


Figure 5.22: Natural Frequency Response Magnitude Stem Plots for the Initial and Re-Positioned Rotor

the average difference between the two curves is approximately 29%. This was determined by fitting a third order polynomial to each data set and then taking the definite, analytic integral of these polynomials' difference. The bounds on the integral are taken as the response approximate response interval, 0 to 1.5. Here, this polynomial approximation is only valid for the given data region.

$$d(S_1, S_2) = \int_0^x |S_1 - S_2| dx \quad (5.9)$$

The polynomial representing the initial data is given as:

$$S_1(x) = 0.3056x^3 - 1.3392x^2 + 2.0083x - 0.0553 \quad (5.10)$$

The polynomial fit to the second set of data, representing the re-positioned rotor, is given as:

$$S_2(x) = 1.8947x^3 - 4.6629x^2 + 3.8451x - 0.0817 \quad (5.11)$$

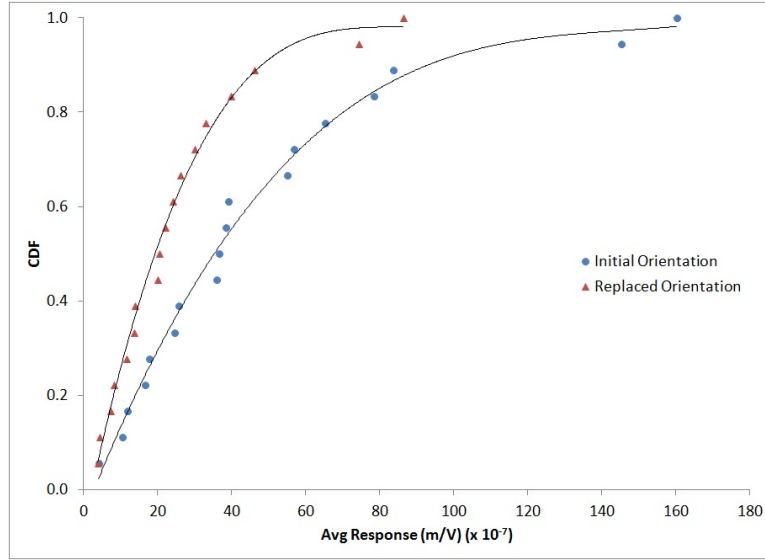


Figure 5.23: CDF vs Response Magnitude for the Initial and Second Rotor Positions

A more traditional method of comparison involves directly comparing response magnitudes at each natural frequency for each respective rotor orientation. Here, the average percent difference (Equation 5.12) between the natural frequency responses is 83%. Examining Figure 5.22 illustrates the large variance associated with these results. For each rotor orientation, 5 test replicates were performed. Within the replicates for the initial rotor orientation, there exists an average response variance across the frequency spectrum of 2.6×10^{-14} (m/V). After the rotor was replaced, the average response variance was 1.3×10^{-13} (m/V). This is a $5 \times$ increase in response variance. While still an extremely small number, this is a significant difference observed simply by adjusting the experimental setup. This variance in forced response would be especially critical if a population of seemingly identical rotors were tested. A wide range of peak responses would not necessarily be indicative of the rotors' true behavior.

$$\% \text{ Diff.} = \left(\frac{\text{high resp.} - \text{low resp.}}{\text{low resp.}} \right) \times 100 \quad (5.12)$$

5.4.3 Refined Experimental Results.

By capitalizing on the techniques outlined in Section 5.4, additional TWE experiments were performed. Analogous to the procedure discussed in Section 5.4.2, the rotor was tested in one orientation, removed from its pedestal, replaced, and tested again. As before, this introduced a tremendous amount of experimental uncertainty into the scenario. Figures 5.24 and 5.25 show the magnitude FRFs for both rotor configurations using the new experimental setup techniques and data acquisition parameters. These figures have superimposed the FRFs for multiple replicates. There is little difference shown between runs. Peak responses at each natural frequency are also shown in Figures 5.26 and 5.27. One reason for the relatively constant response magnitudes is a direct consequence of allowing the response from the $(n - 1)^{th}$ to decay before applying the n^{th} input.

Figures 5.26 and 5.27 provide the individual response magnitudes at each natural frequency. The average difference between the peak responses at each natural frequency is 8.47%. Improving the experimental setup methodology and using a sufficient data acquisition time, an approximate 880% improvement is realized compared to the initial results from Section 5.4.2. The average variance across the experimental frequency spectrum for this first rotor orientation's test replicates (Figure 5.26) is $2.03 \times 10^{-14}(\text{m/V})$. The experimental results for the rotor in the second position showed a forced response variation between its test replicates of $2.63 \times 10^{-14}(\text{m/V})$. Compared to the results obtained in Section 5.4.2, these response variances are nearly constant - thus indicating little difference in experimental results. This demonstrates using carefully defined experimental procedures gives repeatable results.

Figure 5.28 shows the CDF vs. Average Response Magnitude for the two rotor orientations. Here, the difference between each curve is approximately 2.2%. Compared to Figure 5.23, the new CDF vs. Response Magnitude curves show very little difference. Results for Figure 5.28 were found using the same technique for Figure 5.23: a third

order polynomial was analytically integrated across the approximate response interval. The polynomial approximations are, again, only valid for the data range. The equations representing the CDFs for the first and second rotor positions, respectively, are given as:

$$S_1(x) = 0.0000005x^3 - 0.0002x^2 + 0.0236x - 0.0522 \quad (5.13)$$

$$S_2(x) = 0.0000005x^3 - 0.0002x^2 + 0.0241x - 0.0707 \quad (5.14)$$

5.4.4 Section Conclusion.

In this section, experimental results for traveling wave excitation were shown. First, results were obtained using general laboratory practices, which did not dictate any methodology for experimental setup or data acquisition. The initial results were produced from testing a rotor in two different orientations within the experiment. Between these two sets of experimental replicates, the average difference in response magnitude was 83%. For the initial rotor orientation, the average response variance between test replicates was 2.6×10^{-14} (m/V). Results from the rotor's second orientation showed a $5 \times$ increase in response variance. The existing experimental methodology gives little confidence into the process of experimentally evaluating a population of rotors.

New experimental procedures were developed which focused on rotor alignment and setup, consistent scan point identification, and data acquisition time. Using these procedures, consistent results were obtained for a rotor's forced response. These new procedures demonstrated an approximate 880% improvement in test replicate consistency, over the course of multiple rotor orientations. The average difference between response magnitude was 8.47%. The response variance between test replicates for the first rotor orientation was 2.03×10^{-14} (m/V) and 2.63×10^{-14} (m/V) for the second orientation. The significant reduction in response difference between each orientation's the test replicates and near constant response variance demonstrates the effectiveness of the new experimental methodology.

5.5 Summary of Experimental Technique

The purpose of this section is to summarize the previous section for the proper experimental technique when performing traveling wave excitation. This summary will reference the previous section, as necessary, for the proper techniques. Appendix F provides an additional list of equipment necessary to configure the experiment.

Experimental Setup. For the proper experimental setup techniques, reference Section 5.4. This will ensure both the input locations and measurement locations are placed in their optimal locations.

Frequency Range of Interest. In performing the traveling wave test, the researcher does not merely place the rotor into the test fixture and begin sweeping through frequencies. Rather, prior to the test, the modes of interest and their corresponding natural frequencies must be known. Since the rotors undergoing testing are not merely random pieces of metal, their modal information is typically known beforehand. This information usually comes from the manufacturer. Such information may include specific EO excitation levels and critical modes and respective frequencies of interest. Once this information is known, these will become input parameters for the experiment.

To avoid signal corruption due to windowing⁸, the range of input frequencies is larger than the range of frequencies containing the modes of interest. When mapping information from the time to the frequency domains, there is an assumption of signal periodicity. A window function operates on the signal, typically forcing it to zero at the beginning and end of its duration. It ensures a periodic signal for mapping into the frequency domain. However, if there is important signal information at the extreme ends, the window function would zero out this information. Together with a larger excitation range, the range of frequencies on which the system performs its measurements is also kept larger than the frequency range of interest. This also ensures any negative effects of windowing is avoided.

⁸Windowing is also discussed in Paragraph 5.5

For example, with the Purdue Transonic Research Compressor, the first bending mode in the blades is between 1200 Hz and 1430 Hz. The frequency range of interest is indicated in Figure 5.29. The extreme ends of the data acquisition range is kept away from this range.

Total Acquisition Time. Once the experiment is set up and the desired frequency range is known, the next step is to define the total acquisition time. This is the amount of time the system will actually record information before beginning the next input sequence. This is a function of the system damping in the frequency range of interest. Note, the total acquisition time includes the input sweep time as well. The system begins to record the rotor response as soon as the input is applied. The input time should be no smaller than 1 second for each 1kHz of input frequency.

Discussed in Section 5.4, an initial traveling wave test is required for this step. Because the exact acquisition time is not known at this point, the researcher is encouraged to use as many FFT lines as possible, as the system will increase or decrease the total acquisition time accordingly, depending on the number of lines selected. Performing this initial, exaggerated increased time test performs several critical functions:

1. This initial, exceedingly long scan ensures the response from the $(n-1)^{th}$ input has sufficiently decayed before the n^{th} input is applied.
2. It identifies the highest natural frequency for the mode family of interest
3. It allows for a damping estimate which is used to define the system time constant

Section 5.4, Subsection 5.4.0.4 shows the half power method used as the method by which the damping is estimated. From this estimate, a time constant is defined. Rao [60] says the time for a system to settle to 2% of its original value is given as 4 time constants. The researcher will use the worst case, or largest, time constant, to define the time satisfying the 2% criterion.

In the PolyTec user interface, the number of FFT lines is then adjusted until the total acquisition time meets or exceeds the time prescribed using the 2% criterion. This ensures there is no overlap between the response from the $(n-1)^{th}$ input and n^{th} input. Furthermore, the maximum resolvable frequency (denoted as *bandwidth* in the PolyTec system) should be reduced to ensure only the frequencies of interest are captured. From Figure 5.29, the highest natural frequency of this mode is readily identified. If the maximum resolvable frequency is set just beyond that of the highest natural frequency of interest, the user is afforded more flexibility in manipulating the data acquisition parameters. This is illustrated in Figure 5.30. In particular, this affects the frequency resolution, which is discussed next.

Frequency Resolution. Recall from Chapter 3, Section 3.10, the relationship between frequency resolution, sampling frequency, total acquisition time, and the FFT block size.

Given the maximum resolvable frequency, the PolyTec system automatically selects the sample rate, f_s . The system defines the sample rate as approximately 2.5 times the maximum resolvable frequency. This alleviates any aliasing effects realized when sampling a signal. Because the maximum resolvable frequency has now been reduced to just above the highest frequency of interest, the number of FFT lines can be increased to improve the frequency resolution. Graphically, this places the FFT, or spectral, lines closer together. Physically, this means smaller frequency components can be captured to recreate the signal. Comparing Figures 5.29 and 5.30, note the difference in the start and stop (max resolvable) frequencies. Assume, for instance, the researcher uses 6400 FFT lines. In Figure 5.29, this equates to a frequency resolution of 0.15625 Hz. The 1000 Hz spread of frequencies is divided into 6400 frequency “bins”. In contrast, reducing the frequency window to 300 Hz, as shown in Figure 5.30, gives a frequency resolution of 0.046875 Hz. While the desired frequency range is still captured in each case, reducing the range of frequencies can significantly improve frequency resolution.

5.6 Mistuning Amplification Factor

In Section 5.4, a process was developed which provides consistent, stable experimental responses. Even with inconsistent forced response magnitudes, as shown in Figure 5.21, the rotor's natural frequencies still coincide. Since the rotor response magnitudes produced within the TWE experiment are much much lower than what would be realized during operation, performing component life expectancy calculations on the raw TWE data is not trivial. However, the consistent data does provide an important piece of information which is as unique to the individual rotor as its own mistuning pattern⁹. With the consistent TWE forced responses, a rotor's Mistuning Amplification Factor (MAF) can be defined. This factor is defined as the maximum blade response divided by the average blade response for a given mode (Equation 5.15). A single rotor was used for this illustration. Assuming a blade's MAF remains constant for a given mode, a maximum mistuned response can be estimated if the external forcing function is known.

$$\text{MAF} = \frac{\text{max blade response}}{\text{average blade response}} \quad (5.15)$$

Recall Figure 5.21. Here, The same traveling wave experiment produces very different response magnitudes, despite indicating the same natural frequencies. Table 5.6 gives the MAF for the experimental rotor upon exciting the blades' first bending mode. Examining this table shows striking differences and inconsistencies in the resulting MAF.

⁹pattern of natural frequencies for the frequency range of interest

Table 5.3: Damping Ratio Estimates for Two Different Sweep Rates

Frequency (Hz)	5 Second Sweep Time Damping Estimate	1 Second Sweep Time Damping Estimate	Percent Difference
1204.91	0.00014692	0.00014773	0.553
1207.51	0.00013170	0.00013996	6.273
1262.02	0.00003408	0.00005626	65.085
1273.32	0.00004241	0.00006754	59.243
1283.6	0.00006155	0.00006856	11.380
1296.94	0.00006709	0.00006168	8.764
1304.07	0.00007362	0.00005751	28.016
1308.23	0.00005348	0.00005351	0.052
1315.46	0.00005930	0.00005929	0.013
1315.98	0.00008512	0.00006079	40.023
1321.01	0.00005981	0.00005905	1.299
1327.46	0.00006705	0.00008512	26.963
1332.98	0.00005027	0.00004201	19.663
1341.36	0.00012004	0.00014388	19.860
1356.7	0.00009288	0.00010393	11.890
1374.21	0.00006987	0.00007932	13.522
1417.66	0.00011076	0.00009593	15.456
1442.95	0.00009288	0.00009702	4.460

Table 5.4: Sweep Rate Settling Time Comparison

Frequency (Hz)	5 Second Sweep 2% Crit. Settling Time	1 Second Sweep 2% Crit. Settling Time	Percent Diff.
1204.91	3.596	3.577	0.553
1207.51	4.003	3.767	6.273
1262.02	14.802	8.966	65.085
1273.32	11.788	7.403	59.243
1283.6	8.058	7.234	11.380
1296.94	7.317	7.958	8.764
1304.07	6.631	8.488	28.016
1308.23	9.099	9.095	0.052
1315.46	8.161	8.162	0.013
1315.98	5.683	7.958	40.023
1321.01	8.057	8.162	1.299
1327.46	7.153	5.634	26.963
1332.98	9.500	11.368	19.663
1341.36	3.954	3.299	19.860
1356.7	5.052	4.515	11.890
1374.21	6.630	5.841	13.522
1417.66	4.054	4.681	15.456
1442.95	4.750	4.547	4.460

Table 5.5: Modified Acquisition Parameters

Bandwidth (kHz)	1.5625
Total FFT Lines	25,600
Sampling Frequency (kHz)	4
Frequency Resolution (mHz)	61.351
Total Acquisition Time (sec)	16.38
Total Input Time (sec)	1

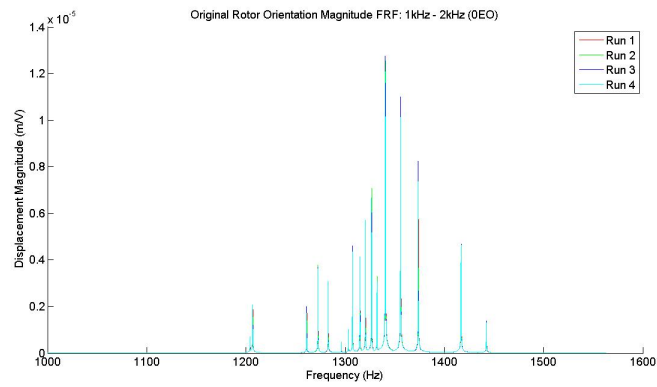


Figure 5.24: First Rotor Position Magnitude FRF Using the New Techniques

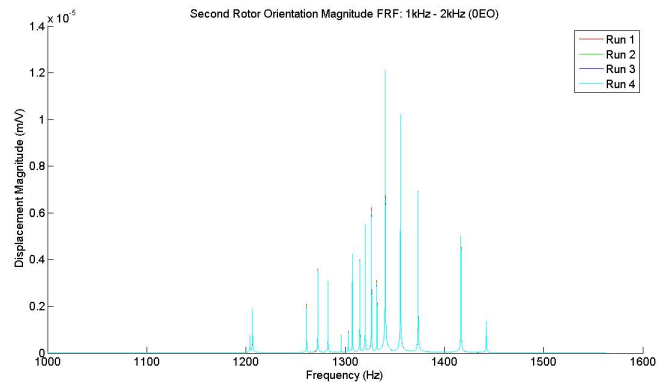


Figure 5.25: Second Rotor Position Magnitude FRF Using the New Techniques

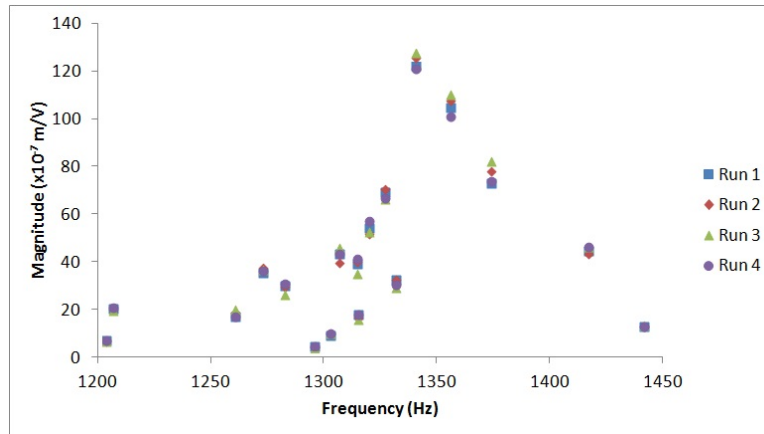


Figure 5.26: First Rotor Position Natural Frequency Responses Using the New Techniques

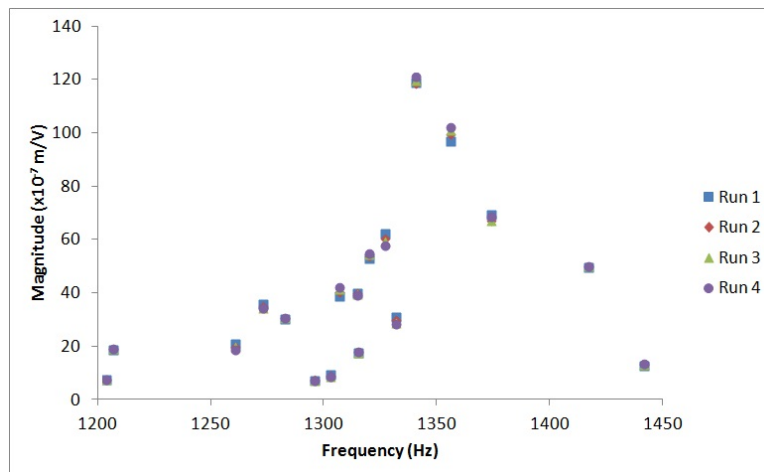


Figure 5.27: Second Rotor Position Natural Frequency Responses Using the New Techniques

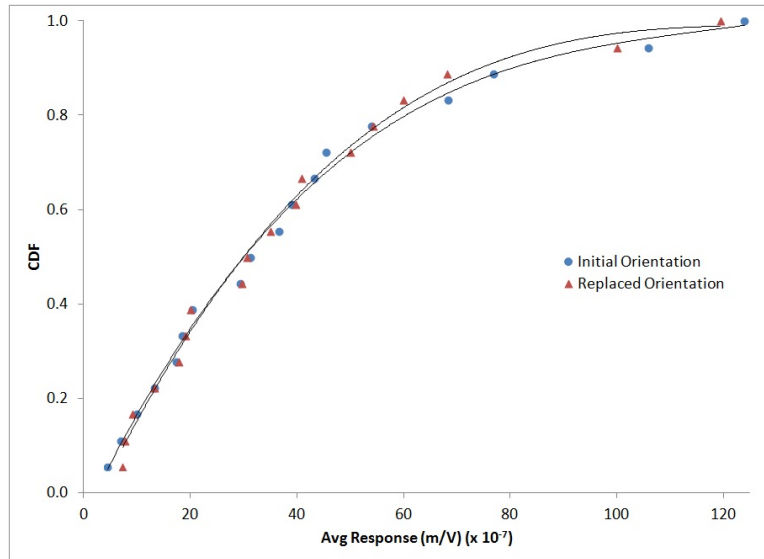


Figure 5.28: CDF vs Response Magnitude for the Initial and Second Rotor Positions Using the New Techniques

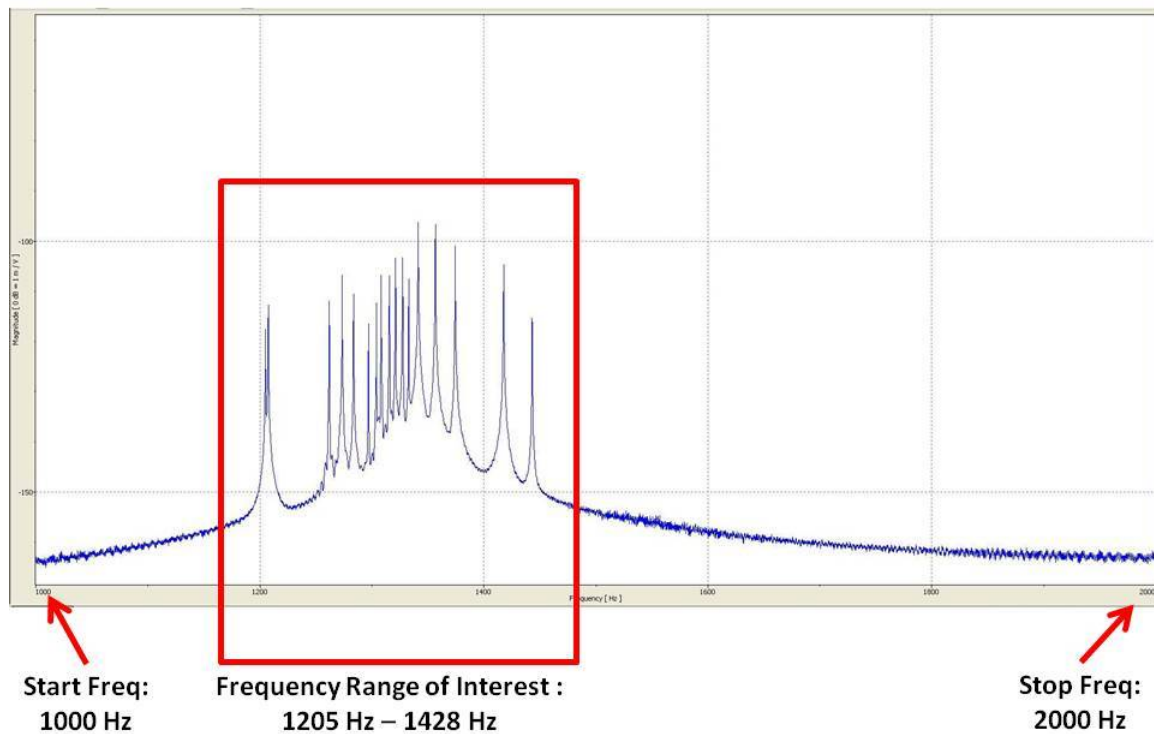


Figure 5.29: Indicating the Frequency Range of Interest

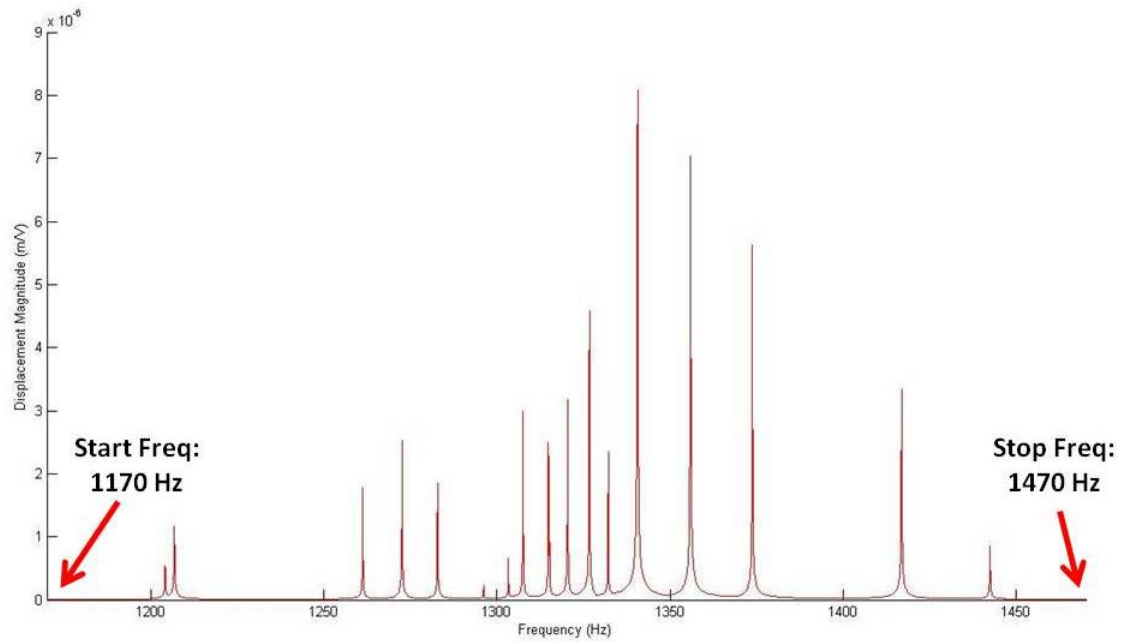


Figure 5.30: Indicating the Frequency Range of Interest

Table 5.6: Mistuning Amplification Factor After Initial Experimental Techniques

Orientation 1			
Run	Max Response ($\times 10^{-6}(\text{m/V})$)	Avg. Response ($\times 10^{-8}(\text{m/V})$)	MAF
1	16.07	7.289	220.5
2	16.01	7.298	219.4
3	16.18	7.289	222.0
4	15.98	7.297	219.0
Orientation 2			
1	10.93	8.048	135.8
2	10.89	8.047	135.3
3	10.80	8.051	134.1
4	10.66	8.045	132.5

After performing the improved experimental procedures discussed in the previous section, the rotor's response magnitudes are nearly identical (Figures 5.24 and 5.25). This produces a near constant rotor MAF for the blades' mode 1 behavior. Table 5.7 shows MAF for the rotor is approximately 135. For the blades' first bending mode, the rotor's inherent mistuning will amplify the rotor response 135 times over what the average rotor response.

Comparing Tables 5.6 and 5.7 reinforces the need to ensure rotor forced responses are consistent. Inconsistent responses, and hence inconsistent MAFs, can ultimately lead to erroneous response estimates for increased magnitude forcing functions.

Table 5.7: Mistuning Amplification Factor After Refined Experimental Techniques

Orientation 1			
Run	Max Response ($\times 10^{-6}(\text{m/V})$)	Avg. Response ($\times 10^{-8}(\text{m/V})$)	MAF
1	8.076	5.967	135.3
2	8.107	5.958	136.1
3	8.186	5.958	136.1
4	7.925	5.955	137.5
Orientation 2			
1	7.893	6.130	128.8
2	8.380	6.125	136.8
3	8.450	6.130	137.8
4	8.216	6.133	134.0

5.7 The Experimental Free Boundary Condition

The boundary condition verification in this section will be performed through a direct eigenvalue comparison between the experimental and numerical results. Close agreement between these two quantities indicates the finite element model can be used to predict the modal behavior of a geometrically mistuned rotor. Here, the eigenvalues are the measured natural frequencies.

Applying an input frequency sweep of 1kHz - 2kHz, at 0EO, induces the rotor's first bending mode. The experiment was simulated using the finite element analysis program, ANSYS. The rotor model was developed using the techniques discussed in Chapter 3, Section 3.7. This same frequency range also induced the first bending mode for the system of blades.

Table 5.8 directly compares the ANSYS and experimental eigenvalues. The eigenvalues populating the ANSYS column in Table 5.8 were pulled directly from the ANSYS generated FRF. A percent difference is also provided as a means to directly compare the numerical values. From Table 5.8, on average the two sets of eigenvalues are 0.37% different. Similar results are shown for the remaining EO excitation levels. Table 5.9 shows the comparisons for some additional EO excitation levels. Table 5.10 compares eigenvalues for higher order frequencies inducing torsional and chordwise bending modes. Because the differences in the eigenvalues are so small, it can be assumed the experimental setup does indeed provide a free boundary condition.

Table 5.8: 1kHz-2kHz, 0EO ANSYS and TWE Eigenvalue Comparison

Eigenvalue (Hz) (ANSYS)	Eigenvalue (Hz) (TWE)	Percent Difference
1211	1204	0.58
1217	1207	0.83
1260	1261	0.08
1276	1273	0.24
1284	1283	0.08
1296	1296	0.00
1307	1303	0.31
1320	1307	0.99
1322	1315	0.53
1326	1315.15	0.83
1328	1320	0.61
1330	1327	0.23
1333	1332	0.08
1334	1341	0.52
1354	1356	0.15
1371	1374	0.22
1416	1417	0.07
1438	1442	0.28

Table 5.9: 1kHz-2kHz, Additional EO Level ANSYS and TWE Eigenvalue Comparison

EO	Percent Difference
1	0.26
2	0.22
3	0.15
4	0.27
5	0.23
6	0.38

Table 5.10: 7.5kHz-8.5kHz, Additional 0EO Level ANSYS and TWE Eigenvalue Comparison

TWE Freq. (Hz)	ANSYS Freq. (Hz)	% Diff.	TWE Freq. (Hz)	ANSYS Freq. (Hz)	% Diff.
7547.66	7717	2.24	8055.27	8154	1.23
7620.12	7782	2.12	8073.32	8165	1.14
7667.87	7818	1.96	8092.29	8182	1.11
7698.34	7828	1.68	8098.12	8218	1.48
7728.03	7892	2.12	8110.92	8224	1.39
7751.86	7913	2.08	8140.43	8252	1.37
7793.95	7938	1.85	8169.34	8266	1.18
7810.45	7957	1.88	8176.76	8275	1.20
7843.75	7985	1.80	8213.89	8286	0.88
7864.94	7992	1.62	8240.1	8295	0.67
7873.34	8039	2.10	8261.04	8318	0.69
7931.74	8061	1.63	8288.09	8333	0.54
7958.11	8068	1.38	8307.62	8359	0.62
7973.24	8084	1.39	8391.04	8399	0.09
7984.18	8092	1.35	8425.96	8429	0.04
7995.31	8107	1.40	8447.56	8442	0.07
8001.95	8114	1.40	8456.64	8462	0.06
8017.48	8136	1.48	8488.1	8482	0.07

5.8 Using the Finite Element Model

5.8.1 The ANSYS Input File.

Because multiple finite element simulations would be performed and evaluated, a general MatLab based code was developed to automate the process of generating the ANSYS input files. An example MatLab script is given in Appendix E. Interfacing with ANSYS via the input file permitted minimal involvement from the user. The rotor model was simply opened and the program was directed where to read the input information. The input file prescribes the following elastic properties: Poisson's ratio, density, and elastic modulus.

Poisson's ratio, by definition, is unitless. Since the model was developed using English units, in this system, the density is defined within ANSYS as $\frac{slinch}{in^3}$. Here, a *slinch* is defined as a unit of mass equal to 12 slugs, or $1 \frac{lb_f sec^2}{in}$. The elastic modulus, or Young's modulus, is given in units of $\frac{lb_f}{in^2}$. The system damping ratio (ζ) is also defined. In the current file iteration, both the damping ratio and elastic modulus are constant over the entire model. The damping ratio used in this research was the value estimated from the experimental results. The damping ratio was estimated using the half-power method, as discussed in Reference [61].

The file sets the maximum number of mode shapes the finite element solver shall retain. In this research, this was set to 108. This allows for 6 different modes to be captured for each blade. On this same note, the file defines the frequency range and desired frequency resolution for the harmonic analysis. The file also instructs ANSYS at which nodes the input force is applied and nodes for the output. For simulating the actual traveling wave experiment, the true input and output locations can be defined. Manipulating the MatLab file (shown in Appendix E) is summarized in the following steps:

1. Define the input and output nodes corresponding to the respective locations on the physical rotor

2. Define the frequency range of interest
3. Define the desired EO excitation level
4. Define the damping ratio for the frequency of interest

5.8.2 Finite Element Model Exploration and Validation.

As a tuned rotor only exists within the theoretical confines of a finite element model, its FRF offers up a useful comparison to its theoretical mistuned counterpart. Since the model here only accounts for geometric mistuning, the material properties were constant throughout the models during each analysis.

For the 1kHz - 2kHz frequency range depicted in Figure 5.31, the first bending mode for the blades is approximately 1320 Hz. This FRF was generated in ANSYS by performing a harmonic analysis on a tuned rotor. This model was built from replicating a nominal rotor sector around a central axis. The damping ratio used in the model was estimated from the experimental results of the same frequency band. For an interesting comparison, the tuned

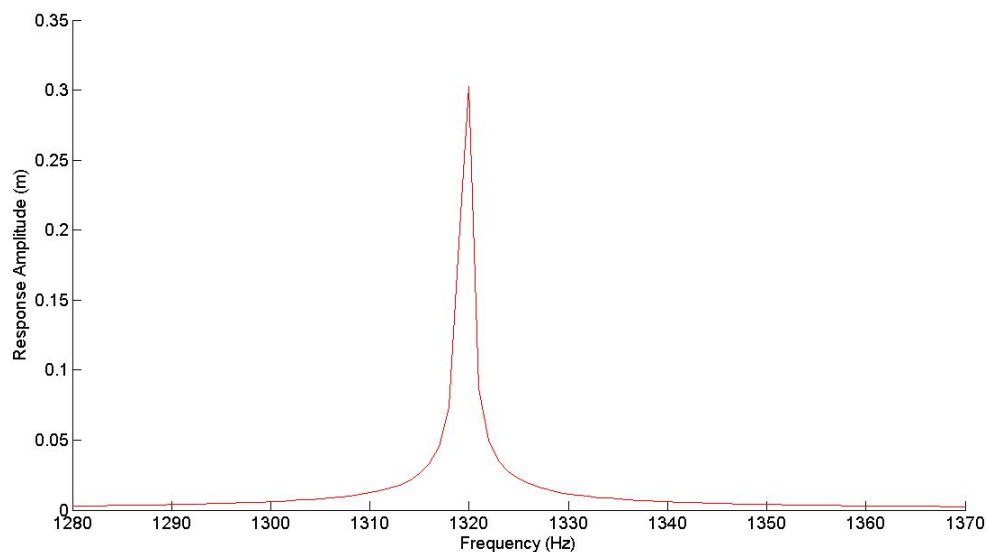


Figure 5.31: Tuned FRF for the Purdue Transonic Research Compressor

Purdue rotor FRF is superimposed onto the ANSYS generated FRF for the actual rotor (Figure 5.32). This frequency range excites the blades' first bending mode.

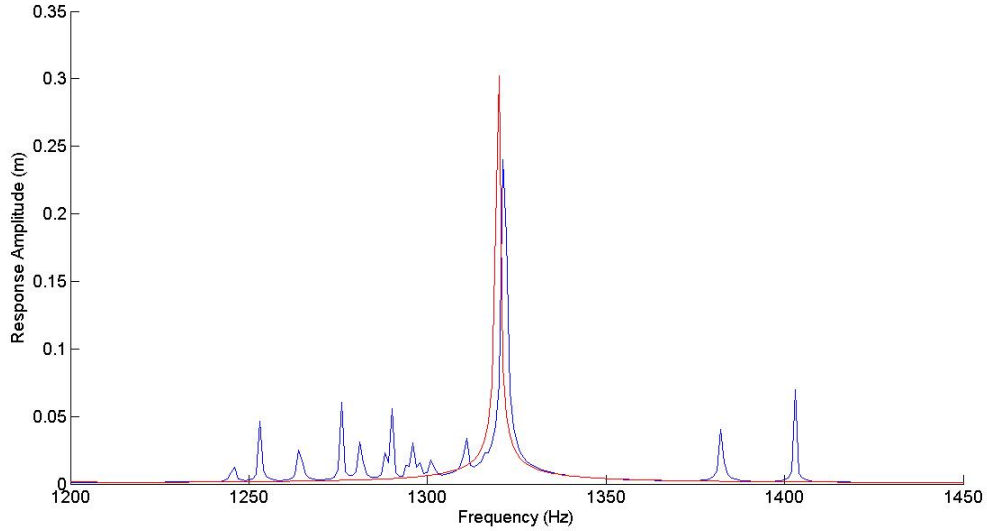


Figure 5.32: Comparison Between the Tuned and Mistuned ANSYS FRFs

Only a single finite element model was developed in the course of this research. Therefore, only experimental results from that specific rotor are utilized here to validate the model. The response quantities compared here are the system eigenvalues. Tables 5.8 and 5.10 provides the values used herein. While the relative percent difference between the two sets of eigenvalues are extremely close, this process here will provide statistical validity. The technique shown in Chapter 3, Section 3.12, Subsection 3.12.2 will be used. For both the model and experiment, there are 54 data points, so this comparative technique is valid. Recall the test statistic given in Equation 3.118.

$$z = \frac{\bar{X} - \bar{Y} - \Delta_o}{\sqrt{\frac{\sigma_X^2}{n_X} + \frac{\sigma_Y^2}{n_Y}}} \quad (5.16)$$

Here, let X represent data from the ANSYS finite element model and Y from the experiment.

Table 5.11: ANSYS and Experimental Eigenvalue Statistics

	ANSYS (X)	Experiment (Y)
Count	48	48
Mean	5866.4	5799.5
Std. Dev.	3250.9	3207.4

The null hypothesis here is that the two groups of samples come from populations whose mean is the same. Using a confidence level of 99%, the significance level, α , is 0.01. The most extreme case exists when forcing the difference between the two samples to be 0. As such, using Equation 3.118 says the test statistic is approximately 0.108. It's corresponding P-Value is found using published tables or Equation 3.119.

$$z = \frac{\bar{X} - \bar{Y} - \Delta_o}{\sqrt{\frac{\sigma_X^2}{n_X} + \frac{\sigma_Y^2}{n_Y}}} \quad (5.17)$$

$$z = \frac{5866.4 - 5799.5 - 0}{\sqrt{\frac{3250.9^2}{54} + \frac{3207.4^2}{54}}} \quad (5.18)$$

$$z = 0.1076 \quad (5.19)$$

$$P(z) = \int_{-\inf}^z \left(\frac{1}{\sqrt{2\pi}} e^{-\frac{u^2}{2}} \right) du \quad (5.20)$$

$$P(z) = \int_{-\inf}^{0.1076} \left(\frac{1}{\sqrt{2\pi}} e^{-\frac{u^2}{2}} \right) du \quad (5.21)$$

$$P(z) = .543 \quad (5.22)$$

The values reveal that the P-Value is greater than α . This implies the null hypothesis is not rejected. Physically, this is interpreted as one saying, with 99% confidence, the eigenvalues the ANSYS model predicts come from the same population as the eigenvalues measured when performing the traveling wave experiment. Stated in another way, the results conclude there does not exist sufficient evidence between the two groups of eigenvalues. For predicting a rotor's natural frequencies, the finite element model and its unique structured light development technique offer a valid alternative to traveling wave testing.

Since the rotor model is now considered a valid representation of the experimental rotor, a direct analysis is made between the tuned and experimental rotor eigenvalues (natural frequencies). This can provide a numerical definition to the level of mistuning present within the rotor. Recall the density with ANSYS is in terms of (slinch/in³), where a *slinch* is defined as a unit of mass equal to 12 slugs, or $1 \frac{lb_f sec^2}{in}$. As compared to the tuned representation, the ANSYS model shows a spread of 211 Hz encompassing the first modes' natural frequencies, while the experimental rotor shows 238 Hz spread across the first bending mode.

Table 5.12: ANSYS Finite Element Model Rotor Model Mechanical Properties

Elastic Modulus (Msi)	28.427
Density (slinch/in ³)	0.00072981
ν_{xy}	0.27

Table 5.13: Tuned and Mistuned Rotor: Blade First Bending Mode Comparison

Tuned	ANSYS FEM	TWE
1st Bend (Hz)	1st Bend (Hz)	1st Bend (Hz)
1320	1211	1204
	1217	1207
	1260	1261
	1276	1273
	1284	1283
	1296	1296
	1307	1303
	1320	1307
	1322	1315
	1326	1315.15
	1328	1320
	1330	1327
	1333	1332
	1334	1341
	1354	1356
	1371	1374
	1416	1417
	1438	1442

5.9 ANOVA Study and Results

An ANOVA was performed using blades on the Purdue Transonic Research Compressor to identify any effects of input-output location dependence in the experiment.

The ANOVA model for this study is discussed in Chapter 3, Section 3.13, Subsection 3.13.3. In this study, the signal input location, response measurement response output location, and EO excitation levels were the experimental variables under consideration. These three factors were chosen since they are under the greatest amount of control when performing the traveling wave experiment.

Section 5.4, Subsection 5.4.0.3, shows the method by which the response output locations were identified. Input locations were assigned by measuring distances from the respective blade edges. Figure 5.33 shows the actuator stand. This was used in lieu of utilizing the entire actuator ring. Because two blades were tested simultaneously, 8 random blades were selected from each of the three rotors. From Chapter 3, Section 3.14, 48 total blades are needed for the test. Selecting 8 blades from each rotor gives 24 samples. The remaining 24 blades were chosen from randomly selecting adjacent blades, giving the 48 blades required to draw any significant conclusions. Two adjacent blades were tested because the EO excitation level was not zero. The electromagnetic actuator is 0.25 inch in diameter. Using this dimension as a reference, three input locations on each blade were defined. The following list, and Figure 5.34, indicate the input and output regions.

1. The actuator edge extends 0.150 inch out from edges A and B on the blade. This places the actuator's conductive element at the blade tip (at the intersection of edges A and B).
2. The actuator edge is flush with blade edges A and B. This places the conductive element 0.125 inch away from edges A and B.
3. The actuator edge is 0.150 inch from edges A and B. The actuator's conductive element is positioned inboard 0.275 inch.

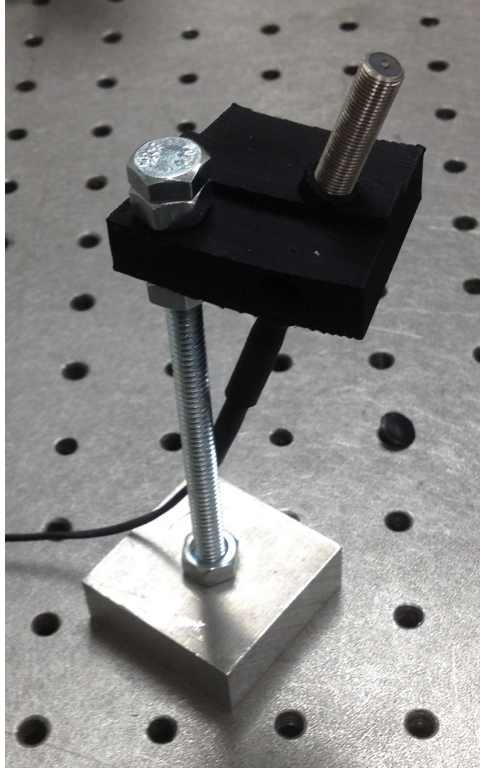


Figure 5.33: Single Actuator Stand

Since two adjacent blades are used for each test, 9 combinations of input locations are available. The blade notation for these input locations are given as follows: (Blade 1, Blade 2).

Two EO excitation levels are used: 1EO and 2EO. On each blade, 5 separate output locations were established. These global locations are given in Table 5.14. Here, Scan Points 1-5 are defined on Blade 1, and Scan Points 6-10 are defined on Blade 2. Three replicates for each factor combination were performed. The excitation system was set to excite the blades and record a response three times in succession. The system then provided the average of these responses. Appendix G gives the details behind performing the series of experiments.

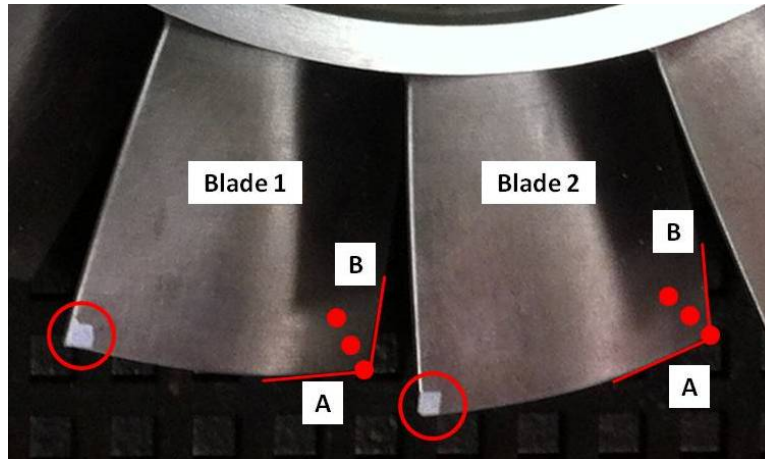


Figure 5.34: Blade Input and Output Regions for the ANOVA

Table 5.14: Global Scan Points Used for Input-Output ANOVA Test: Increased EO Level

Scan Pt.	Horz. Deg.	Vert. Deg.	Global X (in.)	Global Y (in.)
1	-7.154	0.362	-6.002	0.304
2	-7.153	0.270	-6.000	0.227
3	-7.073	0.267	-5.934	0.224
4	-7.067	0.356	-5.929	0.299
5	-7.111	0.314	-5.966	0.263
6	-6.596	2.175	-5.534	1.825
7	-6.622	2.629	-5.555	2.206
8	-6.534	2.616	-5.482	2.195
9	-6.513	2.692	-5.464	2.258
10	-6.566	2.665	-5.508	2.236

For each pair of blades, the data were recorded in a table as shown in Table 5.15. This data table was used for each input location combination. After recording results for the nine

input combinations, the EO level was changed to “2” and the tests were repeated. After completing the full test on a pair of adjacent blades, the rotor was re-oriented, and the scan points were redefined using the locations from Table 5.14. For the research compressor, 17 natural frequencies were consistently observed during each test.

Table 5.15: Example Data Collection Table

1EO			
	Resonant Frequencies		
Scan Point	Frequency Nos. 1 - x		
1	Max Response at Freq. 1	...	Max Response at Freq. x
2	Max Response at Freq. 1	...	Max Response at Freq. x
3	Max Response at Freq. 1	...	Max Response at Freq. x
4	Max Response at Freq. 1	...	Max Response at Freq. x
5	Max Response at Freq. 1	...	Max Response at Freq. x
6	Max Response at Freq. 1	...	Max Response at Freq. x
⋮	⋮	⋮	⋮
9	Max Response at Freq. 1	...	Max Response at Freq. x
10	Max Response at Freq. 1	...	Max Response at Freq. x

Recall for each input and output combination, there exists a unique FRF. Each FRF was observed and the peak response for each natural frequency was recorded. The ANOVA was performed on the recorded responses at each observed natural frequency. The results for this ANOVA are summarized in Tables 5.16, 5.17, and 5.18. An Excel add-on program, DOE Pro, was used to handle the large amount of data and required calculations. Here, only the main effects are shown. All two and three factor interactions exhibited P-Values approaching 1.000; for brevity, this information is not included in the tables. The

results here show the input location is the most significant factor influencing the response magnitude. Three separate tables are shown, each corresponding to a unique rotor.

Table 5.16: ANOVA 3: Increased EO Excitation - Main Effects - Rotor A

Response (Hz)	EO Level P-Val.	Input Location P-Val	Output Locations P-Value
1205	0.206	3.61×10^{-5}	0.998
1262	0.123	8.71×10^{-6}	0.905
1273	0.194	2.56×10^{-5}	0.999
1284	0.401	6.94×10^{-9}	0.999
1297	0.103	1.64×10^{-6}	0.999
1304	0.160	2.89×10^{-4}	0.999
1308	0.239	3.38×10^{-10}	0.999
1316	0.166	3.51×10^{-10}	0.990
1321	0.962	2.26×10^{-8}	0.994
1327	0.335	7.08×10^{-4}	0.999
1333	0.294	1.58×10^{-6}	0.999
1341	0.656	2.41×10^{-6}	0.999
1357	0.362	5.42×10^{-18}	0.891
1375	0.137	1.02×10^{-4}	0.988
1418	0.337	8.58×10^{-8}	0.998
1443	0.179	9.61×10^{-5}	0.987

Table 5.17: ANOVA 3: Increased EO Excitation - Main Effects - Rotor B

Response (Hz)	EO Level P-Val.	Input Location P-Val	Output Locations P-Value
1202	0.280	4.52×10^{-5}	0.981
1269	0.120	8.56×10^{-5}	0.995
1273	0.101	1.56×10^{-5}	0.999
1285	0.301	6.20×10^{-5}	0.999
1297	0.111	1.74×10^{-6}	0.999
1303	0.156	3.00×10^{-3}	0.999
1310	0.250	3.40×10^{-11}	0.999
1316	0.150	2.98×10^{-8}	0.971
1322	0.872	2.25×10^{-7}	0.994
1325	0.321	6.00×10^{-3}	0.999
1330	0.280	2.02×10^{-5}	0.999
1340	0.666	2.50×10^{-5}	0.989
1356	0.352	2.02×10^{-19}	0.997
1377	0.095	2.02×10^{-13}	0.988
1380	0.277	9.92×10^{-5}	0.979
1391	0.180	8.50×10^{-5}	0.990

Table 5.18: ANOVA 3: Increased EO Excitation - Main Effects - Rotor C

Response (Hz)	EO Level P-Val.	Input Location P-Val	Output Locations P-Value
1205	0.210	4.00×10^{-6}	0.999
1262.4	0.021	4.02×10^{-6}	0.999
1272	0.914	3.01×10^{-6}	0.999
1283	0.111	9.95×10^{-6}	0.999
1299	0.752	3.78×10^{-6}	0.999
1300	0.100	3.01×10^{-6}	0.999
1308.2	0.100	3.32×10^{-9}	0.999
1314	0.156	5.91×10^{-9}	0.991
1321.1	0.200	3.21×10^{-9}	0.972
1325	0.030	6.28×10^{-6}	0.999
1331	0.183	2.00×10^{-5}	0.999
1342	0.056	1.01×10^{-5}	0.999
1358.3	0.162	6.82×10^{-9}	0.998
1375	0.337	1.01×10^{-5}	0.998
1380.2	0.373	8.58×10^{-7}	0.998
1390.2	0.179	9.50×10^{-3}	0.991

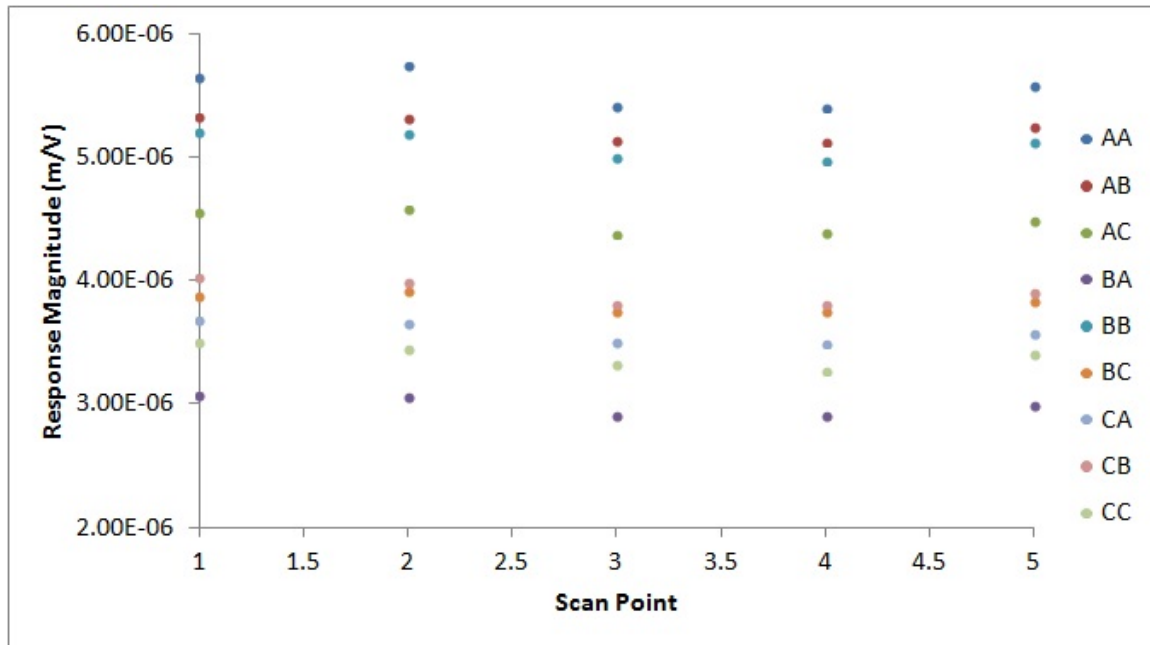


Figure 5.35: Blade 16 ANOVA Results: 1204.9 Hz and 1EO

Examining each blade's response, it is shown that for each natural frequency, the response magnitude is approximately a constant value across all five scan points. A typical example of this trend is shown in Figures 5.35 and 5.36. Here, all nine input location combinations are given. As was expected, the input at Location 1 for each blade (AA) shows the greatest response magnitude. This same response trend was observed for all resonant frequencies measured on each blade. This includes excitation both 1EO and 2EO. Compared to the single blade excitation, the increased EO excitation produces increased response magnitudes because multiple blades are excited simultaneously.

Because the response magnitude is approximately constant across all output locations, an average value is taken and plotted against the measured natural frequencies. This is performed for each input combination. Figures 5.37 and 5.39 show this relationship for two blades used in this ANOVA for 1EO. Figures 5.41 and 5.43 show this relationship for

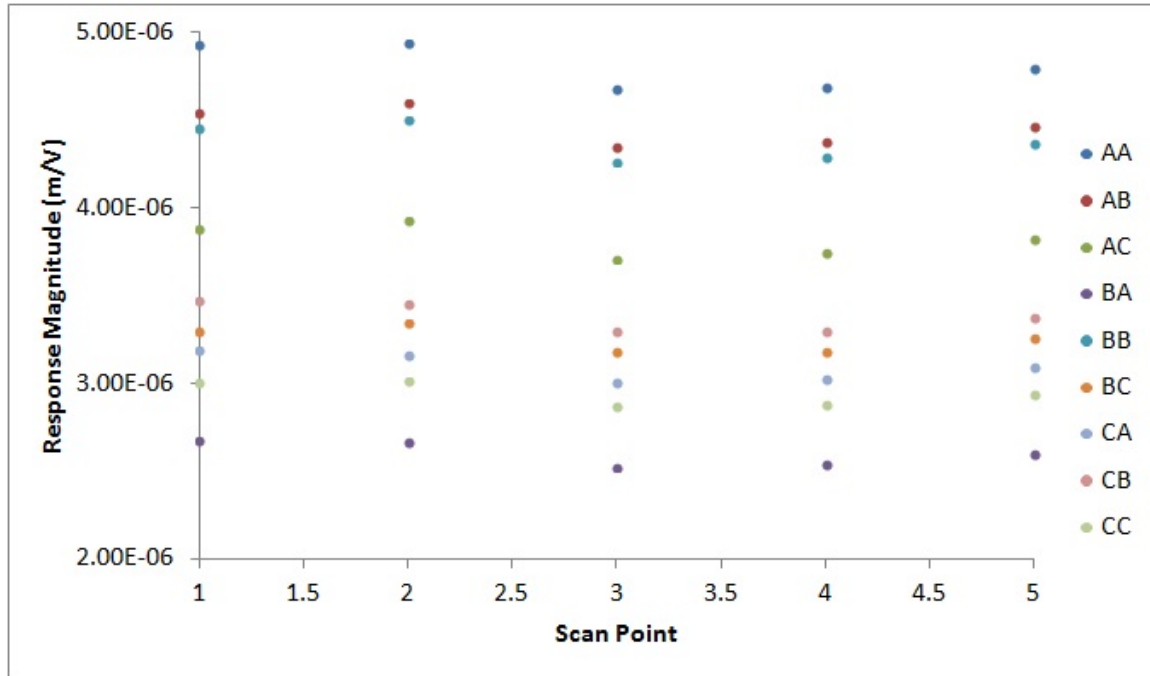


Figure 5.36: Blade 17 ANOVA Results: 1204.9 Hz and 1EO

the two blades used in this ANOVA for 2EO. Figures 5.38, 5.42, 5.40, and 5.44 show the same information, but simply highlight the frequencies associated with Blades 16 and 17. These results continue to indicate placing the input location at the blade tip provides the optimum response. These results continue to indicate how the input location, despite the addition of EO excitation into the analysis, continues to significantly influence the rotor's forced response. This is also the observed trend for the remaining blades tested. In these figures, despite taking measurements at one blade, the response of both blades are clearly seen.

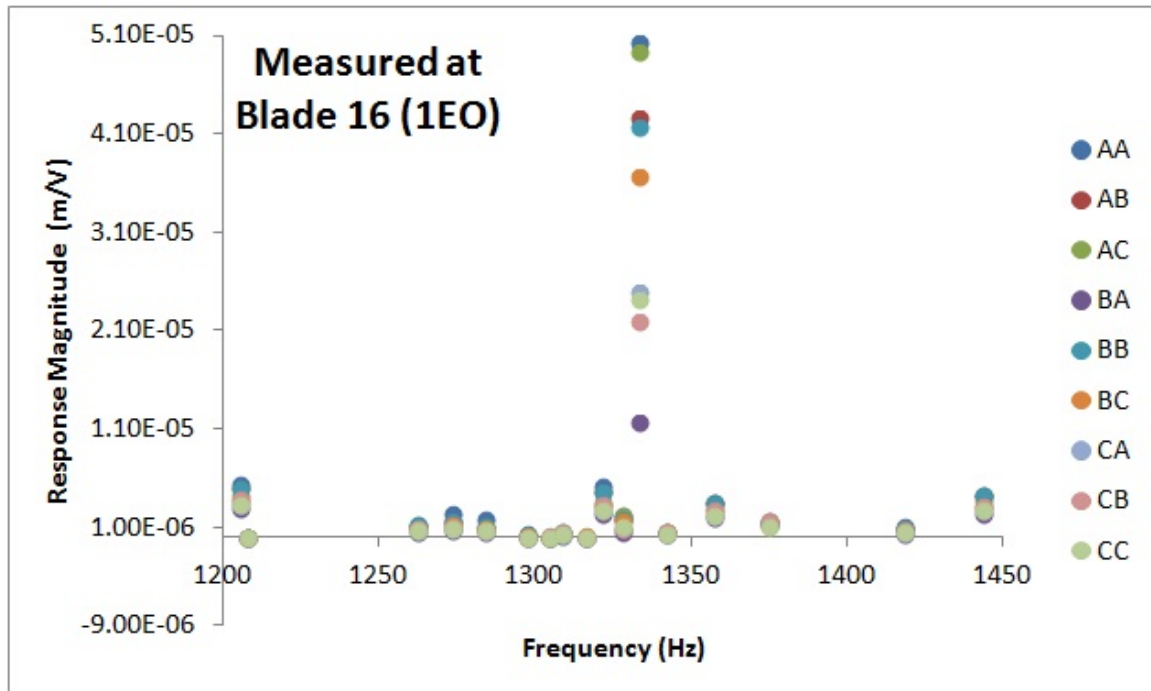


Figure 5.37: Average Responses for Multi-Blade ANOVA (Blade 16, 1EO)

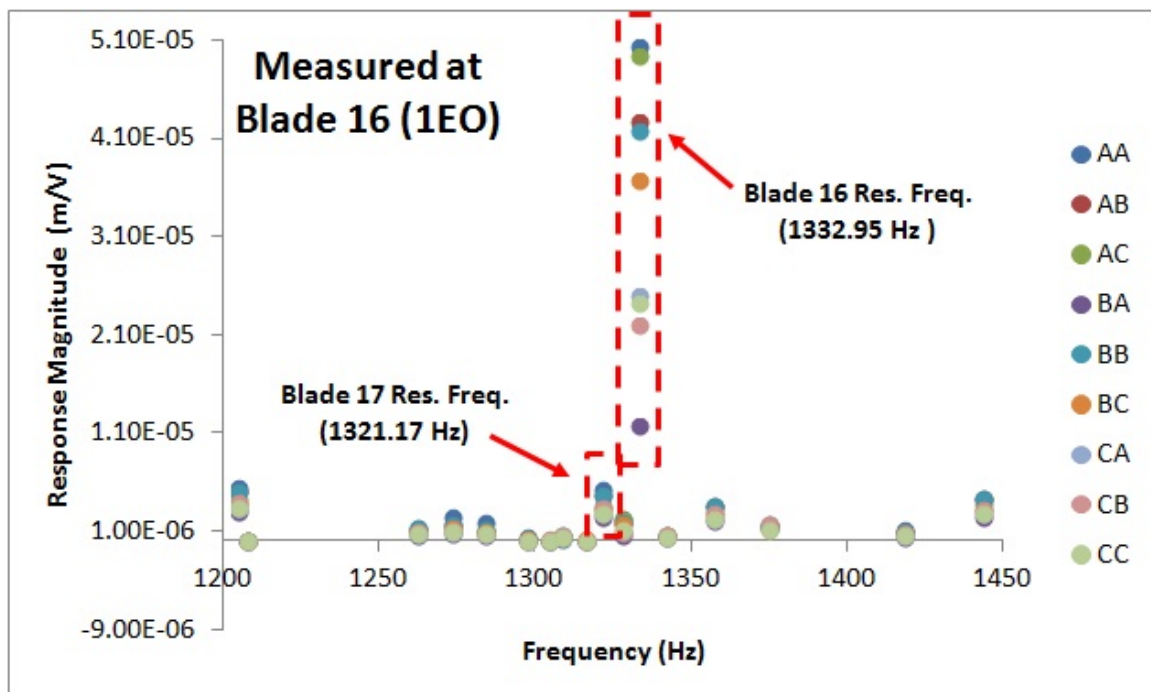


Figure 5.38: Highlighted Frequencies: Average Responses for Multi-Blade ANOVA (Blade 16, 1EO)

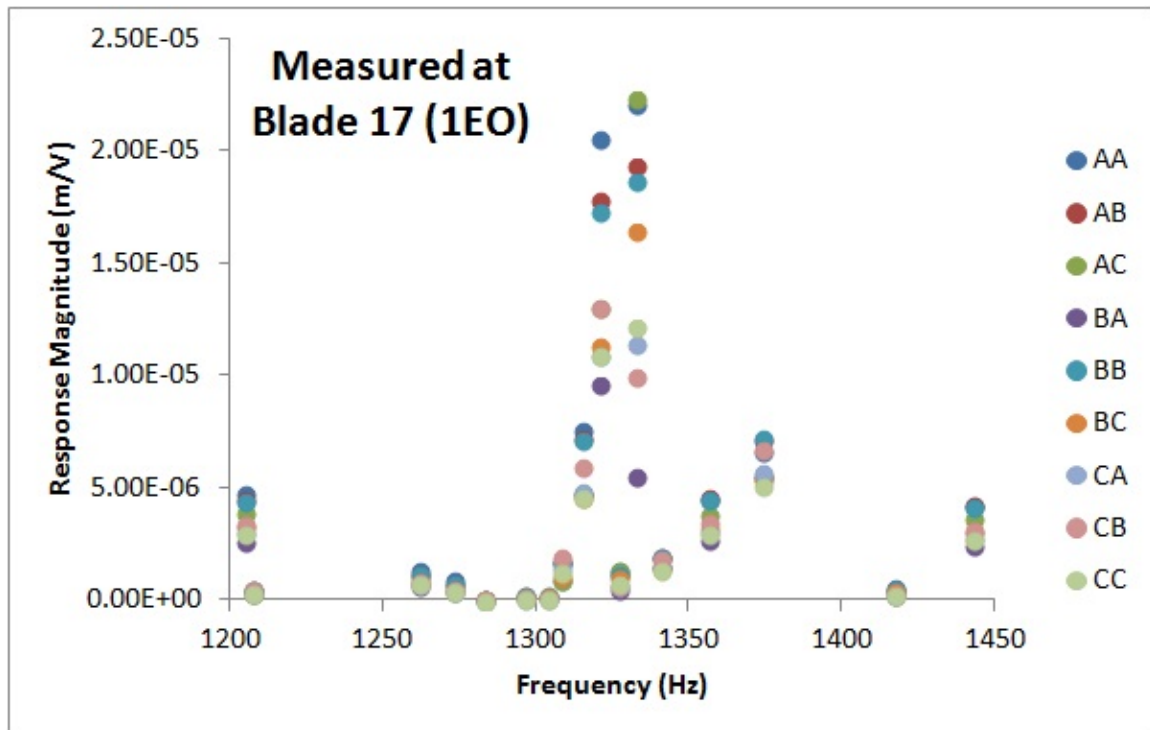


Figure 5.39: Average Responses for Multi-Blade ANOVA (Blade 17, 1EO)

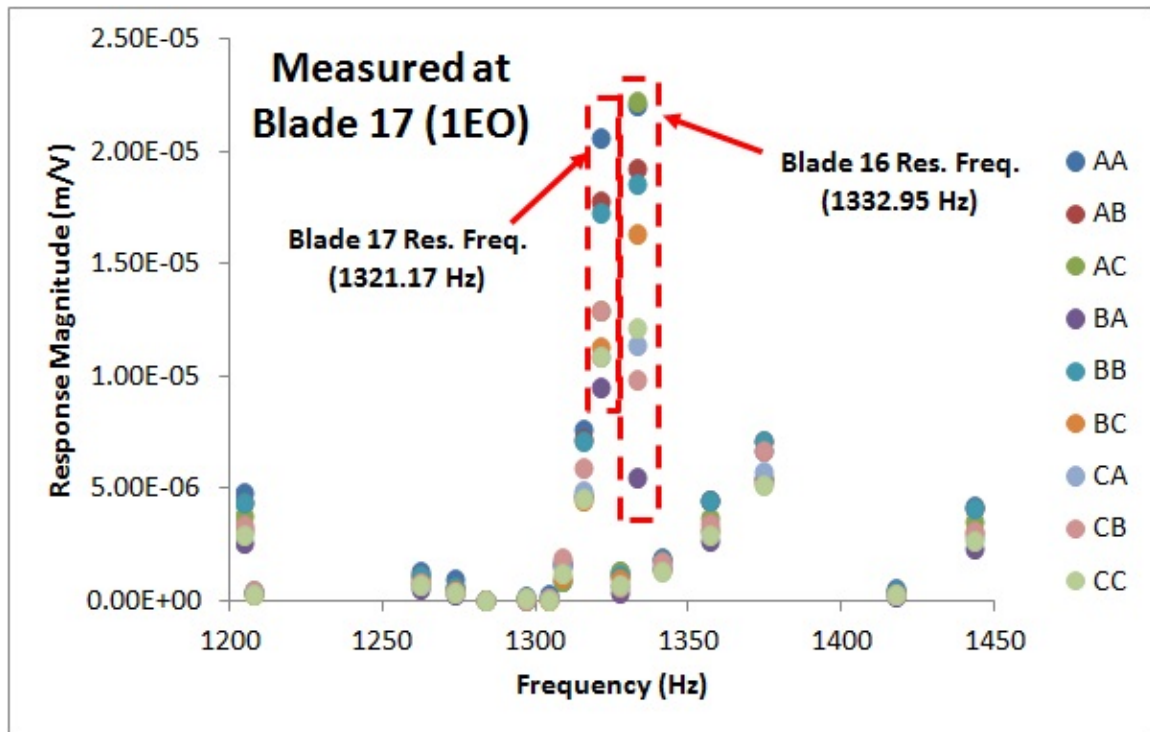


Figure 5.40: Highlighted Frequencies: Average Responses for Multi-Blade ANOVA (Blade 17, 1EO)

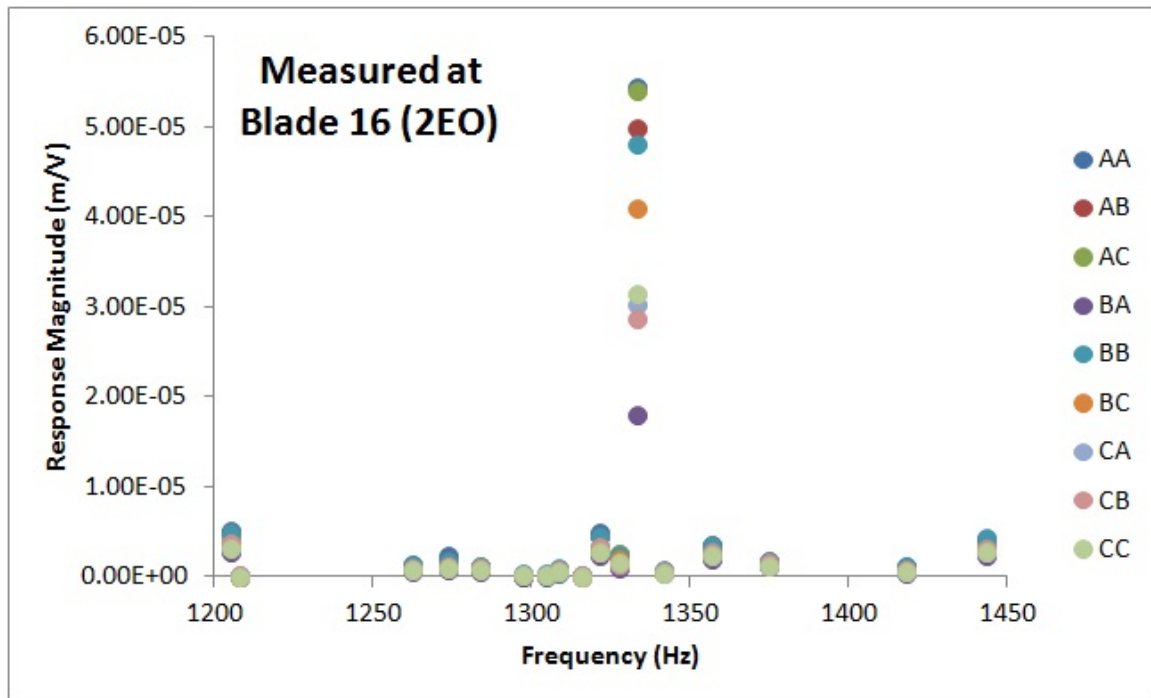


Figure 5.41: Average Responses for Multi-Blade ANOVA (Blade 16, 2EO)

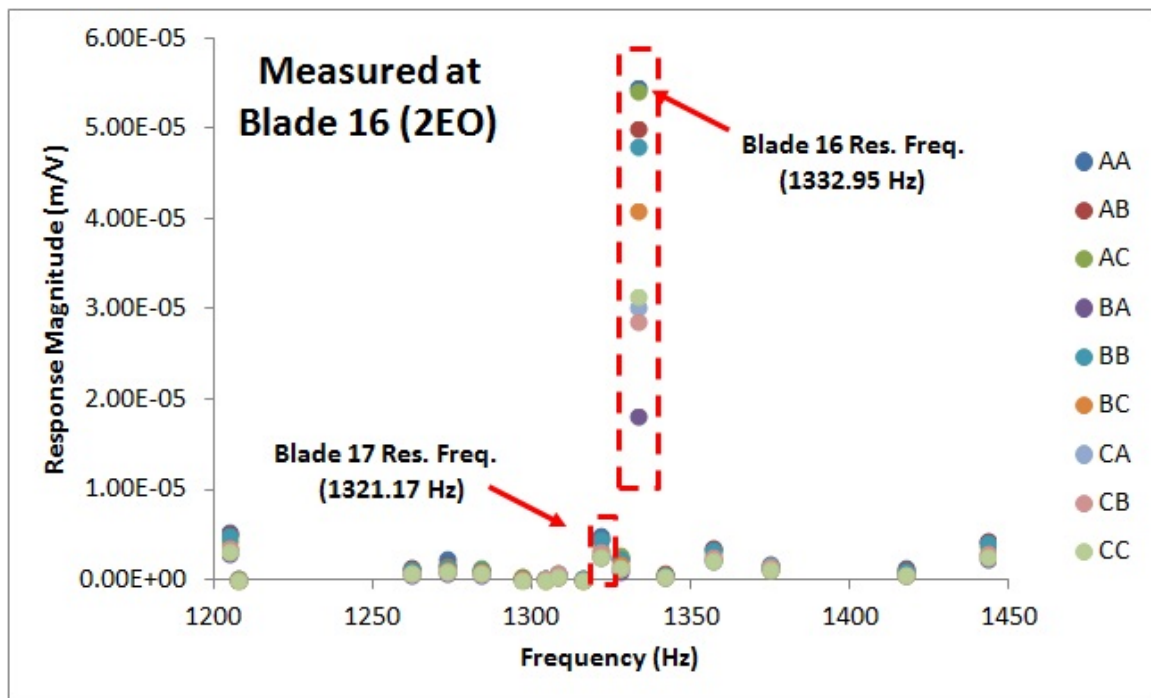


Figure 5.42: Highlighted Frequencies: Average Responses for Multi-Blade ANOVA (Blade 16, 2EO)

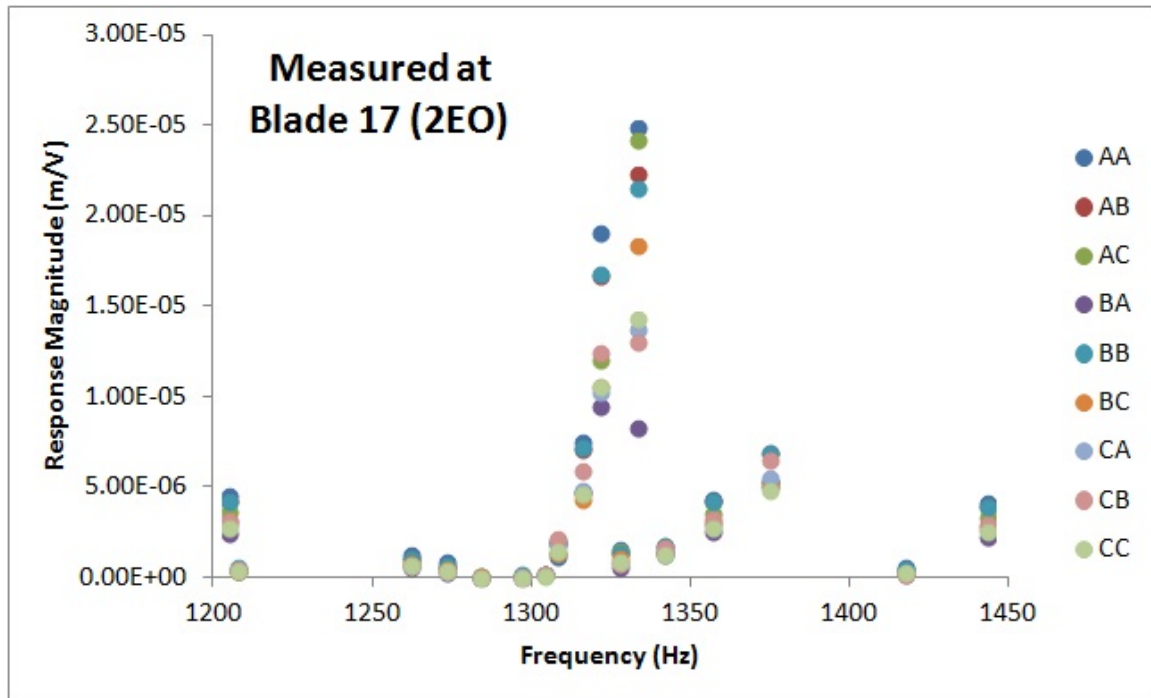


Figure 5.43: Average Responses for Multi-Blade ANOVA (Blade 17, 2EO)

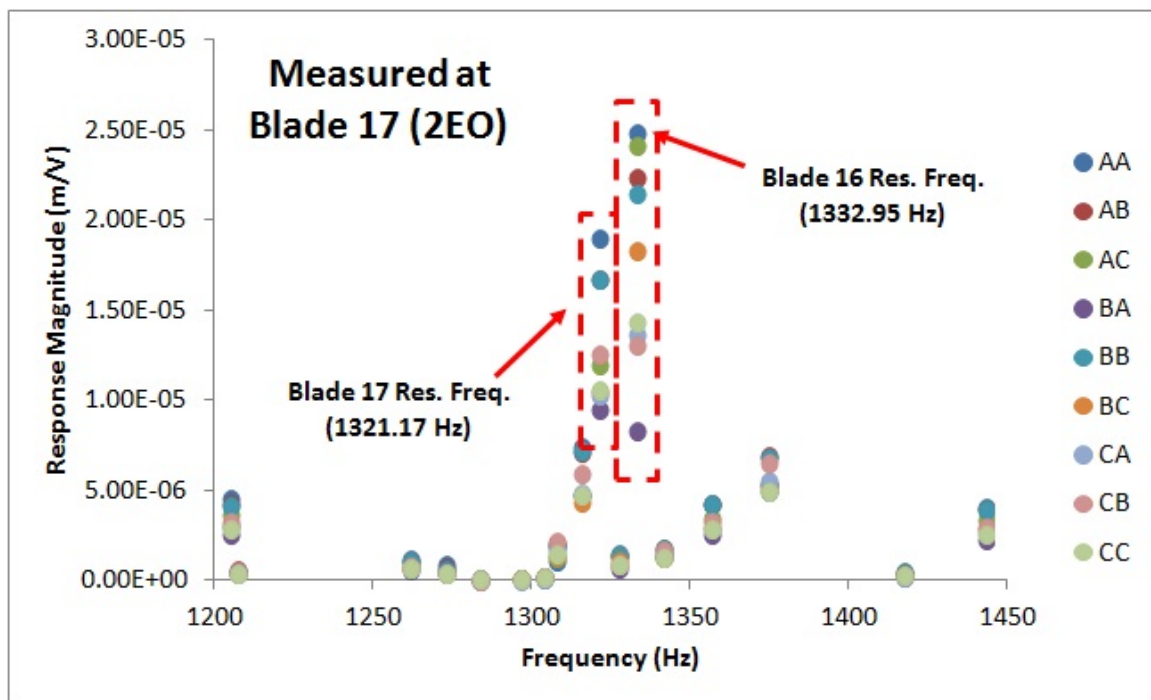


Figure 5.44: Highlighted Frequencies: Average Responses for Multi-Blade ANOVA (Blade 17, 2EO)

5.9.1 Theoretical Cantilever Plate Model: ANOVA Study.

The results in the previous section beg the question: for an isotropic plate with a constant cross section, does the input location play a more significant role in affecting the forced response? Here, the cantilever plate model developed in Appendix B, Section B.5 will be explored in the same manner as the rotor blade. The input and output locations will be used as factors in this analysis. Four levels within each factor will be utilized. The plate properties are shown in Table 5.19. The quantities here are independent of units. The numbers were arbitrarily chosen as part of this exercise. The input and output locations are given in Table 5.20. A sinusoidal load, of magnitude 2, was applied at the indicated input locations, over a 0 to $2 \frac{rad}{sec}$ frequency range. An arbitrary moment in time was selected at which to examine the theoretical results. Here, these results correspond to t equals 20 seconds. The theoretical maximum responses for the cantilever plate are shown in Table 5.21.

The results in Table 5.21 are from a two factor, 4 level analysis. This ANOVA technique is shown in Chapter 3, Section 3.13. As expected, neither factor plays a more dominant role in affecting the plate's forced response. The ANOVA table is provided in Table 5.22. These results show both factors are an equal contributor to the plate's forced response magnitude. The F-Statistic and corresponding P-Value are identical for each factor. To that end, each factor is an equal contributor in determining the plate's forced response.

There are stark differences in the ANOVA results between the theoretical cantilever plate and the population of rotor blades. Summarizing, the ANOVA on the sampled rotor blades indicated the input location is more significant in affecting the response magnitude than the measurement location. When examining the theoretical cantilever plate, the ANOVA illustrated there is no difference between the two factors in affecting the forced response magnitude.

Table 5.19: Theoretical Cantilever Plate Model ANOVA - Mechanical Properties

Length	10
Width	10
Thickness	0.05
Density	10
Poisson's Ratio	0.3
Elastic Modulus ($\times 10^6$)	10

Table 5.20: Theoretical Cantilever Plate Model ANOVA - I/O Locations

Input (x, y)	Output (x, y)
(10,10)	(10, 0)
(9, 9)	(9, 1)
(8, 8)	(8, 2)
(7, 7)	(7, 3)

One factor affecting the difference in the two sets of results stems from the mistuned nature of the blades themselves. Despite careful machining, there will always exist subtle geometric variations from blade to blade and even within each blade. In addition, the blade possesses a variable cross sectional area. Furthermore, there exists material property variations within the blade which are not present in the cantilever plate model. Each of these reasons contribute to differences realized between the actual blade and theoretical cantilever plate ANOVA results.

Table 5.21: Theoretical Cantilever Plate Model ANOVA - Maximum Responses

Output (10, 0)				
Input	(10,10)	(9,9)	(8,8)	(7,7)
Max. Resp.	833.0	668.7	525.8	409.0
Output (9, 1)				
Input	(10,10)	(9,9)	(8,8)	(7,7)
Max. Resp.	668.7	545.4	437.7	347.4
Output (8, 2)				
Input	(10,10)	(9,9)	(8,8)	(7,7)
Max. Resp.	525.8	437.7	359.0	290.4
Output (7, 3)				
Input	(10,10)	(9,9)	(8,8)	(7,7)
Max. Resp.	409.0	347.4	290.4	238.4

Table 5.22: Theoretical Cantilever Plate Model Resulting ANOVA Table

Source	Sum of Squares	DOF	Mean Square	F-Statistic	P-Value
Input Loc.	185067.3	3	61689.1	27.261	0.0000754
Output Loc.	185067.3	3	61689.1	27.261	0.0000754

5.10 Deriving the Experimental Tolerances

Analogous to the technique shown in Chapter 3, Section 3.17.3, a set of tolerances can be derived which will place bounds on the input location. In turn, this will place bounds on the response magnitudes. Detailed in Section 5.9, the input locations serve to drive the response magnitude more significantly than the output locations. The method to ensure

consistent, global and local output locations is developed in Section 5.4. Therefore, the remaining factor influencing the response magnitude is the input location.

From previous single blade experimental work, Figure 5.45 shows the measured response value vs. solenoid location. Here, the solenoid is defined as the actuator's central core. The effect of blade mistuning is evident by the different response magnitudes; each blade was tested using the same actuator.

The significant portion of this figure is the response vs. location curve for each blade. To corroborate these curves, 46 more single blade tests were conducted. This number was chosen to ensure a sufficient sample size. The resulting curves were nearly identical to those depicted in Figure 5.45. For clarity, only two blades are shown in Figure 5.45. The only significant differences lie in the vertical shift in the curves themselves - indicating the inherent mistuning present in each blade.

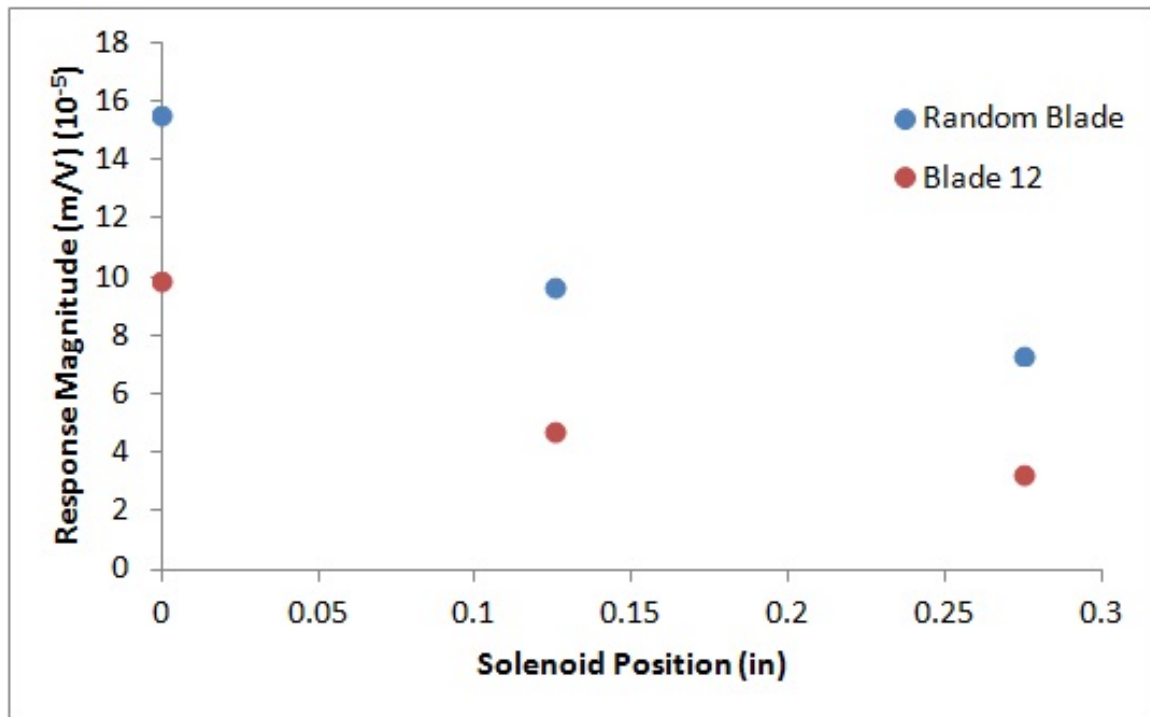


Figure 5.45: Single Blade Response vs. Solenoid Position

The response magnitudes at each input location for 48 blades were recorded. For each input location, an average response magnitude was created and then normalized by the average peak response for all measured blades. An exponential function was then fit to the resulting data curve. The input location was normalized by the average diagonal blade dimension. This was done because the input location was uniformly moved down the blade span and along the blade chord with each test iteration. The resulting response equation and its respective curve is shown in Equation 5.23 and Figure 5.46.

$$f(x) = 0.9522e^{-7.612x} \quad (5.23)$$

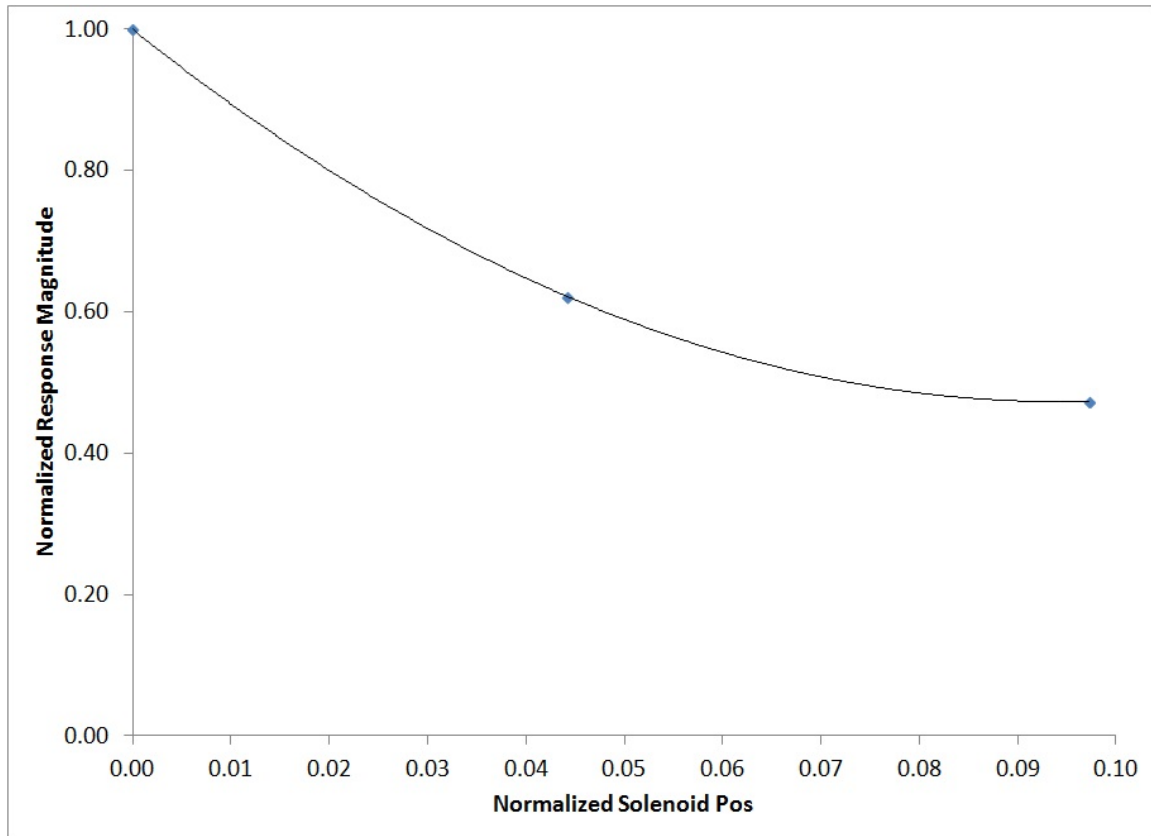


Figure 5.46: Normalized Single Blade Response vs. Normalized Solenoid Position

Using this curve, input location limits can be established which will dictate the maximum response. If the solenoid is placed directly at the blade tip, the measured response will be

greater than or equal to 95% of the maximum blade response. Placing the actuator at 1% of the blade's diagonal dimension ensures the response will be near 90% of its maximum.

To explore whether this input tolerance could be applied to another rotor type, several more tests were carried out on a small population of actual production rotors. These rotors are constructed of titanium and each has 22 blades. The blade dimensions in Figure 5.47 are normalized with respect to the indicated diagonal measurement. Table 5.23 provides the normalized blade dimensions. Figure 5.48 shows the input locations used for this series of validation experiments. The input locations along the indicated diagonal are shown in Table 5.24. The origin for these normalized input locations is the lower left corner of the blade, as indicated in Figure 5.48.

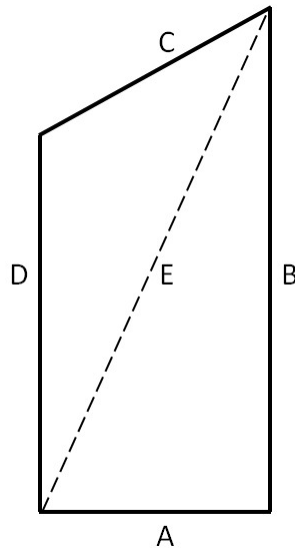


Figure 5.47: Sketch of Validation Blade for Input Tolerances

Table 5.23: Input Tolerance Validation Blade: Normalized Dimensions

A	0.486
B	0.874
C	0.486
D	0.68
E	1.00

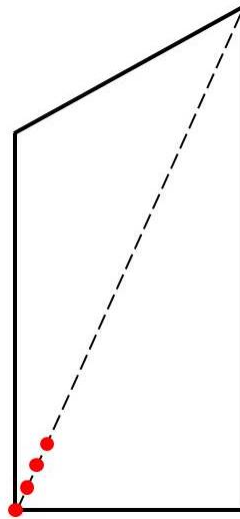


Figure 5.48: Input Tolerance Validation Blade: Input Locations

Table 5.24: Input Tolerance Validation Blade: Normalized Input Locations

Location 1	0.0000
Location 2	0.0366
Location 3	0.1399
Location 4	0.2615

For each experiment, the rotor was centered on the laser vibrometer home position using the techniques outlined in Section 5.4. A new single actuator stand was used for this series of experiments. The initial stand in Figure 5.33 was developed specifically for the

Purdue Transonic Research Compressor. The new stand was needed because the validation rotors' blades twisted around their long axes. The new stand allowed the actuator to remain normal to the blade's surface as the input location was re-positioned along the blade's chord and span.

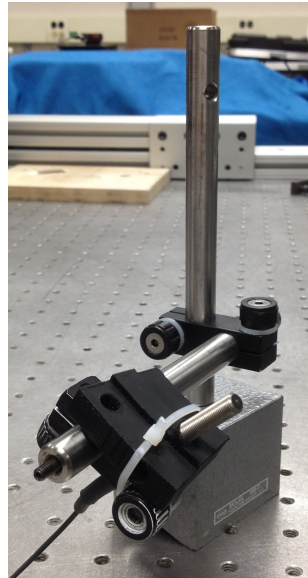


Figure 5.49: Single Actuator Stand for the Validation Rotors

After a blade was evaluated, the rotor was rotated to bring the next blade over the actuator. Each blade used a constant output location. On the PolyTec screen, the output location coordinates for each test were $(-5.370^\circ, 0.501^\circ)$. Since only a finite population of blades was available for this validation test, a sufficient number of blades required testing to draw any significant conclusions. A total of 88 blades were available to test; the peak response at each blade was measured. Equations 3.154 and 3.155 dictated 72 of the 88 blades required testing¹⁰.

Analogous to the behavior seen in Figure 5.45, the differences between each blade was a vertical shift in the exponentially decaying response vs. input location curves. Again, this is indicative of the relative mistuning in the rotor. For each input location, an average of the

¹⁰For 95% confidence in the results

responses was taken. The resulting average was normalized by the peak average response. An exponential function was fit to the resulting normalized data points. The exponential function is given in Equation 5.24 and its corresponding curve is shown in Figure 5.50. As shown with the experimental results from the Purdue Transonic Research Compressor, placing the solenoid directly at a blade's tip will, on average produce a response greater than or equal 97% of the blade's maximum. Similarly, to ensure the blade's response is near 90% of its maximum, the solenoid should be placed at a location corresponding to 1% of the blade's diagonal measurement.

$$f(x) = 0.9674e^{-8.028x} \quad (5.24)$$

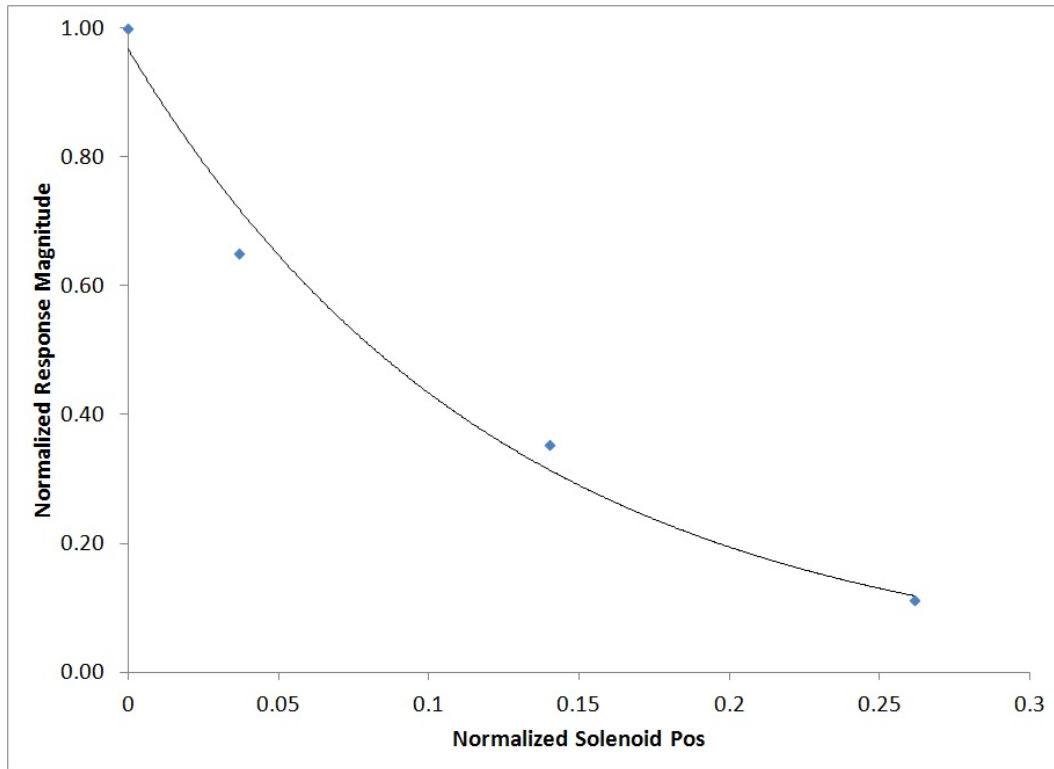


Figure 5.50: Input Tolerance Validation Blade: Normalized Single Blade Response vs. Normalized Solenoid Position

Specific input locations will now be defined using the same technique which defined the measurement points in Section 5.4 in this chapter; polar coordinates were once again

employed. This technique is rooted in centering the rotor on the laser vibrometer's home position. Reference the method developed in Section 5.4. Figure 5.51 gives an example polar coordinate input location. Here, the dashed line on the blade indicates the blade diagonal onto which the input is placed. Figure 5.52 incorporating the 1% input location tolerance on the Purdue Transonic Research Compressor.

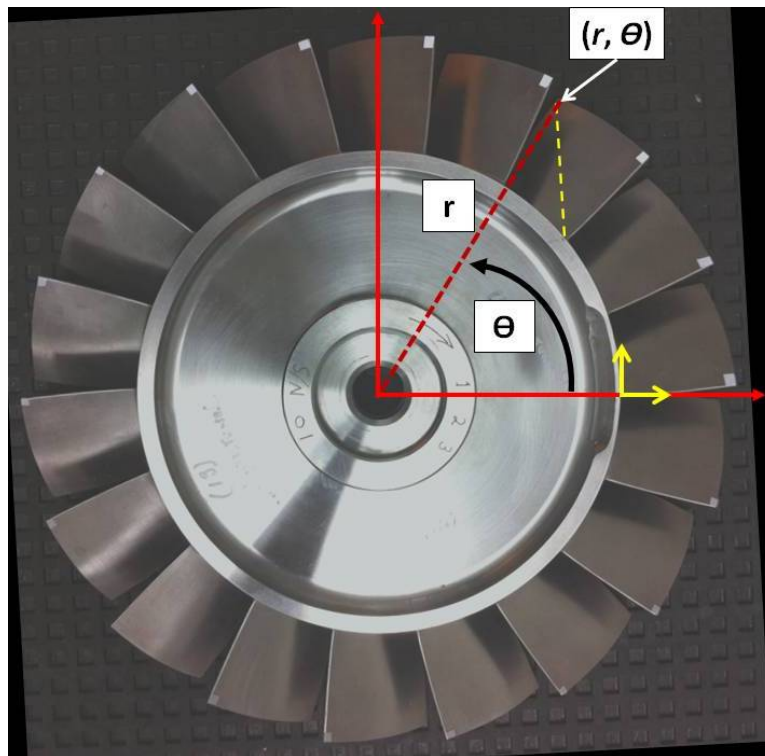


Figure 5.51: Polar Coordinate Input Location

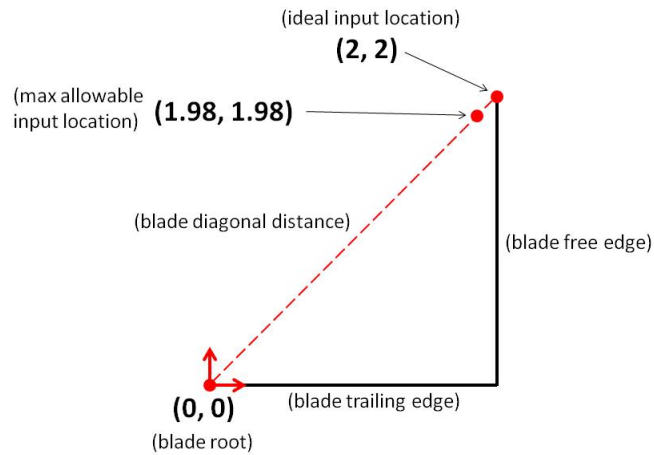


Figure 5.52: Purdue Rotor Tolerance Schematic

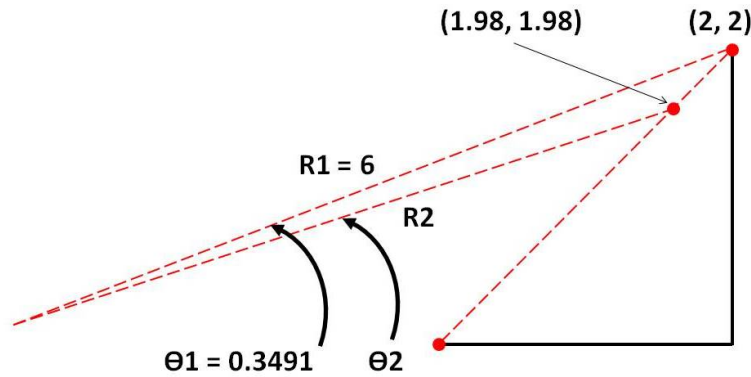


Figure 5.53: Purdue Rotor Tolerance Schematic With Radial and Angular Measurements

The origin is defined at the rotor's center, coincident with the laser vibrometer's home position. Referencing the blade adjacent to the horizontal axis in Figure 5.51 and the measurements in Figure 5.53 a linear relationship exists between the radius and angle for both the ideal input and maximum allowable locations. This technique can be extended to any rotor blade. Table 5.25 provides the ideal and "allowable" input locations, in polar coordinates. These input locations are derived directly from the results in this chapter. The ideal location, ensures the blade will respond, on average, greater than or equal to 97% of

its maximum response. The maximum allowable location ensures the blade will respond, on average, greater than or equal to 90% of its maximum response. Table 5.26 provides these same tolerance values in Cartesian coordinates.

Table 5.25: Global Input Location Positioning Tolerances:

Purdue Transonic Research Compressor (Polar)

	Ideal Location		Allowable Location	
Blade No.	r (in)	θ (rad)	r (in)	θ (rad)
1	6	0.349	5.94	0.346
2	6	0.698	5.94	0.691
3	6	1.047	5.94	1.037
4	6	1.396	5.94	1.382
5	6	1.745	5.94	1.728
6	6	2.094	5.94	2.073
7	6	2.443	5.94	2.419
8	6	2.793	5.94	2.765
9	6	3.142	5.94	3.110
10	6	3.491	5.94	3.456
11	6	3.840	5.94	3.801
12	6	4.189	5.94	4.147
13	6	4.538	5.94	4.492
14	6	4.887	5.94	4.838
15	6	5.236	5.94	5.184
16	6	5.585	5.94	5.529
17	6	5.934	5.94	5.875
18	6	6.283	5.94	6.220

Table 5.26: Global Input Location Positioning Tolerances:

Purdue Transonic Research Compressor (Cartesian)

	Ideal Location		Allowable Location	
Blade No.	x (in)	y (in)	x (in)	y (in)
1	5.638	2.052	5.589	2.012
2	4.596	3.857	4.577	3.786
3	3.000	5.196	3.024	5.113
4	1.042	5.909	1.113	5.835
5	-1.042	5.909	-0.929	5.867
6	-3.000	5.196	-2.862	5.205
7	-4.596	3.857	-4.456	3.928
8	-5.638	2.052	-5.523	2.187
9	-6.000	0.000	-5.937	0.187
10	-5.638	-2.052	-5.649	-1.836
11	-4.596	-3.857	-4.694	-3.641
12	-3.000	-5.196	-3.183	-5.015
13	-1.042	-5.909	-1.296	-5.797
14	1.042	-5.909	0.744	-5.893
15	3.000	-5.196	2.697	-5.293
16	4.596	-3.857	4.330	-4.066
17	5.638	-2.052	5.451	-2.359
18	6.000	0.000	5.928	-0.373

5.11 Tolerance Generalities

In deriving these tolerances for the traveling wave excitation system, a very specific set of input parameters were used. These parameters were EO excitation (Chapter 3, Section 3.4) and input sweep frequencies. This begs the question as to the applicability of such a location tolerance.

5.11.1 Concern 1.

If the input location tolerance for one frequency band and EO level is established, will the location tolerance be applicable to another frequency band and EO level?

The short answer is yes.

Different Input Frequencies. The experimental input and output locations would both be ineffective if node points or nodal lines were located at or passed through the respective locations. In the experiment, however, any nodal diameters remain near each blade's center. Even with a highly mistuned rotor, such as the Purdue Transonic Research Compressor, the nodal diameter lines remain a significant distance away from the input and output locations. In addition, individual blade modes with nodes at the free corners (experimental input and output locations) are of such high order, they are not excited during the traveling wave experiment. Examining a rotor's Campbell diagram shows the modes of greatest concern; these are typically the lower order bending and torsion modes. Node locations with these modes are not located at the blades' free corners. Because experimental excitation frequencies will not invalidate the input and output locations, the input location tolerances are independent of the experimental excitation frequencies.

EO Excitation Levels. For the stationary rotor within the experiment, the EO value serves only to drive the phase difference between each blade (Reference Figure 3.17). The maximum phase difference occurs at EO ($N/2$), where N is the number of blades. With the stationary rotor, the EO excitation also develops a number of nodal diameter corresponding to its respective EO value. For example, 3EO will induce 3 nodal diameters. Even with an

intentionally, highly mistuned rotor, such as the Purdue Transonic Research Compressor, the nodal diameter lines remain a significant distance away from the critical input and output locations. Therefore, experimental input frequency EO excitation level does not adversely affect the established input location tolerances.

5.11.2 Concern 2.

The input location tolerance was developed by examining a population of blade FRFs, and recording the peak response for several different input locations on each blade. Will the rotor response at the different input locations, within the tolerance band, create a problem for the overall rotor response?

The answer to this question is no.

Blade Responses Within the Tolerance Band. The tolerance band was developed by examining the FRFs for a population of rotor blades. The input location was precisely positioned beneath each blade. The peak response was then recorded. The resulting input location tolerance was derived to ensure a blade's peak response is recorded. By precisely positioning both the rotor and input actuators, all input actuators will lie within the prescribed tolerance band.

During the experiment, all blades are excited simultaneously. The scanning laser vibrometer obtains the response output at each blade individually. The system then averages out the blade responses, in the frequency domain, to obtain the overall average rotor response.

FRF Distortion from Windowing and Leakage. In using the Fourier Transform to map from the time to the frequency domains, therein lies an assumption of periodicity with the data. If there exists a great deal of noise with the signal, or there is a significant random component associated with the data, its periodicity is destroyed. This is a chief reason for windowing. It effectively simulates a periodic behavior by “zeroing” out the signal at the

beginning and ends of the window. The window is simply a mathematical expression which operates on the data which forces the data into a periodic shape.

This could cause issues with the signal at the extremes in the window. For this reason, the signal generation component's starting frequency is below the range of frequencies of interest. Furthermore, the signal generation component's ending frequency is above the frequency range of interest. With that being said, the frequency range of interest is known before testing a rotor. As such, the frequency sweeps are only large enough to encompass the frequency range of interest. This strategy places the frequencies of interest near the window's center.

A rectangular window is used within the traveling wave experiment. This window is, in effect, no window. The chief advantage behind the rectangular window is that it does not interfere with a signal's amplitude. Because the TWE is used for mistuned rotors, a range of natural frequencies may exist, corresponding to the same mode in each blade. Other windows, such as the Hanning window, will only allow for peak amplitude at the window's center. In summary, the rectangular window is ideal for the TWE as it does not impinge on the rotor's response amplitudes.

The Issue of Leakage. As discussed in Section 5.5, leakage occurs as a consequence of discretely sampling a continuous signal. Since computer software is used to sample a continuous response, this signal is sampled discretely. Only a finite number of FFT (spectral) lines can be used to represent the signal's frequency components. If a portion of the signal doesn't fit "evenly" into a spectral line, it "leaks" onto adjacent lines, until all components of the signal are accounted for. This is especially problematic for signals which are not periodic, thus violating a key assumption involved in Fourier analysis. Applying a window function can force periodicity into an otherwise non-periodic signal. This ensures a smooth transition from one signal to the next. When performing the TWE experiment as this research prescribes (Section 5.4), there exists a smooth transition from one response

signal to the next. The total acquisition time is defined in such a way so as to ensure the response from the $(n-1)^{th}$ input has decayed before the n^{th} input is applied. Because the signal is essentially zero at its beginning and end, there does not exist a sharp discontinuity between signals. By defining the acquisition time in this manner, the notion of signal periodicity remains a valid assumption.

VI. Conclusion, Contributions, and Future Work

This chapter summarizes and discusses the scientific achievements attributed to this dissertation research. Focusing on an experimental evaluation of engine rotor mistuning, a procedure was developed which can evaluate the level of mistuning in any rotor. As a rotor's mistuning pattern can be attributed to both manufacturing tolerances and wear, providing a means in identifying the level to which a rotor is mistuned provides several pieces of critical information.

Initially, a robust experimental technique was developed for the existing traveling wave experiment which ensures consistent forced response results, independent of a rotor's orientation on the test stand. This technique is summarized in Appendix F. An 880% improvement in test replicate consistency, over the course of multiple rotor orientations, was demonstrated. By ensuring a consistent base is established, confidence is built into the TWE results to effectively produce a mistuned rotor's forced response. Not only does this technique give consistent results, but in turn it also ensures consistency in the experimental setup and measurement locations.

In addressing the measurement locations, this research produced a method by which local blade measurement locations are related to a global coordinate system. In doing this, the measurement points remain consistent from rotor to rotor. Single rotors are seldom evaluated, rather small populations of rotors are tested. By providing a foundation of consistent results and a common method by which the output locations are defined, a true mistuning evaluation is available.

Because the experimental results are now constant, specific attributes of a rotor's forced response are available. Identifying the mistuning pattern, and in turn, the mistuning amplification factor, ultimately aids in evaluating the rotor's remaining useful life. Since the mistuning amplification factor is assumed to be a constant for a given rotor's mode family,

these critical modes can be further evaluated using numerical finite element analyses. Here the forced response amplification would indicate a localized increase in strain energy and thus increased stress levels. For various forcing function magnitudes and excitation patterns, an estimate of the rotor's life can be obtained using the given material's Goodman diagram.

Within the experiment, the free boundary condition assumption was specifically addressed. This was implicitly handled when validating the rotor model against the experimental data, as there exists less than 1 percent difference between the mode 1 natural frequencies from the experiment and finite element model. This was also observed for increased EO excitation levels. Exciting higher order modes demonstrated less than 1.3 percent difference between the model and experiment. Despite being supported atop a pedestal covered with a special vibration isolation material, the rotor's modal behavior mimicked that seen in the numerical simulation. Research was performed to investigate the possibility of defining specific geometric support dimensions for both a beam and a circular plate to effectively simulate a free boundary condition. This analysis was performed by way of finite element simulation. For a supported beam, excited at its first natural frequency, prescribing a beam length to support diameter ratio (L/D) of 20 gives the supported beam's first natural frequency 4.5% different than the true free-free beam. Increasing the (L/D) to 40 places the supported beam's natural frequency to within 0.08% of the free-free beam. This concept was then extended to a circular plate. Defining a plate diameter to support diameter (D/d) ratio of 10 permits the supported plate's natural frequency to lie within 0.58% of the theoretical free plate's natural frequency. Increasing the (D/d) ratio to 20 reduces this difference to 0.0596%. As a consequence of these results, the isolation mat used in the experiment was sized appropriately. Given the 12 inch diameter rotor, the pad sitting atop its pedestal was 1.2 inches in diameter.

This research also validated the method by which the finite element model was developed/constructed and this model's ability to predict the experimental rotor's natural frequencies. Therefore, the tuned approximation can be considered a valid "nominal" representation of the experimental rotor. To that end, when comparing the FRF for the tuned approximation for a given mode, to its experimental counterpart, the degree to which the mistuning affects the rotor becomes immediately apparent. As this research developed a method to produce consistent experimental results using the traveling wave excitation equipment, comparing a specific rotor's tuned approximation to its corresponding experimental results aids in quantifying the mistuning present for a rotor population.

Lastly, capitalizing on the effectiveness of the newly developed experimental procedures this research produced a set of experimental input tolerances. Deciding to establish these tolerances stemmed from ANOVA results obtained through testing a population of blades on both the current research compressor and from blades on a different rotor type. These results were conclusive: the response magnitude is more sensitive to the input location than the output location. To that end, the output locations are set at the outside blade corners, opposite from the input location. The method by which the measurement points are defined was previously discussed, thus leaving only the input location as a variable. Once again, a population of blades from both the existing research compressor and the other rotor type was studied. Exciting single blades at a time, three separate input locations were used on each blade. These input locations were placed along the blades' long diagonal dimension - as measured from the outside tip location towards the opposite corner at the root. The results from all tests illustrated the same results: if the input location is kept within 1% of the blades' long diagonal dimension, the blade will respond with greater than or equal to 90% of its max response. For the Purdue Transonic Research Compressor, this equates to placing the input location within a window 0.02 inch from

the blade corner. Following the experimental setup procedures set forth in this research and using existing laboratory equipment, this tolerance level is completely realistic. This linear type tolerance was also extended to a polar relationship using a technique similar to what produced the global and local measurement points. Using the laser vibrometer's home position as a global coordinate reference, ideal and allowable radial and angular coordinates were developed.

In summary, this research addressed several items of interest to the turbine engine community. First, a rigorous procedure was developed which can determine the amount of mistuning within a rotor. Accompanying this contribution, a process was developed and numerically validated to consistently produce forced response results when utilizing traveling wave excitation. Furthermore, a unique method which produced the finite element model was validated against experimental results. The experimental boundary condition assumption was also validated using finite element analysis. In addressing the experimental support condition, a numerical analysis demonstrated a structure's free response can be simulated using a method of physical supports. Lastly, an input location tolerance was established so as to ensure each blade responds with peak magnitude.

While the research contributions and methods contained within this document are sound, there exists several remaining items of interest to further the body of knowledge.

Despite the effectiveness the finite element model demonstrated in reproducing the experimental rotor's natural frequencies, the existing research neglected to address any correlation between the experimental and numerical forced response magnitudes. The primary difference here lies in the different forcing functions utilized in each scenario. The TWE equipment makes use of electromagnetic actuators. The force field imparted to the blade is not constant throughout the blade's displacement range. The force magnitude between the blade and actuator is governed by inverse square relationship. Here, the force magnitude decreases with the square of the distance between the actuator and blade. While

this method of excitation provides consistent EO excitation, it is not representative of the excitation type realized in an actual engine. In the finite element model, in contrast, the loading magnitude is a constant force applied to the blades. Updating the numerical model to produce the same response magnitudes seen in the TWE experiment would involve modifying the existing forcing function to recognize the non-linear forcing type utilized in the TWE.

Also noteworthy, the current finite element model is only valid for linear responses for the given rotor. While the TWE response is always linear because the magnitude of excitation is on the order of *micropounds*, the finite element model will provide rotor response magnitudes for the rotor would induce permanent deformation for a real rotor. These plastic deformations are not realistic depictions of true non-linear material behavior, which occurs post-yielding. The model's implicit assumption dictating the applied load and the blade response be linearly related is incorrect.

While the TWE experiment is a valid method to experimentally evaluate mistuning on any rotor, the finite element model developmental method was only validated for an IBR. Recall these rotors are carved from a single piece of material, or created by welding several components together. The insertion type rotor was not evaluated in the course of this research. Here, the level of complexity involved in developing the finite element model increases tremendously. Rather than scanning the rotor as a single entity, each component requires a separate scan. After scanning, a solid model of each piece would then be constructed. A finite element model would then developed from each solid component. Within the modeling program, these separate components would be assembled. The associated technique to develop the model would require significant modifications to account for the inherent damping and contact present at the component interfaces, as well as any variation between the joints around the rotor hub. These maladies are not present

in the IBR, nor would they be present if the entire insertion type rotor was scanned as a monolithic entity.

Further model validation would entail a direct complex eigenvector comparison between the numerical model and experiment. The traveling wave equipment currently produces the complex FRF for each scan point. The finite element program provides the real FRF for each output location. The finite element input file can be modified to instruct ANSYS to produce a complex FRF for each output location. With the complex FRFs, both magnitude and phase information is produced. While the real FRF information can certainly be used to establish a degree of correlation between the experiment and numerical solution. Given the experimental and numerical complex eigenvalues, further model validation would be performed using the MAC and COMAC as discussed in Chapter 3, Sections 3.8 and 3.9.

Even with significant differences in blade geometries, the 1% tolerance established on the research compressor remained true for the validation rotor. As these rotors possess blades which are relatively flat and rectangular, the input location tolerance was not verified on blades with significant twist or a non-rectangular planform. Nor have the tolerances been verified on advanced rotor types exhibiting blades with curved edges. The tolerances could be verified on these types of blades through invoking a transformation between the curved surface and the Cartesian plane. Assuming there exists a transformation matrix between the flat reference plane and highly curved blade surface, the input tolerances could be generalized to any blade.

Bibliography

- [1] J. A. Beck, “Stochastic mistuning simulation of integrally bladed rotors using nominal and non-nominal component mode synthesis methods,” Master’s thesis, Wright State university, 2010.
- [2] R. D. Fulayter, *Mistuned Fan and Compressor Rotors Utilizing NSMS*. PhD thesis, Purdue University, 2004.
- [3] J. M. Brown, *Reduced Order Modeling Methods for Turbomachinery Design*. PhD thesis, Wright State University, 2008.
- [4] M. P. Castanier and C. Pierre, “Modeling and analysis of mistuned bladed disk vibration: Status and emerging directions,” *Journal of Propulsion and Power*, vol. 22, pp. 384–396, March 2006.
- [5] C. C. Lin and M. P. Mignolet, “Effects of damping and damping mistuning on the forced vibration response of bladed disks,” *Journal of Sound and Vibration*, vol. 193, no. 2, pp. 525–543, 1996.
- [6] 38th AIAA/ASME/ASCE/AHS/ASC Structures, Structural Dynamics and Materials Conference, *Effects of Damping on a Blade-Disk Assembly*, April 1997.
- [7] H. H. Yoo, J. Y. Kim, and D. J. Inman, “Vibration localization of simplified mistuned cyclic structures undertaking an external harmonic force,” *Journal of Sound and Vibration*, vol. 261, pp. 859–870, 2003.
- [8] J. J. Hollkamp and R. W. Gordon, “Modal testing of a bladed disk,” tech. rep., Air Force Research Laboratory, 1998.
- [9] J. Judge and C. Pierre, “Experimental investigation of mode localization and forced response amplitude magnification for a mistuned bladed disk,” *Journal of Engineering for Gas Turbines and Power*, vol. 123, pp. 940–950, 2001.
- [10] 40th AIAA/ASME/SAE/ASEE Joint Propulsion Conference and Exhibit, *Experimental Investigation of Geometric Uncertainty Effects on Blade Forced Response*, July 2004.
- [11] IMAC-XXIII, *Epistemic Uncertainty Quantification Tutorial*, February 2009.
- [12] I. Kalova and M. Lisztwan, “Industrial applications of triangulation technique,” tech. rep., International Federation of Automatic Control (IFAC), 2005.
- [13] G. Gerig, “Structured lighting.” Slides from CS6320 - 3D Computer Vision. Carnegie Mellon University, School of Computer Science, 2012.

- [14] D. Fofi, T. Sliwa, and Y. Voisin, “A comparative survey on invisible structured light,” *SPIE*, pp. 90–98, 2004.
- [15] K. S. Pennington and P. M. Will, “A grid coded technique for recording 3-dimensional scenes illuminated with ambient light,” *Optics Communication*, vol. 2, pp. 167–169, September 1970.
- [16] Conference on Diagnostic and Therapeutic Technology in Dentistry, *Optical Methods to Measure Shape and Size*, October 1987.
- [17] 43rd AIAA/ASME/ASCE/AHS Structures, Structural Dynamics, & Materials Conference, *A Traveling Wave Excitation System for Bladed Disks*, April 2002.
- [18] D. D. Maio, *SLDV Technology for Measurement of Mistuned Bladed Disc Vibration*. PhD thesis, Imperial College London - Department of Mechanical Engineering, 2007.
- [19] *PolyTec Hardware Manual: PolyTec Scanning Vibrometer PSV-400*.
- [20] C. Nave, “Quarter wave plate.” <http://hyperphysics.phy-astr.gsu.edu/hbase/phyopt/quarwv.html>, November 2013.
- [21] A. Kaszynski, J. Beck, and J. Brown, “Uncertainties of an automated optical 3d geometry measurement, modeling, and analysis process for mistuned ibr reverse engineering,” ASME Turbo Expo, June 2013.
- [22] A. W. Leissa, *Vibration of Plates*. Scientific and Technical Informatin Division, Office of Technology Utilization, National Aeronautics and Space Administration, 1969.
- [23] T. Burn, “Jet engine cutaway with diagram.” website: <http://www.cgcookie.com/blender/images/jet-engine-cutaway-with-diagram/>, November 2013.
- [24] “3-d scanner gets the blues.” website: <http://www.qualitydigest.com/inside/quality-insider-news/3-d-scanner-gets-blues.html>.
- [25] J. F. Mark, “Analytical and experimental vibration analysis of variable update rate waveform generation,” Master’s thesis, Wright State University, 2011.
- [26] S.-H. Lim, R. Bladh, and M. Castanier, “Compact, generalized component mode mistuning representation for modeling bladed disk vibrations,” *AIAA Journal*, vol. 45, pp. 2285–2298, September 2007.
- [27] D. Young, “Vibration of rectangular plates by the ritz method,” *Journal of Applied Mechanics*, vol. 17, pp. 448–453, March 1950.

- [28] A. A. L. A. Technologies, “Stainless steel al 17-4 precipitation hardening alloy.” www.alleghenyludlum.com, 2006.
- [29] J. Brown and R. Grandhi, “Probabilistic analysis of geometric uncertainty effects on blade modal response,” ASME Turbo Expo, July 2003.
- [30] L. Chen and S. S. Rao, “Fuzzy finite element approach for the vibration analysis of imprecisely defined systems,” *Finite Elements in Analysis and Design*, vol. 27, pp. 69–83, 1997.
- [31] A. Keerti and E. Nikolaidis, “Combined approximations for efficient probabilistic analysis of structures,” *AIAA Journal*, vol. 42, July 2004.
- [32] C. Pierre and D. V. Murthy, “Aeroelastic modal characteristics of mistuned blade assemblies: Mode localization and loss of eigenstructure,” tech. rep., National Aeronautics and Space Administration (NASA), July 1991.
- [33] Y. J. Yan and P. L. Cui, “Vibration mechanism of a mistuned bladed disk,” *Journal of Sound and Vibration*, vol. 317, pp. 294–307, 2008.
- [34] A. Rivas-Guerra and M. P. Mignolet, “Local/global effects of mistuning on the forced response of bladed disks,” *Journal of Engineering for Gas Turbines and Power*, vol. 126, pp. 131–141, January 2004.
- [35] C. Pierre, “Mode localization and eigenvalue loci veering phenomena in disordered structures,” *Journal of Sound and Vibration*, vol. 126, no. 3, pp. 485–502, 1988.
- [36] D. Laxalde and F. Thouverez, “Mistuning identification and model updating of an industrial blisk,” *International Journal of Rotating Machinery*, 2007.
- [37] T. M. Bartsch, “High cycle fatigue science and technology program,” Tech. Rep. AFRL-PR-WP-TR-2002-2060, Air Force Research laboratory, AFRL/RZTS, May 2002.
- [38] “Usaf accident investigation boards.” <http://usaf.aib.law.af.mil/AIBInfo.html>, July 2013.
- [39] C. M. Firrone and T. Berruti, “An electromagnetic system for the non-contact excitation of bladed disks,” *Experimental Mechanics*, vol. 52, pp. 447–459, 2012.
- [40] M. Nikolic, *New Insights Into the Blade Mistuning Problem*. PhD thesis, Imperial College London / University of London, August 2006.
- [41] A. V. Srinivasan, “Flutter and resonant vibration characteristics of engine blades,” *Journal of Engineering for Gas Turbines and Power*, vol. 119, pp. 742–775, 1997.
- [42] D. J. Ewins, “Vibration characteristics of bladed disc assemblies,” *Journal of Mechanical Science*, vol. 12, no. 5, pp. 165–186, 1973.

- [43] M. T. Bah, P. B. Nair, A. Bhaskar, and A. J. Keane, "Statistical analysis of the forced response of mistuned bladed disks using stochastic reduced basis methods," *AIAA Journal*, 2002.
- [44] M. P. Mignolet and A. J. Rivas-Guerra, "Identification of mistuning characteristics of bladed disks from free response data - part i," *Journal of Engineering for Gas Turbines and Power*, vol. 123, April 2001.
- [45] M. P. Mignolet and A. J. Rivas-Guerra, "Identification of mistuning characteristics of bladed disks from free response data - part ii," *Journal of Engineering for Gas Turbines and Power*, vol. 123, April 2001.
- [46] M. T. Yang and J. H. Griffin, "A normalized modal eigenvalue approach for resolving modal interaction," *Journal of Engineering for Gas Turbines and Power*, vol. 119, no. 3, pp. 647–650, 1997.
- [47] M. T. Yang and J. H. Griffin, "A reduced order model of mistuning using a subset of nominal modes," *Journal of Engineering for Gas Turbines and Power*, 2001.
- [48] A. Sinha, "Reduced order model of a bladed rotor with geometric mistuning," *Journal of Turbomachinery*, vol. 131, July 2009.
- [49] D. M. Feiner and J. H. Griffin, "A fundamental model of mistuning for a single family of modes," *Journal of Turbomachinery*, 2002.
- [50] D. M. Feiner and J. H. Griffin, "Mistuning identification of bladed disks using a fundamental mistuning model - part i: Theory," *Journal of Turbomachinery*, 2004.
- [51] D. M. Feiner and J. H. Griffin, "Mistuning identification of bladed disks using a fundamental mistuning model - part ii: Application," *Journal of Turbomachinery*, vol. 26, pp. 159–165, 2004.
- [52] J. P. Ayers, D. M. Feiner, , and J. H. Griffin, "A reduced order model for transient analysis of bladed disk forced response," tech. rep., Carnegie Mellon University, 2005.
- [53] M. R. Rossi, D. M. Feiner, and J. H. Griffin, "Experimental study on the fundamental mistuning model (fmm) for probabilistic analysis," tech. rep., Carnegie Mellon University, 2002.
- [54] C. Pierre, S. L. Ceccio, and M. P. Castanier, "Experimental based development and validation of mistuning models for bladed disks," tech. rep., Air Force Office of Scientific Research, 2004.
- [55] C. Pierre, S. L. Ceccio, and M. P. Castanier, "Experimental based development of phenomenological mistuning models for bladed disks," tech. rep., Air Force Office of Scientific Research, 2004.

- [56] C. Pierre, S. L. Ceccio, and M. P. Castanier, "Next-generation modeling, analysis, and testing of the vibration of mistuned bladed disks," tech. rep., Air Force Office of Scientific Research, 2007.
- [57] T. Peng and S. K. Gupta, "Model and algorithms for point cloud construction using digital projection patterns," *Journal of Computing and Information Science in Engineering*, vol. 7, pp. 372–381, July 2007.
- [58] L. Yao and W. A. Sethares, "Sensor placement for on-orbit modal identification via a genetic algorithm," *AIAA Journal*, vol. 31, pp. 1922–1928, October 1993.
- [59] M. D. Sensmeier and K. I. Nichol, "Optimum placement of sensors for vibration measurements on turbin blades," *AIAA Journal*, 1998.
- [60] S. S. Rao, *Vibration of Continuous Systems*. John Wiley and Sons, Inc., 2007.
- [61] L. Meirovitch, *Fundamentals of Vibrations*. McGraw-Hill, 2001.
- [62] S. Laborde and A. Calvi, "Spacecraft based sine vibration test data uncertainties investigation based on stochastic scatter approach," *Mechanical Systems and Signal Processing*, vol. 32, pp. 69–78, 2012.
- [63] A. Sinha and S. Chen, "A higher order technique to compute the statistics of forced response of a mistuned bladed disk assembly," *Journal of Sound and Vibration*, vol. 130, no. 2, pp. 207–221, 1989.
- [64] C. Lykins, D. Thomson, and S. L. C. Pomfret, "The air force's applications of probabilistics to gas turbine engines," *AIAA Journal*, 1994.
- [65] 46th AIAA/ASME/ASCE/AHS/ASC Structures, Structural Dynamics & Materials Conference, *Assessment of Probabilistic Methods for Mistuned Bladed Disk Vibration*, April 2005.
- [66] C. Soize, "A comprehensive overview of a non-parametric probabilistic approach of model uncertainties for predictive models in structural dynamics," *Journal of Sound and Vibration*, vol. 288, pp. 623–652, 2005.
- [67] S. Salicone, *Measurement Uncertainty: An Approach via the Mathematical Theory of Evidence*. Springer Science and Business Media, LLC, 2007.
- [68] K. Alvin, W. Oberkampf, K. Diegert, and B. Rutherford, "Uncertainty quantification in computational structural dynamics: A new paradigm for model validation," tech. rep., Sandi National Laboratories, 1998.
- [69] B. M. Ayyub and G. J. Klir, *Uncertainty Modeling and Analysis in Engineering and the Sciences*. Taylor and Francis Group, 2006.

- [70] 5th World Congress on Computational Mechanics, *Role of Non-Determinism in Verification and Validation of Computational Solid Mechanics Models*, July 2002.
- [71] S. Adhikari, “Uncertainty propagation in structural dynamics.” Uncertainty Quantification and Management in Aircraft Design - Advanced Simulation Research Centre, Bristol, November 2012.
- [72] J. Doyle, “Analysis of feedback systems with structured uncertainties,” vol. 129, IEE Proceedings, November 1982.
- [73] M. Steinbuch, J. Terlouw, O. Bosgra, and S. Smit, “Uncertainty modeling and structured singular value computation applied to an electromechanical system,” vol. 139, IEE Proceedings, May 1992.
- [74] T. Hasselman, “Quantification of uncertainty in structural dynamic models,” *Journal of Aerospace Engineering*, vol. 14, pp. 158–165, October 2001.
- [75] T. Hasselman and G. Lloyd, “A top down approach to calibration, validation, uncertainty quantification, and predictive accuracy assessment,” *Computational Methods in Applied Mechanics and Engineering*, vol. 197, pp. 2596–2606, 2008.
- [76] M. Rahimi, “Uncertainty treatment in forced response calculations of mistuned bladed disks,” *Mathematics and Computers in Simulation*, vol. 80, pp. 1746–1757, 2010.
- [77] T. L. Geers, “An objective error measure for the comparison of calculated and measured transient response histories,” tech. rep., Lockheed Palo Alto Research Laboratory, 1984.
- [78] D. M. Russell, “Error measures for comparing transient data, parts i and ii,” 68th Shock and Vibration Symposium, November 1997.
- [79] W. L. Oberkampf and M. F. Barone, “Measures of agreement between computation and experiment: Validation metrics,” *Journal of Computational Physics*, vol. 217, pp. 5–36, 2006.
- [80] ECCOMAS Thematic Conference on Computational Methods in Structural Dynamics and Earthquake Engineering, *Uncertainty in Structural Dynamics: Experimental Case Studies on Beams and Plates*, June 2007.
- [81] 10th International Conference, Recent Advances in Structural Dynamics (RASD), *Uncertainty Based Experimental Validation of Nonlinear Reduced Order Models*, 2010.
- [82] B. S. de Lima and N. F. Ebecken, “A comparison of models for uncertainty analysis by the finite element method,” *Finite Elements in Analysis and Design*, 2000.

- [83] H.-Z. Huang and H.-B. Li, "Perturbation finite element method of structural analysis under fuzzy environments," *Engineering Applications of Artificial Intelligence*, pp. 83–91, 2005.
- [84] G. Fraccone and M. Ruzzene, "Assessment of uncertainty in response estimation for turbine engine bladed disks," *Journal of Sound and Vibration*, vol. 317, pp. 625–645, 2008.
- [85] G. M. C. Fraccone, *Bayesian Networks for Uncertainty Estimation in the Response of Dynamic Structures*. PhD thesis, Georgia Institute of Technology, August 2008.
- [86] J. Coey, *Magnetism and Magnetic Materials*. Cambridge University Press, 2010.
- [87] J. A. Beck, J. A. Justice, O. E. Scott-Emuakapor, T. J. George, and J. M. Brown, "Next generation traveling wave excitation system for integrally bladed rotors." Preprint submitted to Elsevier February 19, 2014.
- [88] Fabreeka Vibration and Control, *Fabcel Pads: For Reduction of Low Frequency Vibration*, June 2011. www.fabreeka.com.
- [89] S. Timoshenko, *Vibration Problems in Engineering*. D. Van Nostrand Company, Inc., 2nd edition ed., 1937.
- [90] L. Xin, H. Wenguang, and S. Haoliang, "The theory and application of structured light photogrammetry with known angle," *The International Archives of the Photogrammetry, Remote Sensing and Spatial Information Sciences*, 2008.
- [91] R. L. Keizer, H. Jun, and S. M. Dunn, "Structured light: Theory and practice and practice and practice...," *SPIE*, vol. 1406, pp. 88–97, 1990.
- [92] F. Chen, G. M. Brown, and M. Song, "Overview of three dimensional shape measurement using optical methods," *Optical Engineering*, vol. 39, pp. 10–22, January 2000.
- [93] C. Je, S. W. Lee, and R.-H. Park, "High contrast color stripe pattern for rapid structured light range imaging," 2004.
- [94] GOM mbH - Gesellschaft für Optische Messtechnik, *ATOS Triple Scan - Revolutionary Scanning Technique*.
- [95] International Deep Drawing Research Group (IDDRG) 2008 International Conference, *Validation and Optimization of Numerical Simulations by Optical Measurements of Tools and parts*, June 2008.
- [96] D. E. Holland and M. P. Castanier, "Testing and calibration procedures for mistuning identification and traveling wave excitation of bladed disks," *Journal of Engineering for Gas Turbines and Power*, vol. 132, April 2010.

- [97] P. F. Pai and S. Y. Lee, “Non-linear structural dynamics characterization using a scanning laser vibrometer,” *Journal of Sound and Vibration*, pp. 657–687, 2003.
- [98] “Tessellation.” <http://en.wikipedia.org/wiki/Tessellation>, June 2013.
- [99] R. Scopigno and D. Zorin, eds., *Registration of Point Cloud Data from a Geometric Optimization Perspective*, Eurographics Symposium on Geometry Processing, 2004.
- [100] R. J. Allemang and D. L. Brown, “A correlation coefficient for modal vector analysis,” tech. rep., University of Cincinnati, 1982.
- [101] P. Blaschke and D. J. Ewins, “The mac revisited and updated,” in *IMAC XV - 15th International Modal Analysis Conference - Current Horizon for Structural Damage Detection*, pp. 147–154, Society for Experimental Mechanics, 1997.
- [102] R. J. Allemang, “The modal assurance criterion - 20 years of use and abuse,” *Journal of Sound and Vibration*, pp. 14–21, August 2003.
- [103] W. Navidi, *Principles of Statistics for Engineers and Scientists*. McGraw Hill Higher Education, 2010.
- [104] J. Mandel, *The Statistical Analysis of Experimental Data*. Dover Publications, Inc., 1964.
- [105] “Design of experiments.” <http://en.wikipedia.org/wiki/Designofexperiments>, July 2013.
- [106] D. C. Montgomery, *Design and Analysis of Experiments*. John Wiley and Sons, Inc., 8 ed., 2013.
- [107] “Why $p=0.05$.” <http://www.jerrydallal.com/LHSP/p05.htm>, May 2012.
- [108] Y. Dodge, *The Concise Encyclopedia of Statistics*. Springer Science, 2008.
- [109] “Determining sample size: How to ensure you get the correct sample size.” website: <http://www.qualtrics.com/blog/determining-sample-size/>.
- [110] M. L. Boas, *Mathematical Methods in the Physical Sciences*. John Wiley and Sons, Inc., third ed., 2006.
- [111] L. Rayleigh, *Theory of Sound*. Dover Publications, second american edition ed., 1945.
- [112] G. Cox, A. Palazotto, J. Beck, and J. Brown, “The experimental foundation used to validate a reduced order model for mistuned rotors,” in *2014 AIAA Science and Technology Forum and Exposition (SciTech 2014); National Harbor, MD*, no. AIAA-2014-0099, American Institute for Aeronautics and Astronautics (AIAA), January 2014.

- [113] “Thales’ theorem.” website: <http://www.mathworld.wolfram.com/ThalesTheorem.html>.
- [114] P. J. Torvik, “On estimating system damping from frequency response bandwidths,” *Journal of Sound and Vibration*, pp. 6088–6097, 2011.
- [115] I. Voyles and C. Roy, “Evaluation of model validation techniques in the presence of uncertainty,” in *2014 AIAA Science and Technology Forum and Exposition (SciTech 2014); National Harbor, MD*, no. AIAA-2014-0120, American Institute for Aeronautics and Astronautics (AIAA), January 2014.
- [116] W. Ritz, “Über eine neue method sur losung gewisser variationsprobleme der mathematische physik,” *Journal fur Reine and Angewandte Mathematik*, vol. 135, pp. 1–61, 1909.
- [117] R. C. Colwell and H. C. Hardy, “The frequencies and nodal systems of circular plates,” *Philisophical Magazine*, vol. 24, no. 165, pp. 1041–1055, 1937.

Appendix A: Frequency Response Functions

A.1 FRF Information

A.1.1 Frequency Response Function Discussion.

Fundamentally, the FRF is the ratio of system response to the system input in the frequency domain. This is shown in the following equation.

$$H(\omega) = \frac{X(\omega)}{F(\omega)} \quad (\text{A.1})$$

Here, ω is the frequency variable, $X(\omega)$ is the system response, and $F(\omega)$ is the system input. As each of these variables are a function of frequency, this implies each is represented in the frequency domain. The foundation of the FRF lies in the mapping from the time domain to the frequency domain. This is performed through the Fourier Transform.

$$F(f) = \int_{-\infty}^{\infty} f(t)e^{-2\pi i k x} dt \quad (\text{A.2})$$

Because computers sample at discrete times, rather than continuously, the Fourier Transform can be represented in the following manner.

$$F(k) = \frac{1}{N} \sum_{r=0}^{N-1} x_r e^{\frac{-i2\pi k r}{N}} \quad (\text{A.3})$$

The variable N is the number of signal samples taken. The variable r represents the time steps which range from 0 to $N - 1$. Finally, k and x represents a frequency harmonic and the temporal variables, respectively. For each frequency harmonic, k , the signal is evaluated for each discrete time step. The Fourier Transform is applied to both the input and response signals.

Two techniques are shown for deriving a system's FRF. The first technique is used when distinct signal frequencies may not be necessarily known *a priori*. The second technique can be used when the specific harmonic forcing is known. With this precisely

known input, the system's output for this harmonic can be measured. In each case, the system response will be measured.

A.1.1.1 First FRF Method.

Creating the FRF for the first scenario involves multiple steps, as it is not simply the ratio of Fourier Transforms. The FRF is a ratio of two Power Spectral Density (PSD) quantities. Like the FRF, the PSD also gives a signal's frequency content. It provides the power of a signal distributed over a range of frequencies. To create the FRF, an input auto PSD and output cross PSD is needed.

There is no phase information associated with the auto PSD because it is a real valued, even function. The cross PSD, on the other hand, is an odd function and does possess phase information. Intuitively, this phase relationship is possible because there may exist a phase difference in signals between the input and output.

The input auto PSD is calculated by taking the product of the input signal's Fourier Transform and its complex conjugate. The asterisk (*) represents the complex conjugate.

$$S_{xx} = \text{Input}^* \times \text{Input} \quad (\text{A.4})$$

The output cross PSD is the product of the input signal's Fourier transform and the corresponding output's complex conjugate.

$$S_{xy} = \text{Input}^* \times \text{Output} \quad (\text{A.5})$$

Finally, the ratio of the output cross PSD to the input auto PSD gives the FRF.

$$H1 = \frac{S_{xy}}{S_{xx}} \quad (\text{A.6})$$

A.1.1.2 Second FRF Method.

The second method for developing the system's FRF involves using discrete points to create the graph. Using this strategy implies the input frequency is known. The system input is applied at the known frequency. Next, the system's maximum response is recorded.

This gives a single point on the FRF. This process is repeated for different frequencies. Typically, the ordinate on the FRF is in units of decibels (dB). This unit is used because of its ability to represent both large and small quantities on the same scale. Converting from response amplitude to decibels is performed through the following equation.

$$Y_{dB} = 20\log_{10}(Y_{mag}) \quad (A.7)$$

By ascertaining the maximum forced response for a system at 10,000 different frequencies between 1 and 1,500. $\frac{rad}{sec}$, the following FRF is produced.

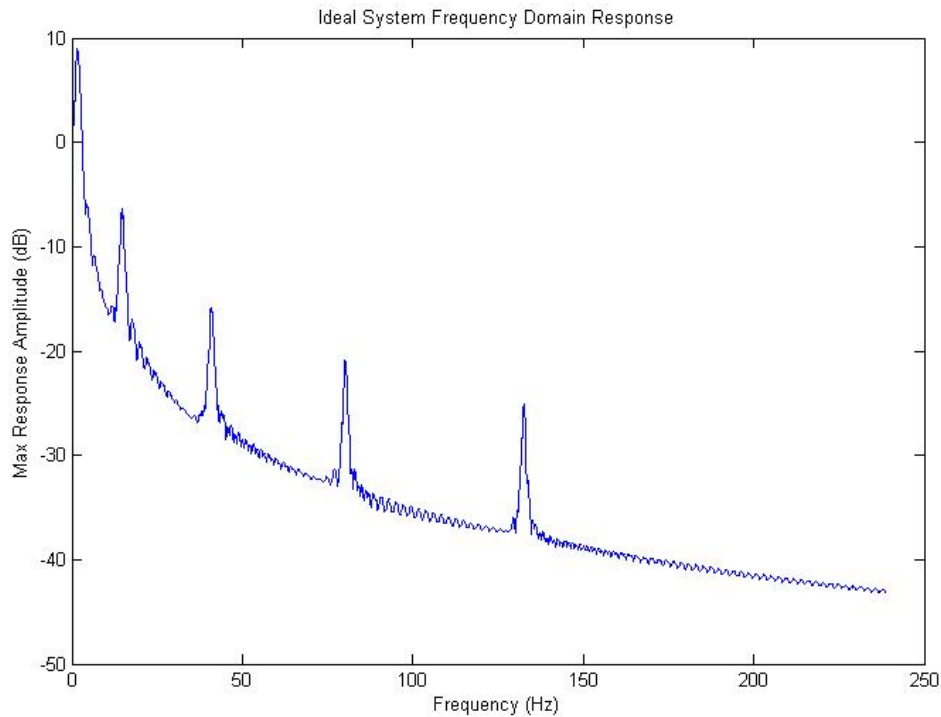


Figure A.1: Ideal System FRF

On this FRF, the frequencies associated with the first five bending modes of the simply supported beam are clearly seen. Each natural frequency, corresponding to its own bending mode, is seen with each peak on the FRF.

Appendix B: Previous Authors' Equation Derivations

The information in Appendix provides additional insight into the ideas and rationale behind some of the previous researchers' work.

B.1 Hollkamp Development

The section will illustrate how Hollkamp developed the equation of motion used in his research. Following a simplified approach for a two degree of freedom system, the process illustrates how Hollkamp developed his model.

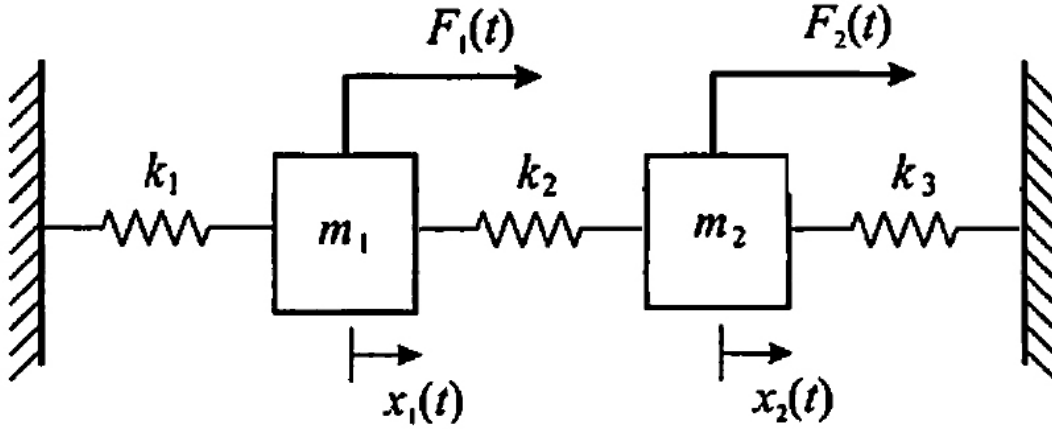


Figure B.1: Simple Two Degree of Freedom System

Here, the mass matrix is given as:

$$[m] = \begin{bmatrix} m_1 & 0 \\ 0 & m_2 \end{bmatrix} \quad (\text{B.1})$$

Similarly, for each spring, the next equation shows the stiffness matrices.

$$[k] = \begin{bmatrix} k & -k \\ -k & k \end{bmatrix} \quad (\text{B.2})$$

Next, a free body diagram of the two degree of freedom system model is given.

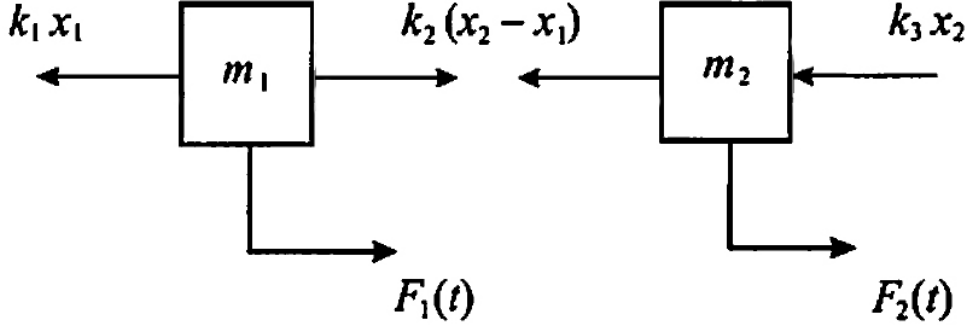


Figure B.2: Simple Two Degree of Freedom System Free Body Diagram

Applying Newton's second law of motion to each mass element produces the following equations for the displacement functions $x_1(t)$ and $x_2(t)$.

$$F = ma \quad (\text{B.3})$$

$$F_1(t) = m_1 \ddot{x}_1 + (k_1 + k_2)x_1 - k_2 x_2 \quad (\text{B.4})$$

$$F_2(t) = m_2 \ddot{x}_2 + (k_2 + k_3)x_2 - k_2 x_1 \quad (\text{B.5})$$

These equations can be recast into matrix form:

$$\begin{bmatrix} m_1 & 0 \\ 0 & m_2 \end{bmatrix} \begin{Bmatrix} \ddot{x}_1 \\ \ddot{x}_2 \end{Bmatrix} + \begin{bmatrix} k_1 + k_2 & -k_2 \\ -k_2 & k_2 + k_3 \end{bmatrix} \begin{Bmatrix} x_1 \\ x_2 \end{Bmatrix} = \begin{Bmatrix} F_1(t) \\ F_2(t) \end{Bmatrix} \quad (\text{B.6})$$

Thus:

$$[m]\ddot{x} + [k]x = F(t) \quad (\text{B.7})$$

Multiplying through by the inverse of the mass matrix produces:

$$\ddot{x} + [m]^{-1}[k]x = [m]^{-1}F(t) \quad (\text{B.8})$$

The middle term is conveniently expressed as the square of the system's natural frequency, ω_n^2 . In the case of a matrix equation, such as this, this middle term is a matrix of the system natural frequencies along the diagonal. This is no different from what it seen in Hollkamp's

model. Equation 2.3 gives the representation of the natural frequencies in Hollkamp's work. Hollkamp's coupling term, Equation 2.1, connects each blade to one another. This same connection is seen in Equation B.6 where, when examining the stiffness matrix, the spring k_2 connects masses m_1 and m_2 .

B.2 Yang Development

Yang considers an eigenproblem for an ideal system.

$$K^o \Phi^o = M^o \Phi^o \Omega^{o^2} \quad (\text{B.9})$$

The terms K and M are the system stiffness and mass matrices, respectively. The term Φ^o is a matrix comprised of the system eigenvectors, and the term Ω^o is a diagonal matrix of the system natural frequencies, or eigenvalues.

$$\Phi^o = [\Phi_1^o, \Phi_2^o, \dots, \Phi_N^o] \quad (\text{B.10})$$

$$\Omega^o = \text{diag}(\omega_1^o, \omega_2^o, \dots, \omega_N^o) \quad (\text{B.11})$$

The subscript N represents the number of system degrees of freedom. The ideal system is then perturbed using variations in both the mass and stiffness matrices.

$$(K^o + \Delta K) \Phi = (M^o + \Delta M) \Phi \Omega^{o^2} \quad (\text{B.12})$$

In this formulation, Φ and Ω are the mode shape and natural frequency of the perturbed system.

$$\Phi = [\Phi_1, \Phi_2, \dots, \Phi_N] \quad (\text{B.13})$$

$$\Omega = \text{diag}(\omega_1, \omega_2, \dots, \omega_N) \quad (\text{B.14})$$

And since the ideal system mode shapes form a complete basis, it is possible to describe a perturbed mode in terms of the ideal system modes.

$$\phi_j = \sum_i \phi_i^o \alpha_{ij} \quad (\text{B.15})$$

Here, α_{ij} is the component of the i^{th} unperturbed mode in the j^{th} perturbed mode. Because the modes are orthogonal, Equation B.12 can be expressed as:

$$\Omega^o(I + \Delta I_k)\Omega^o C_\alpha = (I + \Delta I_m)C_\alpha \Omega^2 \quad (\text{B.16})$$

Here, C_α is a matrix of α_{ij} coefficients. If the modal mass is assumed to be unity, the perturbations in the normalized modal mass and stiffness matrices, ΔI_m and ΔI_k respectively, result in:

$$\Delta I_m = \Phi^{oT} \Delta M \Phi^o \quad (\text{B.17})$$

$$\Delta I_k = \Omega^{o-1} \Phi^{oT} \Delta K \Phi^o \Omega^{o-1} \quad (\text{B.18})$$

In a similar manner, the normalized frequency matrix can be defined as:

$$\Gamma = \frac{1}{\varpi} \Omega \quad (\text{B.19})$$

The variable ϖ is a frequency reference, and Γ is a diagonal matrix of frequency terms.

$$\Gamma = \text{diag}(\gamma_1, \gamma_2, \dots, \gamma_N) \quad (\text{B.20})$$

In this formulation, $\gamma_i = \frac{\omega_i}{\varpi}$. Now the perturbed eigenproblem can be expressed as:

$$\Gamma^o(I + \Delta I_k)\Gamma^o C_\alpha = (I + \Delta I_m)C_\alpha \Gamma^2 \quad (\text{B.21})$$

Next, the eigenvalues are perturbed away from their nominal values using random variations. Assume the system has two closely modes with corresponding natural frequencies, ω_1^o and ω_2^o .

$$\varpi = \frac{1}{2}(\omega_1^o + \omega_2^o) \quad (\text{B.22})$$

The variations are defined as:

$$\delta = \frac{1}{2\varpi}|\omega_1^o - \omega_2^o| \quad (\text{B.23})$$

The perturbed modal stiffness and mass matrices are expressed as:

$$\Delta I_k = \begin{bmatrix} k_{11} & k_{12} \\ k_{12} & k_{22} \end{bmatrix} \quad (\text{B.24})$$

$$\Delta I_m = \begin{bmatrix} m_{11} & m_{12} \\ m_{12} & m_{22} \end{bmatrix} \quad (\text{B.25})$$

Now the normalized modal eigenproblem can be written as:

$$\begin{bmatrix} 1 - \delta & 0 \\ 0 & 1 + \delta \end{bmatrix} \begin{bmatrix} 1 + k_{11} & k_{12} \\ k_{12} & 1 + k_{22} \end{bmatrix} \begin{bmatrix} 1 - \delta & 0 \\ 0 & 1 + \delta \end{bmatrix} \begin{Bmatrix} \alpha_{1j} \\ \alpha_{2j} \end{Bmatrix} = \gamma_j^2 \begin{bmatrix} 1 + m_{12} & m_{12} \\ m_{12} & 1 + m_{22} \end{bmatrix} \begin{Bmatrix} \alpha_{1j} \\ \alpha_{2j} \end{Bmatrix} \quad (\text{B.26})$$

The term γ_j depicts a perturbed natural frequency, or eigenvalue.

B.3 Lim Development

The techniques the authors adopt only use a few modes of a mistuned cantilevered blade to develop the model. Because the deviations which induce the mistuning are assumed to be small, any type of small structural mistuning can be accounted for. Their technique is known as component mode mistuning. Applications for this method have also been shown to be useful for handling large structural variations, such as in the case of blade damage.

The following process steps through Lim's development.

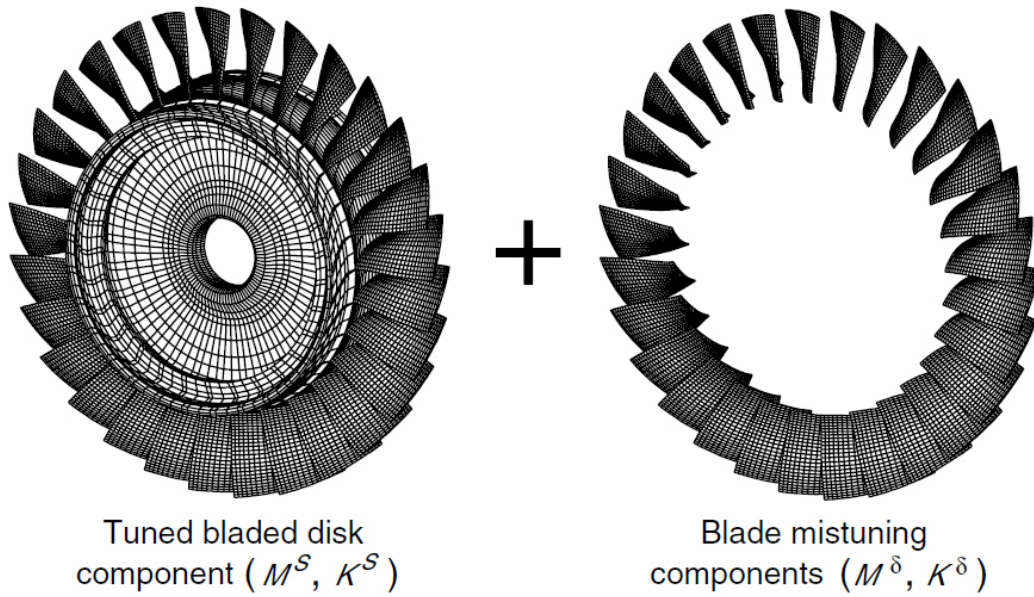


Figure B.3: Substructuring of a Mistuned Rotor [26]

The mistuning components are defined by the differences between the mistuned and tuned blade mass and stiffness matrices. For blade n :

$$M_n^\delta = M_n - M_o \quad K_n^\delta = K_n - K_o \quad (\text{B.27})$$

The authors model the tuned system components as having both *normal* and *attachment* modes. These normal modes are simply the component eigenvectors, and the attachment modes are obtained by applying a unit force to each component interface degree of freedom successively. The subscript, Γ , is a variable for the finite element blade degree of freedom.

$$M_{reduced_{tuned}} = \begin{bmatrix} I & \Phi_{tuned}^T M_{tuned} \Psi_{tuned} \\ \Psi_{tuned}^T M_{tuned} \Phi_{tuned} & \Psi_{tuned}^T M_{tuned} \Psi_{tuned} \end{bmatrix} \quad (\text{B.28})$$

$$K_{reduced_{tuned}} = \begin{bmatrix} \Lambda_{tuned} & \Phi_{tuned}^T K_{tuned} \Psi_{tuned} \\ \Psi_{tuned}^T K_{tuned} \Phi_{tuned} & \Psi_{tuned\Gamma}^T K_{tuned} \Psi_{tuned\Gamma} \end{bmatrix} \quad (\text{B.29})$$

Where in this formulation, Φ is the normal mode and Ψ is the attachment mode. Also, M and K are expressed in physical coordinates, as opposed to modal coordinates. The variable Λ is a diagonal matrix of normal mode eigenvalues. Summarizing the system in physical coordinates, the authors provide the following:

$$x_{tuned} = \begin{Bmatrix} x_{tuned_{disk}} \\ x_{tuned_{blades}} \end{Bmatrix} = \begin{bmatrix} \Phi_{tuned_{disk}} & \Psi_{tuned_{disk}} \\ \Phi_{tuned_{blades}} & \Psi_{tuned_{blades}} \end{bmatrix} \quad (\text{B.30})$$

The authors introduce mistuning using *constraint* modes. A constraint mode is obtained by applying a unit displacement to each interface degree of freedom, successively, with all other interface degree of freedom restrained. Because the authors assume mistuning only occurs with the constraint modes, there are no normal component modes. Thus, the constraint modes completely describe all mistuned motion. When expressed in generalized coordinates, the mass and stiffness matrices are the same as when expressed in physical coordinates. For the N^{th} blade in the system:

$$M_{reduced_{mistuned}} = I^T M_{mistuned} I = M^{mistuned} = B \text{diag}_{n=1,\dots,N} [M_n^{mistuned}] \quad (\text{B.31})$$

$$K_{reduced_{mistuned}} = I^T K_{mistuned} I = K^{mistuned} = Bdiag_{n=1,...,N}[K_n^{mistuned}] \quad (B.32)$$

The overall system is coupled by enforcing a compatibility condition between each component at their respective interfaces. In this paper, this is physically $x_{blades}^{tuned} = x^{mistuned}$.

Enforcing this constraint between the tuned and mistuned components produces:

$$\Phi_{blades}^{tuned} p_{\Phi}^{tuned} + \Psi_{blades}^{tuned} p_{\Psi}^{tuned} = p_{\Psi}^{mistuned} \quad (B.33)$$

This leads to the following equation of motion for the mistuned system.

$$[-\omega^2 M^{synthesized} + (1 + j\gamma)K^{synthesized}]p^{synthesized} = [\Phi^{tuned}\Psi^{tuned}]^T f \quad (B.34)$$

Where the “synthesized” mass and stiffness matrices are defined as:

$$M^{synthesized} = M_{tuned} + \begin{bmatrix} \Phi_{blades}^{tuned^T} M^{mistuned} \Phi_{blades}^{tuned} & \Phi_{blades}^{tuned^T} M^{mistuned} \Psi_{blades}^{tuned} \\ \Psi_{blades}^{tuned^T} M^{mistuned} \Phi_{blades}^{tuned} & \Psi_{blades}^{tuned^T} M^{mistuned} \Psi_{blades}^{tuned} \end{bmatrix} \quad (B.35)$$

$$K^{synthesized} = K_{tuned} + \begin{bmatrix} \Phi_{blades}^{tuned^T} K^{mistuned} \Phi_{blades}^{tuned} & \Phi_{blades}^{tuned^T} K^{mistuned} \Psi_{blades}^{tuned} \\ \Psi_{blades}^{tuned^T} K^{mistuned} \Phi_{blades}^{tuned} & \Psi_{blades}^{tuned^T} K^{mistuned} \Psi_{blades}^{tuned} \end{bmatrix} \quad (B.36)$$

Lastly, the modal coordinates are expressed as:

$$p^{synthesized} = \begin{Bmatrix} p_{\Phi}^{tuned} \\ p_{\Psi}^{tuned} \end{Bmatrix} \quad (B.37)$$

B.4 Yoo Development

This section depicts the development for Yoo’s equation of motion.

$$\begin{bmatrix} ml_1^2 & 0 & \dots & 0 \\ 0 & ml_2^2 & \dots & 0 \\ \dots & \dots & \dots & \dots \\ \dots & \dots & \dots & ml_n^2 \end{bmatrix} \begin{Bmatrix} \ddot{\theta}_1 \\ \ddot{\theta}_2 \\ \vdots \\ \ddot{\theta}_n \end{Bmatrix} + \begin{bmatrix} cl_1^2 & 0 & \dots & 0 \\ 0 & cl_2^2 & \dots & 0 \\ \dots & \dots & \dots & \dots \\ \dots & \dots & \dots & cl_n^2 \end{bmatrix} \begin{Bmatrix} \dot{\theta}_1 \\ \dot{\theta}_2 \\ \vdots \\ \dot{\theta}_n \end{Bmatrix} + \begin{bmatrix} k_r + 2k_t a^2 & -k_t a^2 & \dots & -k_t a^2 \\ -k_t a^2 & k_r + 2k_t a^2 & \dots & 0 \\ \dots & \dots & \dots & \dots \\ -k_t a^2 & 0 & \dots & k_r + 2k_t a^2 \end{bmatrix} \begin{Bmatrix} \theta_1 \\ \theta_2 \\ \vdots \\ \theta_n \end{Bmatrix} = \begin{Bmatrix} l_1 F_o \sin(\Omega t) \\ l_2 F_o \sin(\Omega t) \\ \vdots \\ l_n F_o \sin(\Omega t) \end{Bmatrix} \quad (B.38)$$

The authors then recast the equation in terms on non-dimensional parameters as shown:

$$\alpha_i \equiv \frac{l_i}{l}, \beta \equiv \frac{k_t a^2}{k_r}, \gamma \equiv \frac{T_c}{m}, \omega \equiv T\Omega, f \equiv \frac{T^2 F_o}{ml}, \tau \equiv \frac{t}{T} \quad (\text{B.39})$$

where l represents the nominal length of each pendulum and

$$T = \sqrt{\frac{ml^2}{k_r}} \quad (\text{B.40})$$

These parameters can be reinserted into the equation of motion to obtain a more generalized representation. Be aware since after non-dimensionalizing the parameters, the differentiation is now with respect to τ instead of t . The non-dimensional system is expressed as follows:

$$\begin{aligned} & \begin{bmatrix} \alpha_1^2 & 0 & \dots & 0 \\ 0 & \alpha_2^2 & \dots & 0 \\ \dots & \dots & \dots & \dots \\ \dots & \dots & \dots & \alpha_n^2 \end{bmatrix} \begin{Bmatrix} \ddot{\theta}_1 \\ \ddot{\theta}_2 \\ \vdots \\ \ddot{\theta}_n \end{Bmatrix} + \begin{bmatrix} \gamma\alpha_1^2 & 0 & \dots & 0 \\ 0 & \gamma\alpha_2^2 & \dots & 0 \\ \dots & \dots & \dots & \dots \\ \dots & \dots & \dots & \gamma\alpha_n^2 \end{bmatrix} \begin{Bmatrix} \dot{\theta}_1 \\ \dot{\theta}_2 \\ \vdots \\ \dot{\theta}_n \end{Bmatrix} + \\ & \begin{bmatrix} 1 + 2\beta & -\beta & \dots & -\beta \\ -\beta & 1 + 2\beta & \dots & 0 \\ \dots & \dots & \dots & \dots \\ -\beta & 0 & \dots & 1 + 2\beta \end{bmatrix} \begin{Bmatrix} \theta_1 \\ \theta_2 \\ \vdots \\ \theta_n \end{Bmatrix} = \begin{Bmatrix} \alpha_1 f \sin(\omega\tau) \\ \alpha_2 f \sin(\omega\tau) \\ \vdots \\ \alpha_n f \sin(\omega\tau) \end{Bmatrix} \quad (\text{B.41}) \end{aligned}$$

B.5 Young Development

Because traditional methods do not permit the development of a cantilever plate's equation of motion, approximate methods - such as the Ritz Technique (Reference [116]) must be considered. While the convergence and accuracy of the Ritz Technique has been explored throughout the literature, Young [27] says this method is not always an accurate depiction of reality. Young goes on to state "that this method gives an upper bound for the frequencies, that is, the frequencies calculated by Ritz's procedure are always higher than the exact value." Furthermore, the amount of computational time required to solve

a given problem is directly related to the set of functions used to approximate a body's movement. For a plate, some researchers have used polynomials, “while others have used combinations of the characteristic functions which define the normal modes of vibration of a uniform beam [27]”. This latter technique of using beam functions is shown here. It is noted that this development applies to a homogeneous plate of uniform thickness.

B.5.1 The Ritz Method for a Uniform Plate.

These equations and subsequent development are all taken from D. Young's paper in Reference [27].

Assume there exists a uniform plate which is vibrating harmonically with an amplitude of $w(x, y)$ and angular frequency ω ($\frac{rad}{sec}$). As such, the plate's maximum potential energy is given as:

$$V = \frac{D}{2} \iint \left[\left(\frac{\partial^2 w}{\partial x^2} \right)^2 + \left(\frac{\partial^2 w}{\partial y^2} \right)^2 + 2\mu \frac{\partial^2 w}{\partial x^2} \frac{\partial^2 w}{\partial y^2} + 2(1 - \mu) \left(\frac{\partial^2 w}{\partial x \partial y} \right)^2 \right] dx dy \quad (B.42)$$

The maximum kinetic energy can be expressed as:

$$T = \frac{1}{2} \rho h \omega^2 \iint \omega^2 dx dy \quad (B.43)$$

Equating the potential and kinetic energy relationships produces:

$$\omega^2 = \frac{2}{\rho h} \frac{V}{\iint \omega^2 dx dy} \quad (B.44)$$

Timoshenko (Reference [89]) describes the process to find the plate's natural frequency: Equation B.44 is minimized using expressions for w which satisfy the plate's boundary conditions. Young states “the direct application of the calculus of variations to minimize Equation B.44 leads to the partial differential equation for a vibrating plate.” But rather using this technique, the Ritz Method is employed. Here, the plate deflection, w , is assumed to be a linear series of what are known as “admissible¹¹” functions. The coefficients for each admissible function are adjusted so as to minimize Equation B.44. This is the method

¹¹An admissible function satisfies what are known as “artificial boundary conditions”. These boundary conditions are prescribed as the plate's slope and deflection.

shown in Timoshenko's work (Reference [89]). For rectangular plates, with the edges parallel to the x and y axes, Young uses the following series approximation for the plate deflection, $w(x, y)$:

$$w(x, y) = \sum_{m=1}^p \sum_{n=1}^q A_{mn} X_m(x) Y_n(y) \quad (\text{B.45})$$

When Equation B.45 is substituted into Equation B.44, the right hand side becomes a function of the coefficients, A_{mn} . This expression is then minimized by taking the partial derivative with respect to each coefficient and equating it to zero. As such, this produces a system of equations having the following form:

$$\frac{\partial V}{\partial A_{ik}} - \frac{\omega^2 \rho h}{2} \frac{\partial}{\partial A_{ik}} \iint \omega^2 dx dy = 0 \quad (\text{B.46})$$

Here, the term A_{ik} is any one of the coefficients A_{mn} . The natural frequencies are found from the condition that the determinant of the system equations must vanish.

B.5.2 Characteristic Functions.

As stated, the plate deflection is assumed to be combinations of those characteristic functions defining the normal vibration modes of a uniform beam. Timoshenko (Reference [89]) gives those functions applicable to the cantilever plate, specifically functions for clamped-free and free-free beams (Equation B.47 and Equations B.48 through B.51, respectively).

$$\phi_r = \cosh\left(\frac{\epsilon_r x}{L}\right) - \cos\left(\frac{\epsilon_r x}{L}\right) - \alpha_r \left(\sinh\left(\frac{\epsilon_r x}{L}\right) - \sin\left(\frac{\epsilon_r x}{L}\right) \right) \quad (\text{B.47})$$

$$\phi_1 = 1 \quad (\text{B.48})$$

$$\phi_2 = \sqrt{3} \left(1 - \frac{2x}{L} \right) \quad (\text{B.49})$$

$$\phi_r = \cosh\left(\frac{\epsilon_r x}{L}\right) + \cos\left(\frac{\epsilon_r x}{L}\right) - \alpha_r \left(\sinh\left(\frac{\epsilon_r x}{L}\right) + \sin\left(\frac{\epsilon_r x}{L}\right) \right) \quad (\text{B.50})$$

$$(r = 3, 4, 5, \dots) \quad (\text{B.51})$$

In each of these equations, $r = 1, 2, \dots, \infty$; thus, there are infinite number of functions associated with each equation. The values of α_r and ϵ_r are given in Figure 3.42. **Note:**

in this figure, the subscript m equals the subscript r in Equation B.47. **Note:** in this figure, the the subscript n equals the subscript r in Equations B.48 through B.51. The boundary conditions satisfied in each set of equations are the same as the end conditions of the corresponding beam. That is to say, for a clamped-free condition, there does not exist any displacement or slope at $x = 0$, nor does there exist moment or shear at $x = L$. For a free-free condition, there does not exist moment or shear at either end of the beam ($x = 0$ and $x = L$).

B.5.3 Characteristic Function Orthogonality Relationships.

Each set of functions is orthogonal on the interval 0 to L. As such, for any two functions ϕ_r and ϕ_s in the same set of functions, the following relations hold:

$$\int_0^L \phi_r \phi_s dx = \begin{cases} 1, & \text{if } r = s \\ 0, & \text{if } r \neq s \end{cases} \quad (\text{B.52})$$

$$\int_0^L \frac{d^2 \phi_r}{dx^2} \frac{d^2 \phi_s}{dx^2} dx = \begin{cases} \frac{\epsilon_r^4}{L^3}, & \text{if } r = s \\ 0, & \text{if } r \neq s \end{cases} \quad (\text{B.53})$$

For ϕ_1 and ϕ_2 from the free-free functions:

$$\int_0^L \left(\frac{d^2 \phi_1}{dx^2} \right)^2 dx = \int_0^L \left(\frac{d^2 \phi_2}{dx^2} \right)^2 dx = 0 \quad (\text{B.54})$$

In addition to evaluating the expressions in Equations B.52 and B.53, the following integrals also require evaluation when using these types of functions in the Ritz Method

$$\int_0^L \phi_r \frac{d^2 \phi_s}{dx^2} dx \quad (\text{B.55})$$

$$\int_0^L \frac{d\phi_r}{dx} \frac{d\phi_s}{dx} dx \quad (\text{B.56})$$

For the Clamped-Free and Free-Free beams, Figures B.4 and B.5, respectively provide the values for the integrals in Equations B.55 and B.56.

Values of $\int_0^L \frac{d\phi_r}{dx} \frac{d\phi_s}{dx} dx$

$\begin{matrix} s \\ r \end{matrix}$	1	2	3	4	5
1	4.64778	- 7.37987	3.94151	- 6.59339	4.59198
2	- 7.37987	32.41735	- 22.35243	13.58245	- 22.83952
3	3.94151	- 22.35243	77.29889	- 35.64827	20.16203
4	- 6.59339	13.58245	- 35.64827	117.90185	- 48.71964
5	4.59198	- 22.83952	20.16203	- 48.71964	228.13325

Values of $\int_0^L \phi_r \frac{d^2\phi_s}{dx^2} dx$

$\begin{matrix} s \\ r \end{matrix}$	1	2	3	4	5
1	0.85824	- 11.74322	27.45315	- 37.39025	51.95662
2	1.87385	- 13.29425	- 9.04222	30.40119	- 33.70907
3	1.56451	3.22933	- 45.90423	- 8.33537	36.38656
4	1.08737	5.54065	4.25360	- 98.91821	- 7.82895
5	0.91404	3.71642	11.23264	4.73605	-171.58466

Figure B.4: Characteristic Function Values for the Clamped-Free Beam [27]

Values of $\int_0^L \frac{d\phi_r}{dx} \frac{d\phi_s}{dx} dx$

$r \backslash s$	1	2	3	4	5	6	7
1	0	0	0	0	0	0	0
2	0	12.00000	0	13.85641	0	13.85641	0
3	0	0	49.48082	0	35.37751	0	36.60752
4	0	13.85641	0	108.92459	0	57.58881	0
5	0	0	35.37751	0	186.86671	0	78.10116
6	0	13.85641	0	57.58881	0	284.68314	0
7	0	0	36.60752	0	78.10116	0	402.22805

Values of $\int_0^L \phi_r \frac{d^2\phi_s}{dx^2} dx$

$r \backslash s$	1	2	3	4	5	6	7
1	0	0	18.58910	0	43.98096	0	69.11504
2	0	0	0	40.59448	0	84.08889	0
3	0	0	-12.30262	0	52.58440	0	101.62255
4	0	0	0	-46.05012	0	55.50868	0
5	0	0	1.80069	0	-98.90480	0	60.12891
6	0	0	0	5.28566	0	-171.58566	0
7	0	0	0.57069	0	9.86075	0	-263.99798

Figure B.5: Characteristic Function Values for the Free-Free Beam [27]

B.5.4 Application of the Ritz Method.

The characteristic functions will be used for the X_m and Y_n terms in Equation B.45. If the plate in Figure B.6 is clamped along the edge $x = 0$ and free along the remaining three edges, the clamped-free equation should be used for X_m and the free-free equation should be used for Y_n . When using one of the characteristic functions for X_m , take $L = a$. Similarly, when using one of the characteristic functions for Y_n , let $L = b$, and then replace x with y .

The appropriate change in subscripts r and s to either m and i or to n and k are to be made in each case.

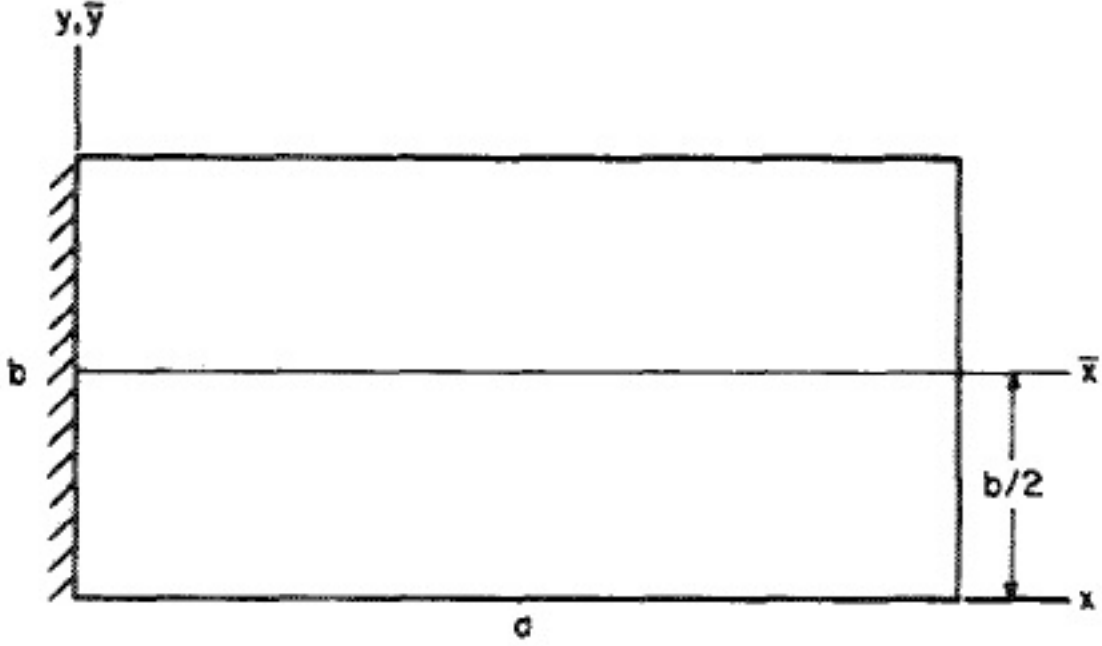


Figure B.6: Plate Coordinate System [22]

To further simplify the problem definition, the following notation is adopted.

$$E_{im} = a \int_0^a X_i \frac{d^2 X_m}{dx^2} dx \quad E_{mi} = a \int_0^a X_m \frac{d^2 X_i}{dx^2} dx \quad (\text{B.57})$$

$$F_{kn} = b \int_0^b Y_k \frac{d^2 Y_n}{dy^2} dy \quad F_{nk} = b \int_0^b Y_n \frac{d^2 Y_k}{dy^2} dy \quad (\text{B.58})$$

$$H_{im} = a \int_0^b \frac{dX_i}{dx} \frac{dX_m}{dx} dx \quad K_{kn} = b \int_0^a \frac{dY_k}{dy} \frac{dY_n}{dy} dy \quad (\text{B.59})$$

Using Equation B.45 and Equation B.42 and using the orthogonal relationships in Equations B.52 and B.53, the set of expressions in Equation B.46 can be reduced to:

$$\sum_{m=1}^p \sum_{n=1}^q [C_{mn}^{(ik)} - \lambda \delta_{mn}] A_{mn} = 0 \quad (\text{B.60})$$

Where:

$$\lambda = \frac{\omega^2 \rho h a^3 b}{D} \quad (\text{B.61})$$

$$\delta_{mn} = 1 \text{ for } mn = ik \quad (\text{B.62})$$

$$= 0 \text{ for } mn \neq ik \quad (\text{B.63})$$

When $mn \neq ik$:

$$C_{mn}^{(ik)} = \mu \frac{a}{b} [E_{mi} F_{kn} + E_{im} F_{nk}] + 2(1 - \mu) \frac{a}{b} H_{im} K_{kn} \quad (\text{B.64})$$

and for the case when $mn = ik$:

$$C_{ik}^{(ik)} = \frac{b}{a} \epsilon_i^4 + \frac{a^3}{b^3} \epsilon_k^4 + 2\mu \frac{a}{b} E_{ii} F_{kk} + 2(1 - \mu) \frac{a}{b} H_{ii} K_{kk} \quad (\text{B.65})$$

There will be one Equation B.60 for each of the pq combinations of ik . The characteristic values of λ are found by ensuring the determinant of this system of equations equals zero.

B.5.5 Square Cantilever Plate.

Assume the plate shown in Figure B.6 is clamped along the edge $x = 0$ and free on the remaining three. Because of these boundary conditions, the X_m term is expressed using the clamped-free functions and the Y_n term is expressed using the free-free functions. Letting $a = b$ and Poisson's ratio = 0.3, Young established the coefficients $C_{mn}^{(ik)}$ for an 18-term series by taking $m = 1, 2, 3$ and $n = 1, 2, 3, 4, 5, 6$. This results in a system of 18 equations via Equation B.60. This system of 18 equations can be divided into 2 groups of 9 equations each. One group includes those equations where $n = 1, 3, 5$ and represents deflection which is *symmetric* about the line $y = b/2$. The other group, consisting of $n = 2, 4, 6$, represents deflection which is *antisymmetric* about the line $y = b/2$. Young provides the coefficients for the symmetrical group. These are shown in Figure B.7.

1	k	$c_{11}^{(1k)}$	$c_{13}^{(1k)}$	$c_{15}^{(1k)}$	$c_{21}^{(1k)}$	$c_{23}^{(1k)}$	$c_{25}^{(1k)}$	$c_{31}^{(1k)}$	$c_{33}^{(1k)}$	$c_{35}^{(1k)}$
1	1	12.36	4.79	11.33	0	10.95	24.72	0	8.72	20.64
1	3	4.79	828.51	244.21	-65.49	-474.80	-342.30	153.10	165.95	234.73
1	5	11.33	244.21	15794.99	-154.94	-549.75	-1637.83	362.23	629.15	170.16
2	1	0	-65.49	-154.94	485.52	-74.14	-175.41	0	18.01	42.61
2	3	10.45	-474.80	-549.75	-74.14	3329.87	1388.69	-50.43	-1526.98	-1061.02
2	5	24.72	-342.30	-1637.83	-175.41	1388.69	24372.88	-119.31	-1247.98	-5675.23
3	1	0	153.10	362.23	0	-50.43	-119.31	3806.55	-256.00	-605.67
3	3	8.72	165.95	629.15	18.01	-1526.98	-1247.98	-256.00	10000.69	3079.54
3	5	20.64	234.73	170.16	42.61	-1061.02	-5675.23	-605.67	3079.54	41370.70

Figure B.7: Cantilever Plate Symmetric Mode Coefficients [27]

The equations obtained from Figure B.7 are expressed as:

$$(12.36 - \lambda)A_{11} + 4.79A_{13} + 11.33A_{15} + \dots = 0 \quad (B.66)$$

$$4.79A_{11} + (828.51 - \lambda)A_{13} + 244.21A_{15} + \dots = 0 \quad (B.67)$$

$$11.33A_{11} + 244.21A_{13} + (15,794.99 - \lambda)A_{15} + \dots = 0 \quad (B.68)$$

Here, only the first three equations are shown; the remaining six equations follow the same pattern, using the information from Figure B.7. Solving this system involves assuming an initial value, such as 1.0, for A_{11} . This results in the following expression:

$$\lambda = 12.36 + 4.79A_{13} + 11.33A_{15} + \dots \quad (B.69)$$

The remaining equations are expressed in the form of the following equation.

$$A_{13} = -(4.79 + 244.21A_{15} + \dots)/(828.51 - \lambda) \quad (B.70)$$

For the first trial, values for the remaining coefficients (A_{13}, A_{15}, \dots) are assumed. Using these initial trial values, λ is found using Equation B.69. The coefficient A_{13} is then determined from Equation B.70. This same procedure is performed for the remaining coefficients. After the values for A_{mn} are calculated, they are substituted back into Equation B.69 and a second value for λ is found. This procedure is repeated until a sufficient level of convergence for λ and A_{mn} is achieved.

Appendix C: Physical Interpretation of the Statistical Concept of "P-Value"

In the course of this research, especially with the ANOVA and its interpretation, I continued to inquire about the physical meaning behind the P-Value. I am including this section to further clarify this concept. Physically, the P-Value is the probability the collected data will be *at least* this *inconsistent* with the hypothesis, assuming the hypothesis is true.

The P-Value is not a direct probability the null hypothesis is true. Rather, a high P-Value means the data is highly consistent with the hypothesis. Conversely, a low P-Value indicates a hypothesis should be rejected. The P-Value does not provide direct probabilities about the hypothesis itself. On the other hand, assume two means were compared, and a P-Value of 0.02 was obtained. This indicates there is a 2% chance of observing a difference in the means as large as was observed, even if the population means were identical.

Appendix D: Circular Plate Equation Derivation

The development to reach this step is given in Reference [60]. The process to derive the free vibration solution from the equation of motion for a circular plate's transverse vibration is shown here. Equation D.1 is the free vibration equation for a circular plate.

$$D\nabla^4 w + \rho h \frac{\partial^2 w}{\partial t^2} = 0 \quad (\text{D.1})$$

Here, the Laplacian is defined as:

$$\nabla^2 = \frac{\partial^2}{\partial r^2} + \frac{1}{r} \frac{\partial}{\partial r} + \frac{1}{r^2} \frac{\partial^2}{\partial \theta^2} \quad (\text{D.2})$$

Using the Laplacian to expand out Equation D.1 gives:

$$\begin{aligned} D \left(\frac{\partial^4 w}{\partial r^4} + \frac{2}{r} \frac{\partial^3 w}{\partial r^3} - \frac{1}{r^2} \frac{\partial^2 w}{\partial r^2} + \frac{1}{r^3} \frac{\partial w}{\partial r} + \frac{2}{r^2} \frac{\partial^4 w}{\partial r^2 \partial \theta^2} \right. \\ \left. - \frac{2}{r^3} \frac{\partial^3 w}{\partial r \partial \theta^2} + \frac{4}{r^4} \frac{\partial^2 w}{\partial \theta^2} + \frac{1}{r^4} \frac{\partial^4 w}{\partial \theta^4} \right) + \rho h \frac{\partial^2 w}{\partial t^2} = 0 \end{aligned} \quad (\text{D.3})$$

Let:

$$w(r, \theta, t) = W(r, \theta)T(t) \quad (\text{D.4})$$

Substituting this expression into Equation D.3 gives:

$$DT(t)[\dots] + \rho h W(r, \theta) \frac{d^2 T(t)}{dt^2} = 0 \quad (\text{D.5})$$

In this equation, the term "[...]" is the expanded portion of Equation D.3. Continuing:

$$\begin{aligned} DT(t)[\dots] &= -\rho h W(r, \theta) \frac{d^2 T(t)}{dt^2} \\ \frac{D}{\rho h} \frac{1}{W(r, \theta)} [\dots] &= -\frac{1}{T(t)} \frac{d^2 T(t)}{dt^2} = \omega^2 \end{aligned} \quad (\text{D.6})$$

Here, since each side of the equation is a function of its own variable type (spatial or temporal) and the equations are equal to one another, it follows that each equation is equal

to a constant. The temporal portion of this expression is:

$$\begin{aligned} -\frac{1}{t(T)} \frac{d^2 T(t)}{dt^2} &= \omega^2 \\ \frac{d^2 T(t)}{dt^2} + \omega^2 T(t) &= 0 \end{aligned} \quad (D.7)$$

Following, the spatial portion can be found via:

$$\begin{aligned} \frac{D}{\rho h} [\dots] &= \omega^2 \\ \frac{D}{\rho h} [\dots] &= W(r, \theta) \omega^2 \\ [\dots] &= W(r, \theta) \frac{\rho h \omega^2}{D} \\ [\dots] - \frac{\rho h \omega^2}{D} W(r, \theta) &= 0 \end{aligned} \quad (D.8)$$

Here, let:

$$\lambda^4 = \frac{\rho h \omega^2}{D} \quad (D.9)$$

And recall:

$$[\dots] = \nabla^4 W(r, \theta) \quad (D.10)$$

Therefore, the circular plate's spatial equation is given as:

$$\nabla^4 W(r, \theta) - \lambda^4 W(r, \theta) = 0 \quad (D.11)$$

Using the definition of the Laplacian (Equation D.2 in the spatial equation produces two separate equations.

$$\frac{\partial^2 W}{\partial r^2} + \frac{1}{r} \frac{\partial W}{\partial r} + \frac{1}{r^2} \frac{\partial^2 W}{\partial \theta^2} + \lambda^2 W = 0 \quad (D.12)$$

$$\frac{\partial^2 W}{\partial r^2} + \frac{1}{r} \frac{\partial W}{\partial r} + \frac{1}{r^2} \frac{\partial^2 W}{\partial \theta^2} - \lambda^2 W = 0 \quad (D.13)$$

These two equations can be further broken down by invoking the separation of variables technique once more. Allowing:

$$W(r, \theta) = R(r)\Theta(\theta) \quad (D.14)$$

Substituting this expression back into Equations D.12 and D.13 and dividing each equation by $R(r)\Theta(\theta)/r^2$ gives:

$$\frac{r^2}{R(r)} \left[\frac{d^2 R(r)}{dr^2} + \frac{1}{r} \frac{dR(r)}{dr} \pm \lambda^2 \right] = -\frac{1}{\Theta(\theta)} \frac{d^2 \Theta}{d\theta^2} = \alpha^2 \quad (\text{D.15})$$

Following the same rationale as before, since each side of the equality is an equation of its own variable, and each equation is equal to one another, it follows that each equation is also equal to a constant. Each side of the equation gives its own type of information. Specifically, the left hand side provides angular displacement information and the right hand side gives radial displacements. Thus, the angular equation can be expressed as:

$$\frac{d^2 \Theta}{d\theta^2} + \alpha^2 \Theta = 0 \quad (\text{D.16})$$

The solution to Equation D.16 is the well known form:

$$\Theta(\theta) = A \cos(\alpha\theta) + B \sin(\alpha\theta) \quad (\text{D.17})$$

And the expression for the radial portion of displacement:

$$\frac{d^2 R}{dr^2} + \frac{1}{r} \frac{dR}{dr} + \left(\pm \lambda^2 - \frac{\alpha^2}{r^2} \right) R = 0 \quad (\text{D.18})$$

The expression for the plate displacement, $W(r, \theta)$, must be a continuous function to make physical sense, the angular portion of the displacement, $\Theta(\theta)$, must be periodic. Proceeding around the circular plate, its period equals 2π . Thus the displacement function can be expressed as:

$$W(r, \theta) = W(r, \theta + 2\pi) \quad (\text{D.19})$$

Since the angular displacement is periodic around the plate's circumference, the term α must be an integer value. Let this integer equal m . The equation describing the radial portion of the plate's displacement can again be expressed as two separate equations:

$$\frac{d^2 R}{dr^2} + \frac{1}{r} \frac{dR}{dr} + \left(\lambda^2 - \frac{\alpha^2}{r^2} \right) R = 0 \quad (\text{D.20})$$

$$\frac{d^2 R}{dr^2} + \frac{1}{r} \frac{dR}{dr} - \left(\lambda^2 + \frac{\alpha^2}{r^2} \right) R = 0 \quad (\text{D.21})$$

Equation D.20 is a Bessel differential equation of order α with an argument λr . The solution of said equation is given as:

$$R_1(r) = C_1 J_m(\lambda r) + C_2 Y_m(\lambda r) \quad (D.22)$$

The terms J_m and Y_m are Bessel functions of the first and second kind, respectively. Each of these Bessel functions is of order m . Equation D.21 is a Bessel differential equation of order α with an imaginary argument $i\lambda r$. The solution to this equation is given by:

$$R_2(r) = C_3 I_m(\lambda r) + C_4 K_m(\lambda r) \quad (D.23)$$

The terms I_m and K_m are modified Bessel functions of the first and second kind. Again, these equations are of order m . Using this information, the general solution to Equation D.11 is therefore:

$$W(r, \theta) = \left[C_m^{(1)} J_m(\lambda r) + C_m^{(2)} Y_m(\lambda r) + C_m^{(3)} I_m(\lambda r) + C_m^{(4)} K_m(\lambda r) \right] (A_m \cos(m\theta) + B_m \sin(m\theta)) \quad (D.24)$$

Here, the variable m takes on integer values (0,1,2,...). The constants $C_m^{(1)}, C_m^{(2)}, C_m^{(3)}, C_m^{(4)}, A_m, B_m$, and λ depend on the plate's boundary conditions.

For this work, the circular plate has free edges. Analogous to other continuous structures with a free edge, a free boundary does not possess moment or shear. The moment resultant is given as:

$$M_r = -D \left[\frac{\partial^2 w}{\partial r^2} + \nu \left(\frac{1}{r} \frac{\partial w}{\partial r} + \frac{1}{r^2} \frac{\partial^2 w}{\partial \theta^2} \right) \right] = 0 \quad (D.25)$$

And the shear:

$$V_r = Q_r + \frac{1}{r} \frac{\partial M_{r\theta}}{\partial \theta} \quad (D.26)$$

Expanding out the differential in the shear equation gives:

$$-D \left[\frac{\partial}{\partial r} (\nabla^2 w) + \frac{1-\nu}{r} \frac{\partial}{\partial \theta} \left(\frac{1}{r} \frac{\partial^2 w}{\partial r \partial \theta} - \frac{1}{r^2} \frac{\partial w}{\partial \theta} \right) \right] = 0 \quad (D.27)$$

Substituting the moment and shear expressions into Equation D.24, gives the circular plate's frequency equation. Leissa shows this portion of the derivation in Reference [22]. The result is given in Equation D.28. In this equation, the prime notation denotes a “derivative with respect to the argument.” [60]

$$\begin{aligned} & \frac{(\lambda a)^2 J_m(\lambda a) + (1 - \nu)[\lambda a J'_m(\lambda a) - m^2 J_m(\lambda a)]}{(\lambda a)^2 I_m(\lambda a) - (1 - \nu)[\lambda a I'_m(\lambda a) - m^2 I_m(\lambda a)]} = \\ & = \frac{(\lambda a)^2 I'_m(\lambda a) + (1 - \nu)m^2[\lambda a J'_m(\lambda a) - J_m(\lambda a)]}{(\lambda a)^2 I'_m(\lambda a) - (1 - \nu)m^2[\lambda a I'_m(\lambda a) - I_m(\lambda a)]} \end{aligned} \quad (D.28)$$

Rao [60] shows a table (Table D.1) which gives the natural frequencies for a free circular plate with a Poisson's ratio of 0.33. Here, m is the number of nodal diameters. This information was originally found in Leissa [22] and Colwell [117]. Here, the Bessel function roots are found via:

$$(\lambda a)^2 = \omega a^2 \sqrt{\frac{\rho h}{D}} \quad (D.29)$$

Table D.1: Natural Frequencies of Vibration for a Circular Plate with a Free Edge

No. of Nodal Circles (n)	m = 0	m = 1	m = 2	m = 3
0	-	-	5.253	12.23
1	9.084	20.52	35.25	52.91
2	38.55	59.86	83.9	111.3
3	87.80	119.0	154.0	192.1

Appendix E: ANSYS Input File Example

This appendix gives an example MatLab m-file which generates the required text based file for a harmonic analysis within ANSYS. Capt Alex Kaszynski (AFRL/RQTI) developed this code. This code's function is summarized in Table E.1.

Table E.1: Summary of MatLab File Function

Line Numbers	Function
1-2	Clear all workspace variables
3	Define the output file name Give this file the variable name “outputname”
4	Open “outputname” and assign it the variable name <i>fid</i>
7-20	Define the Input and Output node numbers
22-23	Specify the number of modes to solve for in the analysis
25-26	Define the frequency range (Hz)
27-28	Specify the number of steps the analysis should take in this frequency range (frequency resolution)
30	Define number of blades
31	Engine Order excitation level
32	Number of blades
33	load magnitude applied to each blade (lbf)
36-38	Decompose load into real and imaginary components
50	Define Poisson’s ratio
51	Define the density ($\frac{slinch}{in^3}$)
52	Define the elastic modulus (psi)
92-114	Set the force at each input node
124-125	Set the damping ratio (ζ)

```

1  clc
2  clear all
3  outputname = strcat(pwd, './_Modal_SUP_Analysis.inp');
4  fid = fopen(outputname, 'w+');
5
6
7  node      = [4929, 31691:18430:326571]; % Output Nodes
8  out       = node;                      % Variable for Output Nodes
9
10 % Output Nodes
11 % node_out      = [338931, 338997, 339063, 339129, 339195, 339261,...
12 %               339327, 339393, 339459, 339525, 339591, 339657,...
13 %               339723, 338601, 338667, 338733, 338799, 338865];
14 % out           = node_out;
15
16 % Input Nodes
17 % node_in       = [4929, 31691, 50121, 68551, 86981, 105411,...
18 %               123841, 142271, 160701, 179131, 197561, 215991,...
19 %               234421, 252851, 271281, 289711, 308141, 326571];
20 % in            = node_in;
21
22 nmodes        = 108;                % original
23 %nmodes = 18;
24
25 fr_range      = [1150 1450]; % original
26 %fr_range      = [1250 1300];
27 Loadsteps     = 300;                % original
28 %Loadsteps     = 50;
29
30 blade         = 1; % Output blade
31 EO            = 1; % Engine Order

```



```

32 N          = 18; % Number of Blades
33 Fmag       = .000001; % Magnitude of Force (lbf)
34
35 % Force as a function engine order
36 F = ...
    Fmag*(cos(2*pi*EO*(0:1:N-1)'/N)+sqrt(-1)*sin(2*pi*EO*(0:1:N-1)'/N)); ...
    % Fmag Forcing in Z-Dir
37 Freal = real(F);
38 Fimag = imag(F);
39
40
41
42 %-----
43 %                               MODAL ANALYSIS AND DATA RETRIEVAL
44 %-----
45
46
47 fprintf(fid, '/PREP7\n');
48 fprintf(fid, 'ALLSEL\n');
49 fprintf(fid, 'ALLSEL\n');
50 fprintf(fid, 'MP,      NUXY,  1,  0.270\n');           % Poisson
51 fprintf(fid, 'MP,      DENS,  1,  7.2981E-04\n');     % Density ...
    (slinch/cubic inch)
52 fprintf(fid, 'MP,      EX,   1,  29.9255E06\n');     % Elastic ...
    Modulus (psi)
53 fprintf(fid, 'EMODIF,ALL,MAT,1\n');
54
55
56 % ANALYSIS is Free-Free
57
58
59 % Modal analysis parameters

```

```

60 fprintf(fid, '/SOLU\n');
61 fprintf(fid, 'ANTYPE,2,new\n');
62 fprintf(fid, 'MODEOPT,lanb,%i,1,40000\n', nmodes);    % original
63 %fprintf(fid, 'MODEOPT,lanb,%i,1,1350\n', nmodes);
64 fprintf(fid, 'EQSLV,SPARSE\n');
65 fprintf(fid, 'LUMPM,0\n');
66 fprintf(fid, 'MXPAND,,,,YES\n');
67 fprintf(fid, 'PSTRES,0\n');
68 fprintf(fid, 'BCSOPTION,,INCORE\n');
69 fprintf(fid, 'SOLVE\n');
70 fprintf(fid, 'FINI\n');
71
72 % Output mode Frequencies
73 % fprintf(fid, '/POST1\n');
74 % fprintf(fid, '/OUTPUT,MODES_RST,txt\n');
75 % fprintf(fid, 'SET,LIST\n');
76 % fprintf(fid, '/OUTPUT,TERM\n');
77
78
79 %-----
80 %               HARMONIC ANALYSIS AND DATA RETRIEVAL
81 %-----
82 fprintf(fid, '/PREP7\n');
83
84 % Clear Forces
85 fprintf(fid, 'ALLSEL\n');
86 % fprintf(fid, 'F,ALL,FX,0\n');
87 % fprintf(fid, 'F,ALL,FY,0\n');
88 % fprintf(fid, 'F,ALL,FZ,0\n');
89 fprintf(fid, 'DDEL,ALL,ALL\n');    % Delete degree of freedom constrains
90
91 % Set Force

```

```

92 for ii=1:length(node)
93     fprintf(fid,'F,%i,FZ,%f,%f\n',node(ii),Freal(ii),Fimag(ii));
94 end
95
96 % Components of load applied at each blade
97 % Radial_X = [0.0284, 0.2077, 0.3619, 0.4725, 0.5261, 0.5162,...
98 %             0.4440, 0.3183, 0.1543, -0.0284, -0.2077, -0.3619,...
99 %             -0.4725, -0.5261, -0.5162, -0.4440, -0.3183, -0.1543];
100 %
101 % Tangent_Y = [0.5292, 0.4945, 0.3995, 0.2563, 0.0822, -0.1018,...
102 %              -0.2735, -0.4123, -0.5013, -0.5298, -0.4945, ...
103 %              -0.3995,...
104 %              -0.2563, -0.0822, 0.1018, 0.2735, 0.4123, 0.5013];
105 % Set Force
106 for ii=1:length(node)
107     fprintf(fid,'F,%i,FZ,%f,%f\n',node(ii),Freal(ii),Fimag(ii)); ...
108         % Pure Z
109         %(Pure Z was originally here)
110 %     fprintf(fid,'F,%i,FX,%f,%f\n',in(ii),Radial_X(ii),0.0);
111 %     fprintf(fid,'F,%i,FY,%f,%f\n',in(ii),Tangent_Y(ii),0.0);
112 %     fprintf(fid,'F,%i,FZ,%f,%f\n',in(ii),-0.8480,0.0); % ...
113         Constant FZ (doesn't change around rotor circumference)
114 end
115
116
117 fprintf(fid,'NSEL,ALL\n');
118
119 % Analysis
120 fprintf(fid,'/solu\n');

```

```

121 fprintf(fid, 'antype,3,new\n');
122 fprintf(fid, 'HROPT,MSUP\n');
123 fprintf(fid, 'HROUT,OFF\n');
124 %fprintf(fid, 'DMPRAT,0.00002\n');    % original
125 fprintf(fid, 'DMPRAT,0.00007882\n'); % Updated Damping Ratio for ...
    the blades' first bend freq. range.
126
127
128
129
130 fprintf(fid, 'OUTPR,BASIC,1\n');
131 fprintf(fid, 'LUMPM,0\n');
132 fprintf(fid, 'NSUBST,%i\n', Loadsteps);
133 fprintf(fid, 'EQSLV,SPARSE\n');
134 fprintf(fid, 'HARFRQ,%i,%i\n', fr_range(1), fr_range(2));
135 fprintf(fid, 'PSTRES,0\n');
136 fprintf(fid, 'KBC,1\n'); % Step not Ramp input
137 fprintf(fid, 'SOLVE\n');
138 % fprintf(fid, 'save\n');
139 fprintf(fid, 'FINI\n');
140
141 % Modal Superposition Solution Expansion
142 fprintf(fid, '/SOLU\n');
143 fprintf(fid, 'EXPASS,ON\n');
144 fprintf(fid, 'NUMEXP,ALL,,NO\n');
145 fprintf(fid, 'SOLVE\n');
146 fprintf(fid, 'FINI\n');
147
148
149 % HARMONIC ANALYSIS Write Results
150 fprintf(fid, '/post26\n');

```

```

151 fprintf(fid,'PLCPLX,0\n'); % Specifies the part of a complex ...
    variable to ...
152                                % display 0 - Amplitude, 1 Phase ...
                                angle, 2 real, 3 imaginary
153 fprintf(fid,'PRCPLX,1\n'); % Defines the output form for complex ...
    variables
154                                % 0 - Real and imaginary, 1 - ...
                                Amplitude and
155                                % phase
156
157 for ii=1:size(out,2)
158     fprintf(fid,'NSOL,2,%i,U,X\n',out(ii));
159     fprintf(fid,'NSOL,3,%i,U,Y\n',out(ii));
160     fprintf(fid,'NSOL,4,%i,U,Z\n',out(ii));
161
162     if ii<10
163         fprintf(fid,'/OUTPUT,blade0%i,vec\n',ii);
164     else
165         fprintf(fid,'/OUTPUT,blade%i,vec\n',ii);
166     end
167     fprintf(fid,'PRVAR,2,3,4\n');
168     fprintf(fid,'/OUTPUT,TERM\n');
169 end
170
171
172 fprintf(fid,'/POST1\n');
173 fprintf(fid,'/OUTPUT,DrivingFreq,txt\n');
174 fprintf(fid,'SET,LIST\n');
175 fprintf(fid,'/OUTPUT,TERM\n');
176 fclose(fid);

```

Appendix F: Additional Experimental Equipment and Revised Technique

Aside from the equipment discussed in Chapter 4, this appendix adds several items to that list. The items in this appendix are used in the revised experimental setup. The following list those items:

- Standard level
- T-Square
- Laser Straight Edge

Here, the level is used to ensure both the actuator ring and rotor stack (rotor atop its central pedestal) are level. If the components are not level, the electromagnetic actuators will no longer be normal to the blade surfaces. The T-square is used in conjunction with the actuator ring to mark diameter locations. Recall Thales' Theorem in Chapter 5, Section 5.4. Lastly, the laser straight edge tools are used in the rotor alignment.

The key points for the revised experimental technique are summarized as follows:

- Center Rotor and its Actuator Ring on the Laser Vibrometer Home Position
- Perform Rotor 2-D Alignment
 - Ensure alignment locations are near the output locations
 - Ensure peak signal return at each alignment locations
- Define the measurement locations around the rotor
 - Define the local measurement locations with respect to the global origin.
 - Perform necessary global to local coordinate transformation to ensure the local measurement locations depict the same points on each blade.

- Focus the laser beam at a measurement location
- Perform initial traveling wave test
- Estimate damping for each natural frequency for the mode of interest
- Define a system time constant
- Define bandwidth as next increment larger than the highest natural frequency for the mode of interest
- Adjust the number of FFT lines to define the total acquisition time as greater than or equal to 4 time constants

Appendix G: Additional Details for the ANOVA Process in Chapter 5.9

When performing the ANOVA for each pair of blades, maintaining constant input and output locations for each pair of blades is critical. This is the rationale for invoking the techniques in Chapter, 5, Section 5.4, Subsection 5.4.0.3 when defining the scan point array. Because a population of blades was tested, any experimental variability requires careful control. For reference, Figure G.1 provides the input location information. Recall Table 3.12 for the 3 factors and their respective levels.

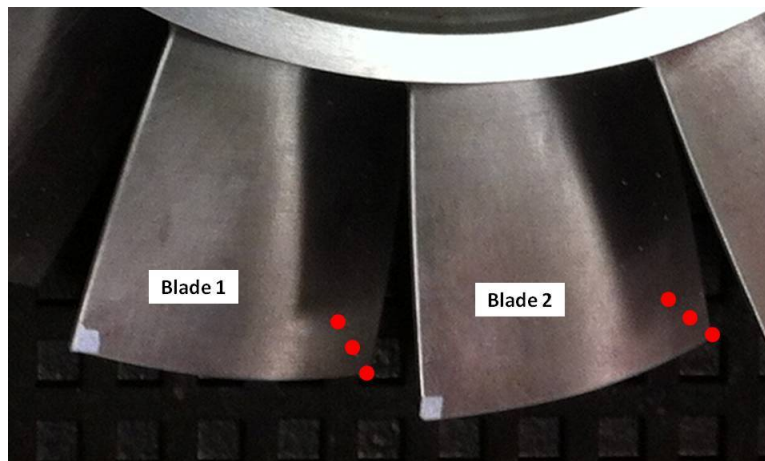


Figure G.1: Blade Input Regions for the ANOVA

Starting with a prescribed EO level, the input actuators are positioned at the outboard input locations. The excitation system then sweeps through a specified range of frequencies. In this research, this frequency range excited the blades' first bending mode. Analogous to the standard traveling wave test, the blades are excited and a response is measured at a point. This is repeated three times for each output location. This process produces the three replicates per output location. This process is repeated for all ten output locations.

The PolyTec system produces both an overall average FRF and individual scan point FRFs depicting the blades' response. The individual FRFs are of interest here. Figure G.2 gives a sample of a data table recorded for two blades.

In Figure G.2, the input locations for each blade are denoted as "A", indicating the actuator is at the most outboard location. For each natural frequency, the peak response is measured at each output location. This is highlighted in Figure G.3. After recording the peak response from each output location and natural frequency, one blade's input location is incremented inward to the next location. The excitation and measurement process is repeated for all 9 input location combinations, as indicated in Figure G.4.

After recording the maximum responses at each natural frequency, at each output location, and for each input combination, the ANOVA can be performed. This ultimately produces 90 observations at each natural frequency. This is determined by way of the 9 input combinations and 10 output locations. The ANOVA is performed at each natural frequency, as highlighted in Figure G.5. For the research compressor, 17 natural frequencies were easily observed during each test. For the 2 levels of EO excitation, this produced 3,060 data points. This is for a single pair of blades. In this research, 24 pair of blades on the research compressor were tested. This produced 73,440 data points.

Using the Excel add-on program, DOE Pro, the response data was organized according to the respective factor levels, for each natural frequency, as demonstrated in Table G.1. The table is significantly truncated from what was actually collected. The factor levels Table G.1 continue to be incremented until all 180 combinations of EO, input location, and output location for the data points are captured. For each natural frequency, DOE Pro produces an ANOVA table: indicating the main effects, interactions, sum of squares, degrees of freedom, mean square, F-statistic, and P-value. Figure G.2 illustrates a sample ANOVA table.

Input Loc.	Scan Point	Resonant Frequency (Hz)					
		1204.895	1207.52	1261.96	1417.664	1443.238
Blade 1 A	1	5.459E-06	1.140E-07	1.489E-06	1.337E-06	4.412E-06
	2	5.423E-06	1.136E-07	1.460E-06	1.324E-06	4.354E-06
	3	5.211E-06	1.061E-07	1.410E-06	1.251E-06	4.141E-06
	4	5.189E-06	1.093E-07	1.400E-06	1.273E-06	4.135E-06
	5	5.321E-06	1.080E-07	1.444E-06	1.294E-06	4.257E-06
	AVG	5.321E-06	1.102E-07	1.441E-06	1.296E-06	4.260E-06
Blade 2 A	6	4.689E-06	4.421E-07	1.309E-06	5.657E-07	4.247E-06
	7	4.730E-06	4.373E-07	1.313E-06	5.586E-07	4.226E-06
	8	4.466E-06	4.131E-07	1.234E-06	5.287E-07	3.958E-06
	9	4.474E-06	4.107E-07	1.242E-06	5.347E-07	3.996E-06
	10	4.544E-06	4.250E-07	1.273E-06	5.439E-07	4.079E-06
	AVG	4.581E-06	4.256E-07	1.274E-06	5.463E-07	4.101E-06

Figure G.2: Sample Data Table

Input Loc.	Scan Point	Resonant Frequency (Hz)					
		1204.895	1207.52	1261.96	1417.664	1443.238
Blade 1 A	1	5.459E-06	1.140E-07	1.489E-06	1.337E-06	4.412E-06
	2	5.423E-06	1.136E-07	1.460E-06	1.324E-06	4.354E-06
	3	5.211E-06	1.061E-07	1.410E-06	1.251E-06	4.141E-06
	4	5.189E-06	1.093E-07	1.400E-06	1.273E-06	4.135E-06
	5	5.321E-06	1.080E-07	1.444E-06	1.294E-06	4.257E-06
	AVG	5.321E-06	1.102E-07	1.441E-06	1.296E-06	4.260E-06
Blade 2 A	6	4.689E-06	4.421E-07	1.309E-06	5.657E-07	4.247E-06
	7	4.730E-06	4.373E-07	1.313E-06	5.586E-07	4.226E-06
	8	4.466E-06	4.131E-07	1.234E-06	5.287E-07	3.958E-06
	9	4.474E-06	4.107E-07	1.242E-06	5.347E-07	3.996E-06
	10	4.544E-06	4.250E-07	1.273E-06	5.439E-07	4.079E-06
	AVG	4.581E-06	4.256E-07	1.274E-06	5.463E-07	4.101E-06

Figure G.3: Highlighted Sample Data Table

Input Loc.	Scan Point	Resonant Frequency (Hz)					
		1204.895	1207.52	1261.96	1417.664	1443.238
Blade 1 A	1					
	2					
	3					
	4					
	5					
	AVG					
Blade 2 A	6					
	7					
	8					
	9					
	10					
	AVG					
....
						
						
						
						
Blade 1 C	1					
	2					
	3					
	4					
	5					
	AVG					
Blade 2 C	6					
	7					
	8					
	9					
	10					
	AVG					

Figure G.4: Extended Sample Data Table

Input Loc.	Scan Point	Resonant Frequency (Hz)					
		1204.895	1207.52	1261.96	1417.664	1443.238
Blade 1 A	1					
	2					
	3					
	4					
	5					
	AVG					
Blade 2 A	6					
	7					
	8					
	9					
	10					
	AVG					
.....
						
						
						
						
Blade 1 C	1					
	2					
	3					
	4					
	5					
	AVG					
Blade 2 C	6					
	7					
	8					
	9					
	10					
	AVG					

Figure G.5: Highlighted Extended Sample Data Table

Table G.1: DOE Pro Data Organization for ANOVA

Blade No.	EO Level	Input Loc.	Output Loc.	Max Response
1	1	1	1	
1	1	1	2	
1	1	1	3	
1	1	1	4	
1	1	1	5	
2	1	1	6	
2	1	1	7	
2	1	1	8	
2	1	1	9	
2	1	1	10	
1	1	1	1	
1	1	1	2	
1	1	1	3	
1	1	1	4	
1	1	1	5	
2	1	2	6	
2	1	2	7	
2	1	2	8	
2	1	2	9	
2	1	2	10	

Table G.2: Sample ANOVA Table from DOE Pro

Natural Frequency x					
Factor	Sum of Squares	DOF	Mean Square	F-Statistic	P-Value
EO Excitation (A)		(2-1)			
Input Location (B)		(3-1)			
Output Location (C)		(10-1)			
Interaction (AB)		(2-1)(3-1)			
Interaction (AC)		(2-1)(10-1)			
Interaction (BC)		(3-1)(10-1)			
Interaction (ABC)		(2-1)(3-1)(10-1)			
Error		(180-1)-(sum of other DOF)	N/A	N/A	
Total		(180-1)	N/A	N/A	N/A

Vita

Major Geoffrey S. Cox graduated from the United States Air Force Academy in May 2003. There, he received a Bachelor of Science degree in Mechanical Engineering. Assigned to Robins AFB, GA from 2003 - 2007, he worked in the C-5 Galaxy program office and developed and instructed a new Aircraft Battle Damage Repair Engineering program for AFMC. Further, Major Cox created and led a new replacement training unit concept which prepared all new incoming 62E officers for work in the Air Logistics Center. In 2007, Major Cox transitioned to Wright Patterson AFB, OH to attend the Air Force Institute of Technology. There, he earned a Master of Science degree in Aeronautical Engineering. His thesis focused on the thermo-mechanical properties of center reinforced aluminum, which is a new member of the fiber metal laminate material family. Major Cox was next assigned to the Air Force Research Lab. Here, he served as an integral member of the Analytical Mechanics Branch of the Air Vehicles Directorate, as a deputy branch chief and capability lead for aircraft sustainment. In 2011, Major Cox was assigned back to the Air Force Institute of Technology to pursue his Doctor of Philosophy in Aeronautical Engineering. His research focuses on the experimental uncertainty associated with the forced vibrations of integrally bladed rotors.

REPORT DOCUMENTATION PAGE					<i>Form Approved</i> OMB No. 0704-0188	
The public reporting burden for this collection of information is estimated to average 1 hour per response, including the time for reviewing instructions, searching existing data sources, gathering and maintaining the data needed, and completing and reviewing the collection of information. Send comments regarding this burden estimate or any other aspect of this collection of information, including suggestions for reducing this burden to Department of Defense, Washington Headquarters Services, Directorate for Information Operations and Reports (0704-0188), 1215 Jefferson Davis Highway, Suite 1204, Arlington, VA 22202-4302. Respondents should be aware that notwithstanding any other provision of law, no person shall be subject to any penalty for failing to comply with a collection of information if it does not display a currently valid OMB control number. PLEASE DO NOT RETURN YOUR FORM TO THE ABOVE ADDRESS.						
1. REPORT DATE (DD-MM-YYYY)		2. REPORT TYPE		3. DATES COVERED (From — To)		
15-09-2014		Doctoral Dissertation		Oct 2011–Sept 2014		
4. TITLE AND SUBTITLE				5a. CONTRACT NUMBER		
EXPERIMENTAL UNCERTAINTY ASSOCIATED WITH TRAVELING WAVE EXCITATION				5b. GRANT NUMBER		
				5c. PROGRAM ELEMENT NUMBER		
6. AUTHOR(S)				5d. PROJECT NUMBER		
Cox, Geoffrey S., Major, USAF				5e. TASK NUMBER		
				5f. WORK UNIT NUMBER		
7. PERFORMING ORGANIZATION NAME(S) AND ADDRESS(ES)				8. PERFORMING ORGANIZATION REPORT NUMBER		
Air Force Institute of Technology Graduate School of Engineering and Management (AFIT/EN) 2950 Hobson Way WPAFB, OH 45433-7765				AFIT-ENY-DS-14-S-26		
9. SPONSORING / MONITORING AGENCY NAME(S) AND ADDRESS(ES)				10. SPONSOR/MONITOR'S ACRONYM(S)		
Air Force Research Lab, Aerospace Systems Directorate 1950 5th Street Wright-Patterson AFB, OH 45433-7251 POC: Jeffrey Brown, Ph.D. email: jeffrey.brown.70@us.af.mil				AFRL/RQ		
				11. SPONSOR/MONITOR'S REPORT NUMBER(S)		
12. DISTRIBUTION / AVAILABILITY STATEMENT						
DISTRIBUTION STATEMENT A: APPROVED FOR PUBLIC RELEASE; DISTRIBUTION UNLIMITED						
13. SUPPLEMENTARY NOTES						
This work is declared a work of the U.S. Government and is not subject to copyright protection in the United States.						
14. ABSTRACT						
<p>This dissertation research produces the experimental techniques required to evaluate mistuning in any rotor. Within operation, a rotor is subjected to a unique pattern of frequencies acting to excite the rotor. Utilizing traveling wave excitation, a rotor's critical frequencies and the respective excitation pattern are reproduced. Individual rotor blade frequency response functions are evaluated and statistically analyzed. The experimental results serve to not only verify the degree to which a rotor is mistuned, but also to provide an indication of the forced response amplification the mistuning induces. Within the experiment, definitive specifications were developed to ensure peak rotor responses. Numerical simulations of the experiment were performed in ANSYS using a model developed by way of structured light scanning. With experimental and numerical eigenvalue differences of less than 1%, the unique modeling technique, capturing a rotor's geometric mistuning, is a valid method to predict a rotor's natural frequencies. Furthermore these same numerical results serve to validate the experimental free boundary assumption.</p>						
15. SUBJECT TERMS						
Mistuning, Forced Vibrations, Experimental Uncertainty, Traveling Wave						
16. SECURITY CLASSIFICATION OF:			17. LIMITATION OF ABSTRACT	18. NUMBER OF PAGES	19a. NAME OF RESPONSIBLE PERSON	
a. REPORT	b. ABSTRACT	c. THIS PAGE			Dr. Anthony N. Palazotto (ENY)	
U	U	U	UU	322	19b. TELEPHONE NUMBER (include area code) (937) 255-3636 x4599 anthony.palazotto@afit.edu	